TECHNICAL REPORT STANDARD TITLE PAGE

1. Report No.	2. Government Accession No.	3. Recipient's Catalog No.
MIT-MSL-RE-81		

4. Title and Subtitle	5. Report Date
A Hazard Definition for Wake Turbulence Encounter During Terminal Area Operations	March 30, 1973
	6. Performing Organization Code
7. Author(s) Raymond B. Harlan and Stephen J. Madden, Jr.	8. Performing Organization Report No.
9. Performing Organization Name and Address The Measurement Systems Laboratory Massachusetts Institute of Technology 265 Massachusetts Avenue Cambridge, Mass. 02139	10. Work Unit No.
	11. Contract or Grant No. DOT-TSC-166
12. Sponsoring Agency Name and Address Department of Transportation Transportation Systems Center Kendall Square, Cambridge 02139	13. Type of Report and Period Covered Final Report
	14. Sponsoring Agency Code

15. Supplementary Notes

16. Abstract

A six-degree-of-freedom vortex encounter simulation has been developed for use on a hybrid computer to determine the hazard potential for terminal area operations. Complete trajectory data for landing, horizontal flyby, and climbing flights are presented and conclusions are drawn from these results. A hazardous condition is defined as having the roll angle exceed ten degrees and/or the flight path angle become steeper than -4 1/2 degrees at any point along the flight path with the aircraft under autopilot control. For the two trailing aircraft which were simulated (DC-9 Series 10 and KC-135), the minimum safe separation from a single vortex, 100 feet above the ground, ranges from 75 to 130 feet for vortices with a strength of 5000 ft^2/sec. A simplified sensitivity analysis shows that the controllability of an aircraft is about twice as sensitive to changes in vortex proximity than to changes in wingspan, but if the near wingtip proximity is chosen to be the independent variable, controllability is nearly independent of aircraft size. These results are substantiated by the computer simulation.

17. Key Words	18. Distribution Statement
Wake turbulence hazard, Wake vortex, Aircraft response.	Document is available to the public through the National Technical Information Service, Springfield, Virginia 22151

19. Security Classif. (of this report)	20. Security Classif. (of this page)	21. No. of Pages	22. Price
UNCLASSIFIED	UNCLASSIFIED	238	

Form DOT F 1700.7 (8-69)

Acknowledgement

This final technical report covers the work performed under Department of Transportation Contract DOT-TSC-166 (DSR 73093) during the period May 18, 1972 to March 30, 1973. This work was performed by the M.I.T. Measurement Systems Laboratory, Cambridge, Massachusetts. This laboratory gratefully acknowledges the use of the hybrid computer facility at the Charles Stark Draper Laboratory, Cambridge, Massachusetts, and the assistance of Dr. Robert G. Stern and Messrs T. Basil Smith and Richard R. Hildebrant.

This document is disseminated under the sponsorship of the Department of Transporation in the interest of information exchange. The United States Government assumes no liability for its contents or use thereof.

ABSTRACT

A six-degree-of-freedom vortex encounter simulation has been developed for use on a hybrid computer to determine the hazard potential for terminal area operations. Complete trajectory data for landing, horizontal flyby, and climbing flights are presented and conclusions are drawn from these results. A hazardous condition is defined as having the roll angle exceed ten degrees and/or the flight path angle become steeper than -4 1/2 degrees at any point along the flight path with the aircraft under autopilot control. For the two trailing aircraft which were simulated (DC-9 Series 10 and KC-135), the minimum safe separation from a single vortex,100 feet above the ground,ranges from 75 to 130 feet for vortices with a strength of 5000 ft^2/sec. A simplified sensitivity analysis shows that the controllability of an aircraft is about twice as sensitive to changes in vortex proximity than to changes in wingspan, but if the near wingtip proximity is chosen to be the independent variable, controllability is nearly independent of aircraft size. These results are substantiated by the computer simulation.

Table of Contents

		Page
Nomenclature		
Chapter 1	Introduction	
Chapter 2	The Six-Degree-of-Freedom Vortex Encounter Simulation	
Chapter 3	Hazard Definition	
Chapter 4	Summary	
References		
Appendix A	Aircraft Modelling Program	
Appendix B	Vortex Encounter Simulation	
Appendix C	Digital Autopilot	
Appendix D	Aircraft Aerodynamic and Flight Condition Data	
Appendix E	Vortex Geometry	
Appendix F	Proof of Concept Demonstration for Verifying the Accuracy of the Six-Degree-of-Freedom Vortex Encounter Simulation	
Appendix G	Greater Southwest Airport Accident	
Appendix H	Simulation Records	

Nomenclature

a	proximity of vortex to wing center	ft
a_1	first wing element containing aileron	
a_i	last wing element containing aileron	
b	wingspan	ft
c	mean aerodynamic chord	ft
C_c	controllability coefficient	
C_D	drag coefficient	
C_{D_0}	drag coefficient at zero angle of attack	
C_{L_0}	lift coefficient at zero angle of attack	
$C_{L_{0_w}}$	wing lift coefficient at zero angle of attack	
$C_{L_{0_t}}$	stabilizer lift coefficient at zero angle of attack	
C_{L_w}	wing lift coefficient at reference flight condition	
C_{L_α}	lift curve slope	
$C_{L_{\alpha_w}}$	wing lift curve slope	
$C_{L_{\alpha_t}}$	stabilizer lift curve slope	
$C_{L_{sp}}$	derivative of lift coefficient with spoiler deflection	
$C_{L_{\delta_e}}$	derivative of lift coefficient with elevator deflection	
C_{ℓ_β}	derivative of rolling moment coefficient with sideslip	
C_{ℓ_r}	derivative of rolling moment coefficient with yawing rate (dC_ℓ/dr)	sec
C_{ℓ_p}	derivative of rolling moment coefficient with rolling rate (dC_ℓ/dp)	sec
$C_{\ell_{\delta_a}}$	der. of rolling moment coeff. with aileron deflection	
b_t	horiz. stabilizer span	

$C_{\ell_{sp}}$	derivative of rolling moment coefficient with spoiler deflections	
$C_{\ell_{\delta_r}}$	derivative of rolling moment coefficient with rudder deflection	
C_{m_0}	pitching moment coefficient at zero angle of attack	
$C_{m_{a.c.}}$	wing pitching moment at zero angle of attack	
C_{m_α}	derivative of pitching moment coefficient with angle of attack	
C_{m_q}	derivative of pitching moment coefficient with pitching rate (dC_m/dq)	sec
$C_{m_{sp}}$	derivative of pitching moment coefficient with spoiler deflection	
$C_{m_{\delta_e}}$	derivative of pitching moment coefficient with elevator deflection	
C_{n_β}	derivative of yawing moment coefficient with side-slip	
C_{n_p}	derivative of yawing moment coefficient with rolling rate (dC_n/dp)	sec
C_{n_r}	derivative of yawing moment coefficient with yawing rate (dC_n/dr)	sec
$C_{n_{\delta_a}}$	derivative of yawing moment coefficient with aileron deflection	
$C_{n_{\delta_r}}$	derivative of yawing moment coefficient with rudder deflection	
$C_{n_{sp}}$	derivative of yawing moment coefficient with spoiler deflection	
C_{y_β}	derivative of sideforce coefficient with side-slip	
C_{y_p}	derivative of sideforce coefficient with rolling rate (dC_y/dp)	sec
$C_{y_{\delta_r}}$	derivative of sideforce coefficient with rudder deflection	
$C_{y_{\beta_r}}$	vertical stabilizer sideforce curve slope	
$C_{y_{\beta_{wb}}}$	wing-body sideforce curve slope	

C_b^p	coordinate transformation matrix, from body to path axes	
D	drag force	lb
d	distance of right vortex to the right of X axis	ft
F	total force vector	lb
F_i	wing loading distribution weighting function	
h_v	vortex height above ground	ft
I_x	moment of inertia about the x body axis	slug ft^2
I_y	moment of inertia about the y body axis	slug ft^2
I_z	moment of inertia about the z body axis	slug ft^2
I_{x_z}	cross moment of inertia	slug ft^2
K	autopilot gain	
L	lift force	lb
L_w	lift of the wing	lb
$\mathcal{L}$	rolling moment	ft-lb
ℓ_r	distance between center of gravity and vertical stabilizer mean aerodynamic center	ft
M	pitching moment	ft-lb
m	mass; also number of wing segments	slugs
N	yawing moment	ft-lb
n	number of stabilizer segments	
P	rolling velocity	rad/sec
Q	pitching velocity	rad/sec
$\bar{q}$	dynamic pressure	lb/ft^2
R	yawing velocity	rad/sec
r	distance from aircraft reference frame center to a point on a flying surface	ft
r_c	vortex core radius	ft
S	wing area	ft^2
S_r	vertical stabilizer area	ft^2
S_t	horizontal stabilizer area	ft^2
s_1	first wing element containing spoilers	
s_i	last wing element containing spoilers	

U	vortex velocity vector	ft/sec
u_i	change in relative wind at i^{th} station due to yawing velocity	ft/sec
V	aircraft velocity with respect to inertial space	ft/sec
V_{rel}	relative wind velocity	ft/sec
X,Y,Z	inertial reference frame coordinates	
x,y,z	body axes	
x',y',z'	stability axes	
x_i	distance behind center of gravity of ith station aerodynamic center	ft
x_c	distance ahead of center of gravity of root quarter chord	ft
x_r	distance between fuselage reference line and vertical stabilizer	ft
x_t	distance between center of gravity and horizontal stabilizer aerodynamic center	ft
x_{wb}	distance between center of gravity and wing-body sideways aerodynamic center	ft
Y	sideforce	lb
α	angle between x body axis and component of V in x-z plane	rad
α_i	angle of attack of ith wing, segment	rad
α_{t_j}	angle of attack of jth stabilizer segment	rad
β	angle between V and x-z plane	rad
β_r	angle of attack of vertical stabilizer	rad
Γ	vortex circulation	ft^2/sec
γ	flight path angle	rad
δ	distance between vortex centerline and point on aircraft	ft
δ_a	aileron deflection	rad
δ_e	elevator deflection	rad
δ_r	rudder deflection	rad
δ_v	horizontal distance between vortices	ft
δ_w	wheel deflection	rad
ϵ	downwash angle	deg.
θ	pitch angle	rad
κ_a	aileron weighting function	

$d\epsilon/d\alpha$

κ_s	spoiler weighting function	
λ	sweepback angle of quarter chord	deg.
υ	distance between vortex centerline and point on aircraft	ft
ξ	distance along y from aircraft centerline to i^{th} segment	ft
σ	dihedral angle	rad
ϕ	roll angle	rad
ψ	heading angle	rad
$\underline{\omega}_{ip}$	angular velocity of path frame with respect to inertial frame	rad/sec
$\underline{\omega}_{bp}$	angular velocity of path frame with respect to body frame	rad/sec
$\underline{\omega}_{ib}$	angular velocity of body frame with respect to inertial frame	rad/sec

Subscripts

com	command
i	wing segment
j	stabilizer segment
trim	value established in trim loops
v	vortex
x,y,z	component along body axes
0	evaluated at zero angle of attack

Chapter 1

Introduction

With the increasing use of heavy jet aircraft in commercial operations, and the consequent threat of accidents due to wake turbulence, efforts to define the hazard potential, develop vortex monitoring systems, and modify minimum separation criteria have been underway for several years. Before the concept of a warning system can be brought to a realistic level, the hazard must be well defined. It is to this end that the work presented here was undertaken.

Quite a few definitions of the hazard region behind the generating aircraft have been offered over the past decade or more [1 to 4]. A number of these and others [5 to 7] began with flight tests and were the outgrowth of conclusions based on the reduced data. Most of the results assumed some relationship between the peak vortex induced rolling moment and the available lateral control moment. The final expressions often attempted to include the ratio of encountering aircraft wingspan to that of the generating aircraft as a significant parameter. For the most part, the hazard definitions were the results of analysing encounters, at altitudes well above those considered in terminal area operations, which often were heavily influenced by pilot inputs (mostly trying to stay in the wake while controlling the induced roll as best possible). To these tests a significant parameter often was the lead distance of the generating aircraft. On the other hand a precision and continuous measure of the proximity of the aircraft to the vortex core was unavailable. At best, pilot estimates using flow visualization (e.g. Corvus oil in jet exhausts) provided this measure.

In the first work begun at M.I.T., in 1970, to develop a hazard definition, a different approach was taken. A three-degree-of-freedom digital computer program examined vortex encounters under landing, horizontal flyby, and climbing conditions. The program used strip theory to model aircraft characteristics and generated forces and moments by integrating over the wing [8].

The Boeing KC-135 and the DeHavilland Twin Otter were simulated as aircraft encountering vortices from Boeing 707 and 747 aircraft. The hazard criterion was the same as earlier papers: a hazard exists when the vortex induced rolling moment exceeds the maximum control moment. The results of this preliminary work indicated that the hazard region depends upon the circulation and wingspan of the generating aircraft and that aircraft of the same size could be potentially hazardous to one another, at least with regard to one the size of a Boeing 707. This last conclusion is in contrast to comments made by Donaldson[4] who suggests that only the 747 and DC-10 present such a hazard.

In the simulation, only freedom in roll and in vertical and lateral translation was considered. The pilot function was introduced by a very simple algorithm which matched control moment with vortex induced moment until the former was saturated. If the vortex moment reduced to below the point of saturation, the matching was resumed with no effort to return to a wings-level condition. Hence, the aircraft was often left with a steady rolling velocity.

As an ongoing effort to properly define the hazard, a full six-degree-of-freedom program with a representative autopilot was chosen not only to provide better understanding of the encounter phenomena, but also to permit complete and objective simulation of the terminal area operation with highly repeatable results. By incorporating a target seeking capability in the autopilot, the normal pilot function in terminal operations could be approximated and trajectories would be kept more nearly on course. As a result the hazard definition relevant to these terminal area operations could be established by examining the dynamic responses of the aircraft along the entire trajectory. The results of the study would establish the minimum safe separation from a vortex which would be the basis for identifying a vortex tracking system's performance requirements.

In the new simulation, strip theory again was used to compute the wing loading, but was modified to give better matching of the nearly elliptic wing loadings and of the roll damping coefficient. Tail surface loads were also considered. The program is described in detail in Chapter 2 and Appendix B.

During the course of completing the first landing encounter simulations with this program, it was noted that the ailerons need not reach saturation before a rather violent response could result. The fact that the autopilot could not sense vortex induced moments, coupled with the autopilot dynamics and short lags representing control surface servo systems, prevented perfect moment matching with the result that some upset was always seen.

It was quickly realized that the heretofore standard hazard criterion was hardly applicable in a landing situation. Though bank angles were affected by the ratio of vortex induced to control torques, the dynamics of the autopilot placed clear limitations on the extent of this influence. After careful consideration, it was decided to place bounds on attitude during the landing phase. Autopilot performance criteria for Instrument Landing System beam capture specify limits of ten degrees on commanded bank angles. It seems reasonable to adopt the same limit for one hazard criterion; if, during a vortex encounter when landing, the roll exceeds ± 10 degrees, a hazard exists. Furthermore, it seems appropriate to place a negative limit on the flight path angle since the landing impact is related to this parameter. An increase of fifty percent over the normal value of -3 degrees appeared to be an acceptable limit; at 130 knots, the vertical component is about 17 ft/sec which is within the structural capacity of landing gears. Hence, the second hazard criterion is that flight path angles cannot exceed -4 1/2 degrees. A third, but very subjective criterion was adopted regarding the aileron commands. If the ailerons approached the saturation level during an encounter, it was considered an extraordinary workload for the pilot. However, these command angles were so closely correlated to the roll angle that this criterion was essentially redundant.

Several terms for describing the distance from the centerline of the vortex to the center of gravity of the encountering aircraft are used interchangeably in this report (e.g. separation, proximity, and approach). Separation does not refer to the distance between vortex generating and encountering aircraft as this parameter is not explicitly relevant to the current work.

Chapter 2

The Six-Degree-of-Freedom Vortex Encounter Simulation

The simulation is performed on a hybrid digital-analog computer. The main digital simulation program generates the vortex induced angle of attack field on each of the flying surfaces, together with that developed as a result of the aircraft's motion. A modified strip theory is used to change these angles into forces and moments which are then converted to analog signals. The rigid body equations of motion are solved in the analog computer. The velocity vector, in "path" axes, and angular velocity components along body axes are returned to the digital section where position and orientation are computed. The program is coupled to a digital autopilot routine which transforms cockpit control commands, and angle and rate information to appropriate control surface commands. A detailed description of the mechanics of the simulation is presented in Appendices B and C.

Program Capabilities

Vortex encounters can be separated into two classes: those nearly normal to the axis of the vortex wherein the response is predominantly in pitch, and those nearly parallel to this axis, with mostly roll response. While the former can pose structural load problems, they are for the most part of short duration and may not produce severely adverse aircraft attitudes. On the other hand, while the integrity of the aircraft is not likely to be threatened by the nearly parallel approach to a vortex, a safe attitude definitely is. Furthermore, except for the very rare case of a lingering vortex from cross runway operations, the parallel

encounter will be the most important to study with respect to terminal operations. The present effort, therefore, focuses on this case, with skew angles not exceeding fifteen degrees in either heading or flight path angle. All possible flight paths (nominally straight) within this framework can be simulated by the program. For example, a landing path considered to be in a vertical plane parallel to a vortex, at arbitrary distances from its center, can be studied. Another example is the diagonal approach wherein both heading and flight path take on small angles to the vortex line, but the trajectory need not intersect that line. In general, a vortex pair and their images below the ground are used to define the wind field. Flexibility of the program permits moving any number of these elements to suppress their influence.

By a nominally straight flight path is meant that which would occur if the vortex were not present. These paths are established from initial conditions for the aircraft at a particular point in space, removed from the vortex. The trim program adjusts ailerons, elevator, and rudder until all vehicle angular rates are reduced to zero. With a given thrust level, this process will result in some flight path angle. Thrust is then adjusted, through a potentiometer, until in steady state the desired flight path angle is reached. Heading is an independent parameter typed in through the computer console along with parameters identifying aircraft position and velocity, and vortex position and strength.

Several methods of control over the path of the aircraft can be exercised, each being a mode in the digital autopilot (see Appendix C). The most basic mode is one where stick and wheel commands from the cockpit control are transmitted directly to the simulated control surface, with no autopilot functions being performed. This mode is used mainly to observe transient responses of the aircraft to impulse control surface deflections for the purpose of verifying the aircraft modelling as it relates to the dynamic characteristics. The second mode option is the Stability Augmentation System (SAS) wherein angle rates are fed back to couple with stick and wheel commands and provide damping. The normal autopilot function is the Control Stick Steering (CSS) mode in which attitude is maintained. This mode features integrators

in the pitch and roll command chains which permit changes in pitch or heading with pulse type commands of finite duration and alleviate the need to hold the control off center once the new flight condition is achieved. Finally, a target seeking mode (ILS) is used to keep the aircraft on a predetermined flight path in the face of small disturbances. This mode is needed to minimize flight path deviations during a vortex encounter so as to maintain reasonable control over the aircraft separation from the vortex axis. Although ILS implies a landing system, the equations were formulated to accommodate any flight path angle or heading; in essence, to permit seeking a target anywhere.

While the simulation is intended to examine segments of flights where thrust is constant, this parameter can be changed during a run. Thrust is, normally controlled through a ten-turn potentiometer which is somewhat difficult to change rapidly. Through switching, a quarter-turn potentiometer to which is fastened a knob similar to the thrust levers in a cockpit, can be substituted. In either case, the thrust responds immediately to the command; no dynamic thrust response program is simulated.

Program Output

The analog output of the program consists of two strip chart recordings of parameters associated with the lateral and longitudinal degrees of freedom, and an x-y plot of the lateral and vertical position of the aircraft, with the axes of the vortices normal to the paper. A digital printout of all of these parameters, and some of the aircraft physical characteristics also can be generated, with a minimum time step of 0.2 second. A sample is shown in Figure 2-1. As explained in Appendix B, alpha and beta relate the inertial velocity vector to the body coordinate frame, and are not the normal angle of attack and sideslip. As the program was adapted from another simulation, some of the variables have changed meaning or have become obsolete. The flap variable shown has no relevance to the present program, as the aircraft is modelled for a particular flap setting which cannot be modified. Position is measured in the inertial frame, with the X axis along the ground, parallel to the vortex axis. The parameters elemomslp, ailemomslp, and rudmomslp are control moment derivatives. The last line of the printout identifies the vortex parameters of circulation, core diameter, height, lateral separation, and position of the right vortex in the inertial frame.

```
TIME =    .00        M. I. T. VORTEX SIMULATION

AIRCRAFT PARAMETERS
     MASS = 3105      CHORD =  20.20    SPAN = 130.00    WING AREA = 2400.00
     IX =  1722000.      IY =  2067000.      IZ =  3790000.      IXZ=  .0000000

COCKPIT CONTROL SETTINGS
     STICK =   .000   WHEEL =   .000   RUDDER =  .000   FLAP =  -.000

SURFACE POSITION SERVO COMMANDS
     ELV =   -5.96   RUDDER =  -2.04   AILERON =  -.46

SURFACE POSITIONS
     ELV =   -5.96   RUDDER =  -2.04   AILERON =  -.46

ENGINE DATA SUMMARY
     CTC =  .08   DTC =  .09
     EG.1 =  1238   EG.2 =  1238   EG.3 =  1238   EG.4 =  1238

AIRCRAFT STATE SUMMARY
     RHO =   .2356112E-02    DYNAMIC PRESSURE =    33.646
     ALTITUDE =  300   RATE OF CLIMB (FT./MIN.) =  -527
     V(FT/SEC) =     169   VE(FT/SEC) =  168   IAS(KNOTS) =   99      MACH =  .152
     THETA =  6.88   PHI =  .00   HEADING =  .01   ALPHA =  9.87   BETA =  .01
     P =    .021    Q =    .007    R =    .024

POSITION,VELOCITY,FORCES AND MOMENTS
     X          Y          Z          XDOT       YDOT       ZDOT
   .000E 00   .000E 00  -.300E 03   .169E 03   .000E 00   .680E 01

     LIFT       DRAG       SIDERC     ROLMOM     PCHMOM     YAWMOM
   .996E 05   .104E 05  -.345E 03   .491E 05  -.121E 06  -.331E 05

     CIRC       VOR HT     VOR SEP    RT VOR POS   CORE     FLTPTH
   .700E 04   .1[illegible]E 03   .100E 04   .100E 04   .7[illegible]E 01  -.29[illegible]E 01
```

Figure 2-1 Sample Digital Print-Out

Program Limitations

During the course of studying vortex encounters with the simulation, a limitation on the size of the airplane which could be handled by the program was discovered. The basic digital computation cycle for generating forces and moments lasts 0.2 second. If a real time scaling is used in the analog, which was the case for the present effort, a time lag corresponding to the length of this cycle will be present in the force and moment history. This has the effect of introducing a phase shifting nonlinearity which becomes increasingly significant as the natural frequencies of the aircraft are raised. Such is the case for small, highly maneuverable craft. The simulation of a Piper PA-30 "Twin Commanche" was attempted as the final member of a series of three aircraft (the others were DC-9 Series 10 and KC-135). The frequency of the longitudinal short period mode for this airplane is about one Hz while that of the dutch roll mode is about 2.5 Hz.

When first simulating this aircraft, the mechanism of the nonlinearity was not considered. The response was highly unstable in pitch, even with no control perturbations. Efforts were made to move the center of gravity forward, to provide a greater degree of static stability, with the result that the responses got worse. Finally, in an effort to comprehend the problem, the moment of inertia about the y axis was increased an order of magnitude which stabilized the airplane. Of course, the short period was increased by $\sqrt{10}$, which made the nonlinearity much less significant. The center of gravity was returned to its original point and the moment of inertia was reduced until the instability appeared. Then the center of gravity was shifted forward. The instability got worse, not better; hence, the center of gravity was moved rearward. The response improved, and the process of lowering the moment of inertia and moving the balance point was continued until the original moment of inertia was used. To achieve marginal stability under this condition, the center of gravity had to be placed one foot or 20% M.A.C. behind its original position of 25% M.A.C. Further rearward movement of an additional half foot resulted in static instability.

TP# 12348

In pursuing the reason for this response to center of gravity movement, it was learned that although the static margin increases as the center of gravity is moved forward, the short period frequency also increases. Thus, the nonlinearity introduced by the computation cycle becomes the dominant factor in the dynamic response and overrides the normally stabilizing nature of this balance point shift. At the other end of the scale, the far aft movement mentioned above pushed the center of gravity beyond the neutral point.

It was hoped that the autopilot could be used to improve the stability realized with the 45% balance point. However, any pitch angle feedback effectively tightened the control loop, increased the response frequency, and returned the simulation to its unstable state. In review of the results of trying to simulate this aircraft, it appears that aircraft with rigid body modes having frequencies in excess of about 0.3 Hz cannot be simulated satisfactorily in real time by this program. Due to a number of conditions existing at the time, an attempt to expand the time base of the simulation could not be made. This is indeed unfortunate, as the Piper PA-30 is representative of a large field of small aircraft. Study of vortex encounters with this aircraft would have permitted essentially complete coverage of the most important spectrum of aircraft with regard to the wake turbulence problem. Some controversy exists over the size of aircraft most susceptible to hazardous upset, when kept at a fixed distance from a vortex. While the completed simulations shed but little light on this subject, the sensitivity analysis presented in the next chapter does indicate the extent to which the argument is worth pursuing.

Chapter 3

Hazard Definition

The simulation studies examined three flight regimes with respect to vortex encounter: landing, horizontal flyby, and climbing. With a few climbing flights the exception, all encounters were with clockwise rotating vortices fixed at 100 feet above the runway. The objective of the study was to identify the minimum acceptable proximity to a vortex for safe completion of the mission. The dividing line of a safe encounter is defined by the hazard criteria given in Chapter 1, namely that the roll angle is not to exceed ten degrees, nor is the flight path angle to become steeper than -4 1/2 degrees at any point along the trajectory.

Simulation runs were grouped in families with members having a number of commonalities such as vortex circulation, flight path angle, heading, and initial altitude. In general only one parameter, namely initial lateral position or altitude (in the case of horizontal flights) was varied to distinguish these members. Eight types of families were included in the study. Each has a distinct orientation with respect to the inertial reference frame which includes the vortex line as the direction of X axis. Flight path angle (γ) is the direction of the trajectory above or below the axis, and heading (ψ) is the direction of the trajectory clockwise from this axis. In the list of families given below, "vertically" implies that the flight path lies in a vertical plane parallel to the vertical plane containing the vortex. The families are:

a) landing vertically ($\gamma = -3°$, $\psi = 0$)

b) landing diagonally, L to R ($\gamma = -3°$ or $-15°$, $\psi = 3°$ or $15°$)

c) landing diagonally, R to L ($\gamma = -3°$ or $-15°$, $\psi = -3°$ or $-15°$)

d) horizontal flyby, L to R ($\gamma = 0$, $\psi = 3°$ or $15°$)

e) horizontal flyby, R to L ($\gamma = 0$, $\psi = -3°$ or $-15°$)

f) climb vertically ($\gamma = 15°$, $\psi = 0$)

g) climb diagonally L to R ($\gamma = 15°$, $\psi = 15°$)

h) climb diagonally R to L ($\gamma = -15°$, $\psi = -15°$)

Among these, three autopilot modes were employed: Stability Augmentation System (SAS), Control Stick Steering (CSS), and Instrumentation Landing System (ILS). Not all permutations were explored; the KC-135 was used as the basic tool, and the DC-9 was used to supplement the data to indicate the sensitivity of a smaller aircraft. There were, however, a few runs made with this aircraft alone, such as the climbing studies.

For the purpose of defining the hazard, only landing or horizontal flyby conditions with the autopilot in the ILS mode will be considered. The results of the climbout study are discussed below; the hazard criteria must be reassessed for this special case. Restriction to the ILS mode is a convenience to maintain some control over aircraft-vortex separation, as use of the CSS mode leads to flight paths which often curve well away from the vortex.

To provide a basic reference of safe proximities to various single vortices near the ground, Table 3-1 shows results of the simulation study for two aircraft. Both passage to the left and to the right of the vortex are considered. As an aid to understanding the curvature of the flight path induced by the vortex, the minimum proximity of a corresponding straight path through the same initial point is included in parentheses after each safe proximity. In most cases the two differ by only a few feet or less, indicating the vortex does not significantly alter the flight path for these distances. Regardless of the choice of this gauging parameter, the table is intended to show three significant results of the study: first, to identify the general order and range of minimum safe proximities, second to suggest the insensitivity to vortex strength, and third to indicate the insensitivity to varying aircraft. It is not intended to define the minimum safe approaches under all conditions.

The most dangerous type of encounter is seen to be a right-to-left diagonal approach, with the aircraft passing to the left of the vortex. The upwash tends to prolong the encounter with the consequence of a more severe dynamic response. Although the safest proximity for a vortex with a circulation of 7000 ft^2/sec is listed as 130 feet, the next closer run at 103 feet exhibited no difference in maximum roll angle, but had a minimum flight path angle of -5 degrees, which exceeds the hazard criterion.

IP-12346

Table 3-1 Minimum Safe Proximities to Vortices

Vortex Height = 100 feet Circulation (Γ) is Clockwise

KC - 135

Type of Approach	Γ ft²/sec	Closest Safe Proximity To Left	Closest Safe Proximity To Right
landing vertically	7000	103(100) ft	92(100) ft
	5000	>50(>50)	70(75)
	3000	>50(>50)	72(75)
	1500	75(75)	75(75)
	700	75(75)	75(75)
landing diagonally L to R	7000	70(75)	93(100)
	5000	70(75)	75(75)
landing diagonally R to L	7000	130(125)	78(75)
	5000	78(75)	75(75)
horizontal flyby L to R ψ=3°	7000	75(75) above vortex	
	5000	75(75) "	"
	3000	50+(50+) "	"
	1500	50(50) "	"
horizontal flyby R to L ψ=3°	7000	100 (100) "	"
	5000	100 (100) "	"
	3000	75 (75) "	"

DC - 9

Type of Approach	Γ ft²/sec	Closest Safe Proximity To Left	Closest Safe Proximity To Right
landing vertically	7000	80(75) ft	94(100) ft
	5000	79(75)	96(100)
	3000	77(75)	73(75)
landing diagonally L to R	7000	70(75)	115(125)
landing diagonally R to L	7000	100(100)	78(75)
horizontal flyby L to R or R to L ψ=3°	7000	75(75) above vortex	

It is important to the understanding of where a hazardous condition begins to present the results of the simulation in a form which can explicitly show sensitivities to vortex proximity and strength. It is useful to this end to plot the maximum roll and flight path angles, the two most important attitude angles, as functions of the minimum approach distance. Even this can be misleading because, it must be remembered, the variables plotted represent one instant in the course of a dynamic encounter and do not fully interpret its history.

Figures 3-1 through 3-6 illustrate the trends set in responses to the various types of encounters. In vertical and diagonal landings, the aircraft is more easily upset flying to the right of the vortex than to the left for comparable distances from the vortex. This is the result of the difference in response to a downwash as opposed to the response to an upwash. An upwash tends to bouy the airplane and perhaps afford a longer recovery time before the airplane lands. However, in so doing, the pitch response suffers, and for the weaker vortices tends to limit the minimum safe proximity. The most significant characteristic of these responses is exemplified by the roll angle curves for the stronger vortices. These all show very steep slopes when the aircraft is close enough to respond violently. This steepness identifies the very high sensitivity to small changes in proximity to the vortex. Of far less importance in relation to this, are the sensitivities to vortex strength and differences in wingspan. That this is true can be observed by the relatively close grouping of points on the curves for roll angles below ten degrees and flight path angle exceeding -4 1/2 degrees, regardless of vortex strength, for all of the landing cases. For the KC-135 these tend to be located in the region of seventy-five to one hundred feet. The DC-9 exhibits a similar distribution of points in the safe encounter region; it is difficult to clearly identify significant differences in the responses of the two aircraft at comparable minimum approach distances.

Horizontal flybys show somewhat less of a sensitivity to proximity than landings, for comparable distances. However, this sensitivity becomes very high when the distance diminishes to, say, twenty feet. Pitch is the dominant response for the KC-135, and is aggravated by large heading angles skew to the vortex axis.

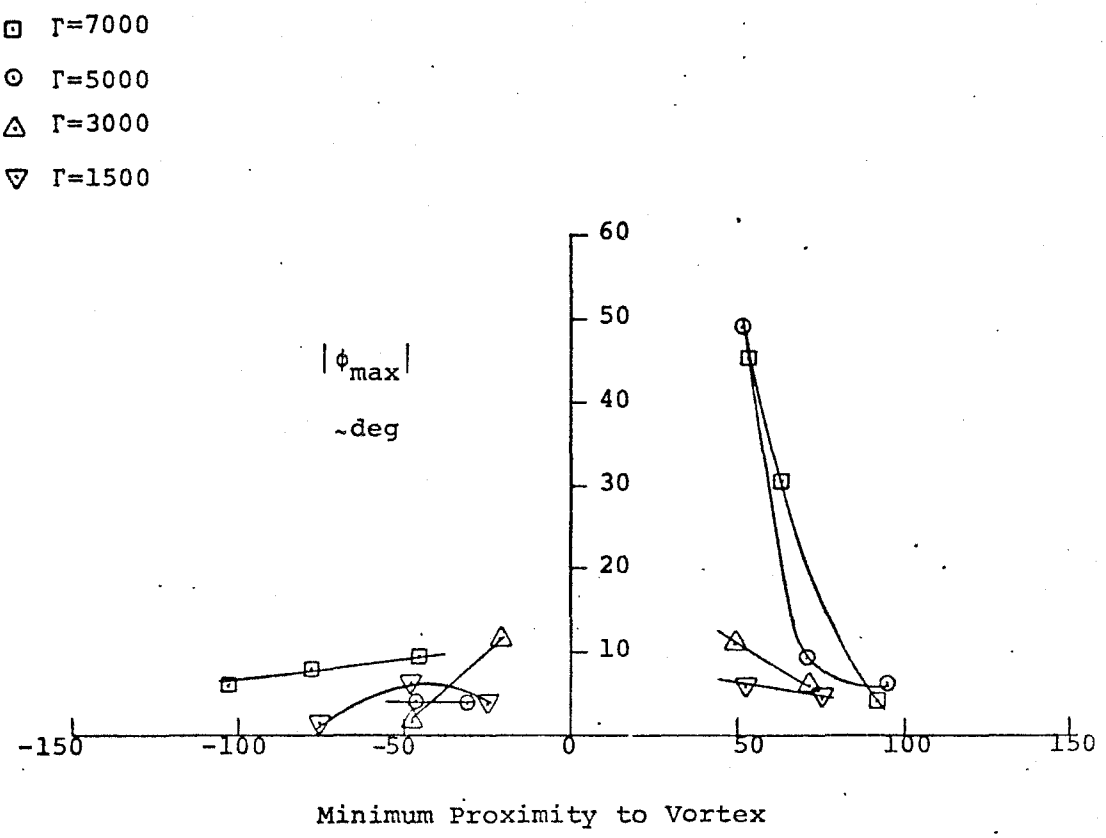

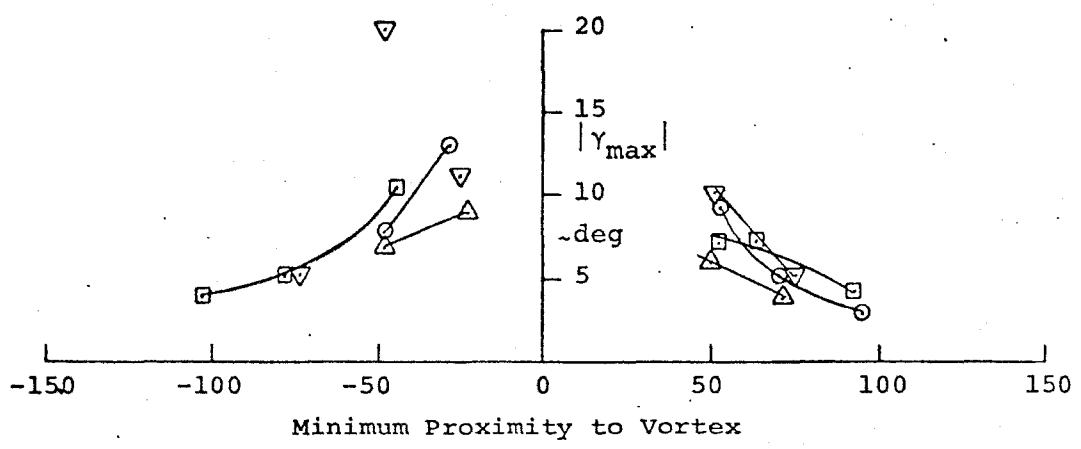

Figure 3-1 KC-135 Encounter Sensitivities - Vertical Landings

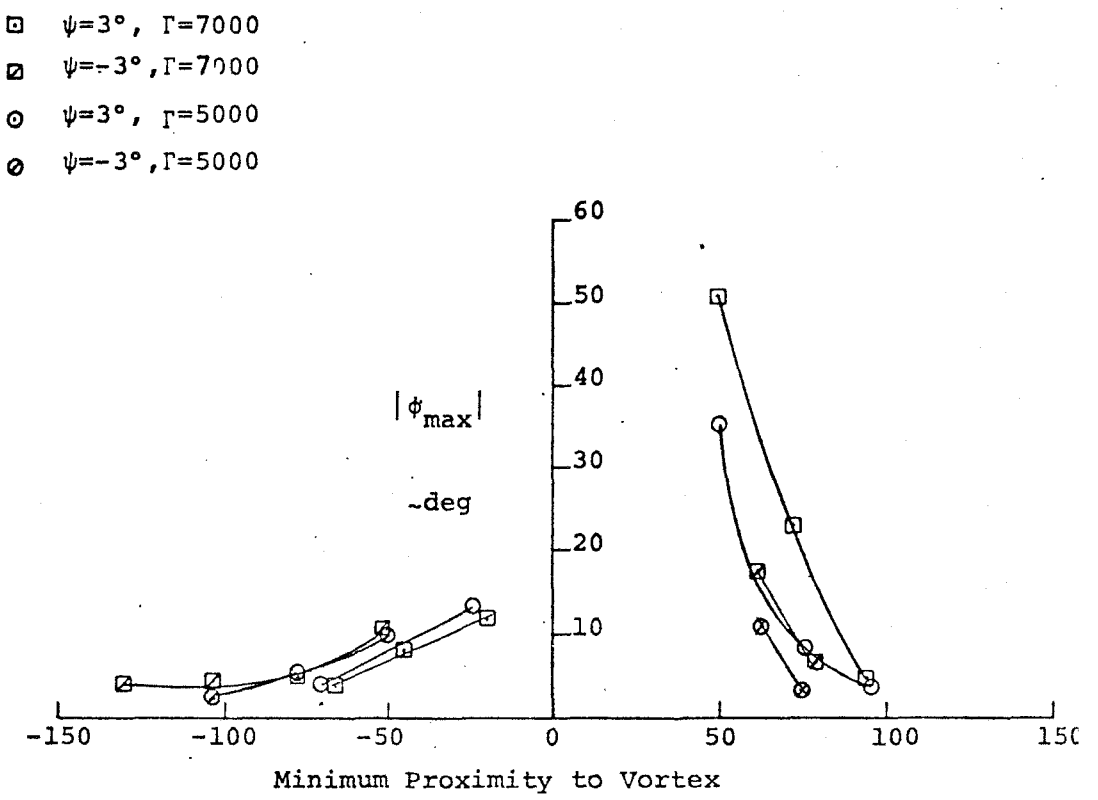

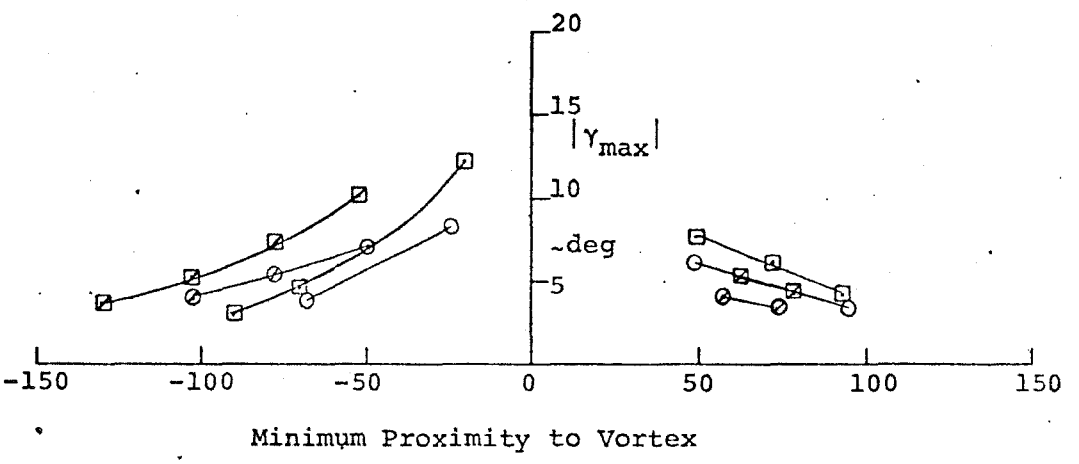

Figure 3-2 KC-135 Encounter Sensitivities - Diagonal Landings

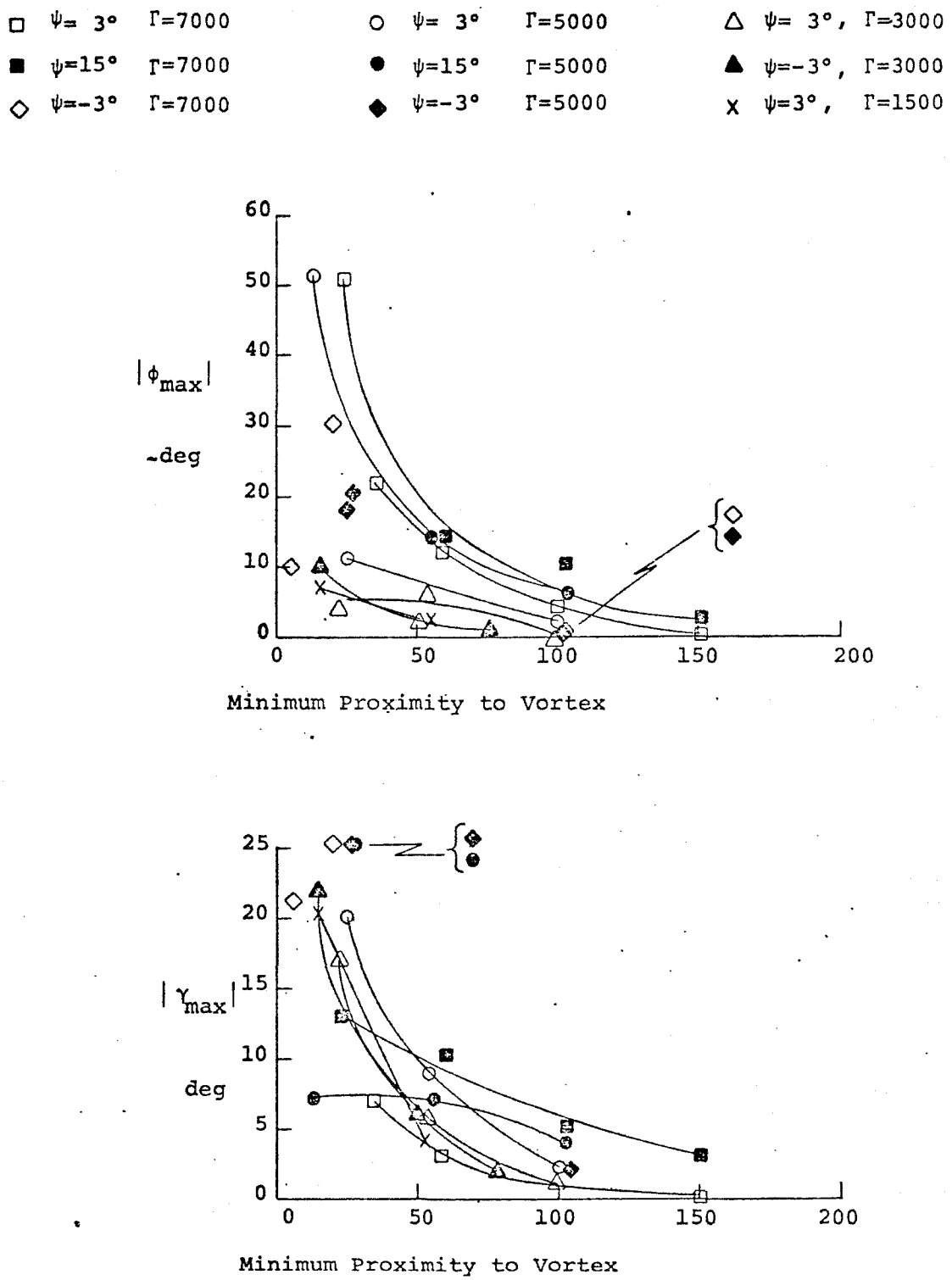

Figure 3-3 KC-135 Encounter Sensitivites - Horizontal Flybys

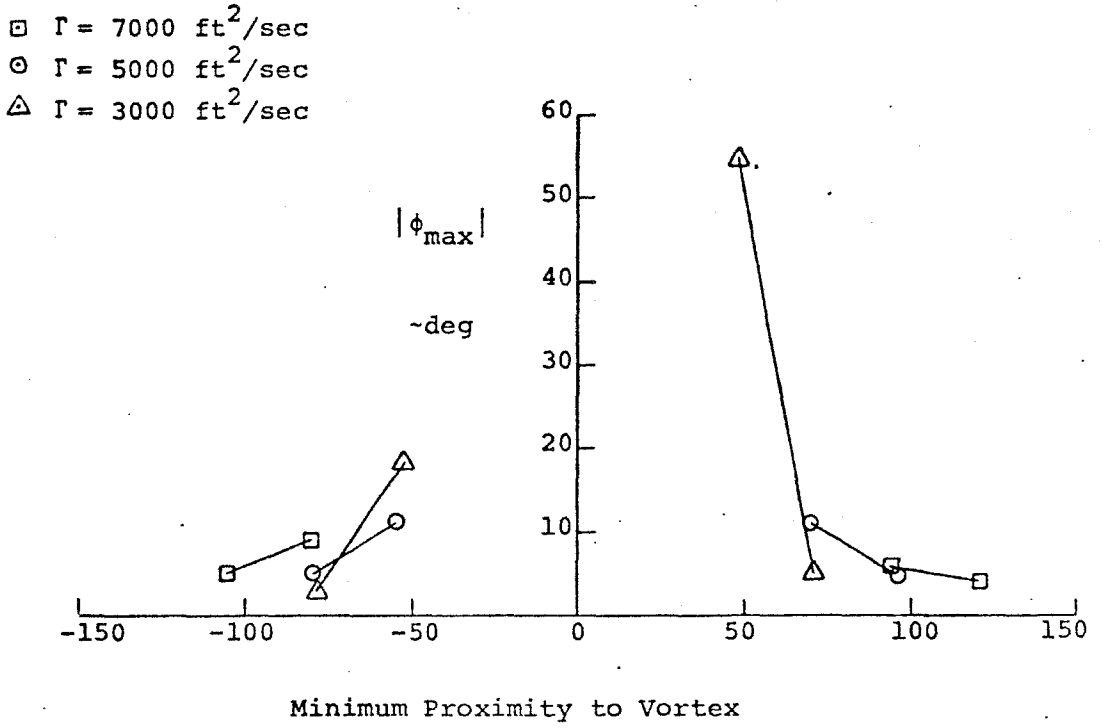

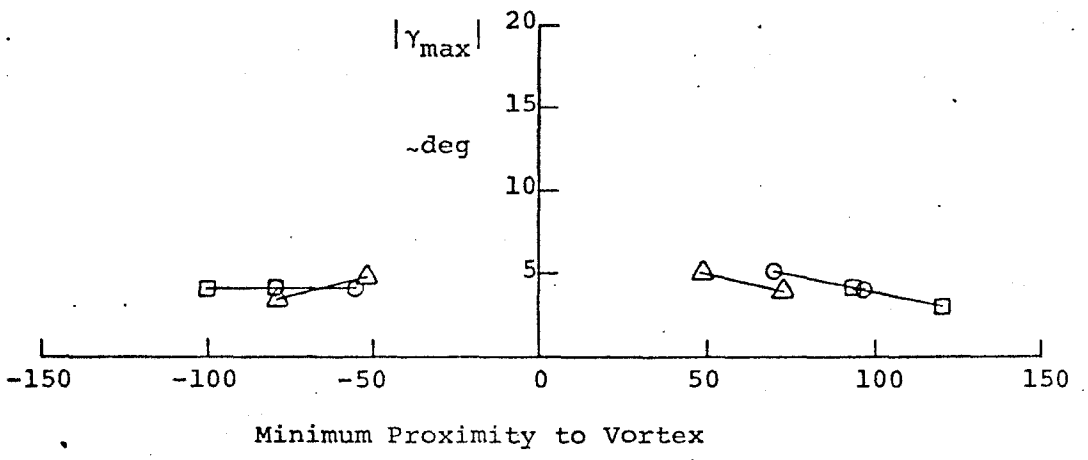

Figure 3-4 DC-9 Encounter Sensitivities - Vertical Landings

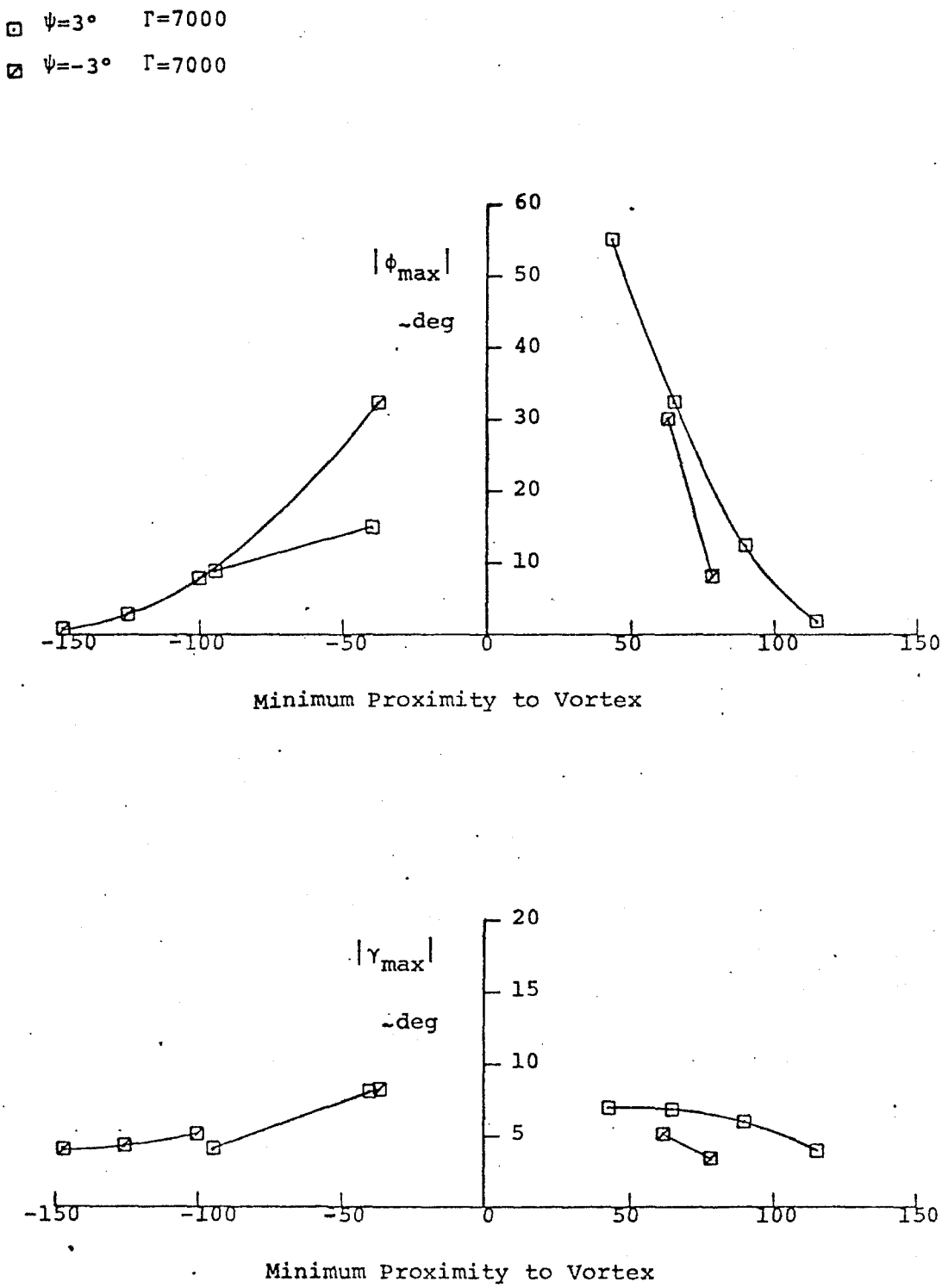

Figure 3-5 DC-9 Encounter Sensitivities - Diagonal Landings

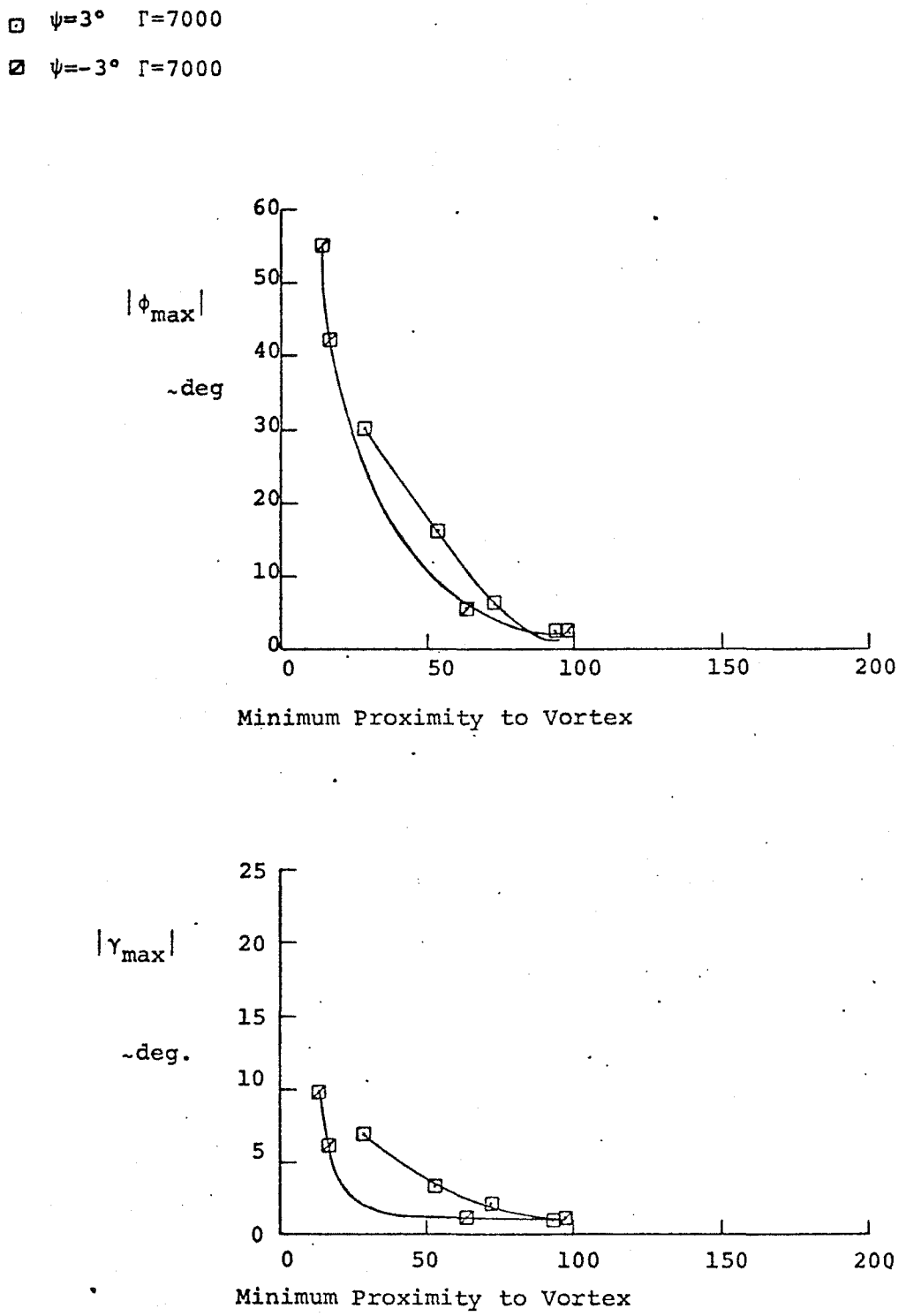

Figure 3-6 DC-9 Encounter Sensitivites - Horiztonal Flybys

The DC-9 is less sensitive in pitch than the KC-135, although it shows similar roll responses. As a result, the roll angle is the limiting safety factor for the DC-9 in this case.

While it is difficult to explain all of the breaks in what may appear to be well formed patterns in these sensitivity curves, it is easier, and perhaps more useful, to support the simulation runs with a simplified sensitivity analysis. For this, it is convenient to return to the often used ratio of available roll control moment to vortex induced moment. This is not to say that the hazard definition is to revert to the loss of control, but rather that the value of this ratio implies the degree of control which can be exerted over the influence of the vortex and that it should correlate well with the hazard definitions presented herein. The objective of the analysis is to develop sets of curves of this controllability parameter as functions of wingspan and minimum vortex proximity in order to examine the slopes of these curves and thereby confirm the sensitivities to these two variables shown by the simulation results.

The curves show that the aircraft was in danger before a wingtip reached the core of the vortex. For most runs, the core never touched the airplane. Assuming this to be the case, and that no wing segments stall, the rolling moment can be developed analytically as a function of wing geometry, vortex strength, and distance of the aircraft from the vortex. As further simplifications, it is assumed that the wing is rectangular, untapered, and unswept, and that the wings are level when the closest proximity occurs. In order to remove the influence of dynamics from the controllability parameter, it is assumed that roll rate contributes negligibly to the roll moment.

For a given type of aircraft (e.g. transport), the normalized maximum roll rate, $\frac{Pb}{2V}$, is for the most part a constant. This implies that, with full ailerons, all aircraft of this type will reach the same steady-state wingtip helix angle at a particular airspeed. Since aircraft landings are of prime concern here, it is convenient to restrict the analyses to a single airspeed. The relationship between control moment and this helix angle depends upon the damping in roll.

$$C_{\ell_{\delta_a}} \delta_{a_{max.}} = C_{\ell_{\hat{p}}} \frac{Pb}{2V} \qquad 3\text{-}1$$

The roll damping coefficient depends only upon wing geometry (aspect ratio, taper ratio, etc.)[9] and, since the geometry is fixed in this analysis, this coefficient can be assumed constant. Hence, the control moment coefficient is also constant and variation in the controllability parameter is dependent only on the vortex induced rolling moment.

This rolling moment can be expressed as

$$\mathcal{L} = \int_{-b/2}^{b/2} C_{L_\alpha} \alpha c q \xi \quad d\xi \qquad 3\text{-}2$$

If the center of the wing is at a distance (a) from the vortex, the angle of attack at ξ is

$$\alpha = \frac{\Gamma}{2\pi V(\xi + a)} \qquad 3\text{-}3$$

Integrating the moment equation yields

$$\mathcal{L} = \frac{q\, C_{L_\alpha}\, \Gamma c b}{2\pi V} \left\{1 - \frac{a}{b} \ln \left(\frac{1+b/2a}{1-b/2a}\right)\right\} \qquad 3\text{-}4$$

For the convenience of this analysis, let the controllability parameter be normalized to eliminate the influence of V, Γ, C_{L_α}, and the roll control coefficient. The resulting controllability coefficient is:

$$C_c = \frac{b}{1 - \frac{a}{b} \ln \left(\frac{1+b/2a}{1-b/2a}\right)}$$

Figure 3-7 illustrates the variation of this expression with wingspan for several minimum approach distances while Figure 3-8 shows the cross plot. The reason behind the high sensitivity of the landing runs to small changes in proximity and the lower sensitivity to aircraft span is immediately apparent by comparing these two figures. The slopes of the curves in Figure 3-8 range from 2.0 at a = 200 ft. to as high as 3.3 at a = 70 ft. and b = 120, whereas the magnitude of the slopes of Figure 3-7 is only one for the smaller wingspans. The slopes increase with wingspan, as could be expected because a wingtip gets much closer to the vortex core. However, the maximum slope is only -2.5 for b = 100 and a = 60, where the wingtip is but ten feet from the center of the vortex. It could be said that the controllability coefficient is about twice as sensitive to changes in minimum approach distance as to changes in wingspan, when the wingtip is not close to stall.

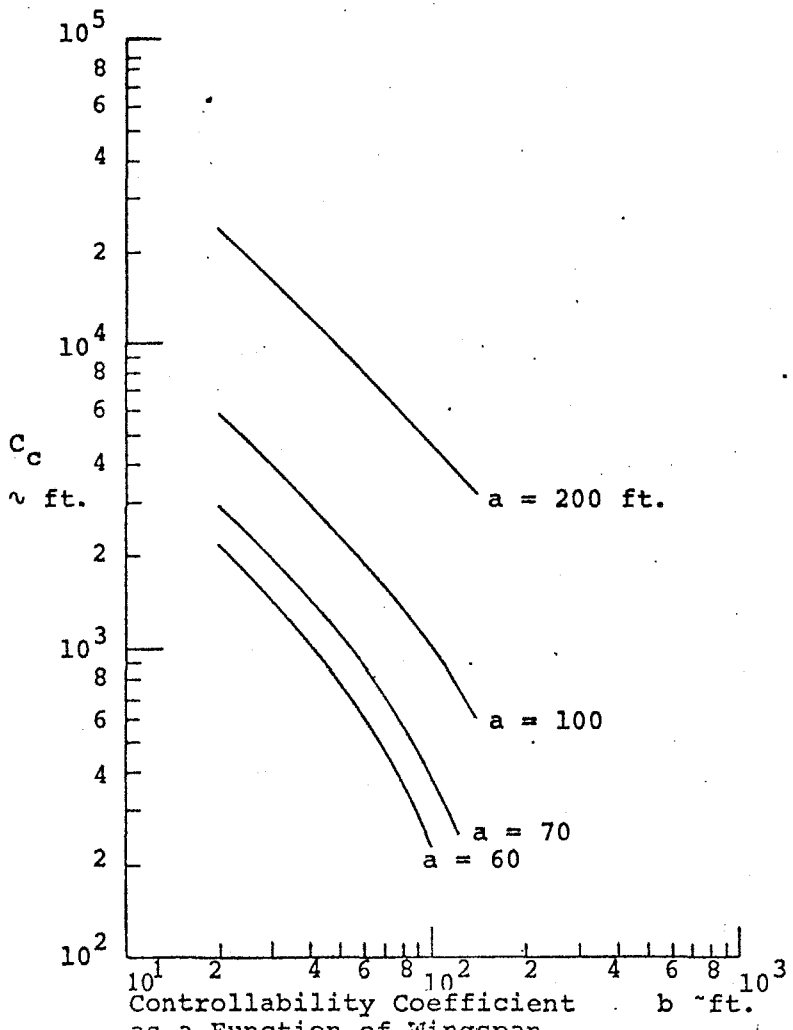

Controllability Coefficient as a Function of Wingspan
Figure 3-7.

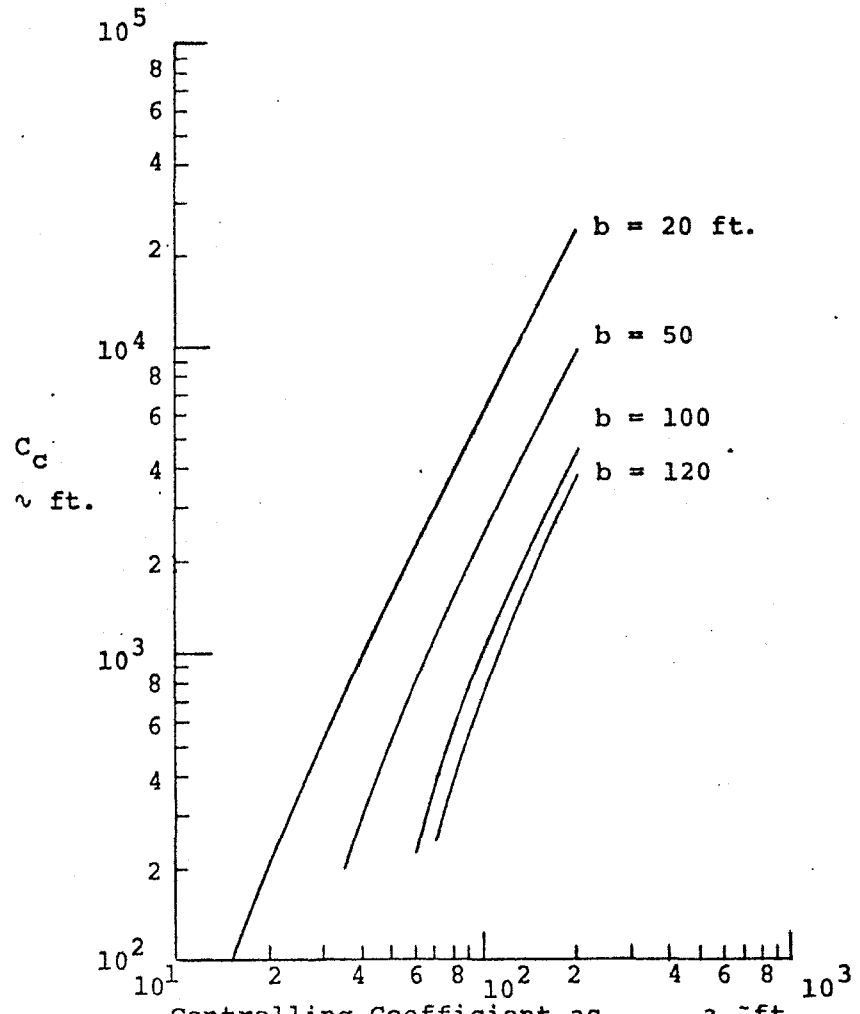

Controlling Coefficient as a Function of Vortex Proximity
Figure 3-8.

If one ignores the small change in rolling moment produced by shifting or extending the furthermost wingtip with respect to the vortex, and considers the major effect of changing the position of the near wingtip, this statement appears quite logical. If, for example, the minimum approach distance is decreased five feet, there will be an additional five feet of wing in the strong upwash field, whereas if the wingspan is increased by the same measure only half that will be placed in the strong upwash field.

If these curves are examined carefully it is seen that the upset-to-aircraft size relationship is really a matter of the proximity of the near wingtip. To emphasize this point, the controllability coeffiecient is also plotted as a function of wingspan, with the nearest wingtip separation held constant. The slopes of these curves (fig. 3-9) are very shallow, and decrease as the separation diminishes. The top curve represents a marginally safe control situation when compared with the data presented in figures 3-1 to 3-6. The controllability coefficient is altered by only a factor of two over the entire range of wingspans shown. The factor is practically unity for the fifteen foot wing separation; however, this would result in violent upsets for all but the weakest vortices. Nevertheless, it does confirm that the proposition of controllability being independent of aircraft size, if minimum wingtip proximities are fixed, is valid, and becomes increasingly accurate as the vortex is more closely approached.

Another way to state the hazard definition, with regard to aircraft size, is that the larger the airplane, the bigger must be the minimum proximity with respect to the center of the vehicle. It must be reiterated that a single aircraft velocity is assumed. If velocity differences for this range of wingspans are considered, it must be recalled that controllability is proportional to velocity. This dependence would flatten the upper curve and better substantiate the hypothesis that controllability is a function of wingtip separation, not aircraft size. When comparing specific aircraft, differences of wing geometry, control system specifications, and dynamic responses as well as velocity will affect the minimum safe approach distance. The analysis presented here serves to assess the effect of the common sizing variable (wingspan) with regard to the hazard potential from a sensitivity point of view.

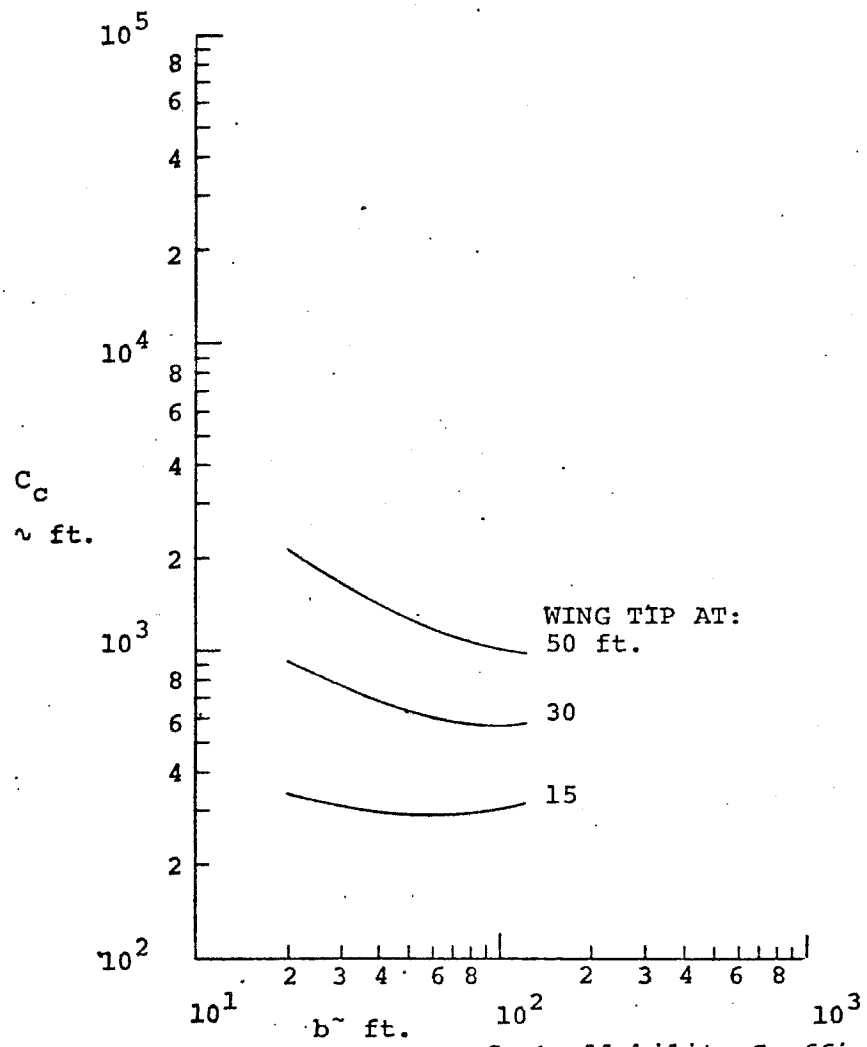

Figure 3-9. Controllability Coefficient as a Function of Wingspan, For Constant Vortex-Wingtip Separations.

The area in which this analysis may appear to be weak is in the dependence on vortex strength. Controllability is inversely proportional to the circulation; differences in an aircraft's responses to various strength vortices should be readily apparent. Yet, figures 3-1 through 3-6, representing the simulation data, often show markedly similar maximum roll or flight path angles in responses to vortices with strengths varying even by a factor of two. There are two principal causes for this sort of behavior. First, although the figures are plotted as functions of minimum vortex proximity they say nothing about the complete trajectories which have a major influence on these resulting maximum angles. In short, the dynamics of the encounter should be examined to fully understand the effect of the vortex strength. The data presented in appendix H provides an opportunity to do this. Second, while the ILS equations are desensitized when the terminal point is closely approached, strong control commands still can be generated if sufficient altitude and track errors accumulate as the result of the encounters. Because of this, some flight path instability can occur; it is often difficult to separate this phenomenon from the normal response to the vortex encounter, except to note that if pitch or roll angles peak very close to the ground, it is most likely due to the sensitivity of the ILS equations.

The final subject to be discussed under hazard definition concerns vortex encounters under climb conditions. These studies were made with the DC-9 in Control Stick Steering autopilot mode. There was no need for the ILS mode, because trajectories remained relatively straight until well beyond the vortex, and in all but one run these passed within just a few feet of a vortex center. The exception, not included in the table below, was initialized further to the left so as to pass within seventy-five feet of the vortex. The maximum roll angle was four degrees and the angle of attack did not exceed three degrees. Table 3-2 summarizes the results of this work. The maximum angle of attack is tabulated to indicate the possibility of stall. It must be remembered that this parameter is an angle relating the inertial velocity vector to the x body axis. Since the aircraft passes through the center of the vortex, stall would be alleviated on the right wing, due to the downwash field, but would likely occur over some regions of the left wing for most of the encounters.

Table 3-2 Summary of Climb Simulations

Type of flight	Vortex Circulation	$\lvert\phi_{max.}\rvert$	$\lvert\alpha_{max}\rvert$
Vertical climb	5000 ft^2/sec	>50 deg	22* deg
" "	5000	>50	22
" "	3000	40	11
" "	1500	12	5
Diagonal climb L toR	5000	32	18*
" " " " "	5000	34	15
" " " " "	3000	22	9
Diagonal climb R " L	5000	35	9
" " " " "	3000	23	5

* double vortex system, h_v = 1000 ft, δ_v = 122 ft; paths passed through left vortex (circulation CW). All others single vortex at 100 feet.

The first observation which can be made from the data given in the table is that diagonal encounters are less severe than vertical ones. This may be due to the fact that the total skew angle to the vortex axis is greater for diagonal flights than for vertical flights, thereby reducing the length of time the aircraft is close to the vortex. The second observation to be made is that none of the runs passes the safety criteria set forth earlier in this chapter. Yet, none result in a crash as the airplane ultimately recovers and continues to climb. The data in appendix H show that the flight path angle always stays well positive. Hence, it is difficult to assess the hazard for this type of encounter and for that reason this segment of the study is considered separately. It would appear that several more value judgments, including pilot skills, must be considered to identify the proper hazard criteria for this situation. At the very least, avoiding stall would prohibit flying through vortices stronger than about 3000 ft^2/sec.

One additional form of vortex encounter was investigated. There is the question regarding at what stage of breakup can a vortex be considered no longer a hazard. Because the most common form of vortex dissipation involves the phenomenon analysed by Crow [15], whereby the two vortices interact with one another to induce instability, an effort was made to model this wavy shape.

Unfortunately the computation load became unmanageable if a single vortex was represented by more than two straight lines as shown in figure E-2. This model, however, is considered to be adequately representative as far as a periodic forcing function is concerned.

The results of these runs (120 through 129, appendix H) indicate the same order for safe minimum proximities for landing beside this form of vortex as for the line filament vortex, e.g. 75 to 100 feet for a vortex with a circulation of 5000 ft^2/sec. For a weaker vortex (Γ=2000 ft^2/sec), passage at sixty feet from its extremity can be considered safe, but no passage through it is tolerable.

The response of the aircraft to this form of vortex differs from that to the line filament in that the periodicities in the forcing function excite the dutch roll mode. The fundamental frequency of the forcing function and that of the dutch roll mode nearly coincide at about 0.22 hz. Also to be considered in this response is the added destabilizing contribution of the sensitive localizer error equations near the terminal point. As a consequence all of the landing runs terminate with strong roll oscillations, whereas the pitching motion is not badly disturbed. In effect, then, the forced oscillations offset the fact that the <u>average</u> separation from the vortex, during a safe encounter, is substantially greater than that for a similarly safe encounter with a line vortex.

Finally, two runs were made to examine the behavior of an aircraft flying level near the wavy vortex. The aircraft could be safely flown within the bounds of a vortex with a circulation of 2000 ft^2/sec, although the flight path would stray from a straight line, and would eventually carry the aircraft out of the vortex, despite the autopilot's being in the ILS mode. This safe encounter emphasizes the influence of the sensitive localizer error equations near the terminal point for landing operations.

Chapter 4

Summary

A six-degree-of-freedom vortex encounter simulation has been developed for use on a hybrid computer to identify hazard situations for terminal area operations. Complete trajectory information for landing, horizontal flyby and climbing flights is presented and conclusions are drawn from these results regarding the hazard potential.

A hazardous encounter is defined as one in which, at any point along the flight path, the roll angle exceeds ten degrees, the flight path angle goes below - 4 1/2 degrees, or the ailerons approach the limit of travel for any significant length of time. For the two trailing aircraft simulated in this effort (DC-9 Series 10 and KC-135), the minimum safe proximity (measured from vortex center to fuselage center) to a single vortex lying one hundred feet above the ground ranged from 75 feet to 130 feet for vortices with strengths comparable to that shed by heavy jets (5000 ft^2/sec). Closer approaches generally could be made to the left of a clockwise circulating vortex than to the right. Dangerous encounter conditions always occurred before any portion of an aircraft was immersed in the vortex core or any portion of the flying surfaces stalled. This fact suggested a simplified sensitivity study wherein the vortex proximity and the wingspan became independent variables and the ratio of control moment and vortex induced rolling moment was the dependent variable,controllability. Results of this analysis show that this controllability parameter is about twice as sensitive to changing approach distance as to changing wingspan. Furthermore, if the wingtip proximity is fixed, and the same function is plotted with respect to wingspan, it is seen to be nearly independent of aircraft size, especially for close approaches.

The dependence of peak roll or flight path angles on the strength of a vortex is less pronounced than the sensitivity analysis suggests. The principal reason behind this lies in the dynamic character of the trajectories. Flights past weaker vortices may spend more time close to the core with the result that peaks in roll or flight path angles may be quite similar to those for flight past stronger vortices.

Both the DC-9 and KC-135 experienced substantial upsets with very weak vortices. It is a bit premature, considering the somewhat restricted spectrum of aircraft covered in the present work, to make the broad statement that all aircraft can present a threat of hazard to others of their same kind, but it does appear to be possible from the data generated. These data even suggest, for example, that a Boeing 727 flying at 150 knots and developing a vortex strength of about 4000 ft^2/sec could easily pose a threat to a Boeing 707 which has a 20 percent larger wingspan. Just how far the proposition can be carried is difficult to judge at this point. The greater maneuverability sometimes associated with smaller aircraft may enhance their ability to cope with the weaker vortices to the extent that the generalization no longer applies. However, the case of two 707's cited in the earlier work certainly remains a valid example of an aircraft creating a hazard for another of its kind, even if the gross weight of the generator does not approach the maximum limit.

Climbing flights cannot be judged by the same hazard criteria as landing flights. Although extreme roll and pitch angles resulted from simulated flights through strong vortices, the flight path angle remained positive. A significant measure of the hazard condition is the angle of attack. To avoid stall at any point on the flying surfaces appears to be a rational criterion. To this end, medium sized transports should not be flown through vortices with strengths exceeding 3000 ft^2/sec.

References

1. Kerr, T.H., and Dee, F.W. "A Flight Investigation Into the Persistence of Trailing Vortices Behind Large Aircraft", Tech. Note Aero. 2649, Royal Aircraft Establishment, Sept. 1969.

2. Condit, P.M., and Tracy, P.W. "Results of the Boeing Company Wake Turbulence Test Program," Aircraft Wake Turbulence and Its Detection, Plenum Press, New York, 1971.

3. Crow, S.C,Panel discussion, Aircraft Wake Turbulence and Its Detection, Plenum Press, New York, 1971.

4. Donaldson, C. duP. "A Brief Review of the Aircraft Trailing Vortex Problem", National Aerospace Electronics Conference, Dayton, Ohio, May, 1971.

5. Andrews, W. H. "Flight Evaluation of the Wing Vortex Wake Generated by Large Jet Transports", Aircraft Wake Turbulence and Its Detection, Plenum Press, New York, 1971.

6. Andrews, W. H., et al,"Exploratory Flight Investigation of Aircraft Response to the Wing Vortex Wake Generated by Jet Transport Aircraft", NASA TND-6655, March 1972.

7. Robinson, G.H. and Larson, R. R., "A flight Evaluation of Methods for Predicting Vortex Wake Effects on Trailing Aircraft", NASA TND-6904, November 1972.

8. Madden, S. J. Jr, and Harlan, R. B., "A Program to Analyze and Model Trailing Vortices on Airports", M.I.T. Measurement Systems Laboratory Report RN-69, October, 1971.

9. Pearson and Jones, "Theoretical Stability and Control Characteristics of Wings with Various Amounts of Taper and Twist", NACA TR 635, 1938.

10. "An Aircraft Accident Involving a Delta Air Lines, Inc., DC-9 N 33051, at Greater Southwest International Airport, Ft. Worth, Texas, May 30, 1972", National Transportation Safety Board Docket No. SA-432, 1972.

11. "Estimated Aerodynamic Data for Stability and Control Calculations, Model DC-9 Jet Transport, Series 10", Douglas Aircraft Company Report No. LB-31624, February, 1967.

12. "Performance Handbook, Model DC-9 Series 10 Jet Transport", Douglas Aircraft Company Report MDC J5450/01, February 1972.

13. Madden, S. J. Jr., "Least Squares Estimation of Nonlinear Parameters and Nonlinear Simultaneous Equation Solution," M.I.T. Measurement Systems Laboratory Report RN-72, May 1972.

14. Potter, J. E. et al"Digital Flight Control", M.I.T., Measurement Systems Laboratory Report - to be published.

15. Crow, S.C., "Stability Theory for a Pair of Trailing Vortices," Boeing Scientific Research Laboratory Document D1-82-0918, 1970.

16. "Airplane Data, Model KC-135A Jet Tanker-Transport, for Use in Autopilot Design and Analysis", The Boeing Company Report D-14095, October, 1954.

17. Decker, J.L. "Prediction of Downwash at Various Angles of Attack for Arbitrary Tail Locations", Aeronautical Engineering Review, August, 1966.

18. Koziol, J.S. Jr., "Simulation Model for the Piper PA-30 Light Maneuverable Aircraft in the Final Approach", Transportation Systems Center, D.O.T. Report No. DOT-TSC-FAA-71-11, July, 1971.

Appendix A

Aircraft Modelling Program

Before the six-degree-of-freedom vortex encounter simulation can be used for a specific airplane, the aerodynamic characteristics must be processed to generate a dynamic model which is compatible with the modified strip theory technique used in the simulation. The model is formulated on the basis of satisfactorily reproducing the most significant dynamic characteristics of the airplane when the simulation is run with no vortex and control sufaces are pulsed to induce transient responses.

To model the aircraft, the lift curve slopes and the zero-angle-of-attack lift coefficients for both the wing and stabilizer are determined through the use of a least squares fitting program which attempts to match a number of the aircraft's stability derivatives[13] to analytic expressions for them developed from the modified strip theory. In addition, some lateral derivatives which do not depend upon the wing lift distribution are used to determine the rudder lift curve slope, the fuselage side force slope, and the fuselage lateral center of pressure.

Unfortunately, not all stability derivatives can be derived analytically and for those which can, not all can be developed with a technique as simple as strip theory. Examples of such are the pitching derivatives C_{m_q} and C_{L_q}. The wing contributions of these can be estimated only by considering the velocity distribution along the wing chord and the results are approximate at best.

While some stability derivatives do require a variety of techniques, the largest contributions of the most important derivatives can be estimated with strip theory. These include C_{L_0}, C_{L_α}, C_{m_0}, C_{m_α}, C_{m_q}, C_{Y_p}, C_{n_p}, C_{ℓ_β}, C_{ℓ_r}, and C_{ℓ_p}.

Stability derivatives associated with lateral forces and moments on the fuselage and rudder only are C_{Y_β}, C_{n_β}, and C_{n_r}. This set of thirteen derivatives is used to estimate the dependent parameters described above.

Strip theory tends to overestimate wing contributions to the rotary damping derivatives. It also fails to generate the near-elliptic lift distributions associated with normal wing planforms. In an attempt to improve the modelling of these damping derivatives, yet retain the simple approach of strip theory, the wing lift was modified by an elliptic distribution weighting function. This reduced the lift to zero at the tips and permitted close matching of the modelled roll damping derivative to the actual one. As the primary response of the aircraft to the vortex encounters studied here is roll, faithful reproduction of the roll dynamic characteristics was felt to be the most important criterion of the modelling program. A weighting function is not applied to the stabilizer, which is divided into three segments, or to the rudder, which is considered as a single segment.

The lift on the airplane is the combination of the zero angle of attack lift and the angle of attack induced component. For a non-tapered wing of m segments and stabilizer of n sections the lift is

$$L = \frac{cbq}{m} \sum_{i=1}^{m} (C_{L_{0_w}} + C_{L_{\alpha_w}} \alpha_i) F_i + \frac{qS_t}{n} \sum_{j=1}^{n} (C_{L_{0_t}} + C_{L_{\alpha_t}} \alpha_{t_j}) \qquad \text{A-1}$$

Throughout this appendix, m refers to the number of wing segments and not the mass of the aircraft.
The zero-angle-of-attack lift coefficient can be written by separating terms and normalizing by qS.

$$C_{L_0} = C_{L_{0_w}} \frac{cb}{Sm} \sum_{1}^{m} F_i + C_{L_{0_t}} \frac{S_t}{S} \qquad \text{A-2}$$

Similarly, the lift curve slope can be generated. Note that

$$\frac{d\alpha_t}{d\alpha} = 1 - \frac{\partial \varepsilon}{\partial \alpha} .$$

$$C_{L_\alpha} = C_{L_{\alpha_w}} \frac{cb}{Sm} \sum_1^m F_i + C_{L_{\alpha_t}} \frac{S_t}{S} (1 - \frac{\partial \varepsilon}{\partial \alpha}) \qquad \text{A-3}$$

The separation and normalizing process can be continued for the pitching moment equation. An additional term, $C_{m_{a.c.}}$, is included for the wing for use with aircraft data which is presented in tail-off, tail-on form. For other forms of data, the term is considered to be implicit in the zero-angle-of-attack moment term for the wing.

$$C_{m_0} = - C_{L_{0_w}} \frac{b}{Sm} \sum_1^m F_i x_i + C_{m_{a.c.}} - C_{L_{o_t}} \frac{S_t x_t}{Sc} \qquad \text{A-4}$$

where $x_i = |\xi_i| \tan \lambda - x_c$

$$C_{m_\alpha} = - C_{L_{\alpha_w}} \frac{b}{Sm} \sum_1^m F_i x_i - C_{L_{\alpha_t}} \frac{S_t x_t}{Sc} (1 - \frac{\partial \varepsilon}{\partial \alpha}) \qquad \text{A-5}$$

The rotary damping derivatives and others used in this analysis can be derived in a manner similar to that used above. The local angle of attack at each wing station is assessed in terms of the particular motion, and the resulting lift or moment equation is appropriately normalized to extract the stability derivative in question. The pitch rate induced angle of attack for a wing segment is

$$\alpha_i = \frac{Qx_i}{V}$$

and the damping-in-pitch derivative becomes

$$C_{m_q} = - C_{L_{\alpha_w}} \frac{b}{SVm} \sum_1^m F_i x_i^2 - C_{L_{\alpha_t}} \frac{S_t x_t^2}{SVc} \qquad \text{A-6}$$

The roll induced angle of attack is

$$\kappa_i = \frac{P\xi_i}{V}$$

The roll damping derivative is considered a function of the induced wing loading only; the stabilizer and rudder contributions are small.

$$C_{\ell_p} = - C_{L_{\alpha_w}} \frac{c}{SVm} \sum_1^m F_i \, \xi_i^2 \qquad \text{A-7}$$

The roll induced side force for the wing can be derived by considering the effect of dihedral. As the added lift on a surface is normal to it, the dihedral causes a lateral component to be developed. In roll, the additional lift for the left wing is equal and opposite to that of the right wing. A small contribution from the rudder also is included.

$$C_{y_p} = - C_{L_{\alpha_w}} \frac{cb}{SVm} \sum_1^m F_i |\xi_i| \sin\sigma + C_{y_{\beta_r}} \frac{S_r x_r}{SV} \qquad \text{A-8}$$

The primary contribution to the roll-induced yawing moment comes from the tilting of the lift vector as the angle of attack changes. The forward component of this lift is $L_w \alpha_i'$. While the rudder contributes a small torque associated with the last term in Equation A-8, experience has shown that its elimination results in better modelling.

$$C_{n_p} = - C_{L_w} \frac{c}{SVm} \sum_1^m F_i \xi_i^2 \qquad \text{A-9}$$

Although the drag increases with the square of speed, the yawing moment resulting from drag induced by yaw rate is very small compared with the contribution of the rudder. Also the fuselage contributes negligibly to the yaw damping derivative. For the rudder alone,

$$C_{n_r} = - C_{y_{\beta_r}} \frac{S_r \ell_r^2}{SVb} \qquad \text{A-10}$$

The yaw rate induced rolling moment results from the increase in lift with speed. The change in speed is

$$\frac{2L_w}{V} u_i$$

where u_i is the change in speed at the ith station due to a yawing velocity.

$$u_i = R\xi_i$$

There is a small moment developed by the rudder which is included.

$$C_{\ell_r} = 2C_{L_w} \frac{c}{SVm} \sum_1^m F_i \xi_i^2 - C_{y_{\beta_r}} \frac{S_r \ell_r x_r}{S V b} \qquad \text{A-11}$$

The remaining stability derivatives involve the sideslip angle β. Only the roll moment derivative involves the wing loading distribution directly, and can be considered in a manner similar to that for C_{y_p} through the dihedral effect.

$$C_{\ell_\beta} = - C_{L_{\alpha_w}} \frac{c}{Sm} \sum_1^m F_i |\xi_i| \sin\sigma + C_{y_{\beta_r}} \frac{S_r x_r}{S b} \qquad \text{A-12}$$

While the wing loading distribution influences C_{y_β}, the fuselage also contributes to this derivative and the two are easily combined into a single term.

$$C_{y_\beta} = C_{y_{\beta_{wb}}} + C_{y_{\beta_r}} \frac{S_r}{S} \qquad \text{A-13}$$

Finally, the sideslip induced yawing moment can be derived from this last equation by considering the centers of pressure of the wing-body combination and the rudder.

$$C_{n_\beta} = - C_{y_{\beta_{wb}}} \frac{x_{wb}}{b} - C_{y_{\beta_r}} \frac{S_r \ell_r}{S b} \qquad \text{A-14}$$

Equations A-2 to A-9, A-11 and A-12 are used in a least squares fitting program [13] to solve for the best estimates of $C_{L_{0_w}}$, $C_{L_{\alpha_w}}$, $C_{L_{0_t}}$, and $C_{L_{\alpha_t}}$. The fixed parameters for these equations include the aircraft physical characteristics (c,b,q, etc.) together with the elliptic weighting function F_i, and the full airplane stability derivatives (C_{L_0}, C_{L_α}, etc.). The remaining dependent variables $C_{y_{\beta_{wb}}}$, $C_{y_{\beta_r}}$, and x_{wb} are solved independently from equations A-10, 13, and 14.

The following table indicates the degree to which the airplanes studied were modelled. Some of the cross derivatives do not lend themselves well to this particular analytic technique for certain configurations. This is evident, for example, in C_{y_p} for the DC-9, where the stabilizer contribution is about three times larger than the aircraft data indicates, and the sign of the wing contribution is in error. Note, however, that the prime side force parameter is sideslip, and that it would require a roll rate of fourteen degrees per second to generate an error in side force equivalent to a force produced by one degree of sideslip.

Stability Derivative	DC - 9		KC - 135		Piper PA-30	
	Value	Resid.	Value	Resid.	Value	Resid.
C_{L_0}	1.277	0	.44	0	.29	0
C_{L_α}	5.64	-.0035	4.54	-.0046	5.04	.00125
C_{m_0}	.5419	0	.164	0	.0591	0
C_{m_α}	-1.5181	.0174	-.968	.0413	-1.147	-.0086
C_{m_q}	-.9595	.1388	-.786	-.0717	-.355	.0655
C_{ℓ_β}	-.1788	-.0340	-.195	.0270	-.086	-.0294
C_{ℓ_r}	.0873	-.0257	.1256	-.0150	.0112	-.0015
C_{ℓ_p}	-.0913	-.0103	-.1573	-.0001	-.0511	-.0005
C_{y_p}	.0178	-.0760	.103	-.0079	0	-.0224
C_{n_p}	-.0250	.0021	-.0767	.0006	-.00643	-.00122

The zero residuals on C_{L_0} and C_{m_0} result from $C_{L_{0_w}}$ and $C_{L_{0_t}}$ being present only in these two equations; thus, they can be computed exactly and independently of the least squares fit. Similarly, there are no residuals on C_{n_r}, C_{y_β}, and C_{n_β} which are associated only with $C_{y_{\beta_r}}$, $C_{y_{\beta_{wb}}}$, and x_{wb}.

To this point, only the linearized aerodynamic characteristics of the aircraft have been addressed. The phenomenon of stall is included in the program, both for lift and drag. To help limit the computational load, the lift and drag coefficient variations with angle of attack are reduced to two series of straight line segments. Figure A-1 illustrates the nature of these curves which applies to the wing or stabilizer, with the appropriate parameters inserted.

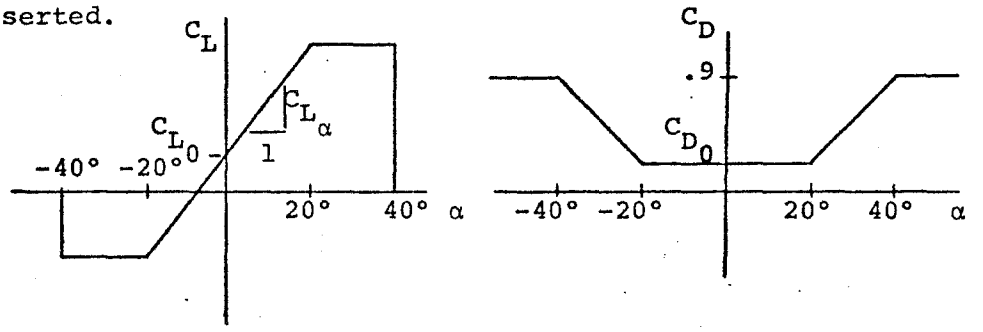

Figure A-1 Lift and Drag Coefficient Models

The lift coefficient curve assumes a fairly gentle stall characteristic. None of the available aircraft data indicated the nature of stall with any precision. The drag coefficient curve approximates the sinusoidal variation of drag with angle of attack, with the upper bound approaching the flat plate coefficient with free stream flow normal to the plate.

In addition to modelling the basic aircraft dynamic characteristics, the control surface effects must be considered. The forces and moments developed by the spoilers include lift, and pitching, rolling and yawing moments. For the ailerons only rolling moment is significant as is pitching moment for the elevators. The rudder generates both sideforce and yawing moment. The characteristics of these control surfaces are assumed to be linear to the travel limit of the surface, with the exception of the spoilers. The pilot's control wheel deflection is used in lieu of spoiler deflection to avoid the strong nonlinear nature of the lift response to this parameter. Using the control wheel also simplifies tying in the autopilot. Curves of lift and the various moments are drawn as functions of wheel deflection from the aircraft aerodynamic

data. All but the yawing and rolling moments are assumed to be linear over the full range of the wheel. These last two are antisymmetric and each half is modelled by a pair of connected straight line segments, with the breakpoint generally near half wheel travel.

Finally, the thrust of the aircraft is continuously adjustable through a potentiometer on the analog computer. The maximum value is the rated sea level thrust. During each encounter run, thrust is assumed constant. During the initialization phase of each run, thrust is adjusted to realize the desired flight path angle.

Appendix B

Vortex Encounter Simulation

The six-degree-of-freedom vortex encounter simulation is an outgrowth of the three-degree-of-freedom program developed under contract to the Transportation Systems Center.[8] The present program makes use of the basic concepts leading to vortex induced forces and moments which were first developed in the earlier program, but with extensions to the wing loading weighting functions and to the additional degrees of freedom. While the first program was underway, a digital autopilot study was also in progress under the direction of Dr. R. G. Stern of the MIT Measurement Systems Laboratory.[14] To perform his task, Dr. Stern developed an aircraft simulation which could handle nonlinear characteristics of the lift and drag curves, as well as those of all of the stability derivatives as they varied over the full Mach number range of the aircraft. He chose to use a hybrid computer facility; rigid body motions resulting from forces and moments described by the stability derivatives were computed by the analog section while solutions for the aerodynamic coefficients, control surface and autopilot functions, and inertial position and orientation were derived in the digital computer. Data displays were provided in both analog and digital forms.

Adapting this program to the vortex encounter problem was inviting for several reasons. The computation was performed in real time and the possibility of having a pilot response to the encounter gave additional credence to the study. A set of cockpit controls and a video display of cockpit instruments had been included in the digital autopilot program. Furthermore, access to the machine between program runs permitted rapid decisions on changing encounter conditions, and could eliminate much needless computation of closely related members of encounter families.

Finally, it appeared that the program might be readily adapted for studying vortex encounters. The integration of forces was performed in "wind" axes in the analog computer; this coordinate frame could be reidentified as "path" axes for the nonuniform wind field case, and would result in no changes to the analog computation scheme. Angles of attack and sideslip would be measured with respect to the inertial velocity vector, rather than the usual free stream relative wind vector

This program was chosen and adapted. The modelling of aerodynamic coefficients over a broad flight regime was of no importance to the present task and was replaced by the modified strip integration technique to compute forces and moments on the aircraft. A routine to generate vortex velocities at points on the aircraft also was added. Numerous other changes were made to the original program to make it conform to the present task. The basic force and moment computation and the rigid body equations of motion are described below.

The vortex arrangement used in the simulation includes a pair of Rankine vortices and their images below the ground. Separations of these vortices could be controlled both vertically and horizontally. The left vortex is used as the center of the inertial reference frame; other vortices are treated as being biased to the side and/or below this vortex. Appendix E provides the details of the geometry and velocity field for these vortices and for a model of ring vortices which have undergone Crow[15] type breakup. Vortex velocity components are transformed to aircraft body axis components for use in computing local angles of attack on the flying surfaces.

The angle of attack at an arbitrary point on the wing can be written as

$$\alpha \simeq \frac{-V_{rel_z} - \sigma V_{rel_y} \operatorname{sgn} \xi}{|V_{rel_x}|} \qquad \text{B-1}$$

The relative velocity is composed of vortex and aircraft linear and rotational velocity components, and is written in the body frame.

$$\underline{V}_{rel} = \underline{U} - \underline{V} - \underline{\omega}_{ib} \times \underline{r}$$

$$= \begin{bmatrix} U_x - V_x + Q\,|\xi|\,\sigma + R\xi \\ U_y - V_y - R(x_c - |\xi|\tan\lambda) - P|\xi|\sigma \\ U_z - V_z - P\xi + Q\,(x_c - |\xi|\tan\lambda) \end{bmatrix} \qquad \text{B-2}$$

Therefore, for the ith wing station,

$$\alpha_i \simeq \{ V_z - U_{zi} + P\xi_i - Q(x_c - |\xi_i|\tan\lambda) - [U_{yi} - V_y - R(x_c - |\xi_i|\tan\lambda)]\sigma\,\mathrm{sgn}\,\xi_i \} / |V_x - U_{xi} - R\xi_i| \qquad \text{B-3}$$

The angle of attack on the stabilizer is influenced by the same kinds of components as is the wing, along with the downwash from the wing. For a particular stabilizer segment, the downwash is computed by following along the flow from that segment to the wing, computing the angle of attack (α_{ij}) at that point on the wing and adding $\partial\varepsilon/\partial\alpha$ times this value to ε_0

$$\varepsilon_j = \varepsilon_0 + \frac{\partial\varepsilon}{\partial\alpha}\,\alpha_{ij} \qquad \text{B-4}$$

As the dihedral effect of the stabilizer, if any, is assumed to be small, the total angle of attack for the jth segment becomes

$$\alpha_{t_j} \simeq \frac{V_z - U_{zj} + P\xi_{tj} + Qx_t}{|V_x - U_{xj} - R\xi_{tj}|} - \varepsilon_j \qquad \text{B-5}$$

For the rudder, the sidewash factor has been included in the lift curve slope. The rudder angle of attack is

$$\beta_r \simeq \frac{-V_{rel_y}}{\left|V_{rel_x}\right|}.$$

$$\simeq \frac{V_y - U_{yr} - R\ell_r + Px_r}{\left|V_x - U_{xr} - Qx_r\right|} \qquad \text{B-6}$$

In normal aeronautical fashion forces and moments developed from aerodynamic effects through flying surface angles of attack are measured along "stability" axes. The x and y axes lie in the plane of symmetry, with x also along the component of relative wind (uniform wind field) in this plane. Because the presence of vortices introduces a nonuniform wind profile across the airplane, some departure from this notation must be made, as there no longer is a single angle of attack. If the relative wind component is replaced by the inertial velocity vector, a unique relationship between the aircrafts' motion and a set of body axes is re-established. Furthermore, it is convenient from a computational standpoint to consider the direction of this vector as one of the axes, thereby rotating the coordinate frame out of the plane of symmetry when the aircraft is in sideslip.

It remains to resolve the forces generated at each flying surface segment along these "path" coordinates. The analog computer generates the path to body axes angles, and the local angles of attack and sideslip can be computed from the equations above; hence, the required coordinate transformation from local wind to path axes can be made. To simplify the digital computation load, the sideslip transformation, is performed in the analog computer. Thus, forces are computed in stability axes in the digital program.

Applying the force and moment modelling described in Appendix A and the local angle transformations described above yields the aerodynamic forces and moments. To these are added the control surface effects. The equations which follow apply to the linear portion of the angle of attack regime. Stall is considered separately as described in Appendix A.

$$L = \frac{cbq}{16} \sum_{1}^{16} F_i \{(C_{L_{0_\omega}} + C_{L_{\alpha_\omega}} \alpha_i)\cos(\alpha_i-\alpha)+C_{D_{0_i}} \sin(\alpha_i-\alpha)+C_{L_{sp}} \kappa_s \delta w\}$$

$$+ \frac{qS_t}{3} \sum_{1}^{3} \{(C_{L_{0_t}} +C_{L_{\alpha_t}} \alpha_{t_j})\cos(\alpha_{t_j}-\alpha)+C_{D_{0_j}} \sin(\alpha_{tj}-\alpha)$$

$$+ \frac{S}{S_t} C_{L_{\delta_e}} \delta_e\} \qquad \text{B-7}$$

$$D = \frac{cbq}{16} \sum_{1}^{16} F_i\{ C_{D_{0_i}} \cos(\alpha_i-\alpha)-(C_{L_{0_\omega}} + C_{L_{\alpha_\omega}} \alpha_i)\sin(\alpha_i-\alpha)\}$$

$$+ \frac{qS_t}{3} \sum_{1}^{3}\{C_{D_{0_j}} \cos(\alpha_{t_j}-\alpha)-(C_{L_{0_t}} + C_{L_{\alpha_t}} \alpha_{t_j})\sin(\alpha_{t_j}-\alpha)\} \qquad \text{B-8}$$

$$Y = \frac{cbq \sin\sigma}{16} \sum_{1}^{16} F_i \left(C_{L_{\alpha_\omega}} \alpha_i - 2C_{L_w} |\xi_i| \frac{R}{V}\right)$$

$$+ C_{Y_{\beta_{wb}}} Sq\beta + C_{Y_{\beta_r}} S_r q\beta_r + C_{Y_{\delta_r}} qS\delta_r \qquad \text{B-9}$$

$$M = - \frac{cbq}{16} \sum_{1}^{16} F_i \{(C_{L_{0_\omega}} + C_{L_{\alpha_\omega}} \alpha_i)x_i + C_{m_{sp}} c \kappa_s \delta_w\}$$

$$- \frac{S_t x_t q}{3} \sum_{1}^{3} \left(C_{L_{0_t}} + C_{L_{\alpha_t}} \alpha_{t_j} + C_{m_{\delta_e}} \frac{Sc}{S_t x_t} \delta_e\right) \qquad \text{B-10}$$

$$N = - \frac{cbq}{16} \sum_{1}^{16} F_i\left\{\frac{\xi_i \alpha_i}{V} (C_{L_{0_\omega}} + C_{L_{\alpha_\omega}} \alpha_i)- C_{n_{\delta_a}} \kappa_a b\delta_a- C_{n_{sp}} \kappa_s b\delta_w\right\}$$

$$- C_{Y_{\dot\beta_{wb}}} S\, x_{wb}\, q\beta- C_{Y_{\beta_r}} S_r \ell_r\, q \left(\beta_r - \frac{P\, x_r}{V}\right)$$

$$+ C_{n_{\delta_r}} q\, Sb\delta_r \qquad \text{B-11}$$

$$\mathcal{L} = -\frac{cbq}{16}\sum_{1}^{16} F_i\{C_{L_{\alpha_\omega}}\xi_i\alpha_i - 2C_{L_w}\frac{\xi_i^2 R}{V}$$

$$- C_{\ell_{\delta_a}}\kappa_a b\,\delta_a - C_{\ell_{sp}}\kappa_s b\delta_w\}$$

$$+ C_{y_{\beta_r}} S_r x_r\, q\,\beta_r + C_{\ell_{\delta_r}} Sbq\delta_r \qquad \text{B-12}$$

κ_a is a weighting function and segment identifier to properly distribute aileron moment in the segments where the ailerons exist. κ_s has the same function for the spoilers.

$$\kappa_a = \frac{16\,S}{cb\sum_{a_1}^{a_i} F_i} \qquad \text{if aileron is in the segment}$$

$$= 0 \qquad \text{if aileron is not in the segment}$$

where a_1 and a_i are the first and final segments with ailerons present. For example, if the ailerons cover the outer three segments, the summed indices would be 1, 2, 3, 14, 15, and 16. For the spoilers,

$$\kappa_s = \frac{16\,S}{cb\sum_{s_1}^{s_i} F_i} \qquad \text{if the spoiler is in the segment}$$

$$= 0 \qquad \text{if the spoiler is not in the segment}$$

With the forces and moments completed, the rigid body equations of motion can be considered. Since the forced motion is observed in path (p) axes,

$$\Sigma\underline{F} = m\left.\frac{d\underline{V}}{dt}\right|_p + m\,\underline{\omega}_{ip} \times \underline{V} \qquad \text{B-13}$$

The angular velocity ω_{ip} can be written in terms of ω_{ib}, ω_{bp} and, since these are measured in body axes, a coordinate transformation matrix from body to path axes.

$$\underline{\omega}_{ib} = \begin{bmatrix} P \\ Q \\ R \end{bmatrix}$$

$$\underline{\omega}_{bp} = \begin{bmatrix} -\dot{\beta}\ \sin\ \alpha \\ -\dot{\alpha} \\ \dot{\beta}\ \cos\ \alpha \end{bmatrix}$$

$$\underline{\omega}_{ip} = \begin{bmatrix} \cos\beta\cos\alpha & \sin\beta & \cos\beta\sin\alpha \\ -\sin\beta\cos\alpha & \cos\beta & -\sin\beta\sin\alpha \\ -\sin\alpha & 0 & \cos\alpha \end{bmatrix} \begin{bmatrix} P - \dot{\beta}\sin\alpha \\ Q - \dot{\alpha} \\ R + \dot{\beta}\cos\alpha \end{bmatrix}$$

$$= C_b^p\ \underline{\omega}_{ip}^b$$

$$= C_b^p \begin{bmatrix} P \\ Q-\dot{\alpha} \\ R \end{bmatrix} + \begin{bmatrix} 0 \\ 0 \\ \dot{\beta} \end{bmatrix} \qquad \text{B-14}$$

Applying this result to equation B-13 produces the individual reaction force components in terms of the variables V, α, and β.

$$\Sigma\underline{F} = \begin{bmatrix} m\dot{V} \\ mV[-P\sin\alpha + R\cos\alpha + \dot{\beta}] \\ mV[P\sin\beta\cos\alpha - (Q-\dot{\alpha})\cos\beta + R\sin\beta\sin\alpha] \end{bmatrix} \qquad \text{B-15}$$

At this point, the forces are in stability axes. They must be transformed to the path axes through β. The final equations for the solution of the linear motion variables are,

$$\dot{V} = \frac{\Sigma F_{x'}}{m}\cos\beta + \frac{\Sigma F_{y'}}{m}\sin\beta \qquad \text{B-16}$$

$$\dot{\alpha} = \frac{\Sigma F_{z'}}{mV\cos\beta} + Q - (P\cos\alpha + R\sin\alpha)\tan\beta \qquad \text{B-17}$$

$$\dot{\beta} = \frac{\Sigma F_{y'}\cos\beta}{mV} - \frac{\Sigma F_{x'}\sin\beta}{mV} + P\sin\alpha - R\cos\alpha \qquad \text{B-18}$$

Implicit in the force terms are components of gravity, which can be computed by using the aircraft orientation matrix C_i^b. The moments are used directly in the Euler equations for the solution of the angular velocity components along body axes.

$$\dot{P} = \frac{\mathcal{L}}{I_x} + \frac{I_{xz}}{I_x}(\dot{R}+PQ) + \frac{(I_y-I_z)}{I_x}QR \qquad \text{B-19}$$

$$\dot{Q} = \frac{M}{I_y} + \frac{(I_z-I_x)}{I_y}RP + \frac{I_{xz}}{I_y}(R^2-P^2) \qquad \text{B-20}$$

$$\dot{R} = \frac{N}{I_z} + \frac{I_{xz}}{I_z}(\dot{P}-QR) + \frac{(I_x-I_y)}{I_z}PQ \qquad \text{B-21}$$

The integration of these three equations is performed by the analog computer. A second set of integrations, to determine the Euler angles (ϕ, θ, and ψ) relating the orientation of the body axes to the inertial reference frame is performed by the digital program. The switch in computers is chosen to minimize integration errors which could accumulate to a significant level over the length of a run. These integrations are performed with a cycle time of .02 second to further maintain accuracy. The Euler angles are used to identify the time history of the aircraft's orientation, and with the aid of the path to body axis transfomation matrix to generate inertial components of velocity which are then integrated to yield aircraft position. An intermediate result of the velocity computation is the aircraft's velocity in body axis which is needed in the flying surface angle of attack equations (B-3, 5, and 6) Finally, with the inertial to path axes matrix established, gravity components can be computed for use in the force equations B-16 to 18. These steps complete the major cycle performed in the digital computer. A block diagram of the computer function is shown in figure B-1.

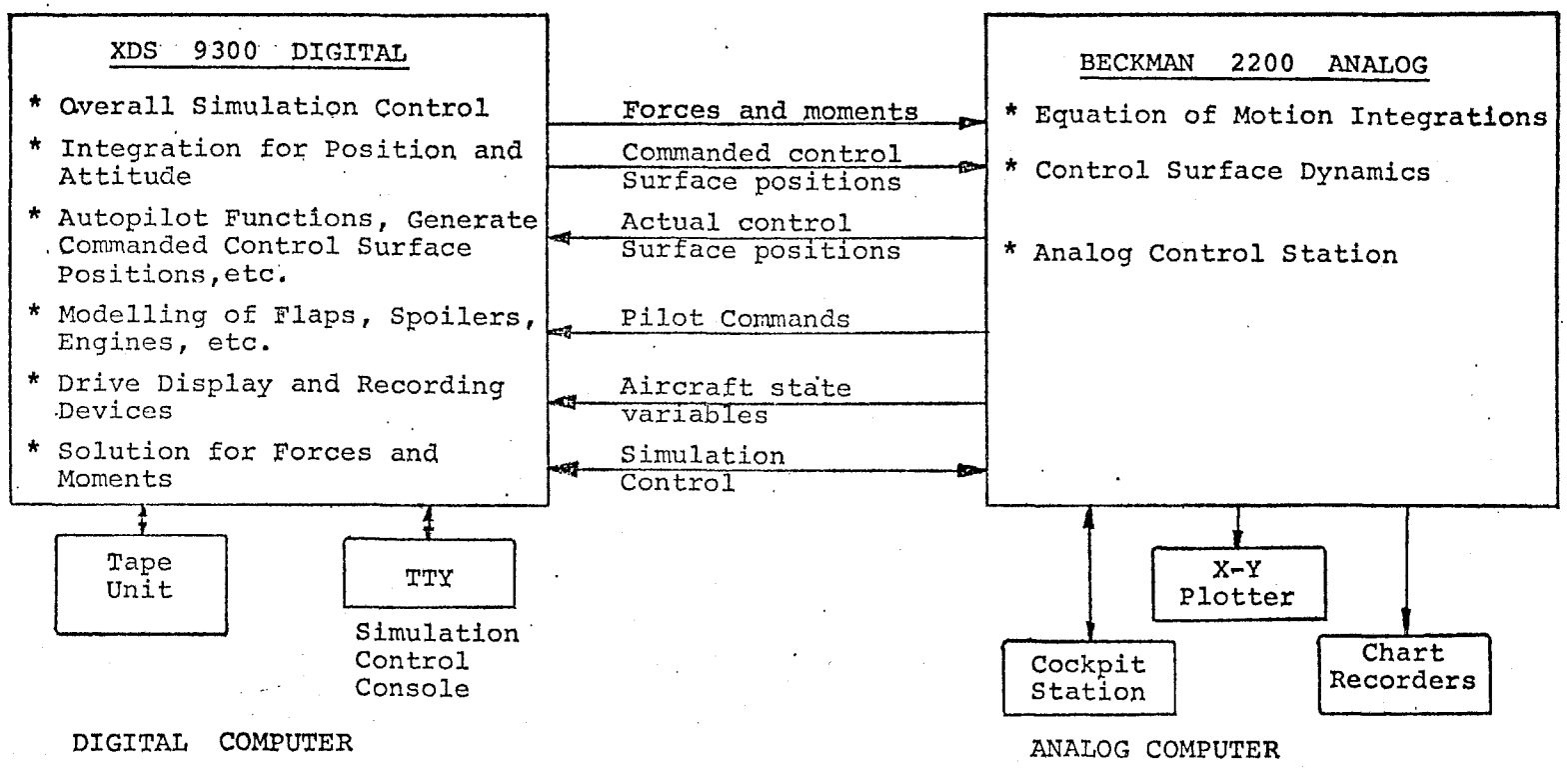

Figure B-1 Simulation Control Diagram

Appendix C

Digital Autopilot

The digital autopilot used in the six-degree-of-freedom simulation was developed by Dr. R. G. Stern under contract to NASA [14]. It was originally designed to be used with a hybrid simulation of the KC-135, and has been adopted and modified for use with the present vortex encounter simulation for this aircraft and the DC-9. No autopilot data was provided for the latter aircraft; gains were adjusted to achieve reasonable responses to stick and wheel impulses.

The autopilot was designed to operate in any one of eight modes; however, only four of these were used during the present work: direct control mode, stability augmentation system mode, control stick steering mode, and instrument landing system mode. The last mode was developed especially for the vortex encounter program. Other modes, such as Mach hold were not included in the present simulation.

Figure C-1 illustrates the block diagram for the direct control modes. With no control inputs, this mode represents the stick-fixed behavior of the aircraft, with no autopilot. It is useful for investigating the dynamic characteristics of an airplane through control perturbations. δ_W is the variable corresponding to the wheel angle in degrees, and is the ratio of maximum angles of the spoilers and the ailerons. It is used in the main vortex routine to generate spoiler moments and forces. The one-tenth second lag is used to represent the control system servo responses.

The stability augmentation system mode (Fig. C-2) adds angle rate and sideslip feedback to provide some degree of stabilization. Its primary purpose is to include the effects of a yaw damper to improve the dutch roll response of swept wing aircraft. With gains K_5, K_7, and K_{18} set to zero, this mode is used to represent

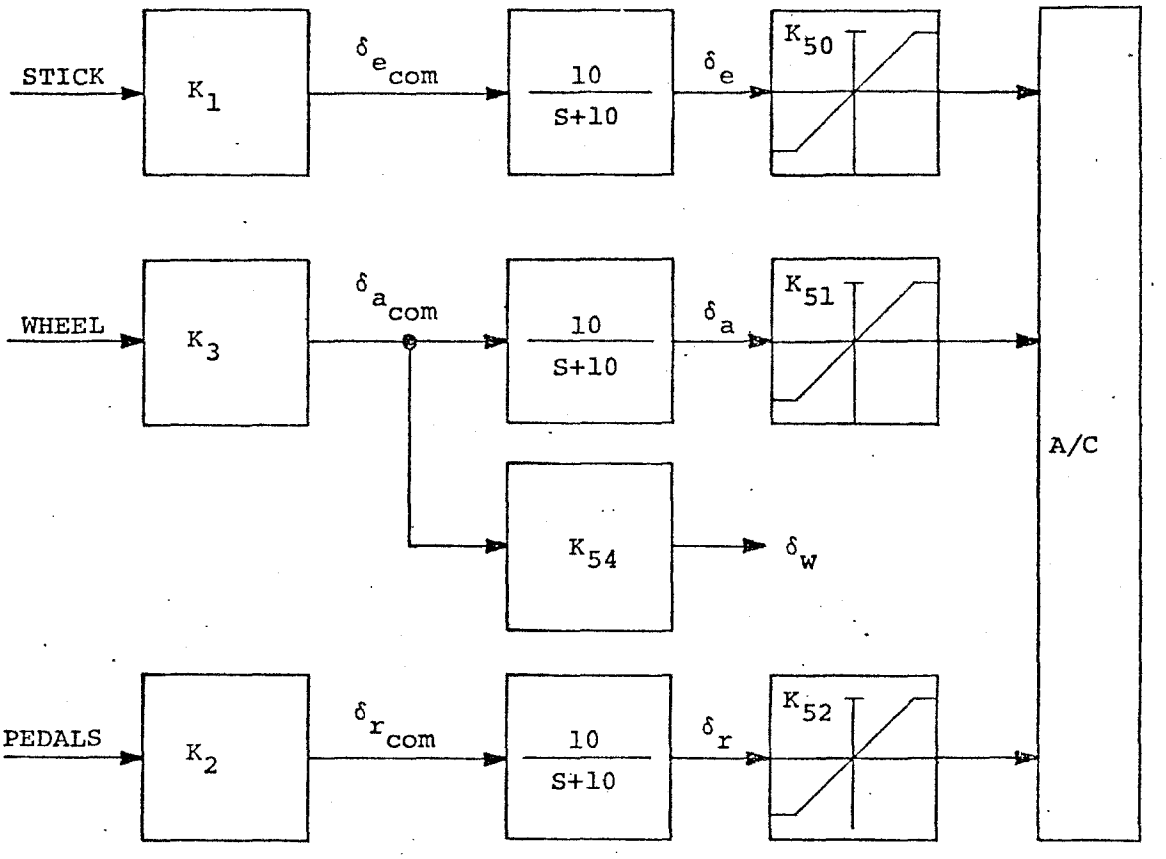

PEDALS CURRENTLY NOT AVAILABLE

Figure C-1. Direct Mode Block Diagram

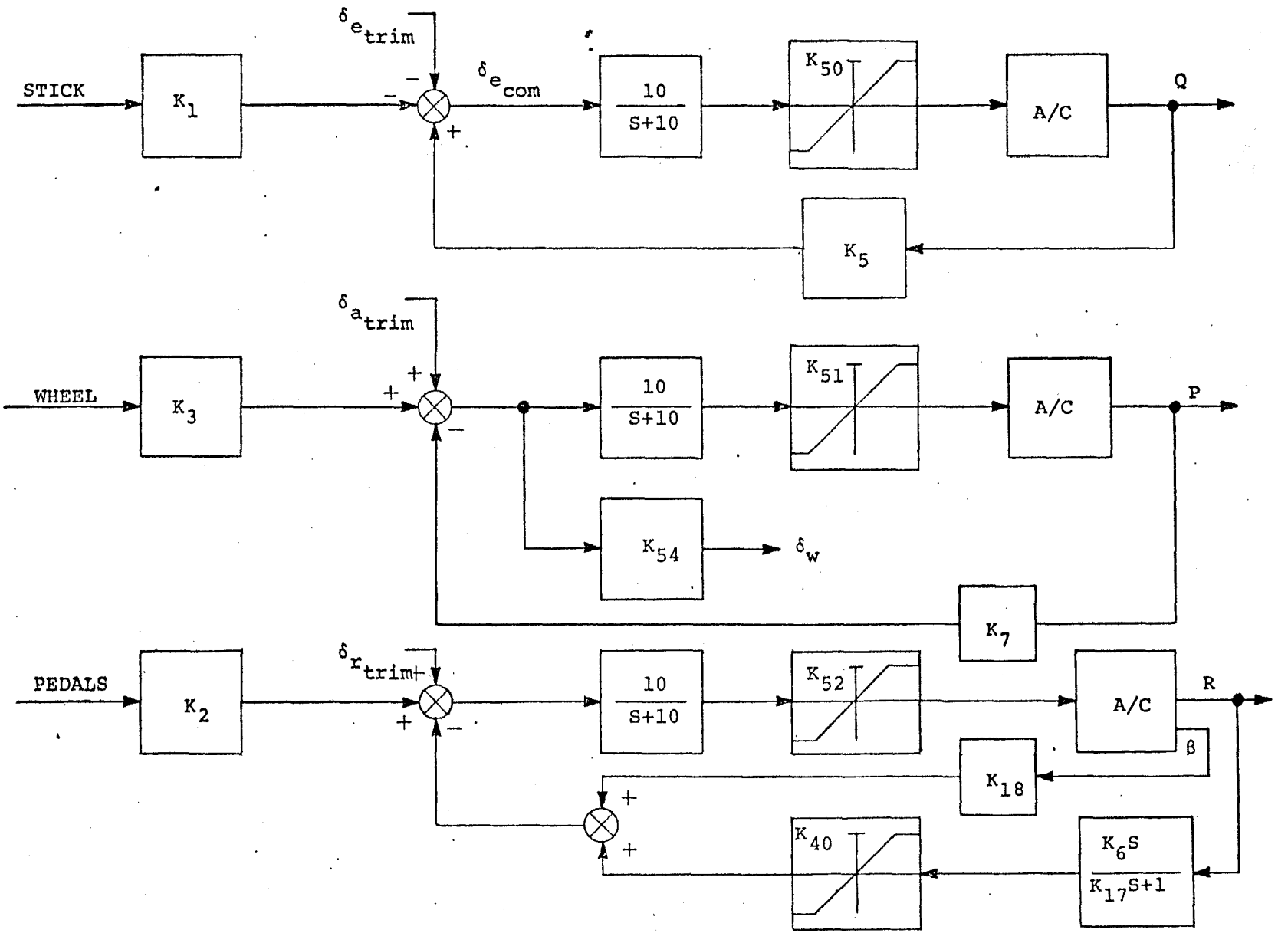

Figure C-2. Stability Augmentation System

the aircraft under pilot control with the autopilot disengaged. The yaw damper is independent of the autopilot and is a high pass yaw rate filter.

Control stick steering is the full normal autopilot mode and includes integrators which follow stick and wheel commands. The result of a short stick command pulse, for example, is a change in pitch angle and permits the pilot to change flight path angle without continuously holding the stick off center. Heading control is similar. Figure C-3 shows the block diagram.

The autopilot design is basic in nature, with rate and angle feedbacks and only two dynamic lags included. One of these lags is associated with the high pass filter of the yaw damper. The other is used to filter the heading command signal which is fed to the roll channel in the heading hold mode. It overcomes the effects of a noisy potentiometer and is of no significance to the dutch roll dynamics of any of the airplanes simulated. Finally, the turn coordinating coupler K_{34} is included in the loop, but was not used by the simulation, as turns were not considered to be important elements of the vortex encounter runs.

The ILS mode routine was written especially for the vortex encounter study to provide a target seeking capability which is not available in the control stick steering mode. The CSS mode maintains attitude only. The ILS equations are not strictly patterned after a conventional system in that 1) the target for both localizer and the glide slope is a single point, 2) the target can be any point in space and is not restrictive to negative flight path angles, and 3) the mode makes use of localizer error rate to provide damping to the heading response as well as to permit much higher response rates than are common to normal localizers. The purpose of the ILS mode is to approximately simulate a pilot's response to turbulent conditions when he has some terminal goal, without involving the broad field of human engineering. As an example of the speed of response to the system, an initial localizer error of 150 feet would be completely eliminated at the end of five seconds. This time would correspond to a change in altitude of 50 feet along a three degree landing glide path.

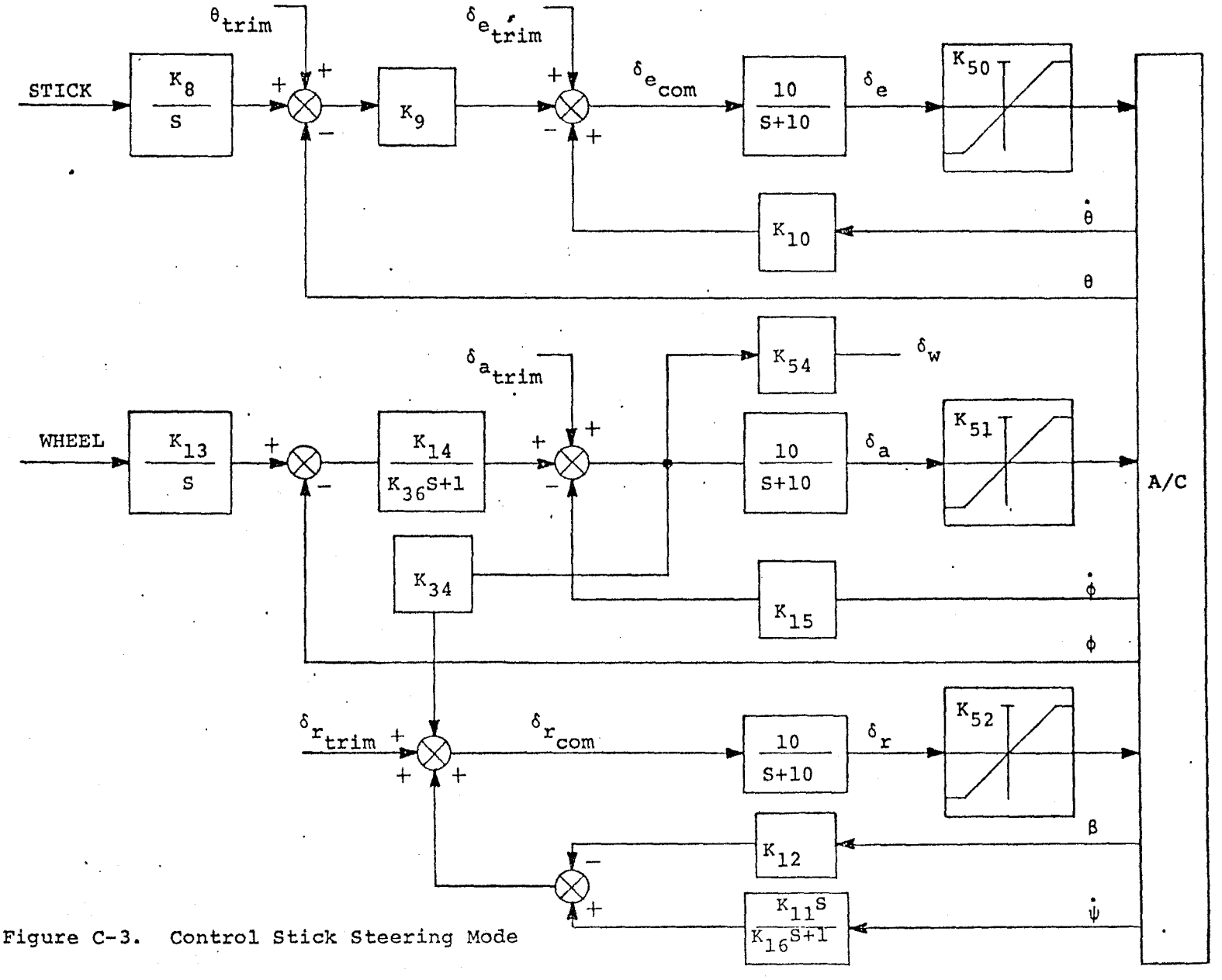

Figure C-3. Control Stick Steering Mode

A block diagram of the ILS mode is given in Figure C-4. The autopilot is the same as for the CSS mode, with the addition of the glide slope and localizer error gain blocks. Pitch and roll angles are limited for large error signals by K_{42} and K_{44}.

An instability can arise near the target as the base distance, through which the error angles are defined, approaches zero. Then, small lateral and vertical errors would be interpreted as relatively large localizer and glide slope errors, and would drive the autopilot hard. To avoid this difficulty, the normalizing base distance is limited to 2,000 feet. In the case of horizontal flight, the base is maintained at 4,000 feet. Test runs without vortices have shown that pitch and roll errors do not exceed one degree at target impact with the above limit imposed and no initial errors at the start of the runs.

Figures C-5 and 6 tabulate the autopilot gains used in the simulation for the DC-9 and KC-135. The Piper PA-30 could not be stabilized with any set of gains.

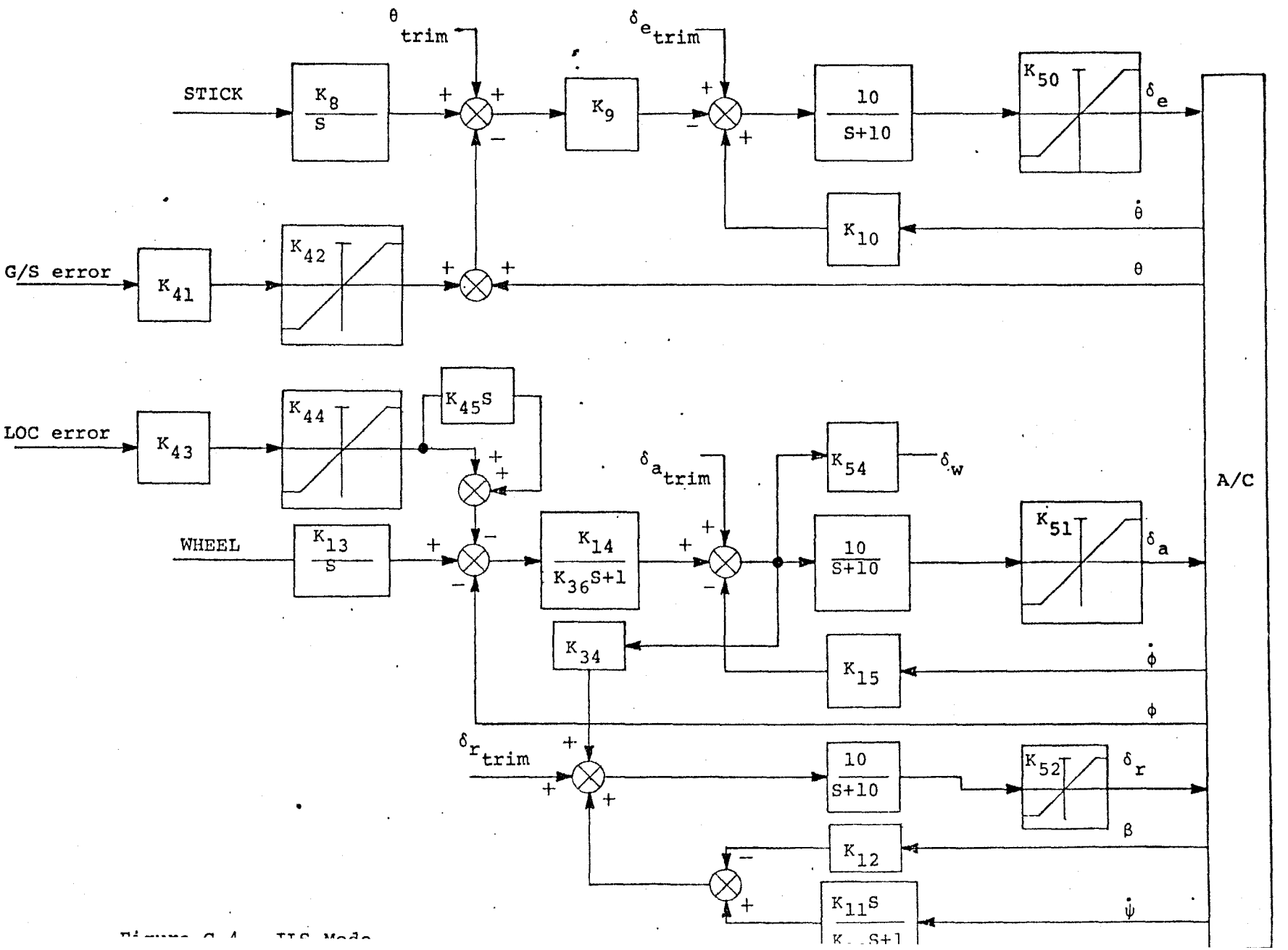

Figure C.4. ILS Mode

DTIME = .20000 MODE= 0

K(1)= 90.00	K(2)= 40.00	K(3)= 18.50	K(4)= .1001E-11	K(5)= 100.0
K(6)= 100.0	K(7)= 50.00	K(8)= .5000	K(9)= 75.00	K(10)= 150.0
K(11)= 200.0	K(12)= 150.0	K(13)= .5000	K(14)= 75.00	K(15)= 50.00
K(16)= 3.000	K(17)= 3.000	K(18)= 50.00	K(19)= 3.000	K(20)= 100.0
K(21)= .3000E-03	K(22)= .1000E-04	K(23)= .3500E-01	K(24)= 5.000	K(25)= .5000
K(26)= .0000	K(27)= .6500	K(28)= .1000	K(29)= 150.0	K(30)= 20.00
K(31)= .5000	K(32)= 10.00	K(33)= 1.500	K(34)= .0000	K(35)= .5000E-01
K(36)= .2000	K(37)= 12.00	K(38)= .0000	K(39)= .0000	K(40)= 30.00
K(41)= 16.40	K(42)= 3.400	K(43)= 15.00	K(44)= 15.00	K(45)= 10.00
K(46)= .0000	K(47)= .0000	K(48)= .0000	K(49)= .0000	K(50)= 30.00
K(51)= 16.50	K(52)= 30.00	K(53)= .0000	K(54)= 4.960	K(55)= .0000
K(56)= .0000	K(57)= .0000	K(58)= .0000	K(59)= .0000	K(60)= .0000
K(61)= .0000	K(62)= .0000	K(63)= .0000	K(64)= .0000	K(65)= .0000
K(66)= .0000	K(67)= .0000	K(68)= .0000	K(69)= .0000	K(70)= .0000
K(71)= .0000	K(72)= .0000	K(73)= .0000	K(74)= .0000	K(75)= .0000
K(76)= .0000	K(77)= .0000	K(78)= .0000	K(79)= .0000	K(80)= .0000
K(81)= .0000	K(82)= .0000	K(83)= .0000	K(84)= .0000	K(85)= .0000
K(86)= .0000	K(87)= .0000	K(88)= .0000	K(89)= .0000	K(90)= .0000
K(91)= .0000	K(92)= .0000	K(93)= .0000	K(94)= .0000	K(95)= .0000
K(96)= .0000	K(97)= .0000	K(98)= .0000	K(99)= .0000	K(100)= .0000

T(1)= .0000	T(2)= .0000	T(3)= .0000	T(4)= .0000	T(5)= .0000
T(6)= .0000	T(7)= .0000	T(8)= .0000	T(9)= .0000	T(10)= .0000
T(11)= .0000	T(12)= .0000	T(13)= .0000	T(14)= .0000	T(15)= .0000
T(16)= .6450E-01	T(17)= .6450E-01	T(18)= .0000	T(19)= .0000	T(20)= .0000
T(21)= .0000	T(22)= .0000	T(23)= .0000	T(24)= .0000	T(25)= .0000
T(26)= .0000	T(27)= .0000	T(28)= .0000	T(29)= .0000	T(30)= .9951E-02
T(31)= .3297	T(32)= .1981E-01	T(33)= .1248	T(34)= .0000	T(35)= .0000
T(36)= .6321	T(37)= .1653E-01	T(38)= .0000	T(39)= .0000	T(40)= .0000
T(41)= .0000	T(42)= .0000	T(43)= .0000	T(44)= .0000	T(45)= .0000
T(46)= .0000	T(47)= .0000	T(48)= .0000	T(49)= .0000	T(50)= .0000
T(51)= .0000	T(52)= .0000	T(53)= .0000	T(54)= .0000	T(55)= .0000
T(56)= .0000	T(57)= .0000	T(58)= .0000	T(59)= .0000	T(60)= .0000
T(61)= .0000	T(62)= .0000	T(63)= .0000	T(64)= .0000	T(65)= .0000
T(66)= .0000	T(67)= .0000	T(68)= .0000	T(69)= .0000	T(70)= .0000

Figure C-5 KC-135 Autopilot Gains

DTIME = .20000 MODE= 0

K(1)= 100.00	K(2)= 40.00	K(3)= 13.00	K(4)= .1001E-11	K(5)= .0000
K(6)= 207.6	K(7)= .0000	K(8)= .5000	K(9)= 25.00	K(10)= 50.00
K(11)= 100.0	K(12)= 12.00	K(13)= .5000	K(14)= 30.00	K(15)= 20.00
K(16)= 1.450	K(17)= 1.450	K(18)= .0000	K(19)= 3.000	K(20)= 100.0
K(21)= .3000E-03	K(22)= .1000E-04	K(23)= .3500E-01	K(24)= 5.000	K(25)= .5000
K(26)= .0000	K(27)= .6500	K(28)= .1000	K(29)= 150.0	K(30)= 20.00
K(31)= .5000	K(32)= 10.00	K(33)= 1.500	K(34)= .0000	K(35)= .5000E-01
K(36)= .2000	K(37)= 12.00	K(38)= .0000	K(39)= .0000	K(40)= 2.000
K(41)= 16.40	K(42)= 3.400	K(43)= 20.00	K(44)= 15.00	K(45)= 10.00
K(46)= .0000	K(47)= .0000	K(48)= .0000	K(49)= .0000	K(50)= 30.00
K(51)= 13.00	K(52)= 30.00	K(53)= .0000	K(54)= 8.770	K(55)= .0000
K(56)= .0000	K(57)= .0000	K(58)= .0000	K(59)= .0000	K(60)= .0000
K(61)= .0000	K(62)= .0000	K(63)= .0000	K(64)= .0000	K(65)= .0000
K(66)= .0000	K(67)= .0000	K(68)= .0000	K(69)= .0000	K(70)= .0000
K(71)= .0000	K(72)= .0000	K(73)= .0000	K(74)= .0000	K(75)= .0000
K(76)= .0000	K(77)= .0000	K(78)= .0000	K(79)= .0000	K(80)= .0000
K(81)= .0000	K(82)= .0000	K(83)= .0000	K(84)= .0000	K(85)= .0000
K(86)= .0000	K(87)= .0000	K(88)= .0000	K(89)= .0000	K(90)= .0000
K(91)= .0000	K(92)= .0000	K(93)= .0000	K(94)= .0000	K(95)= .0000
K(96)= .0000	K(97)= .0000	K(98)= .0000	K(99)= .0000	K(100)= 250.0

T(1)= .0000	T(2)= .0000	T(3)= .0000	T(4)= .0000	T(5)= .0000
T(6)= .0000	T(7)= .0000	T(8)= .0000	T(9)= .0000	T(10)= .0000
T(11)= .0000	T(12)= .0000	T(13)= .0000	T(14)= .0000	T(15)= .0000
T(16)= .1288	T(17)= .1288	T(18)= .0000	T(19)= .0000	T(20)= .0000
T(21)= .0000	T(22)= .0000	T(23)= .0000	T(24)= .0000	T(25)= .0000
T(26)= .0000	T(27)= .0000	T(28)= .0000	T(29)= .0000	T(30)= .9951E-02
T(31)= .3297	T(32)= .1981E-01	T(33)= .1248	T(34)= .0000	T(35)= .0000
T(36)= .6321	T(37)= .1653E-01	T(38)= .0000	T(39)= .0000	T(40)= .0000
T(41)= .0000	T(42)= .0000	T(43)= .0000	T(44)= .0000	T(45)= .0000
T(46)= .0000	T(47)= .0000	T(48)= .0000	T(49)= .0000	T(50)= .0000
T(51)= .0000	T(52)= .0000	T(53)= .0000	T(54)= .0000	T(55)= .0000
T(56)= .0000	T(57)= .0000	T(58)= .0000	T(59)= .0000	T(60)= .0000
T(61)= .0000	T(62)= .0000	T(63)= .0000	T(64)= .0000	T(65)= .0000
T(66)= .0000	T(67)= .0000	T(68)= .0000	T(69)= .0000	T(70)= .0000

Figure C-6 DC-9 Autopilot Gains

Appendix D

Aircraft Aerodynamic and Flight Condition Data

KC-135

The flight condition for the KC-135 was assumed to be a landing configuration with weight of 100,000 lbs., airspeed of 100 knots, and flaps deflected to 30 degrees. Altitude is near sea level. The whole aircraft stability derivatives used in the simulation are tabulated below.[16]

		$C_{m_0} = .1642$
$C_{D_0} = .128$	$C_L = 1.21$	$C_{m_\alpha} = -.968$
	$C_{L_\alpha} = 4.54$	$C_{m_q} = -.7858$
		$C_{m_{\delta_e}} = -.71$
$C_{y_\beta} = -.607$	$C_{\ell_\beta} = -.1950$	$C_{n_\beta} = .1510$
$C_{y_p} = -.103$	$C_{\ell_r} = .1256$	$C_{n_r} = -.0676$
$C_{y_{\delta_r}} = .2408$	$C_{\ell_p} = -.1573$	$C_{n_p} = -.0768$
	$C_{\ell_{\delta_a}} = .0902$	$C_{n_{\delta_r}} = -.1067$
	$C_{\ell_{\delta_r}} = .0033$	$C_{n_{\delta_{sp}}} = .0096$
	$C_{\ell_{\delta_{sp}}} = .0432$	

The aircraft physical parameters are given below.

$b = 131$	$m = 3105$	$S_t = 500$	$x_r = 20$
$c = 20.16$	$I_x = 1.722 \times 10^6$	$b_t = 39.66$	$\varepsilon = 0$
$S = 2433$	$I_y = 2.067 \times 10^6$	$x_t = 63.5$	$\partial\varepsilon/\partial\alpha = .37$
$\sigma = 7$	$I_z = 3.790 \times 10^6$	$S_r = 328.3$	$x_c = 10.2$
$\lambda = 35$	$J_{xz} = 9.04 \times 10^4$	$\ell_r = 62$	

The downwash derivative was computed from reference (17). Each engine has a maximum thrust of 15,000 lbs. Ailerons cover segments 2, 3, 14, and 15 of the wing. Spoilers are in segments 4, 6, 11, and 13. The spoiler program is given in Figure D-1 reproduced from Ref. (16). Spoiler induced moments are developed by using this curve in conjunction with the spoiler derivatives given above.

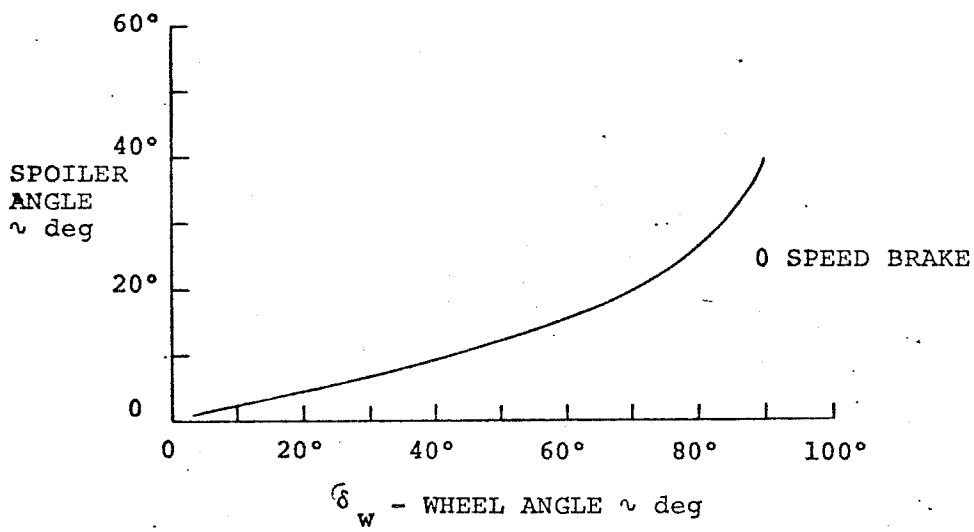

Figure D-1 KC-135 Spoiler Program

The resulting modelled KC-135 can be described by the physical data, control surface derivatives, basic lift and drag coefficients, and downwash characteristics given above together with the estimated lift parameters and spoiler derivatives presented below

$$C_{L_{0_w}} = .484 \qquad C_{L_{\alpha_w}} = 4.175$$

$$C_{L_{0_t}} = -.216 \qquad C_{L_{\alpha_t}} = 2.78$$

$$C_{Y_{\beta_r}} = -2.88 \qquad x_{wb} = -19.8$$

$$C_{Y_{\beta_{wb}}} = -.218$$

$$F_1 = .406 \quad F_2 = .681 \quad F_3 = .848 \quad F_4 = .965$$
$$F_5 = 1.050 \quad F_6 = 1.109 \quad F_7 = 1.147 \quad F_8 = 1.165$$

$$C_{\ell_{sp}} = .000256\ \delta_\omega \qquad |\delta_\omega| < 50°$$

$$= .0128\ \mathrm{sgn}\delta_\omega$$

$$+.000433(\delta_\omega - 50\ \mathrm{sgn}\delta_\omega) \qquad |\delta_\omega| \geq 50°$$

$$C_{n_{sp}} = .0000568\ \delta_\omega \qquad |\delta_\omega| < 50°$$

$$= .00284\ \mathrm{sgn}\ \delta_\omega$$

$$+000096\ (\delta_\omega - 50\ \mathrm{sgn}\ \delta_\omega) \qquad |\delta_\omega| \geq 50°$$

DC-9 Series 10

The aircraft was in a landing configuration with flaps set at 50 degrees, speed 130 knots, and gross weight 73,940 lbs. and C.G. at 27.1% MAC. Tail-off, tail, and whole airplane aerodynamic characteristics were provided by the McDonnell Douglas Corporation[11], thereby permitting a better assessment of the aircraft modelling program's estimation of component contributions to the

stability derivatives. For this airplane, a modified elliptical weighting funtion was used to account for the basic wing loading distribution. The whole aircraft stability derivatives used for the simulation are given below.

		$C_{m_0} = .0201$
		$C_{m_{a.c.}} = -.5229$
$C_{D_0} = .1403$	$C_L = 1.35$	$C_{m_\alpha} = -1.63$
	$C_{L_\alpha} = 5.64$	$C_{m_q} = -.9595$
		$C_{m_{\delta_e}} = -2.149$

$C_{y_\beta} = -1.0772$	$C_{\ell_\beta} = -.1788$	$C_{n_\beta} = .2183$
$C_{y_p} = .01775$	$C_{\ell_r} = .0873$	$C_{n_r} = -.0586$
$C_{y_{\delta_r}} = .3152$	$C_{\ell_p} = -.0915$	$C_{n_p} = -.0250$*
	$C_{\ell_{\delta_a}} = .0531$	$C_{n_{\delta_r}} = -.1604$
	$C_{\ell_{\delta_r}} = .0418$	$C_{n_{\delta_a}} = .00487$

The physical parameters for the aircraft are given below.

$b = 89.35$	$m = 2296.3$	$S_t = 275.5$	$x_r = 11.78$
$c = 11.8$	$I_x = 3.66 \times 10^5$	$b_t = 36.74$	$\varepsilon = 4.50$
$S = 934.3$	$I_y = 8.00 \times 10^5$	$x_t = 46.8$	$\partial\varepsilon/\partial\alpha = .510$
$\sigma = 3$	$I_z = 10.94 \times 10^5$	$S_r = 161$	$x_c = 7.88$
$\lambda = 24$	$J_{xz} = -.65 \times 10^5$	$\ell_r = 36.2$	

* While obtaining clearance to publish this data, Douglas Corporation personnel pointed out an error in this coefficient. It should be -.0131. An error in computing this coefficient was identified; however, this is a small cross derivative which has little importance in the dynamic response of the aircraft.

Each engine produces a maximum thrust of 11,700 lbs. Ailerons cover segments 2, 3, 14, and 15 of the wing, whereas spoilers are in segments 4, 5, 6, 11, 12, and 13. The spoiler forces and moments are presented in Figures D-2 through D-5. The piecewise linear curves used in the simulation are superimposed on the normal curves. The yaw damper functional diagram is given in Figure D-6.
The modelled DC-9 includes the following parameters.

$C_{L_{0_w}} = .139$ $\quad$ $C_{L_{\alpha_w}} = 5.17$

$C_{L_{0_t}} = -.383$ $\quad$ $C_{L_{\alpha_t}} = 3.25$

$C_{y_{\beta_r}} = -4.25$ $\quad$ $x_{wb} = -21.6$

$C_{y_{\beta_{wb}}} = -.344$

$F_1 = .0450$ $\quad$ $F_2 = .0753$ $\quad$ $F_3 = .0939$ $\quad$ $F_4 = 1.4341$

$F_5 = 1.5597$ $\quad$ $F_6 = 1.6477$ $\quad$ $F_7 = 1.7038$ $\quad$ $F_8 = .5295$

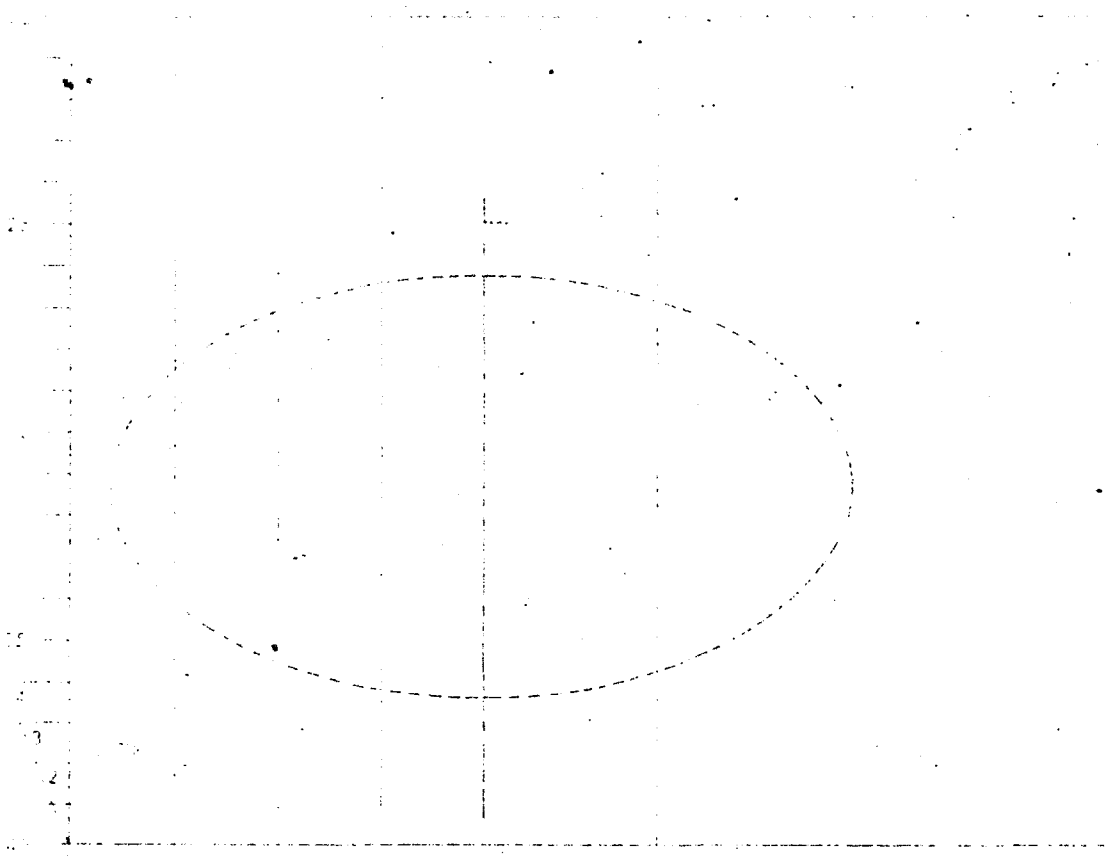

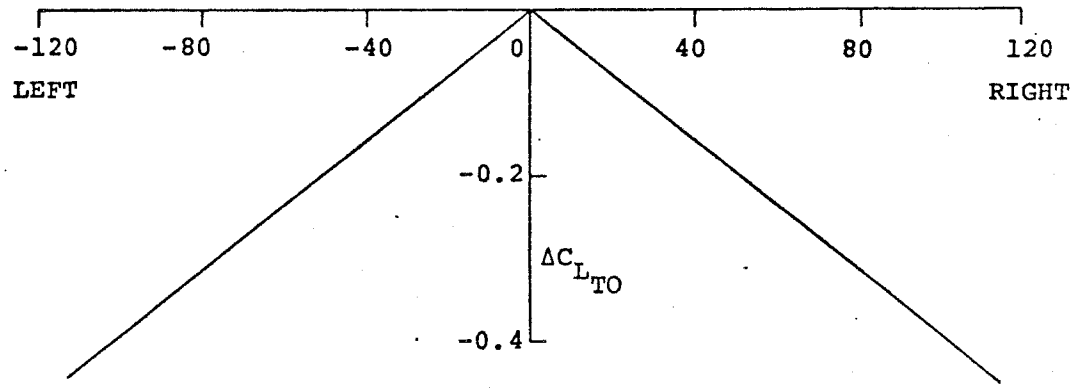

Figure D-2 DC-9 Spoiler Lift Characteristics

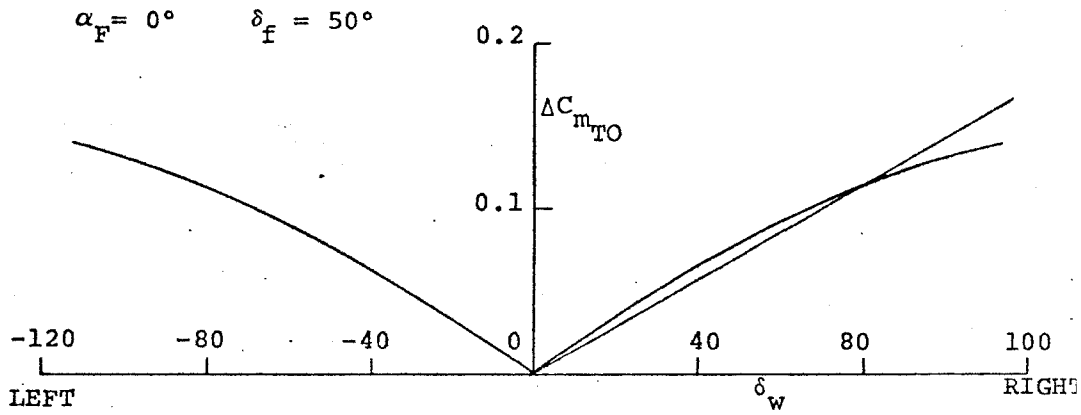

Figure D-3 DC-9 Spoiler Pitching Moment Characteristics

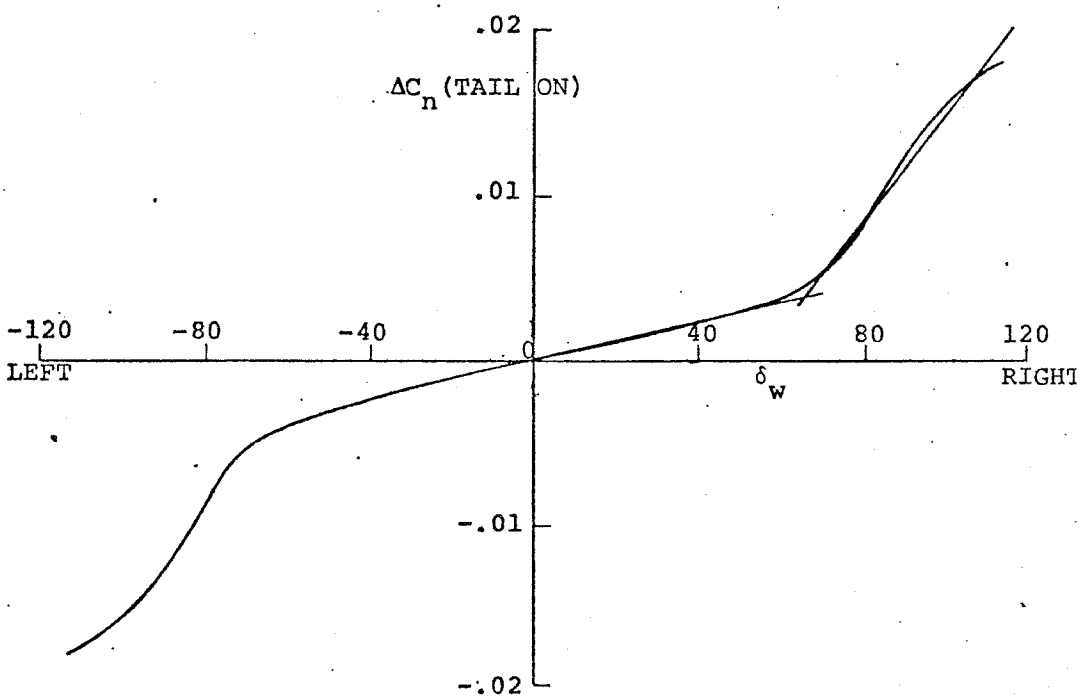

Figure D-4 Spoiler Yawing Moment Characteristics

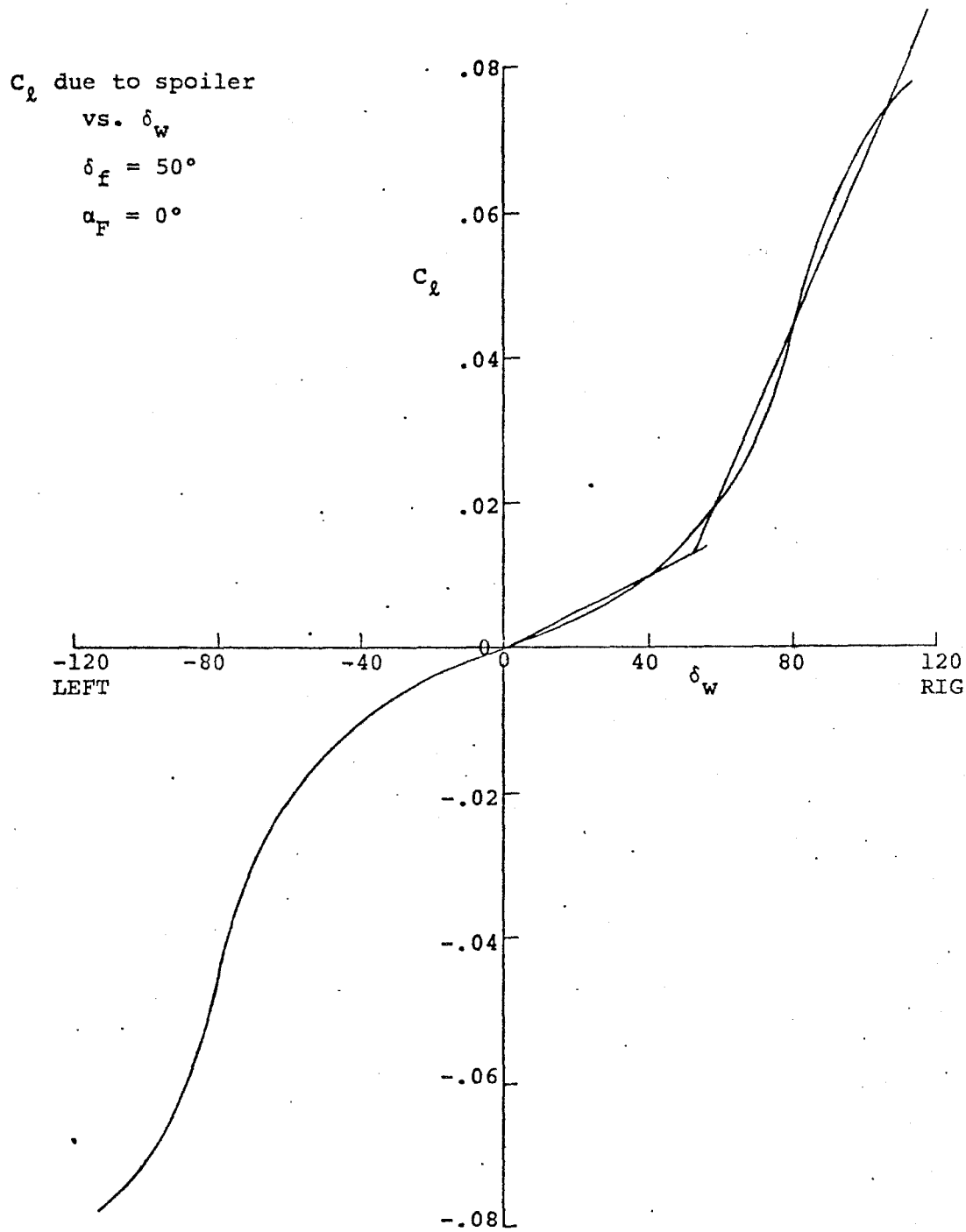

Figure D-5 DC-9 Spoiler Rolling Moment Characteristics

DC-9 YAW DAMPER

TRANSFER FUNCTIONS

(APPROACH GAINS)

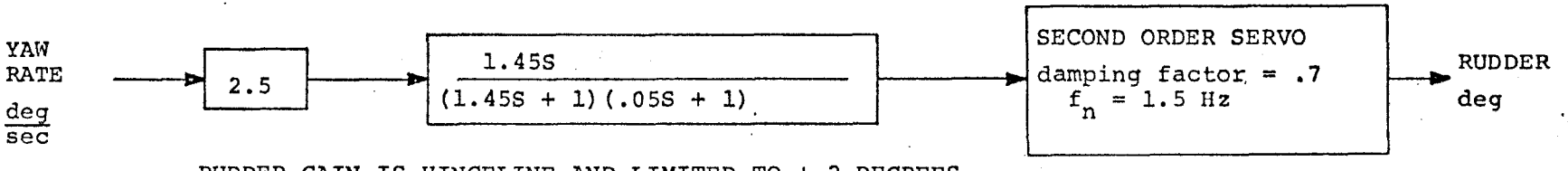

RUDDER GAIN IS HINGELINE AND LIMITED TO ± 2 DEGREES

OPERATES IN SERIES WITH PILOT RUDDER INPUTS

Figure D-6. Yaw Damper

$$C_{L_{sp}} = -.00388 \quad |\delta_\omega|$$

$$C_{m_{sp}} = .00123 \quad |\delta_\omega|$$

$$C_{n_{sp}} = .0000569 \quad \delta_\omega \qquad |\delta_\omega| \leq 65°$$

$$= .0037 \text{ sgn } \delta_\omega + .000313(\delta_\omega - 65 \text{ sgn } \delta_\omega) \qquad |\delta_\omega| > 65°$$

$$C_{\ell_{sp}} = .00025 \ \delta_\omega \qquad |\delta_\omega| \leq 52°$$

$$= .013 \text{ sgn } \delta_\omega + .00111(\delta_\omega - 52 \text{ sgn } \delta_\omega) \qquad |\delta_\omega| > 52°$$

Piper PA-30

The aircraft was assumed to be in a final approach condition with a speed of 104 knots and weight of 3603 lbs. Flaps were set at zero. The data provided by TSC represented a landing configuration for high wind conditions and were originally generated for the study of automatic landing systems as applied to a light, maneuverable aircraft. The whole aircraft stability derivatives used in the simulation follows.[18]

$C_{D_0} = .034$	$C_L = .55$	$C_{m_0} = .0591$
	$C_{L_\alpha} = 5.04$	$C_{m_\alpha} = -1.147$
		$C_{m_q} = -.355$
		$C_{m_{\delta_e}} = -2.87$
$C_{Y_\beta} = -.494$	$C_{\ell_\beta} = -.0860$	$C_{n_\beta} = .0756$
$C_{Y_p} = 0$	$C_{\ell_r} = .01124$	$C_{n_r} = -.0164$
$C_{Y_{\delta_r}} = .143$	$C_{\ell_p} = -.0511$	$C_{n_p} = -.00643$
	$C_{\ell_{\delta_a}} = .0803$	$C_{n_{\delta_r}} = -.0573$
	$C_{\ell_{\delta_r}} = .0115$	

The aircraft physical parameters are:

$b = 35.98$	$m = 112$	$S_t = 50$	$x_r = 3$
$c = 5$	$I_x = 2800$	$b_t = 12.5$	$\varepsilon = 0$
$S = 178$	$I_y = 1900$	$x_t = 12.5$	$\partial\varepsilon/\partial\alpha = .492$
$\sigma = 5$	$I_z = 4510$	$S_r = 15.6$	$x_c = .5$
$\lambda = -4$	$J_{xz} = 80$	$\ell_r = 12.5$	

The downwash derivative was computed from reference (17). Each engine produced a maximum thrust of 370 lbs. Ailerons cover wing segments 1, 2, 3, 14, 15, and 16.

The modelled PA-30 used the following parameters in addition to the physical data and control surface derivatives given above.

$C_{L_{0_w}} = .2897$	$C_{L_{\alpha_w}} = 4.229$
$C_{L_{0_t}} = .00116$	$C_{L_{\alpha_t}} = 5.691$
$C_{Y_{\beta_r}} = -3.00$	$x_{wb} = 0$
$C_{Y_{\beta_{wb}}} = -.231$	

$F_1 = .4363$	$F_2 = .7309$	$F_3 = .9105$	$F_4 = 1.0366$
$F_5 = 1.1274$	$F_6 = 1.1919$	$F_7 = 1.12316$	$F_8 = 1.2513$

Appendix E

Vortex Geometry

There are two types of vortex configurations considered here. The first type consists of two infinitely long vortices, such as those that would be shed by an aircraft in level flight, together with their image vortices in the ground. The second type is used for simulation of Crow-type vortex breakup and consists of an infinite array of straight-line vortex segments which approximate Crow-type vortex loops. The geometry of these configurations and the parameters describing them will be discussed in the same order as above.

Infinite Vortex Segments

The geometry in this case is described in figure E-1.

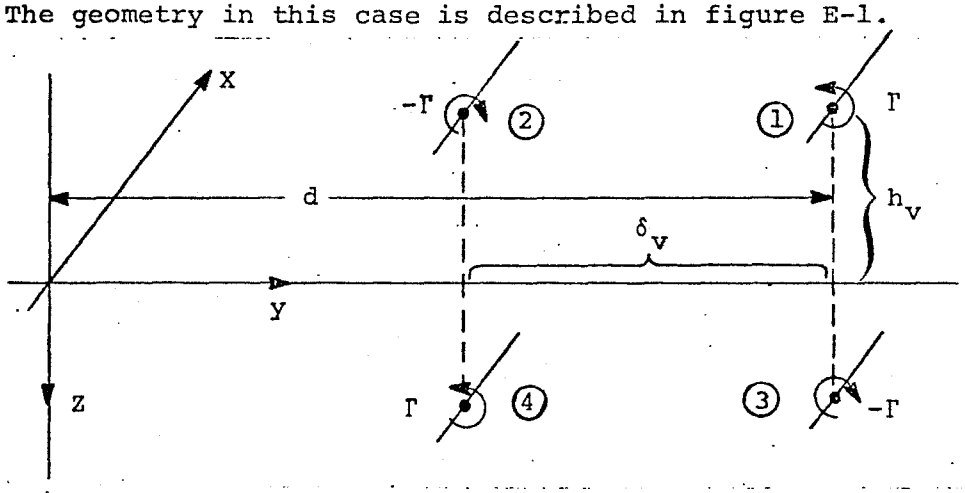

Figure E-1 Four Vortex Geometry

The inertial coordinate system appears on the left of the figure, and it is in terms of this system that the parameters are defined. The altitude of the vortices above the ground is h_v, considered positive.. Likewise, the variables d and δ_v are respectively the

Y position of the right-hand vortex pair and the separation between the vertical pairs. The circulation of each vortex is Γ, and the velocity field is in the direction shown by the arrows. The individual vortex filaments are numbered as shown in the figure.

Consider now a point in the (Y,Z) plane where the vortex induced velocity is desired. Since the vortex segments are infinite in length, in this case there is no dependence of these velocities on the X coordinate. Consider also a generic point (Y_v, Z_v) which describes the vortex axis location.

If we set

$$\delta^2 = (Y-Y_v)^2 + (Z-Z_v)^2, \tag{E-1}$$

then the velocity at (Y,Z) is

$$\begin{pmatrix} 0 \\ V_y \\ V_z \end{pmatrix} = \begin{pmatrix} 0 \\ Z-Z_v \\ -Y+Y_v \end{pmatrix} \frac{\Gamma\nu^2}{2\pi} \tag{E-2}$$

$$\text{where } \nu^2 = \min\left(\frac{1}{r_c^2}, \frac{1}{\delta^2}\right) \tag{E-3}$$

with r_c the core radius of the vortex. This formula presumes, of course, the Rankine vortex model. We now consider formula (E-2) as applied to each of the vortices as numbered in the figure and compute the velocity contribution of each in terms of its location as described by the parameters in the figure.

$$\underline{U}_1 = \begin{pmatrix} 0 \\ Z + h_v \\ -Y + d \end{pmatrix} \frac{\Gamma\nu_1^2}{2\pi}$$

$$\nu_1^2 = \min\left(\frac{1}{r_c^2}, \frac{1}{\delta_1^2}\right)$$

$$\underline{U}_2 = -\begin{pmatrix} 0 \\ Z + h_v \\ -Y + d - \delta_v \end{pmatrix} \frac{\Gamma\nu_2^2}{2\pi}$$

$$\nu_2^2 = \min\left(\frac{1}{r_c^2}, \frac{1}{\delta_2^2}\right)$$

$$\underline{U}_3 = -\begin{pmatrix} 0 \\ Z - h_v \\ -Y + d \end{pmatrix} \frac{\Gamma \nu_3^2}{2\pi}$$

$$\nu_3^2 = \min\left(\frac{1}{r_c^2}, \frac{1}{\delta_3^2}\right)$$

$$\underline{U}_4 = \begin{pmatrix} 0 \\ Z - h_v \\ -Y + d - \delta_v \end{pmatrix} \frac{\Gamma \nu_4^2}{2\pi}$$

$$\nu_4^2 = \min\left(\frac{1}{r_c^2}, \frac{1}{\delta_4^2}\right)$$

The total vortex-induced velocity at (0, Y, Z) is then

$$\underline{U}_1 + \underline{U}_2 + \underline{U}_3 + \underline{U}_4$$

Crow-Type Segments

The geometry in this case is described in Figure E-2. If we

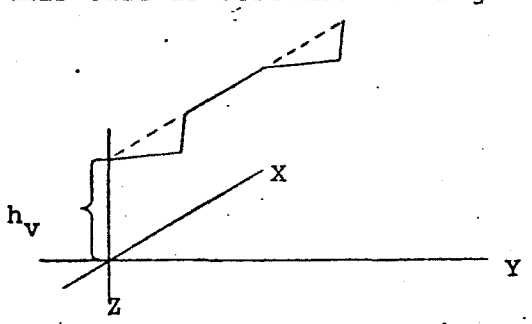

Figure E-2. Crow-Type Geometry

look down into the (X,Y) plane then we see the loop geometry more closely

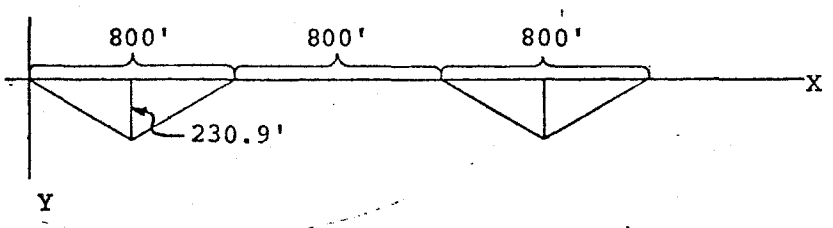

Figure E-3. Loop Geometry

The loops have been approximated by two straight-line vortex segments, each of length 461.8'. The array, as shown in this figure, continues on to infinity in the positive X direction. The flow field generated by this configuration thus approximates the field of the right-hand half of the Crow loops. For each segment a velocity contribution is calculated in a manner similar to that given in Equations (E-1, 2, 3) except that the X position of the aircraft appears explicitly. The altitude of the array is given by h_v in this vortex generation program.

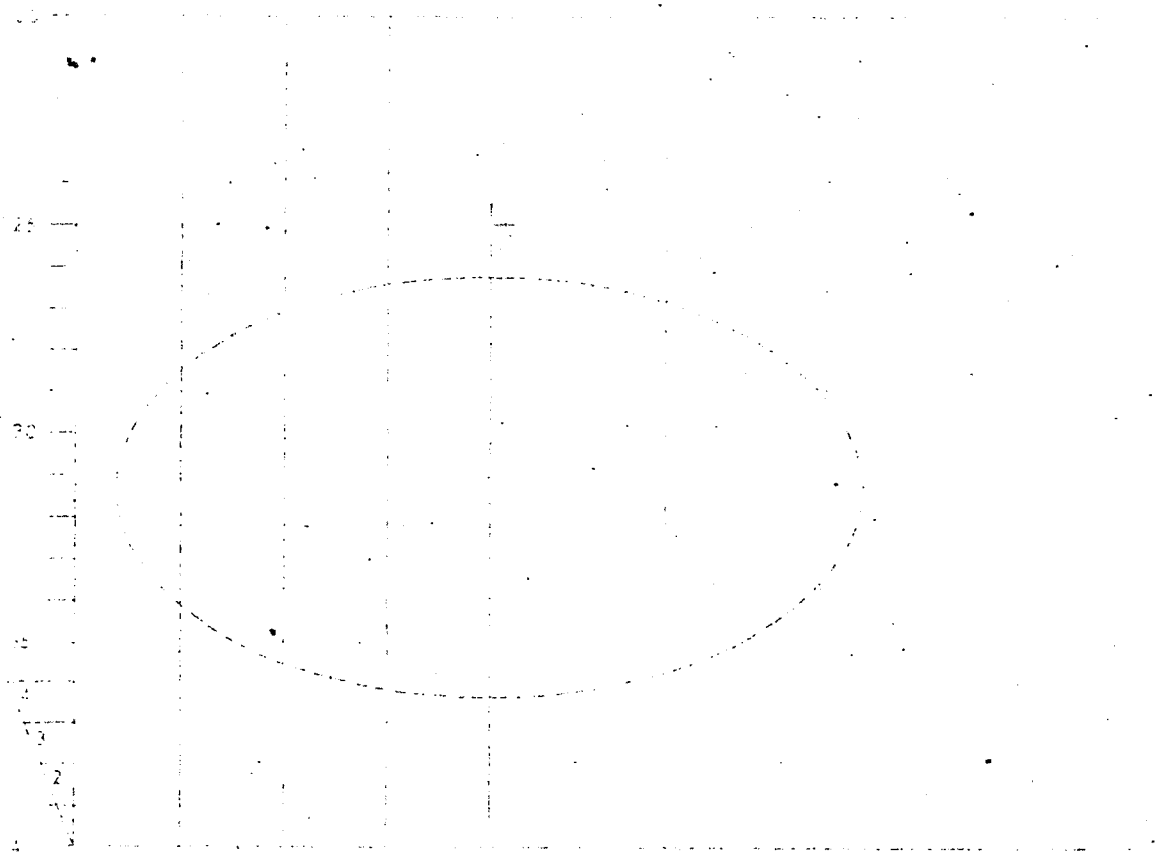

Appendix F

Proof of Concept Demonstration For Verifying the Accuracy of the Six-Degree-of Freedom Vortex Encounter Simulation

There are just two kinds of tests to experimentally verify the accuracy of the six-degree-of-freedom simulation: static tests can be conducted on small scale models in wind tunnels or towing tanks, or dynamic tests which examine complete vortex encounters can be conducted with full scale aircraft. Each has its unique set of advantages and disadvantages. Under static testing, the experiment is fully controlled, permitting simple measurement of forces and moments under precisely set conditions. Flow visualization with the aid of smoke for wind tunnel tests or dye for the towing tank is easily implemented. The repeatability of such tests is excellent. However in static testing, responses to the vortex induced force and torque program cannot be realized because the test model is rigidly mounted on a sting or carriage. Also, aircraft separation (vortex age) is limited by the length of the test section or towing tank. Also, the endurance of the encounter is limited by the length of the towing tank, although the wind tunnel experiment is not restricted in this way. Furthermore, tests cannot be repeated in the towing tanks until the water settles and the dye has been dissapated or neutralized. Vortex images can present special problems in towing tanks; they can be controlled to a greater degree in the circular wind tunnel. In all tests with models, scaling effects must be taken into account when correlating with the full scale aircraft encounter.

Dynamic tests examine complete encounters; a wide variety of these can be included in a test program. Aircraft separation is essentially unlimited; encounters with vortices in various stages of breakup may be possible. No size scaling is necessary for

correlation with the simulation; however, as tests must be conducted at a reasonable altitude for the sake of safety, density and Mach number factors may be significant. Whereas for static tests, control surface deflections may be difficult to implement, they are inherent to full scale testing. Only their time histories need to be measured to reconstruct the complete pilot input program.

The most serious limitations of dynamic testing are associated with the cost of the tests and the difficulty of navigating with respect to the encountering vortex. The latter is extremely difficult with the aid of smoke visualization only, because the smoke does not tend to remain densely entrained in the core. As a result it is nearly impossible for the pilot to judge his position to better than several tens of feet. Further, this limitation prevents the precise repetition of tests. Direct measure of vortex induced forces and moments is not possible; however, with the proper instrumentation, the histories of the translational and rotary motions can be recorded, from which instantaneous loads can be derived.

With this framework of capabilities, it is clear that static testing should verify the basic loading induced by a vortex encounter, but will not predict the total response. Dynamic testing may indicate the borderline conditions of a hazardous encounter and may be a better measure of the overall effectiveness of the simulation than static testing alone could provide. A brief outline of the types of tests which would serve to verify the simulation is presented below:

Static Testing

I Wind tunnel tests

a) Small model of DC-9 or KC-135 mounted on sting balance.

b) Half wing projecting from tunnel floor serves as vortex generator.

c) Hand-held smoke generator aids flow visualization

d) Sting balance instrumented for force and moment measurement.

e) Tests consist of measurements made with vortex at a series of positions along wing line and along line in plane of symmetry. Positions determined visually.

II Towing tank tests

a) Two models needed - DC-9 trailing, heavy jet generating vortices.

b) Ultra violet visible dye used for flow visualization

c) Greater separations than in wind tunnel are studied.

d) Test program essentially same as in wind tunnel.

Dynamic Testing

a) DC-9 following a heavy jet (eg. DC-10)

b) Tests at safe altitude (~10,000 ft). Density and Mach number effects must be scaled.

c) Flaps down configurations - landing and takeoff.

d) Instrumentation to be determined by a study.

e) Tests consist of series of nearly parallel encounters from various directions. Vertical encounters would be at angles consistent with those for landing and takeoff. Three to five degrees should be sufficient for lateral encounters.

Before any dynamic testing is performed, a detailed study of the instrumentation required to measure the rigid body motion must be undertaken to identify the accuracies needed for the full complement of equipment. While flight tests have been conducted in the past, no detailed study has been made to determine the equipment best suited for the measurement of the aircraft's motions or the accuracies required to perform the task. As an adjunct to this study, it should be determined whether or not a wing instrumented with a series of pressure sensors could be used to locate the vortex with sufficient accuracy when it is in close proximity to the wing. Some effort also should be made to determine the feasibility of a tip-mounted acoustic (or other type) vortex sensor to aid in determining the location of the encountered vortex.

Appendix G

Greater Southwest Airport Accident

On May 30, 1972 a DC-9 Series 10 crashed while attempting to land on the same runway used shortly before by a DC-10 making a touch-and-go landing. Observations of witness and subsequent analysis by the National Transportation Safety Board (NTSB) showed the accident was consistent with an encounter with a vortex stationed above the runway. A public hearing was held on August 22, in Ft. Worth, Texas; a docket [10] of the hearing transcript has been published.

By early July the NTSB had reviewed the status of the M.I.T. simulation and requested the investigation of the accident using all of the technical data and witness comments available. The simulation was completed and verifying runs were finished by mid-August.

The NTSB provided physical data for the DC-9, reproductions of the DC-9 cockpit voice recorder, the flight recorder traces for the DC-9 and the digital recording of the DC-10 flight recorder, as well as the results of a digital computer program which reduced the data to generate estimated trajectory information for both aircraft. This data for the DC-10, together with meteorological reports on the wind conditions was used by Dr. James Hallock of the Transportation Systems Center, D.O.T. to generate a time history of the shed vortex profiles. The Douglas Aircraft Company furnished estimated aerodynamic characteristics [11], a performance report [12], and data describing the yaw damper, stall warning indicator, and location of the static pressure ports for the DC-9.

From the data provided, it appeared the DC-9 made its final turn and attempted to land approximately one minute behind the DC-10. Because of a seven-knot quartering tail wind from the left,

the lefthand vortex was held up at about sixty feet above the runway and crossed the runway from right to left (looking up the vortex) about three thousand feet past the middle marker. Witnesses of the accident varied somewhat in their descriptions, but the general concensus is that some lateral rocking took place, followed by the left wing dipping, then the airplane rolled to the right until the wingtip struck the runway, after which the airplane flipped over on its back and slid along the runway, bursting into flames. The roll angle at the point where the wingtip struck probably was between 100 and 130 degrees.

Some uncertainty exists in the impact time as related to the flight and voice recorders. The time chosen by the NTSB corresponds to the start of the second large positive peak in the heading trace. There is another positive peak starting ten seconds earlier and lasting for five seconds for which the board had no explanation. The voice recording perhaps gives a more positive clue to the duration of the encounter. The recording ends with the sound of impact. At 11.1 seconds prior to this the copilot noted some turbulence. At 6.2 seconds prior to impact the call to "go around" was made by the copilot, and takeoff power was called by the pilot within 1.5 seconds. At 4.1 seconds prior to impact one of the stick shakers went off, followed by "I've got it, I've got it" by the copilot at 2.6 seconds before impact. The second stick shaker (on other wing) sounded at 1.7 seconds before impact. These events suggest that the initial effects of the wake turbulence were felt about 11 seconds before hitting and that the major encounter lasted only three or four seconds. The point where the copilot took control (2.6 seconds before impact) may have been just after the left wing dipped and just before the airplane was whipped to the right by the vortex. Had the copilot been holding right wheel, it would have augmented the final roll.

Reconstruction of the trajectory and the vortex profile suggests that the DC-9 approached the vortex from the left at a horizontal projection angle near seven degrees, and the normal flight path angle of 2.5 degrees. The result is that the right wing is the

first to be influenced by the upwash field which induces a left roll. If the heading is maintained and the aircraft is directed to cross the center of the vortex, it will ultimately feel the extreme right rolling moment produced by the vortex circulation. This, indeed, appeared to be the case for this accident.

For the simulation, it was decided to make a series of runs starting 300 feet to the left and several heights above the left vortex to see which encounter yielded results closest to the observed reaction. These were made with the autopilot in the CSS mode; the vortex circulation was chosen to be 5000 ft^2/sec. The best example, run 1-18, first showed a left roll of about 12 degrees, followed by a right roll of 52 degrees. The right wing would have struck the runway about one second after this peak roll point. A plot of the lateral and vertical displacement profile, in relation to the two vortices and their images, is shown in figure G-1, and the analog traces are given in figure G-2. Note that the aircraft is lifted slightly by the initial upwash, but that once significant right roll accumulates, and the aircraft moves into the downwash field, the altitude drops rapidly.

We were also interested in trying to assess the effect of the pilot in this situation. The left roll followed by the rapid right roll suggested that pilot reaction time could serve to worsen the latter upset to some degree. We were not interested in proving pilot error; the upset is exceedingly quick regardless of pilot inputs during the encounter. We wanted to produce the closest likeness to the observed accident and felt that the angle rate feedbacks in the autopilot limited the responses and were not in keeping with normal pilot responses based on visual cues. As a result, several tests were made using a "pilot" attempting to maintain wings level, aided by the analog roll angle trace only. After a number of runs, wherein the "pilot" learned to not overcontrol the airplane, the anticipated response was realized. Using the roll angle cue alone, he could not sense the rapid change in roll rate and was forced to reverse the wheel hard when the roll angle finally changed direction. The x-y plot, figure G-3, indicates the same kind of initial trajectory as for the CSS mode run,

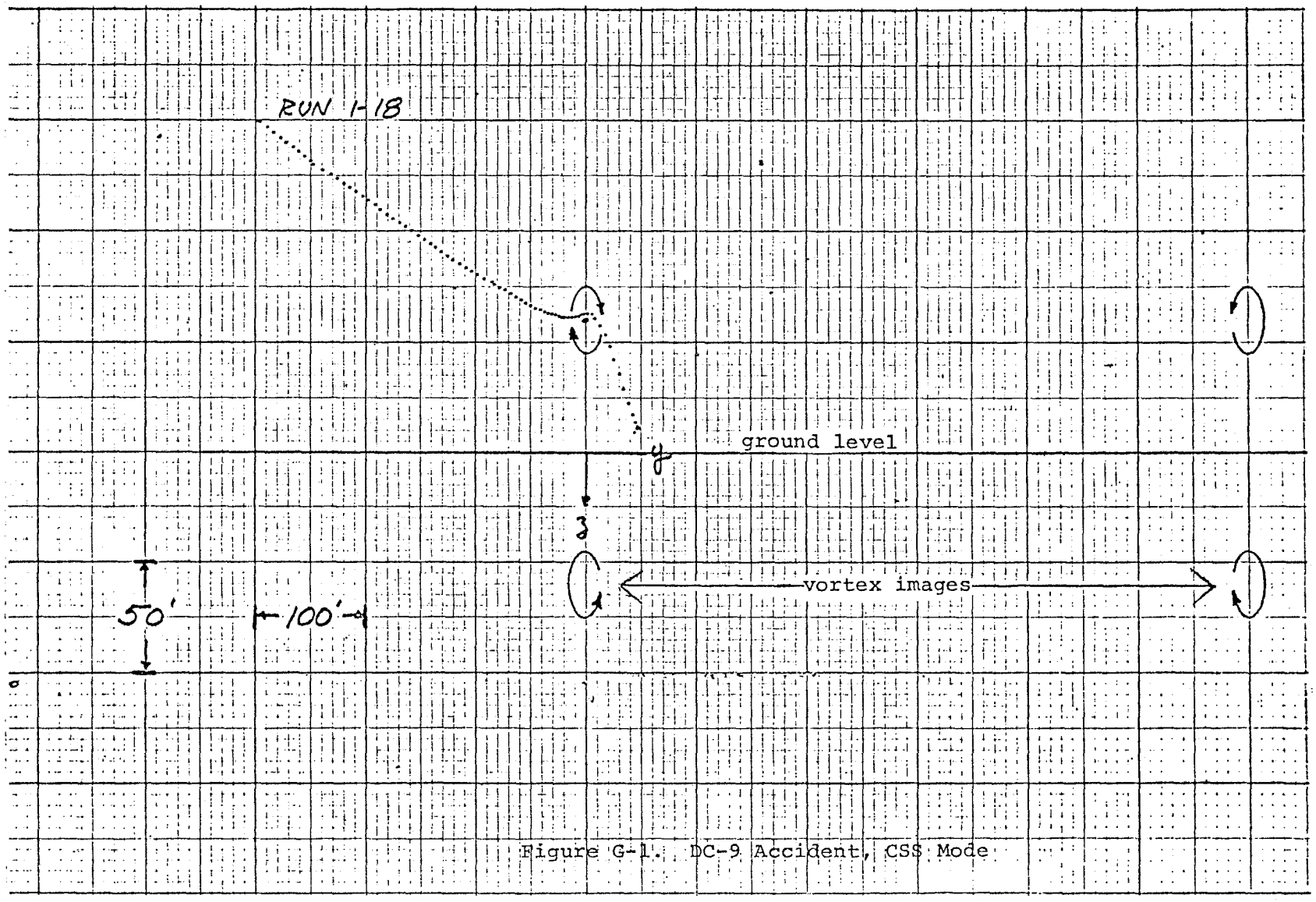

Figure G-1. DC-9 Accident, CSS Mode

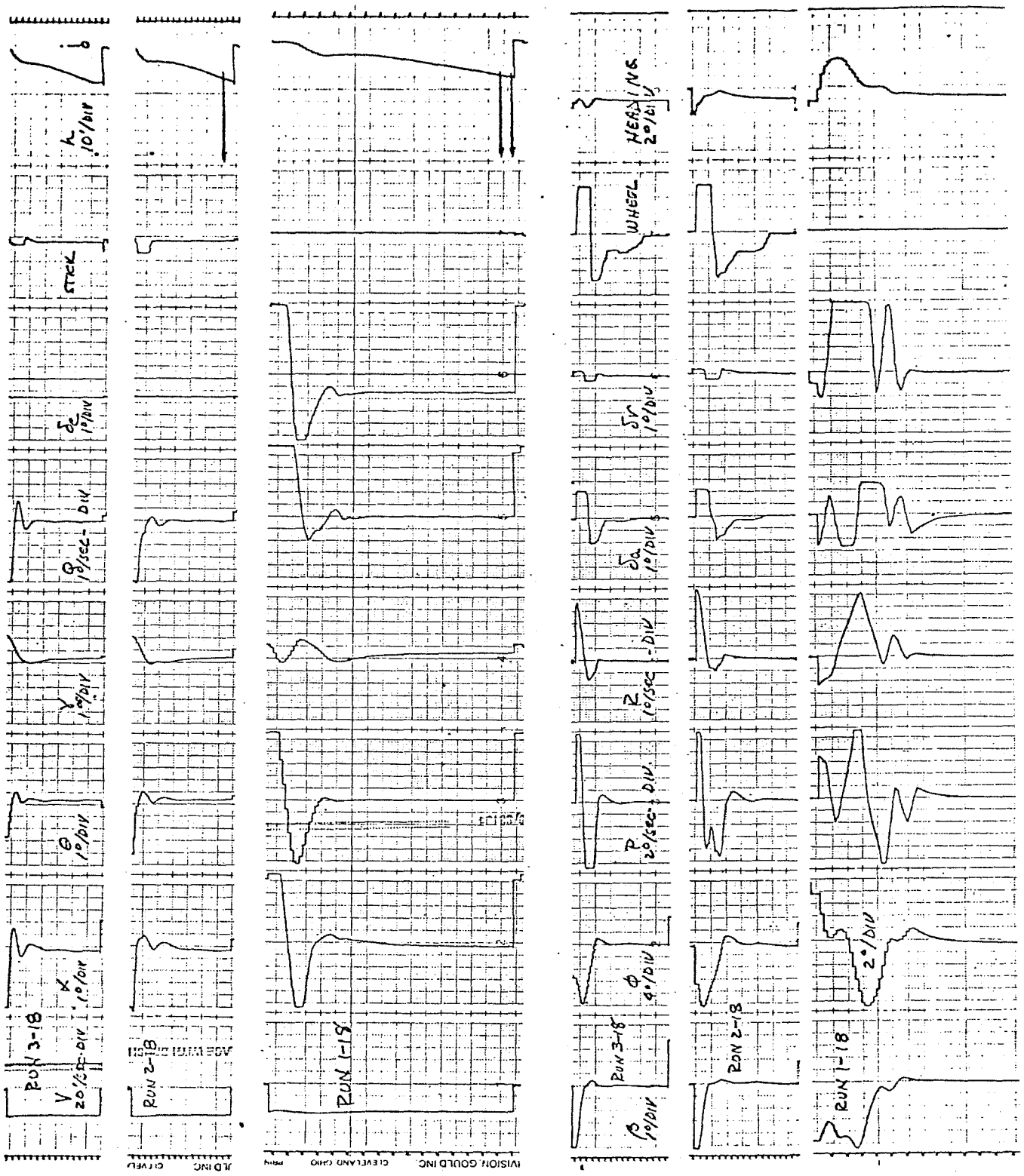

Figure G-2. DC-9 Analog Traces

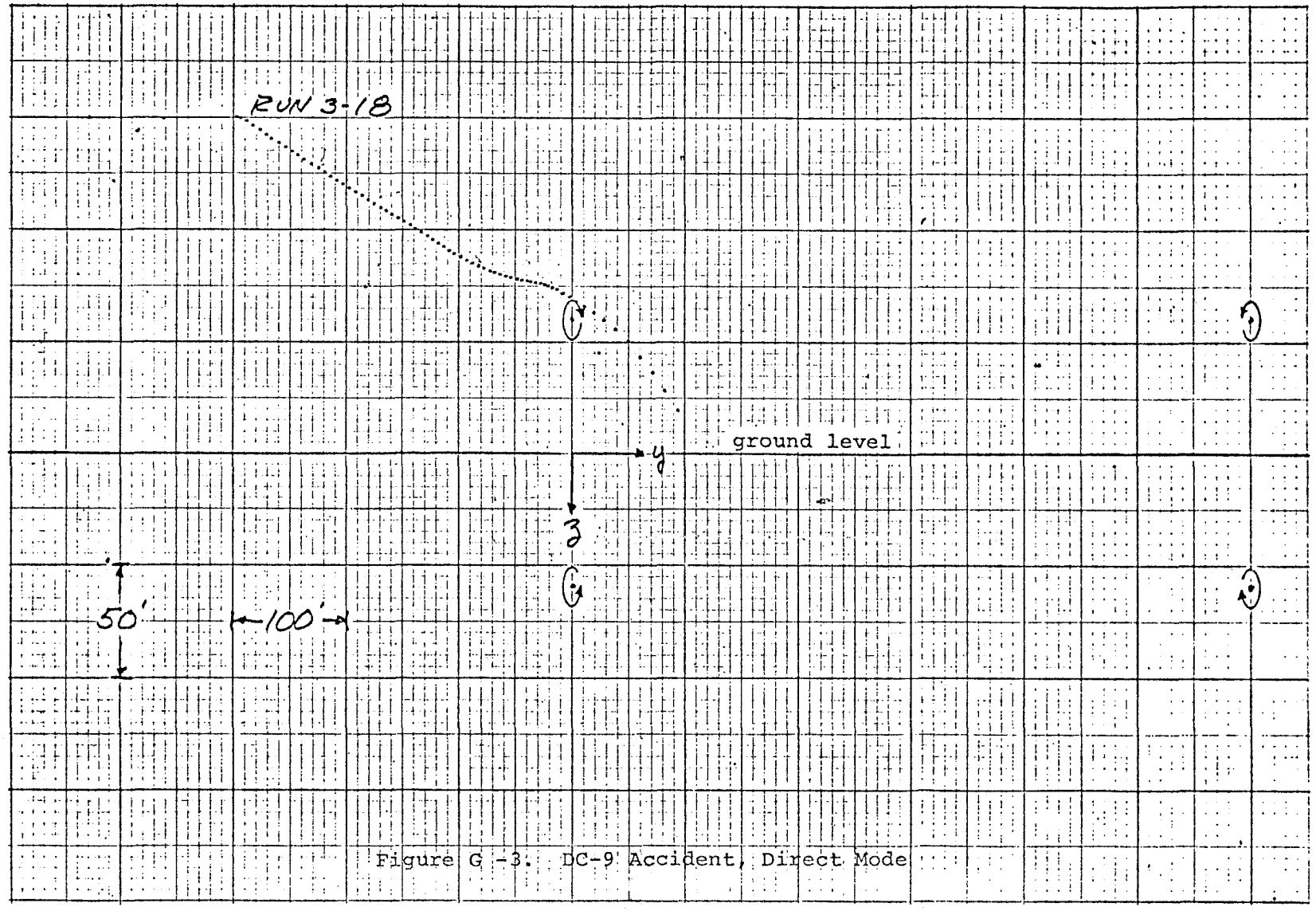

Figure G -3. DC-9 Accident, Direct Mode

but with more positive yaw angle following the major encounter. The analog traces of run 3-18 show a maximum roll angle of 97 degrees which is much closer to the observed value. It is apparent that without the lead information available to the autopilot, the "pilot" has much more difficulty responding to the rapid changes in roll. This, however, is not to say that pilot response was a prime contributor to the result of the accident; it is clear from the runs made with the autopilot that once a DC-9 got into a vortex of this strength, the control capability was insufficent to avoid the violent upset.

Appendix H

Simulation Records

The data presented here are the results of the six-degree-of-freedom simulation runs. They are grouped according to type of flight and aircraft simulated, e.g. DC-9 landing vertically near various strength vortices. A few comments about the data are appropriate. Scaling of the analog recordings was for the most part fixed; however a few runs had several different gains used for roll angle and altitude. These are noted on the individual graphs. Occasional spikes appear in the altitude trace. These appear to be the result of multiplex timing errors but do not affect the response of the aircraft. The data on the x-y plots are nearly all spaced at 0.4 second ; an occasional 0.2 spacing is easily distinguished by the increased density. The zero time point on the analog traces can be identified by either a mark in the timing channel or by large instantaneous changes in P, V, α, Q, and h. The latter method was used in most of the runs.

The following table identifies the runs by aircraft and type of terminal area operation.

I. KC-135 Vertical Landing

single vortex at 100 feet, $\gamma = -3°$, $\psi = 0°$, $h_{i.c.} = 300$ ft.

Run	$Y_{i.c.}$	Γ
1	50 ft	7000 ft^2/sec
2	75	"
3	100	"
4	-50	"
5	-75	"
6	-100	"
7	50	5000
8	75	"
9	100	"
10	-40	"
11	-50	"
12	50	3000
13	75	"
14	-30	"
15	-50	"
16	50	1500
17	75	"
18	-30	"

The pitch angle (θ) trace was inoperative for runs 1 through 15. Note, however that $\gamma = \theta - \alpha$.

Run	$Y_{i.c.}$	Γ
19	-50	1500
20	-75	"
21	50	700
22	75	"
23	-50	"
24	-75	"

II KC-135 Diagonal Landing
single vortex at 100 feet, $\gamma = -3°$, $h_{i.c.} = 300$ ft.

Run	$Y_{i.c.}$	ψ	Γ
25	-270	3 deg	7000 ft^2/sec
26	-305	"	"
27	-340	"	"
28	-130	"	"
29	-95	"	"
30	-60	"	"
31	-25	"	"
32	130	-3	"
33	95	"	"
34	60	"	"
35	25	"	"
36	270	"	"
37	305	"	"
38	-270	3	5000
39	-305	"	"
40	-130	"	"
41	-95	"	"
42	-60	"	"
43	130	-3	"
44	95	"	"
45	60	"	"
46	270	"	"
47	305	"	"

III KC-135 Horizontal Flybys
single vortex at 100 feet

Run	$h_{i.c.}$	ψ	Γ
48	100 ft	3 deg	7000 ft^2/sec
49	150	"	"
50	200	"	"
51	250	"	"
52	100	15	"
53	150	"	"
54	200	"	"
55	250	"	"
56	100	"	5000
57	150	"	"
58	200	"	"
59	100	3	"
60	150	"	"
61	200	"	"
62	100	"	3000
63	150	"	"

Run	$h_{i.c.}$	ψ	Γ
64	200	3	3000
65	100	"	1500
66	150	"	"
67	100	-3	7000
68	150	"	"
69	200	"	"
70	100	"	5000
71	150	"	"
72	200	"	"
73	100	"	3000
74	150	"	"
75	175	"	"

IV DC-9 Vertical Landing
single vortex at 100 feet, $\gamma = -3°$, $\psi = 0°$, $h_{i.c.} = 300$ ft.

Run	$Y_{i.c.}$	Γ
76	100 ft	7000 ft^2/sec
77	125	"
78	-75	"
79	-100	"
80	75	5000
81	100	"
82	-50	"
83	-75	"
84	50	3000
85	75	"
86	-50	"
87	-75	"

V DC-9 Diagonal Landing
single vortex at 100 feet, $\gamma = -3°$, $h_{i.c.} = 300$ ft.

Run	$Y_{i.c.}$	ψ	Γ
88	-270 ft	3°	7000 ft^2/sec
89	-305	"	"
90	-130	"	"
91	-95	"	"
92	-60	"	"
93	-25	"	"
94	270	-3°	"
95	305	"	"
96	130	"	"
97	60	"	"
98	25	"	"
99	-10	"	"

VI DC-9 Horizontal Flybys
single vortex at 100 feet

Run	$h_{i.c.}$	ψ	Γ
100	100 ft	3 deg	7000 ft^2/sec
101	150	"	"
102	175	"	"

Run	$h_{i.c.}$	ψ	Γ
103	200	3 deg	7000 ft^2/sec
104	100	-3	"
105	150	"	"
106	175	"	"
107	200	"	"

VII DC-9 Climbing
single vortex at 100 feet, except runs 108-109 with double vortex at 1000 ft, 122 ft separation.

Run	$Y_{i.c.}$	ψ	Γ
108	-261 ft	15 deg	5000 ft^2/sec
109	-61	0	"
110*	-100	15	"
111	0	0	"
112*	100	-15	"
113*	-100	15	3000
114	0	0	"
115*	100	-15	"
116	0	0	1500
117	-200	15	5000 SAS mode
118	0	0	" " "
119	100	-15	" " "

* no analog data available

VIII KC-135 Vertical Landing
Crow-type vortex waves at 100 feet, $\gamma=-3°$, $\psi=0$, $h_{i.c.}$ = 300 ft.

Run	$Y_{i.c.}$	Γ
120	315 ft	7000 ft^2/sec
121	340	"
122	365	"
123	290	5000
124	340	"
125	100	2000
126	240	"
127	290	"

IX KC-135 Horizontal Flyby
Crow-type vortex waves at 100 feet, $\gamma=0°$, $\psi=0°$ $h_{i.c}$ = 100 ft.

Run	$Y_{i.c.}$	Γ
128	100 ft	2000 ft^2/sec
129	240	"

<u>NOTE</u>: all zero levels are at center scale except for altitude, h, for which zero is located twenty divisions to the right of center. The starting point of a run can be identified by sharp jumps in one or more traces at the bottom of the curves.

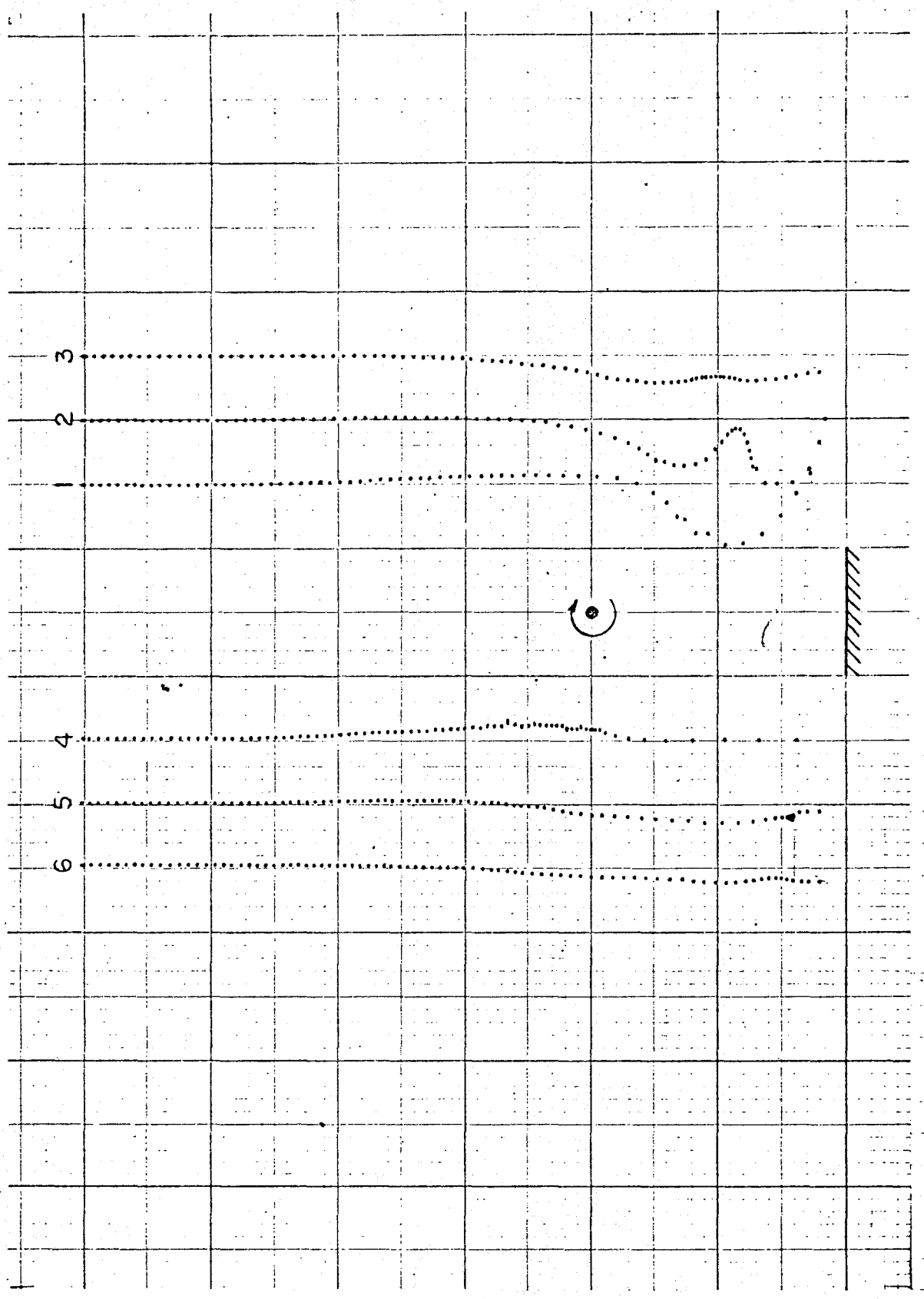
3
2
1
4
5
6

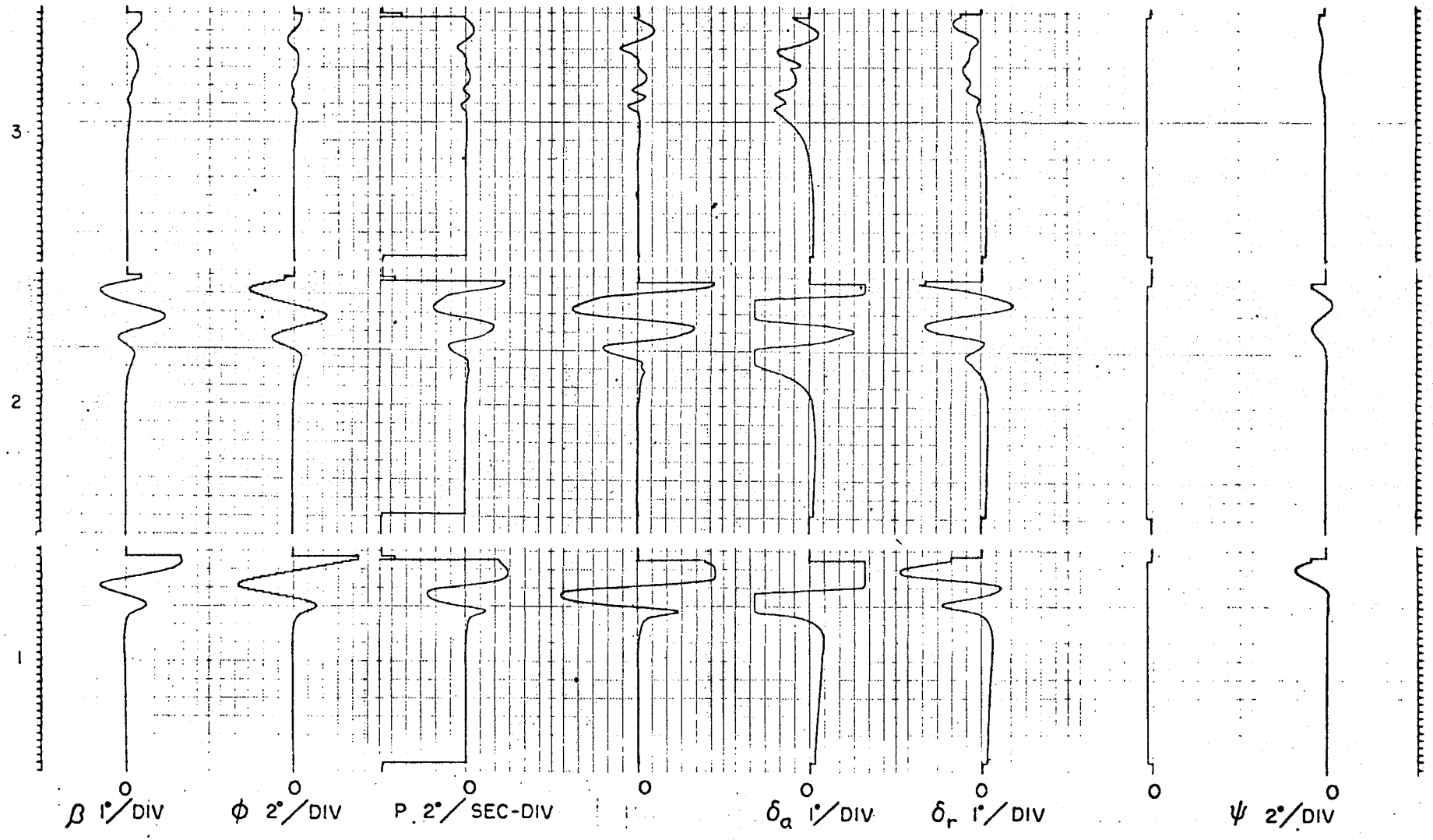
3
2
1
0
β 1°/DIV
0
φ 2°/DIV
0
P 2°/SEC-DIV
0
0
δa 1°/DIV
0
δr 1°/DIV
0
ψ 2°/DIV

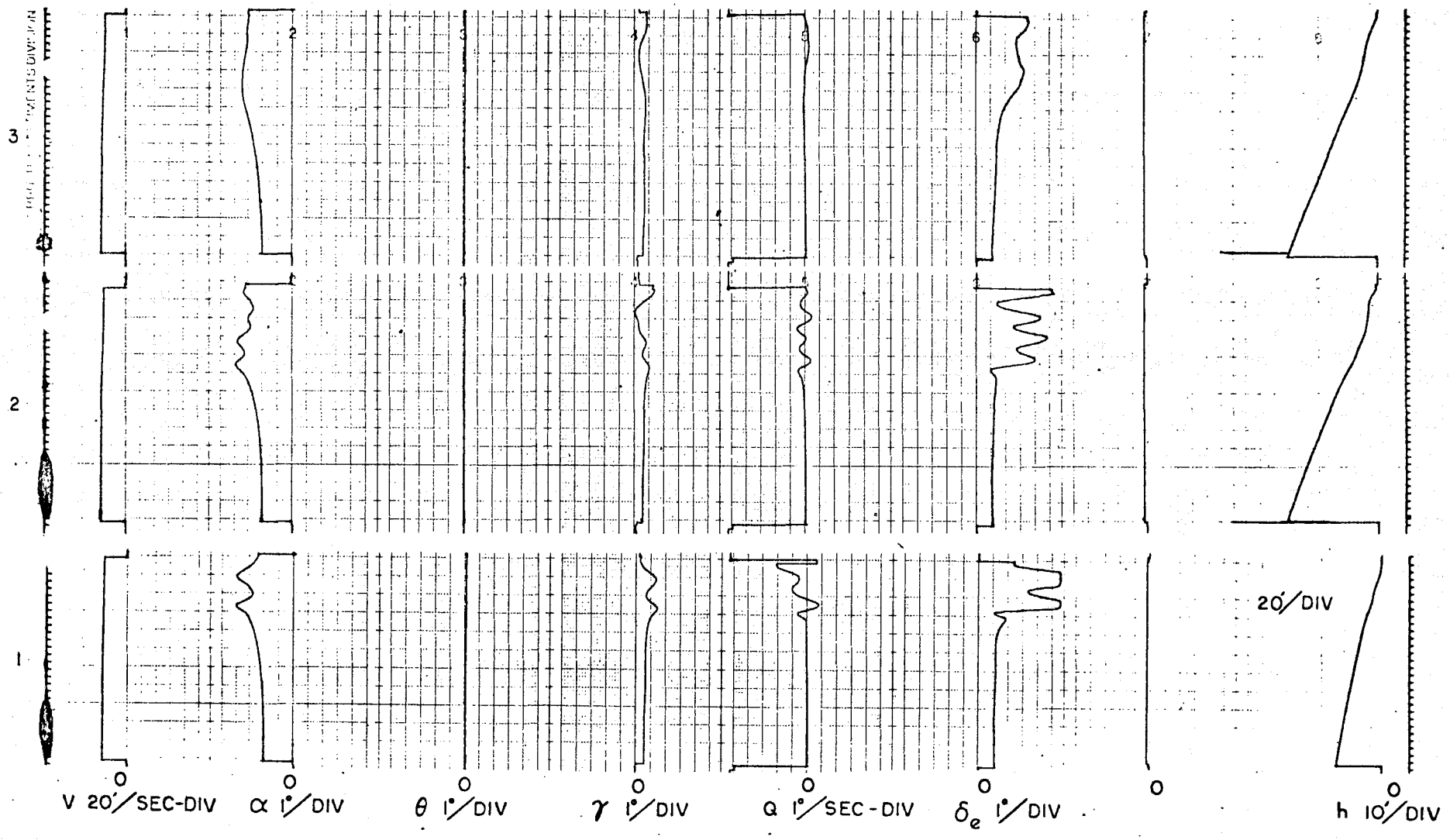
3
2
1
V 20'/SEC-DIV
α 1°/DIV
θ 1°/DIV
γ 1°/DIV
Q 1°/SEC-DIV
δe 1°/DIV
h 10'/DIV
20'/DIV
0

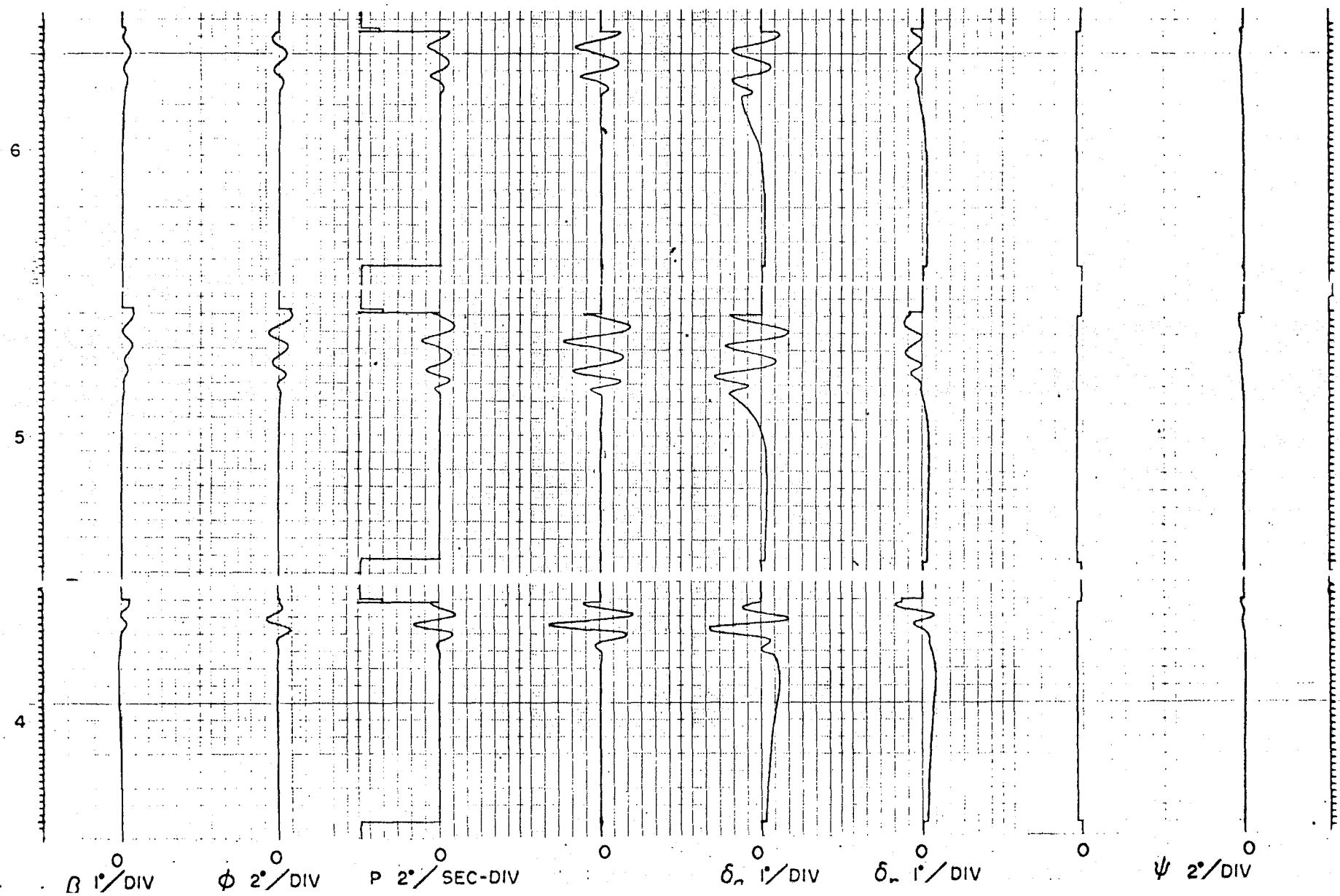
6
5
4
0
0
0
0
0
0
0
β 1°/DIV
φ 2°/DIV
P 2°/SEC-DIV
δa 1°/DIV
δr 1°/DIV
ψ 2°/DIV

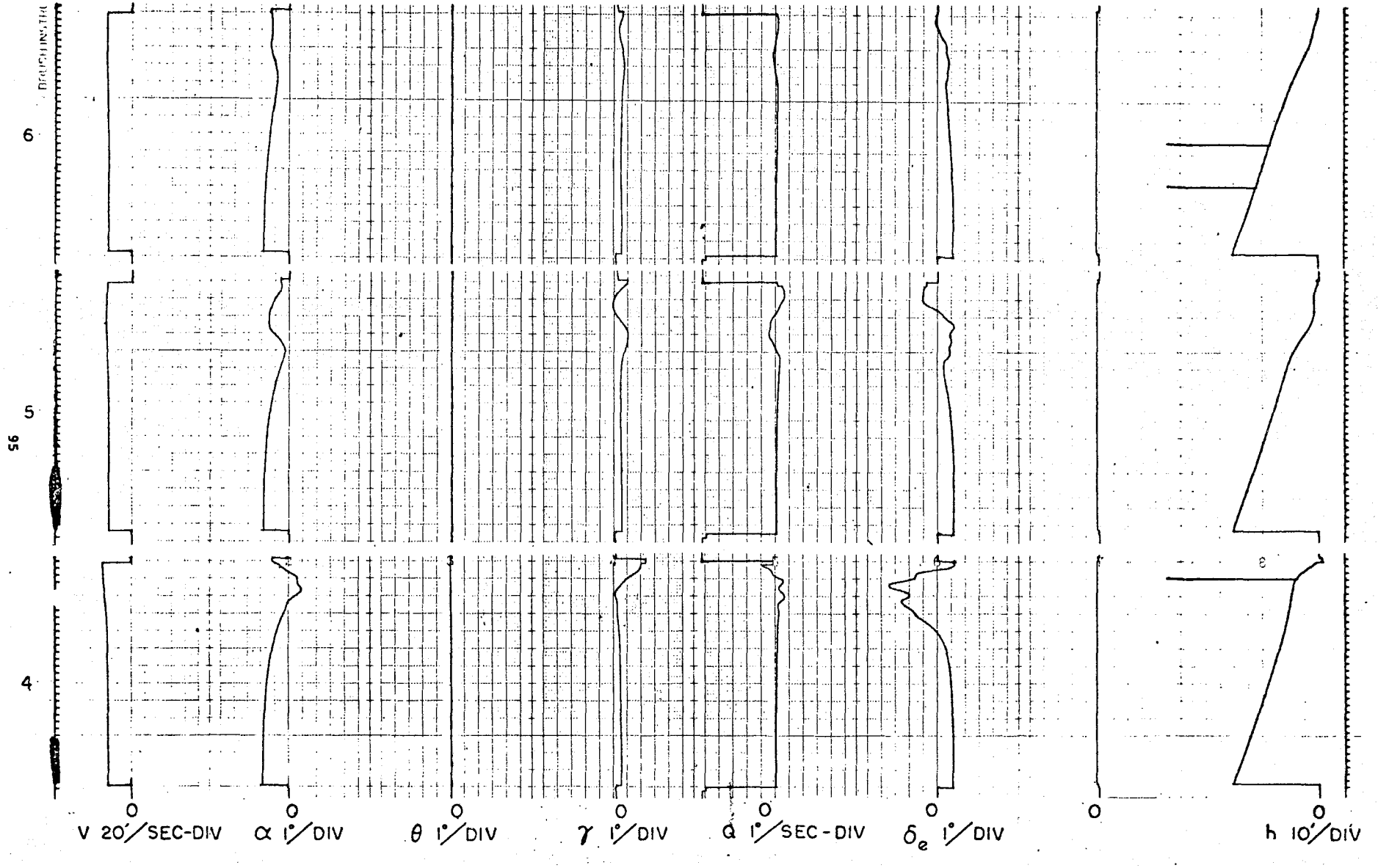
6
5
4
V 20'/SEC-DIV
α 1°/DIV
θ 1°/DIV
γ 1°/DIV
q 1°/SEC-DIV
δ_e 1°/DIV
h 10'/DIV
0

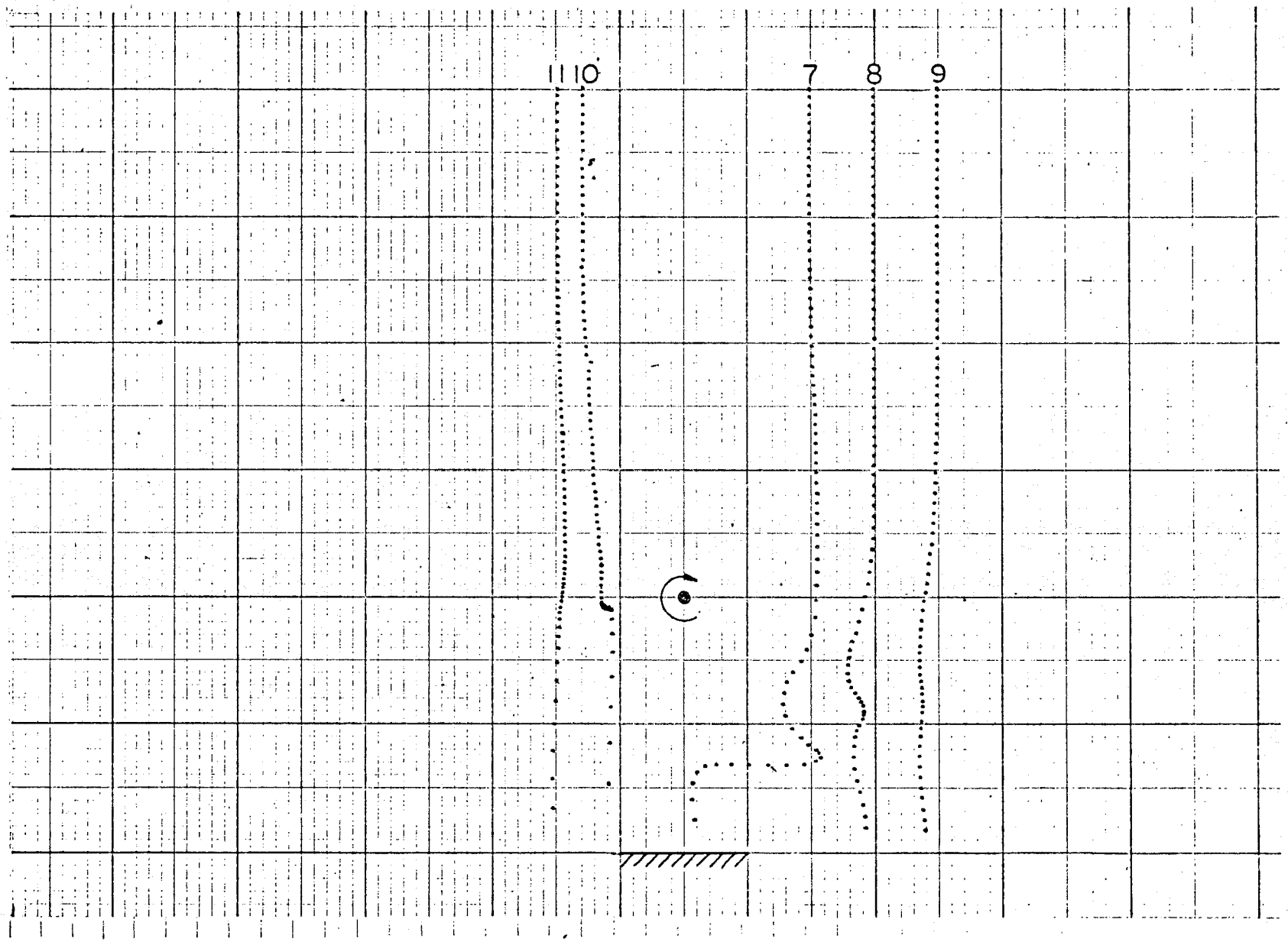
11
10
7
8
9

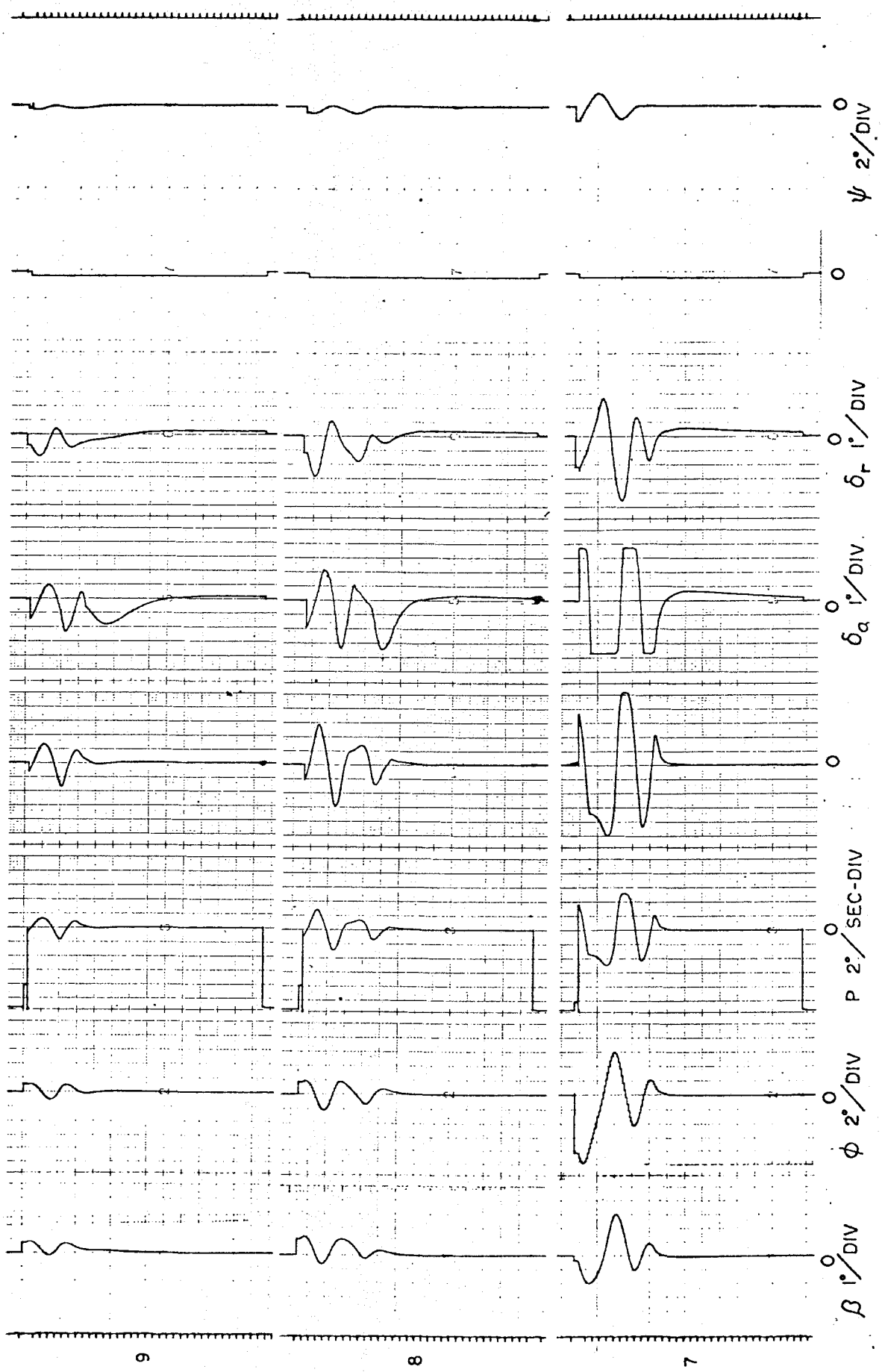
ψ 2°/DIV
0
0
δr 1°/DIV
0
δa 1°/DIV
0
0
P 2°/SEC-DIV
0
φ 2°/DIV
0
β 1°/DIV
0
9
8
7

h 10°/DIV
0
δ_e 1°/DIV
0
Q 1°/SEC-DIV
0
γ 1°/DIV
0
θ 1°/DIV
0
α 1°/DIV
0
V 20'/SEC-DIV
0
9
8
7

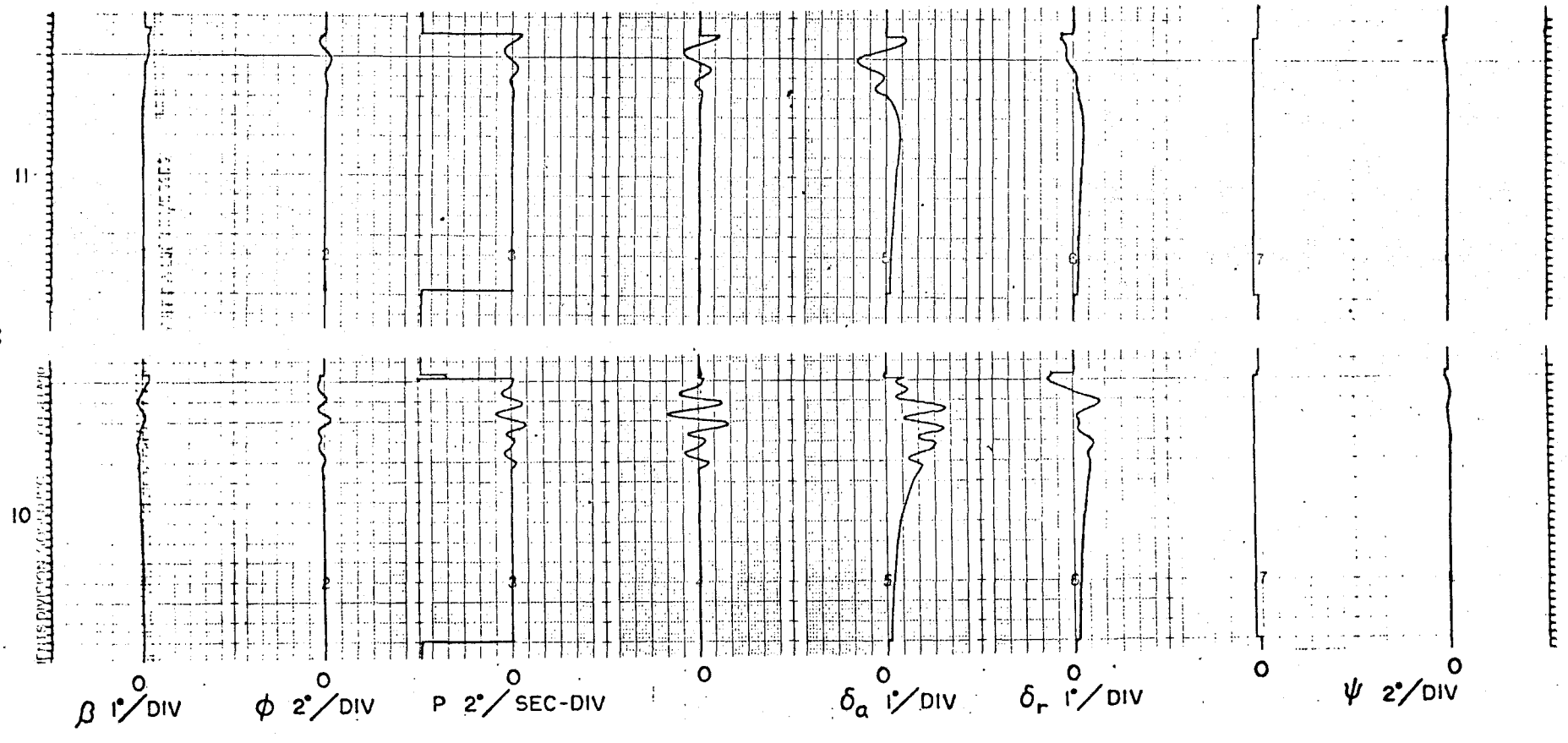
11
10
β 1°/DIV
φ 2°/DIV
P 2°/SEC-DIV
δa 1°/DIV
δr 1°/DIV
ψ 2°/DIV
0
2
3
4
5
6
7

h 10'/DIV
0
0
δ_e 1°/DIV
0
Q 1°/SEC-DIV
0
γ 1°/DIV
0
θ 1°/DIV
0
α 1°/DIV
0
V 20'/SEC-DIV
0
11
10

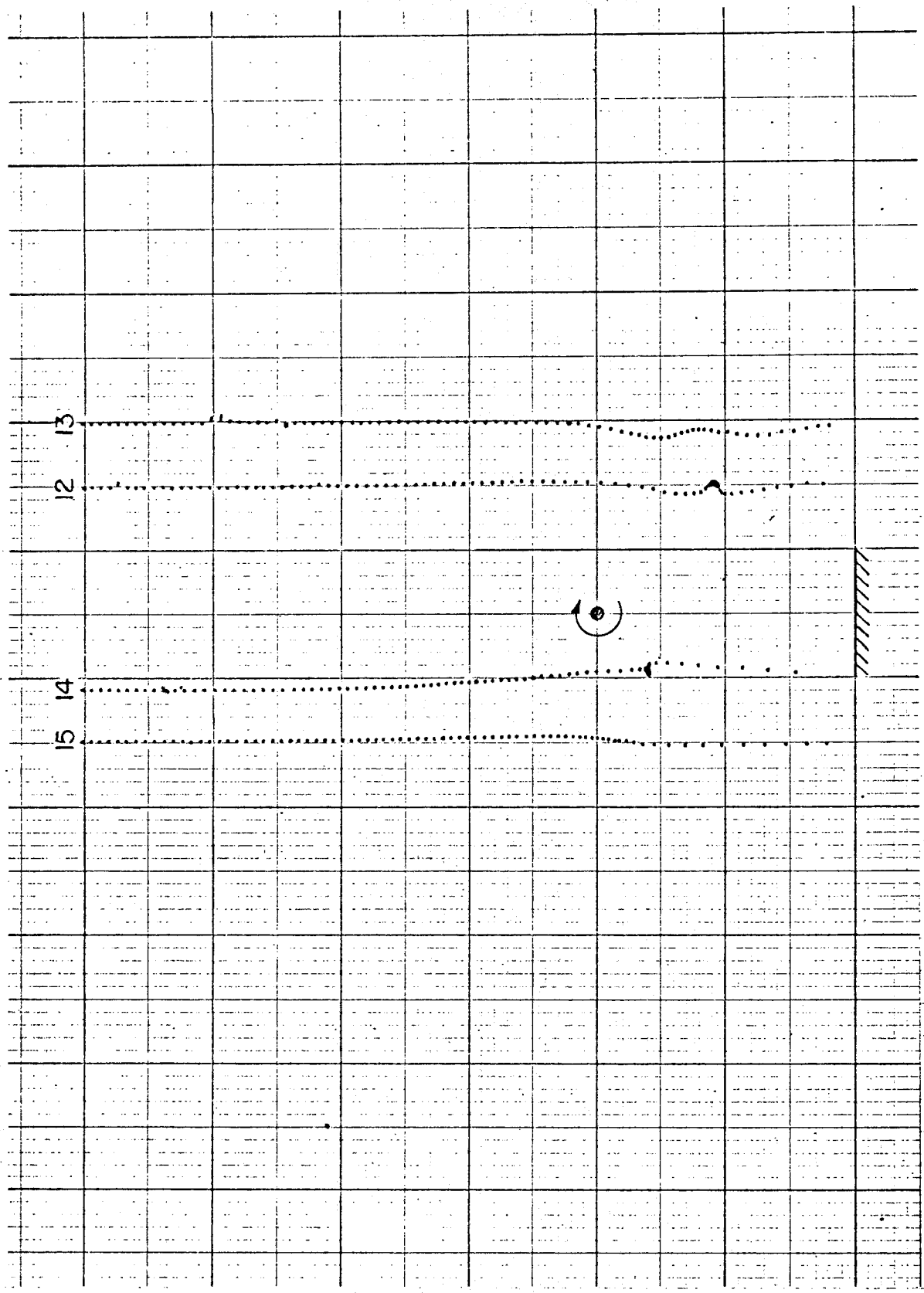
13
12
14
15

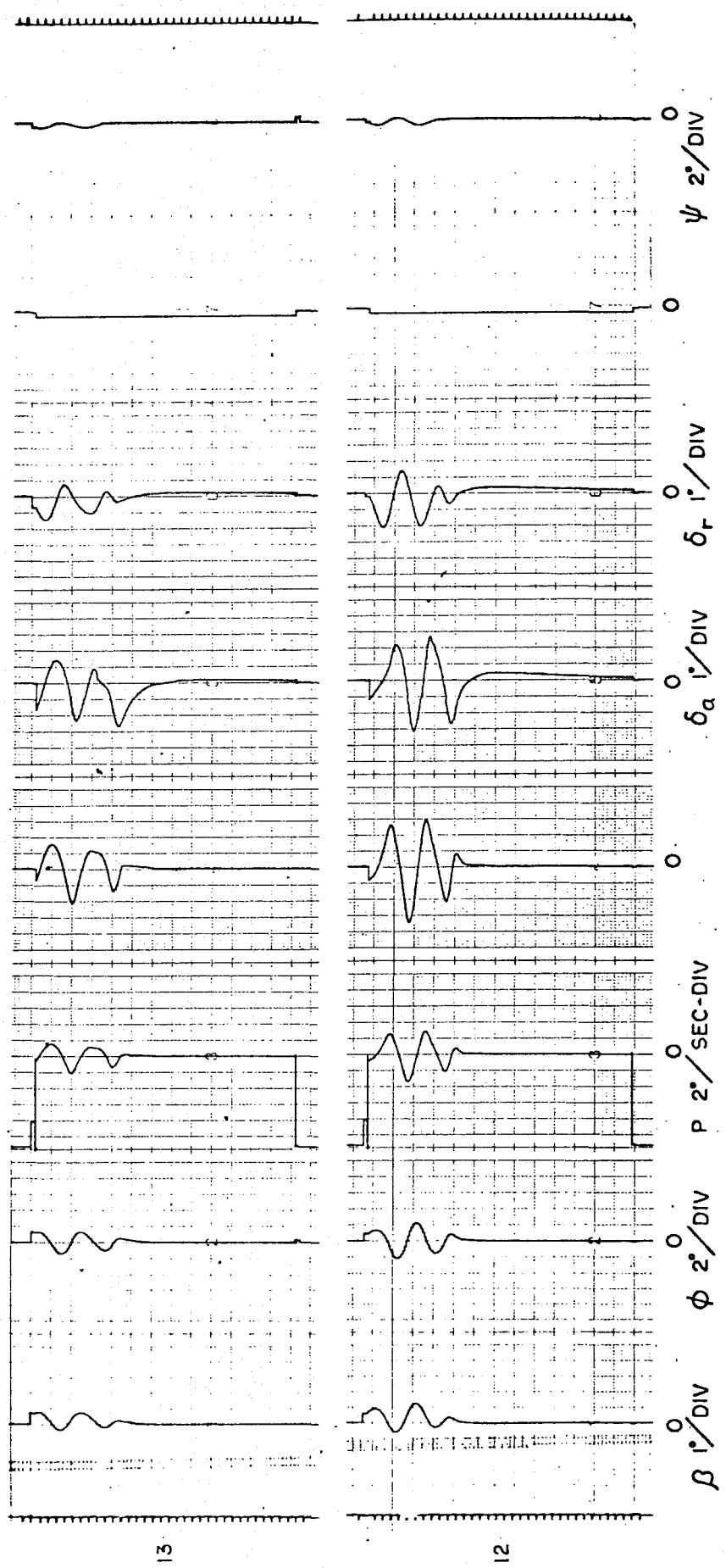
ψ 2°/DIV
0
0
δr 1°/DIV
0
δa 1°/DIV
0
0
P 2°/SEC-DIV
0
φ 2°/DIV
0
β 1°/DIV
0
13
12

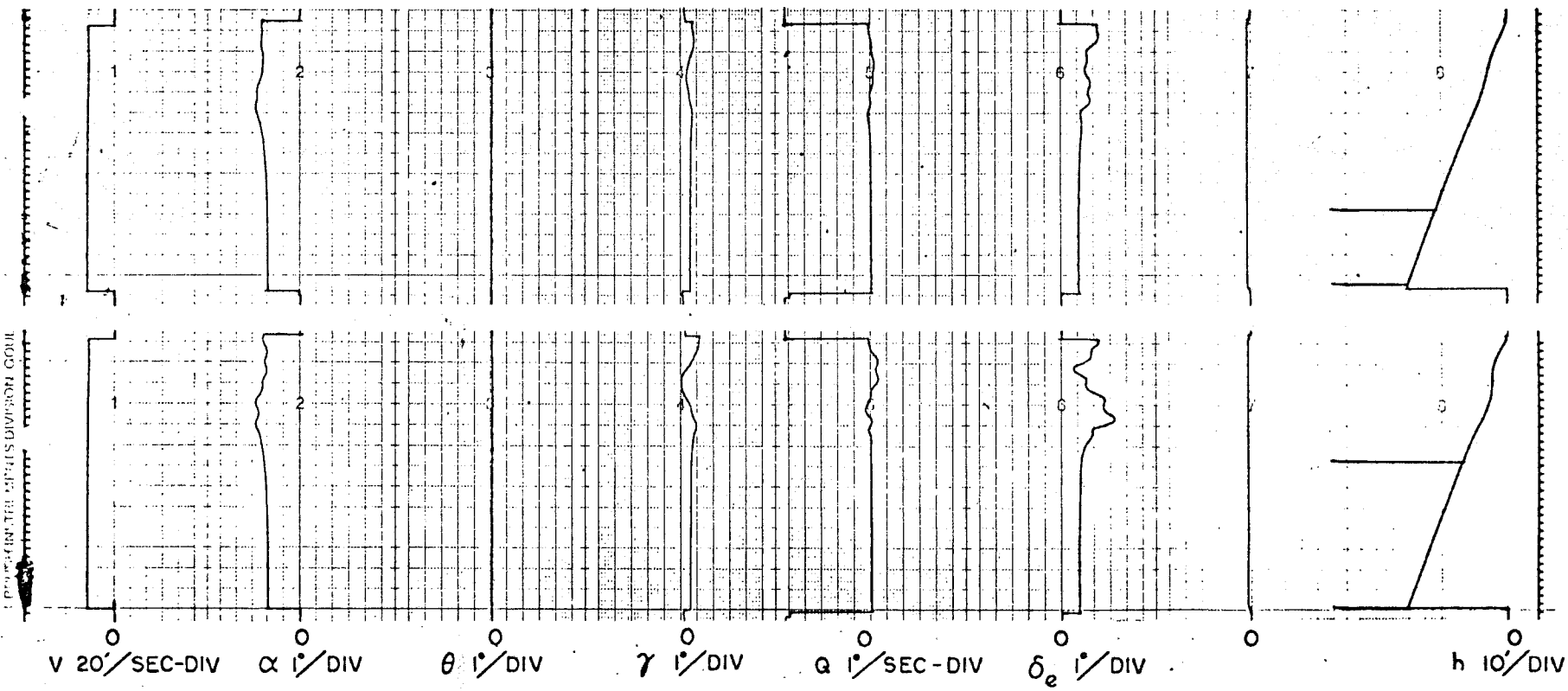
13
12
V 20'/SEC-DIV
α 1°/DIV
θ 1°/DIV
γ 1°/DIV
Q 1°/SEC-DIV
δ_e 1°/DIV
h 10'/DIV

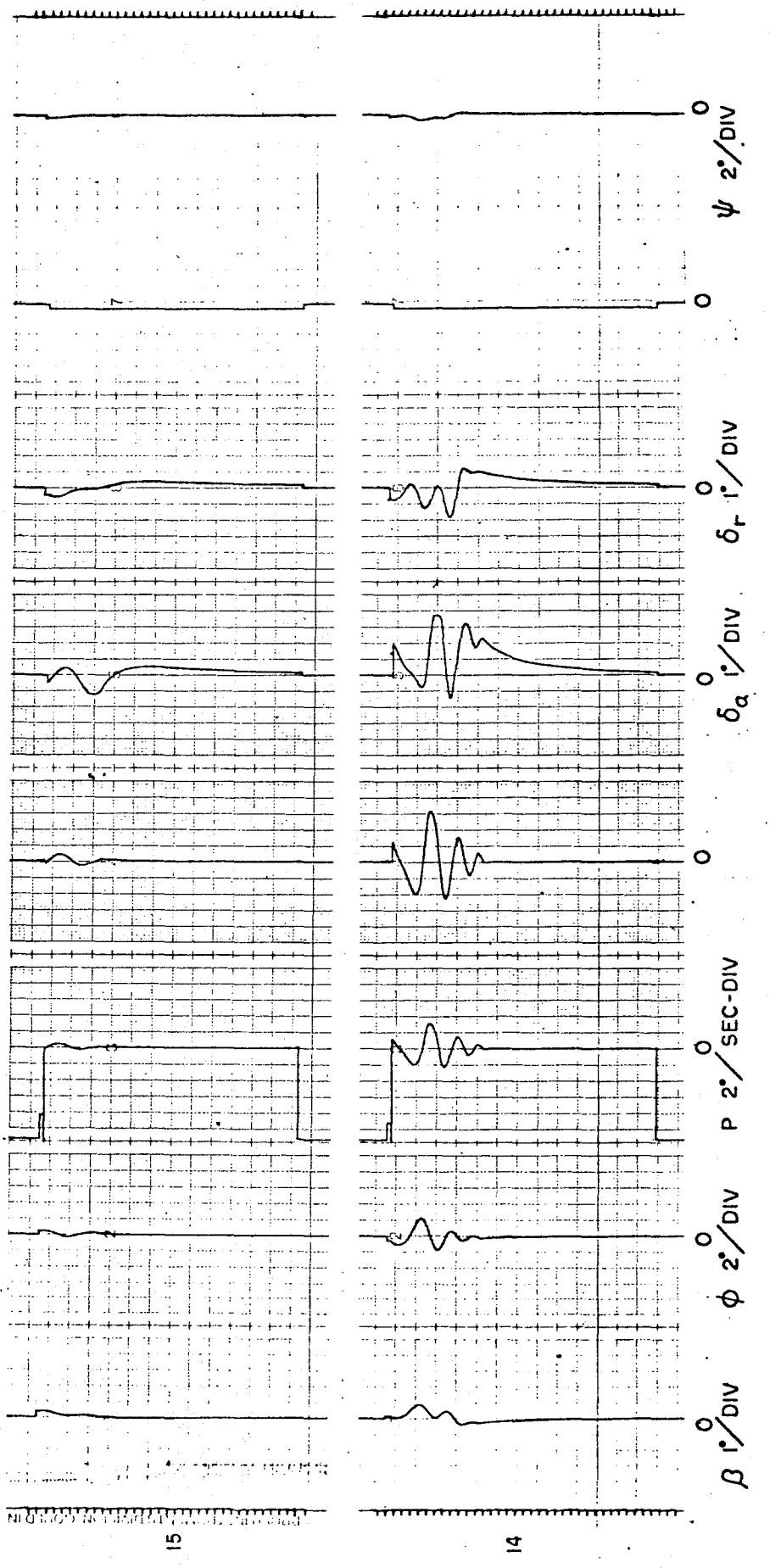
ψ 2°/DIV
0
0
δr 1°/DIV
0
δa 1°/DIV
0
0
P 2°/SEC-DIV
0
φ 2°/DIV
0
β 1°/DIV
0
15
14

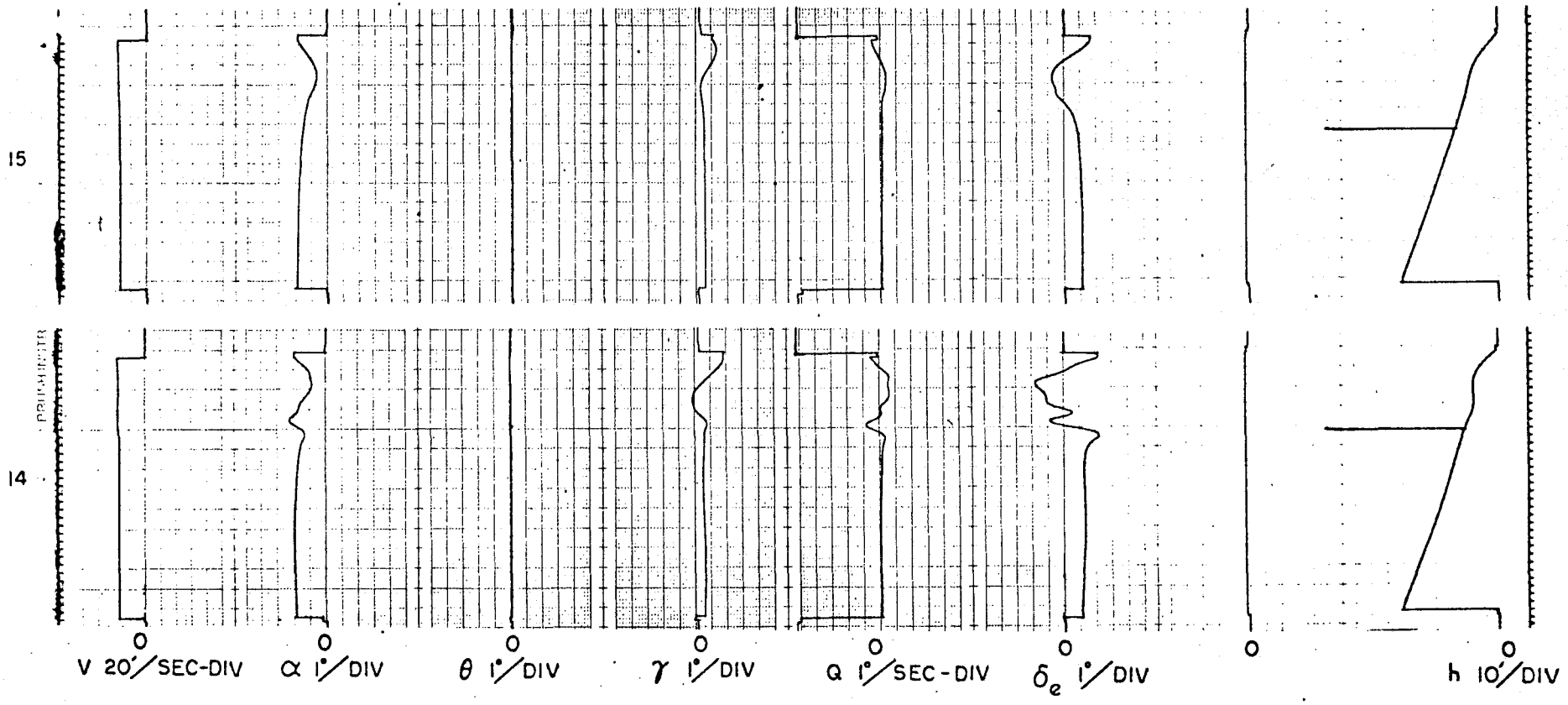
15
14
PRINTER
0
V 20'/SEC-DIV
0
α 1°/DIV
0
θ 1°/DIV
0
γ 1°/DIV
0
Q 1°/SEC-DIV
0
δe 1°/DIV
0
0
h 10'/DIV

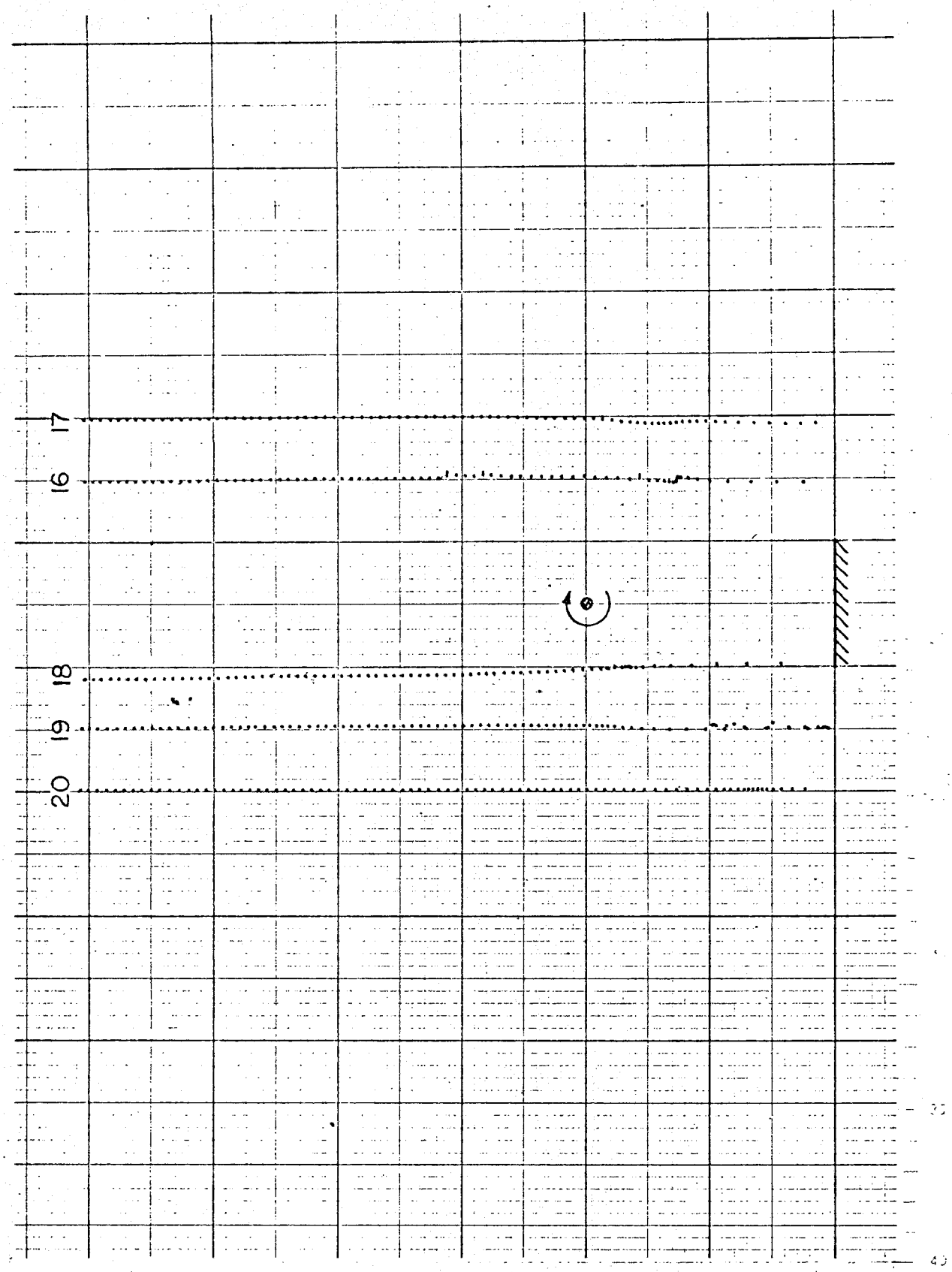
17
16
18
19
20

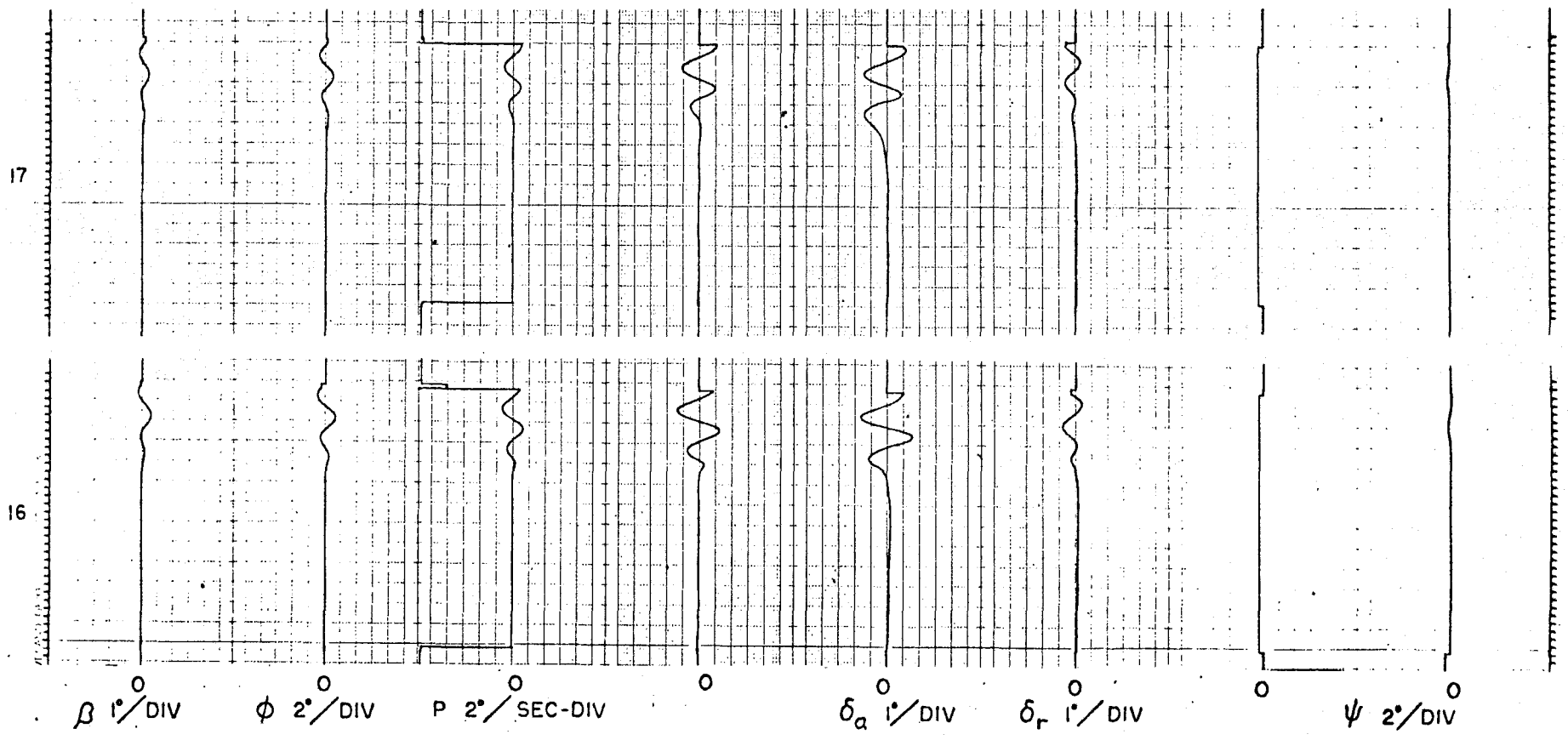
17
16
0
0
0
0
0
0
0
0
β 1°/DIV
φ 2°/DIV
P 2°/SEC-DIV
δa 1°/DIV
δr 1°/DIV
ψ 2°/DIV

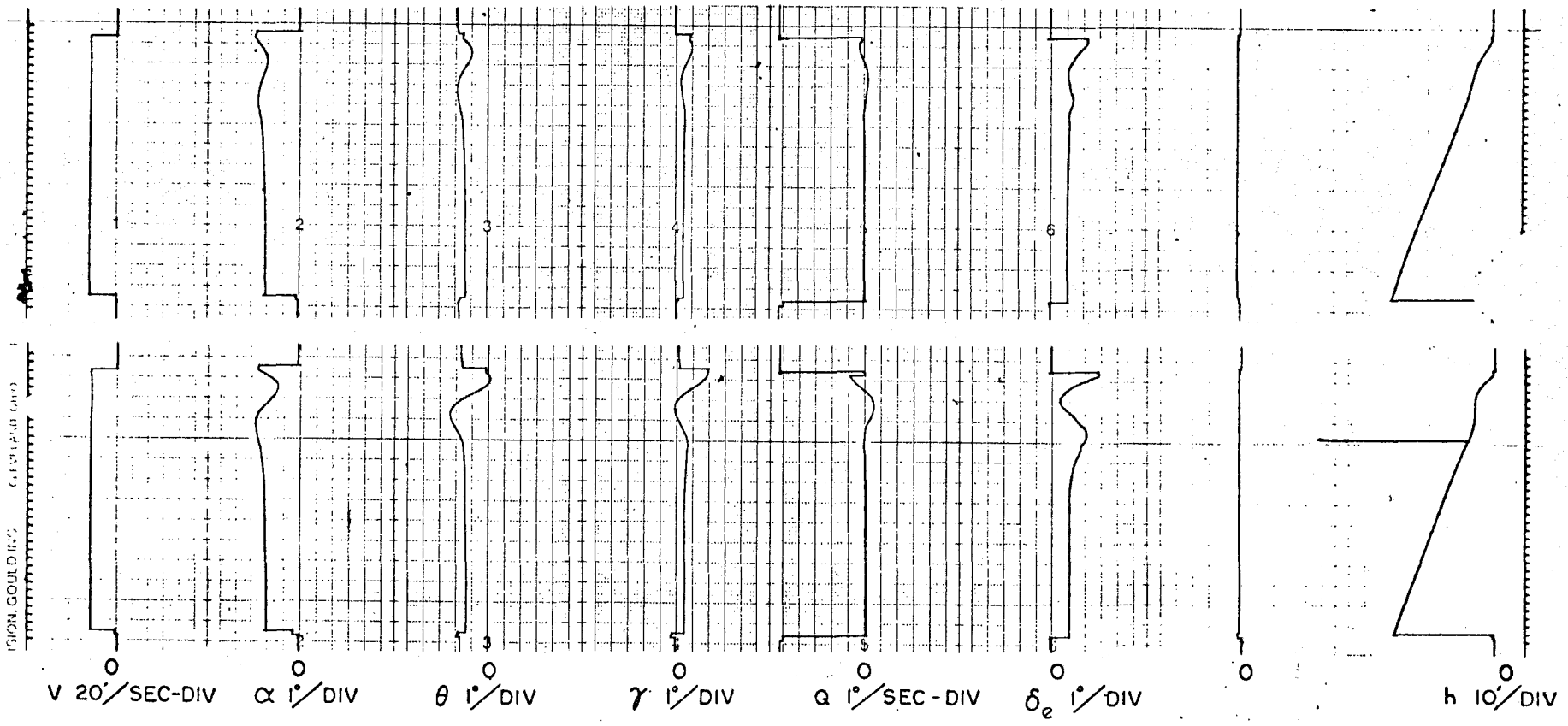
17
16
0
V 20'/SEC-DIV
0
α 1°/DIV
0
θ 1°/DIV
0
γ 1°/DIV
0
Q 1°/SEC-DIV
0
δe 1°/DIV
0
0
h 10'/DIV

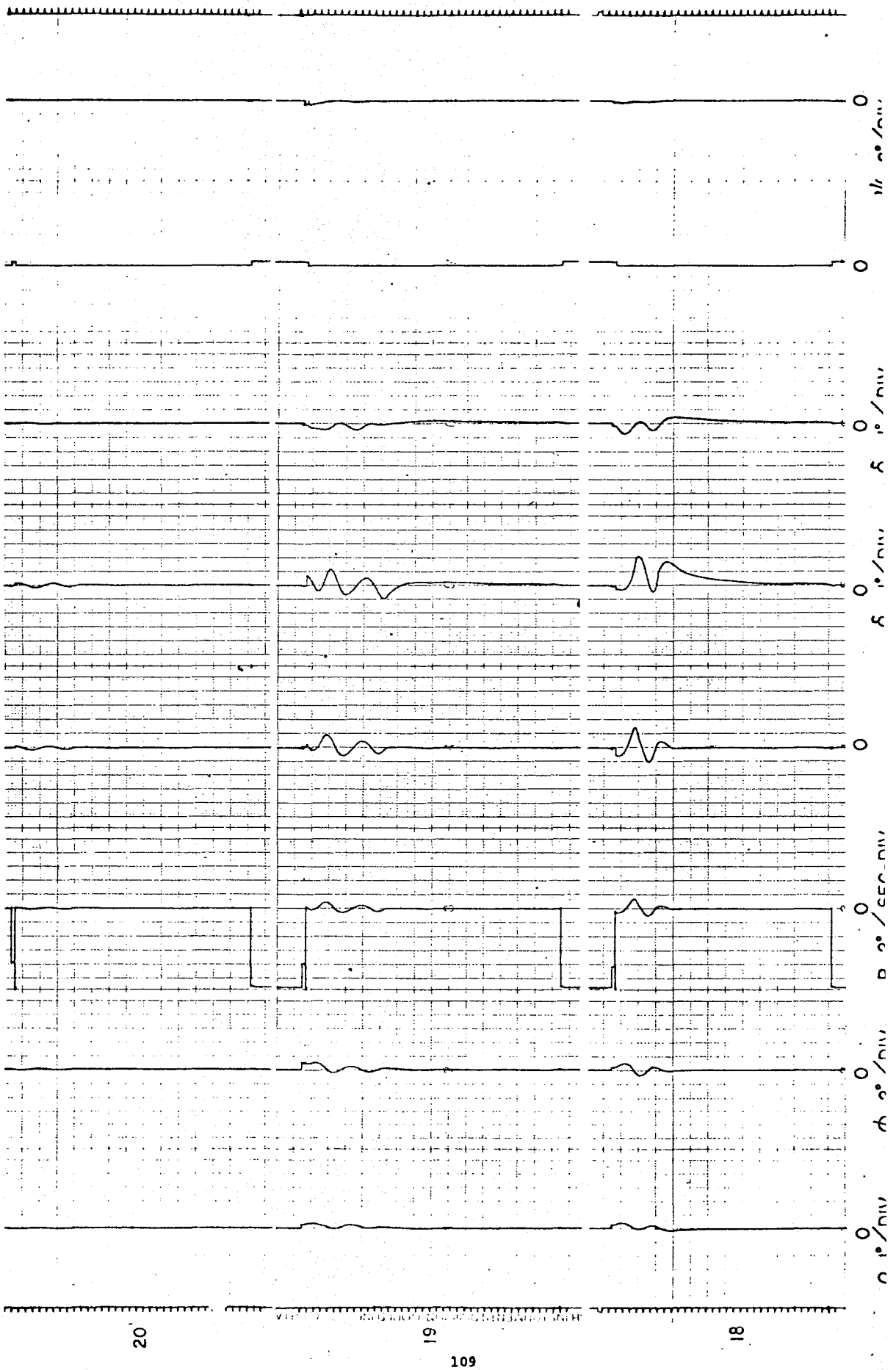
20
19
18
0
0
0
0
0
0
0
0
0
0

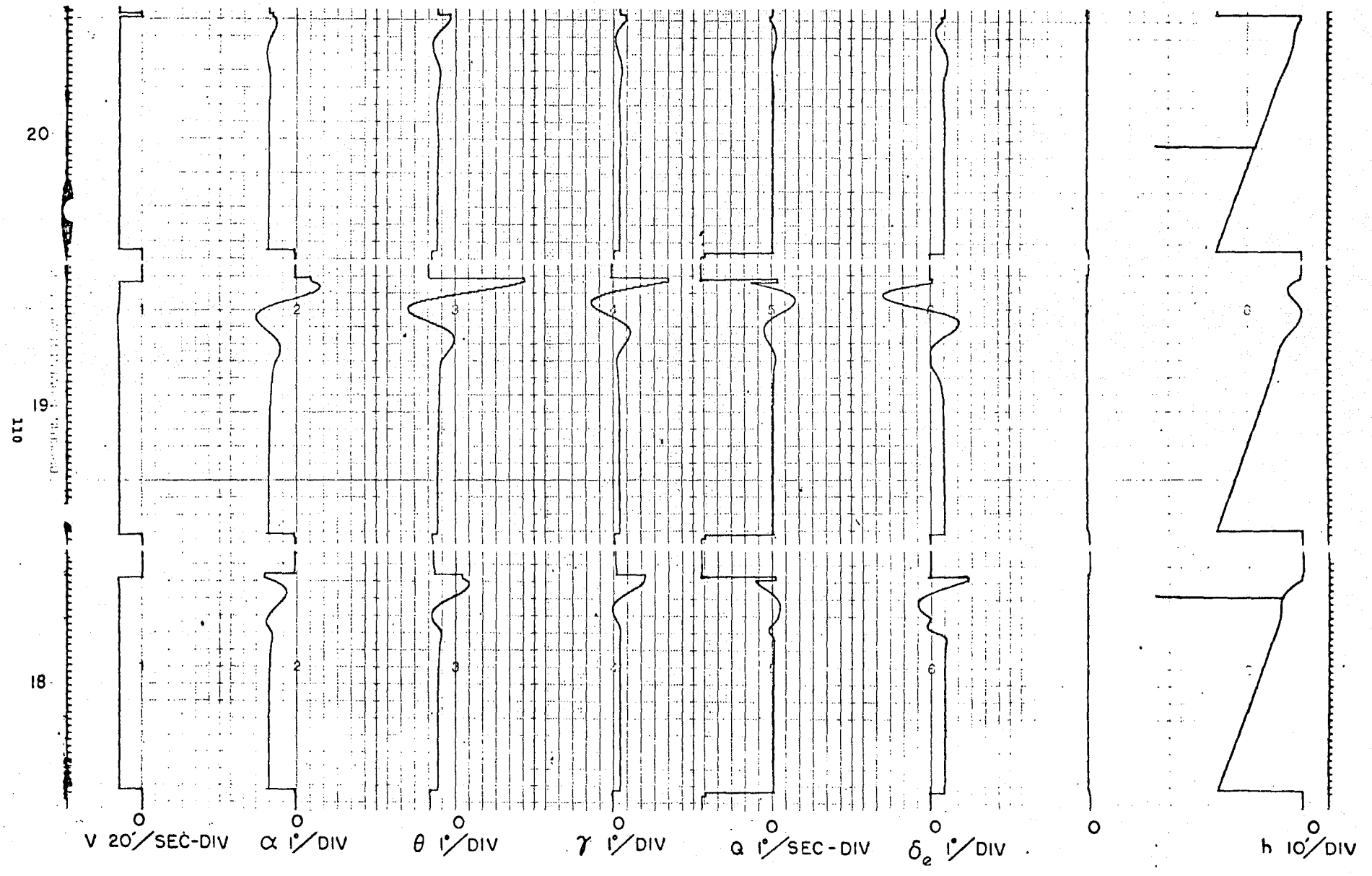
20
19
18
V 20'/SEC-DIV
α 1°/DIV
θ 1°/DIV
γ 1°/DIV
Q 1°/SEC-DIV
δ_e 1°/DIV
h 10'/DIV

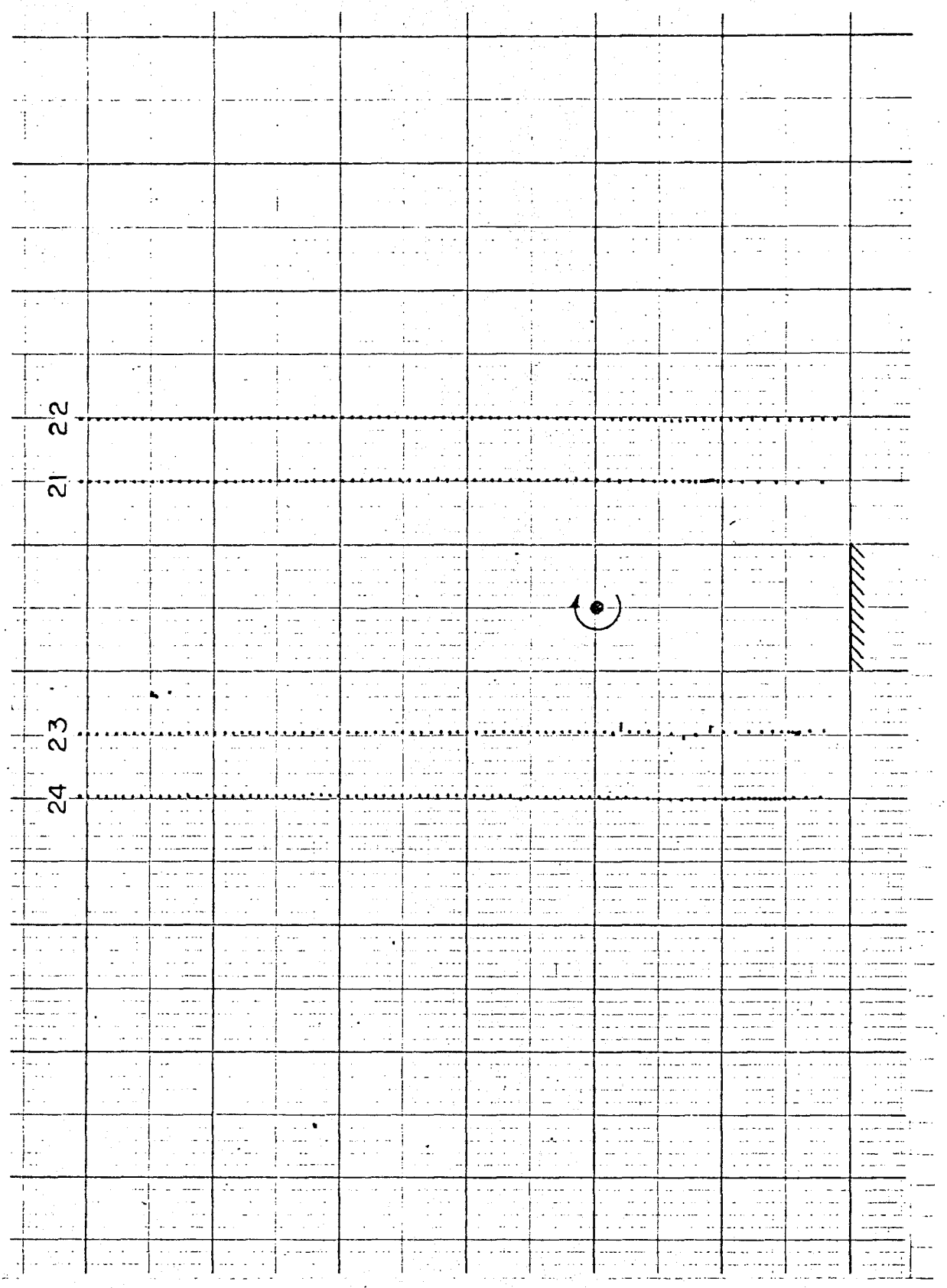
24
23
21
22

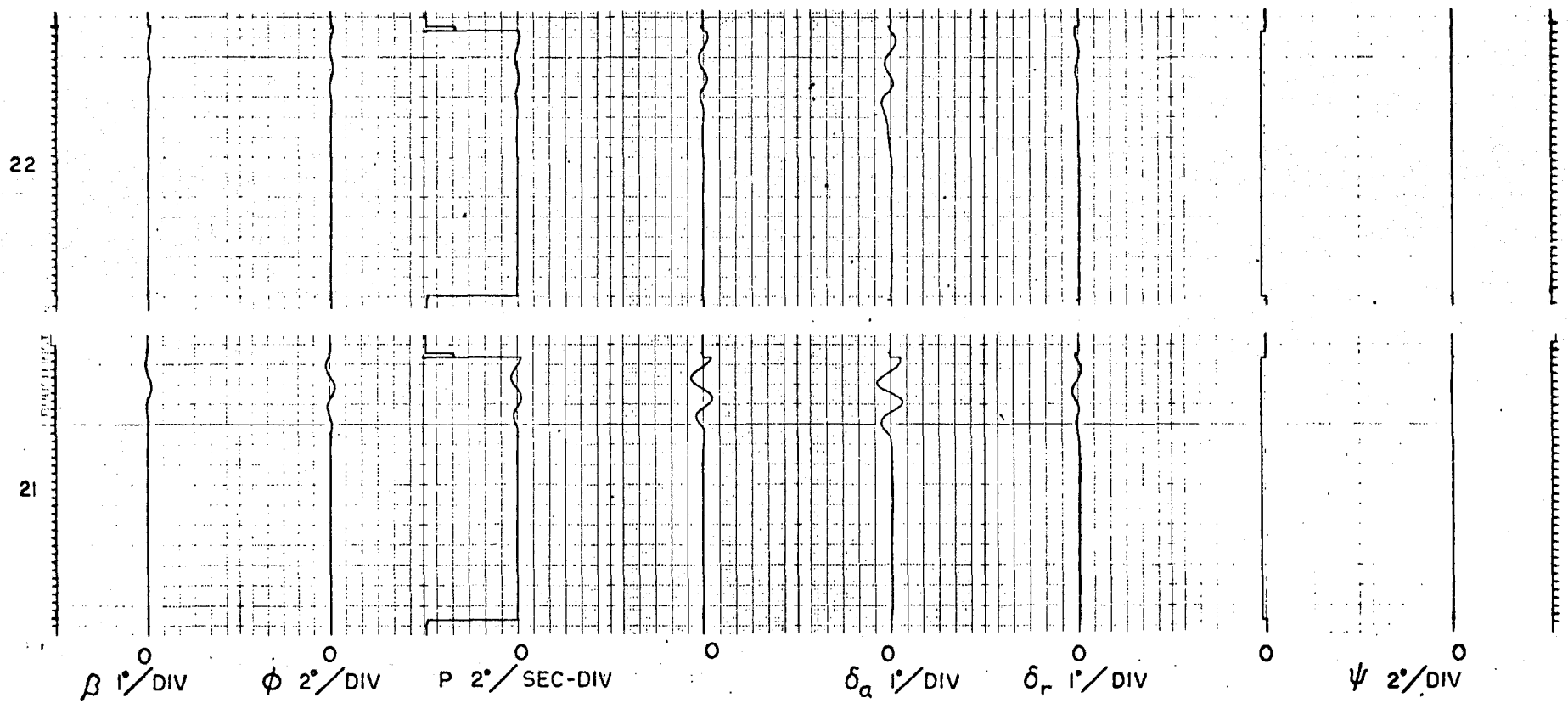
22
21
0
0
0
0
0
0
0
0
β 1°/DIV
φ 2°/DIV
P 2°/SEC-DIV
δa 1°/DIV
δr 1°/DIV
ψ 2°/DIV

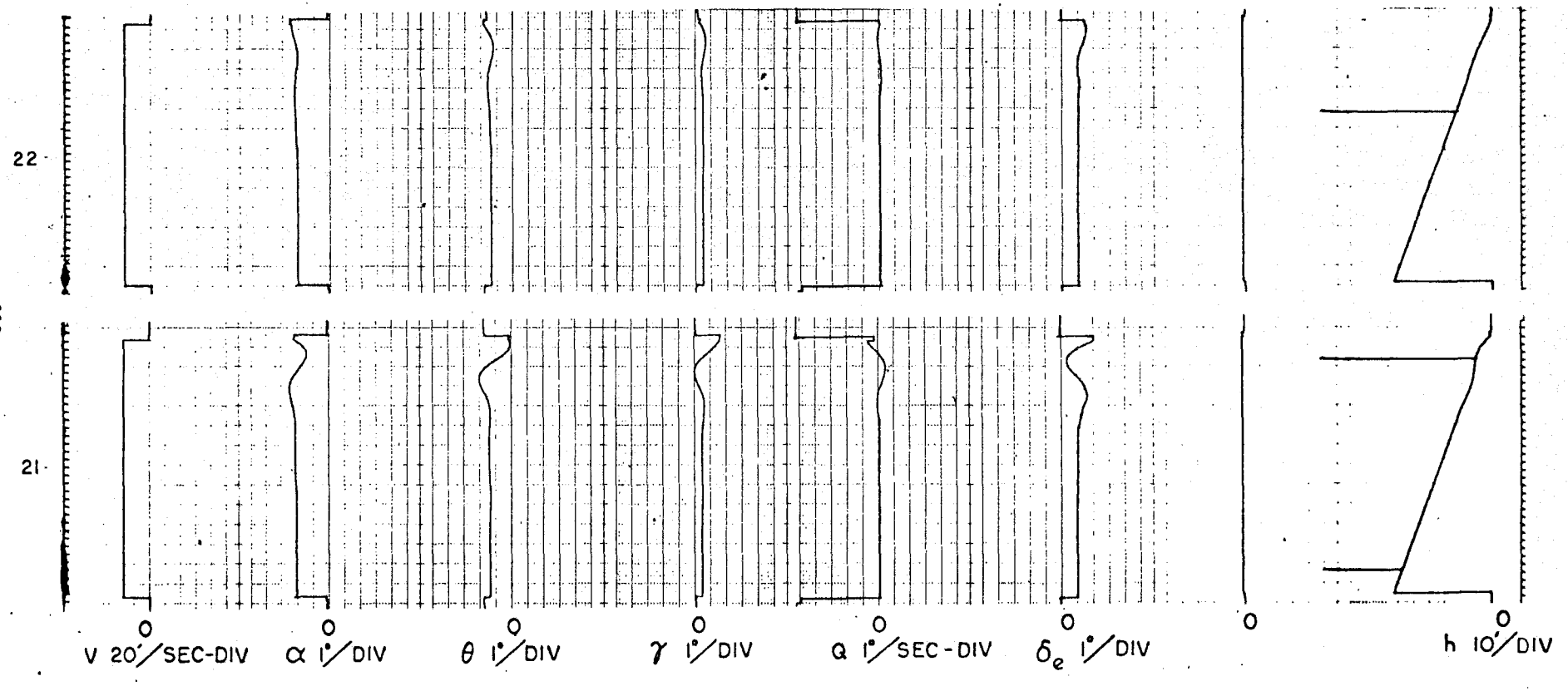
22
21
0
V 20'/SEC-DIV
α 1°/DIV
θ 1°/DIV
γ 1°/DIV
Q 1°/SEC-DIV
δe 1°/DIV
h 10'/DIV

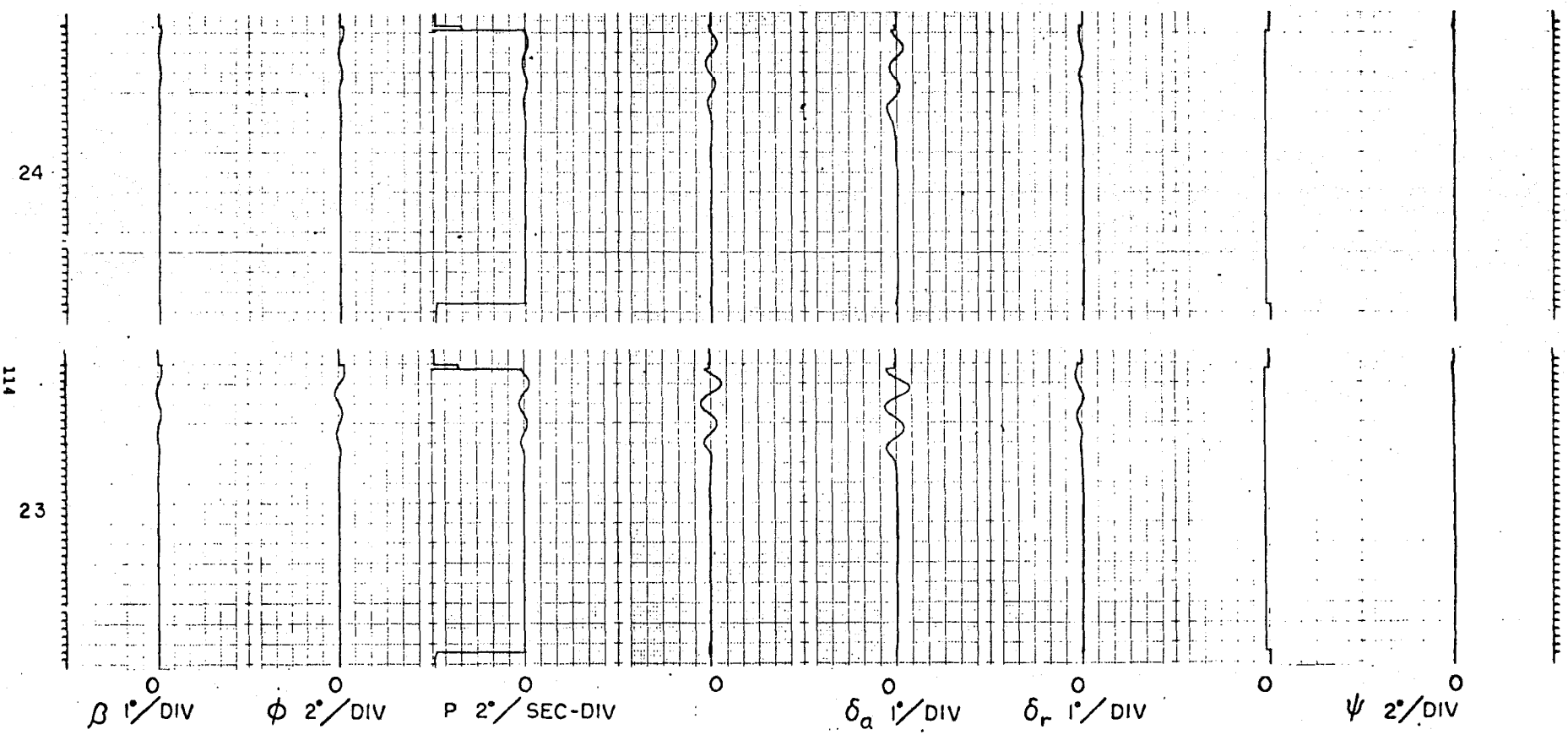
24
23
0
0
0
0
0
0
0
β 1°/DIV
φ 2°/DIV
P 2°/SEC-DIV
δa 1°/DIV
δr 1°/DIV
ψ 2°/DIV

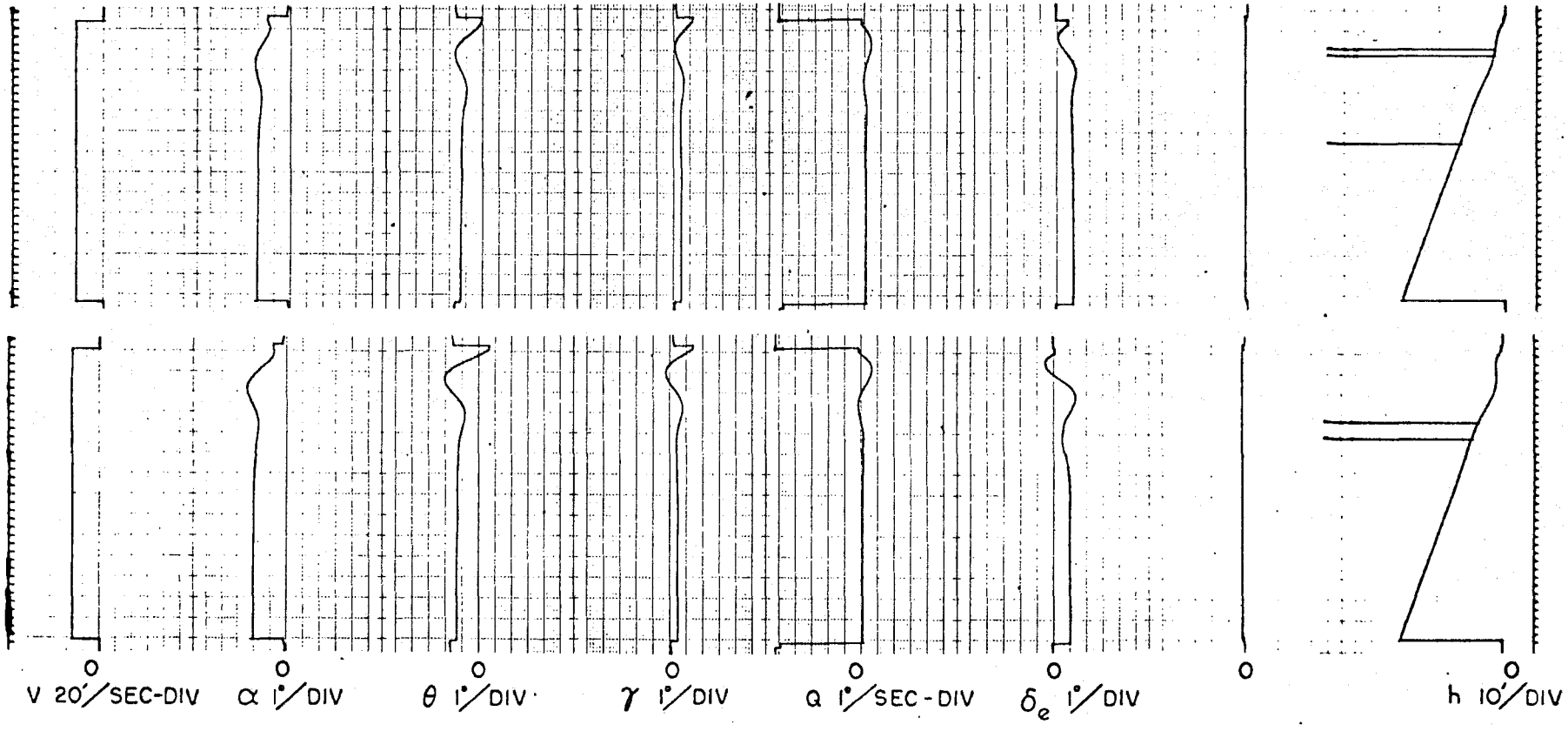
24
23
0
V 20'/SEC-DIV
0
α 1°/DIV
0
θ 1°/DIV
0
γ 1°/DIV
0
Q 1°/SEC-DIV
0
δe 1°/DIV
0
0
h 10'/DIV

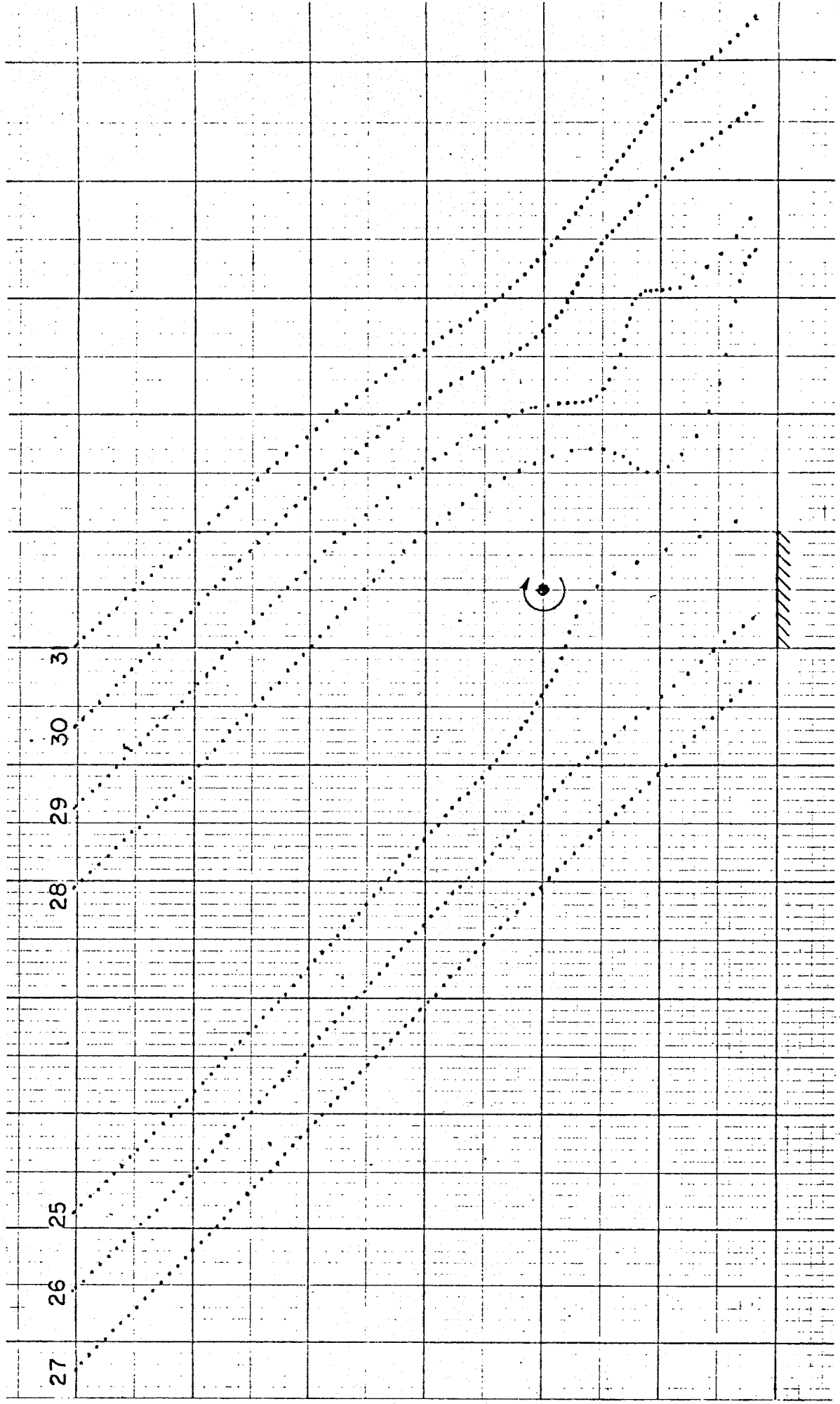
27
26
25
28
29
30
31

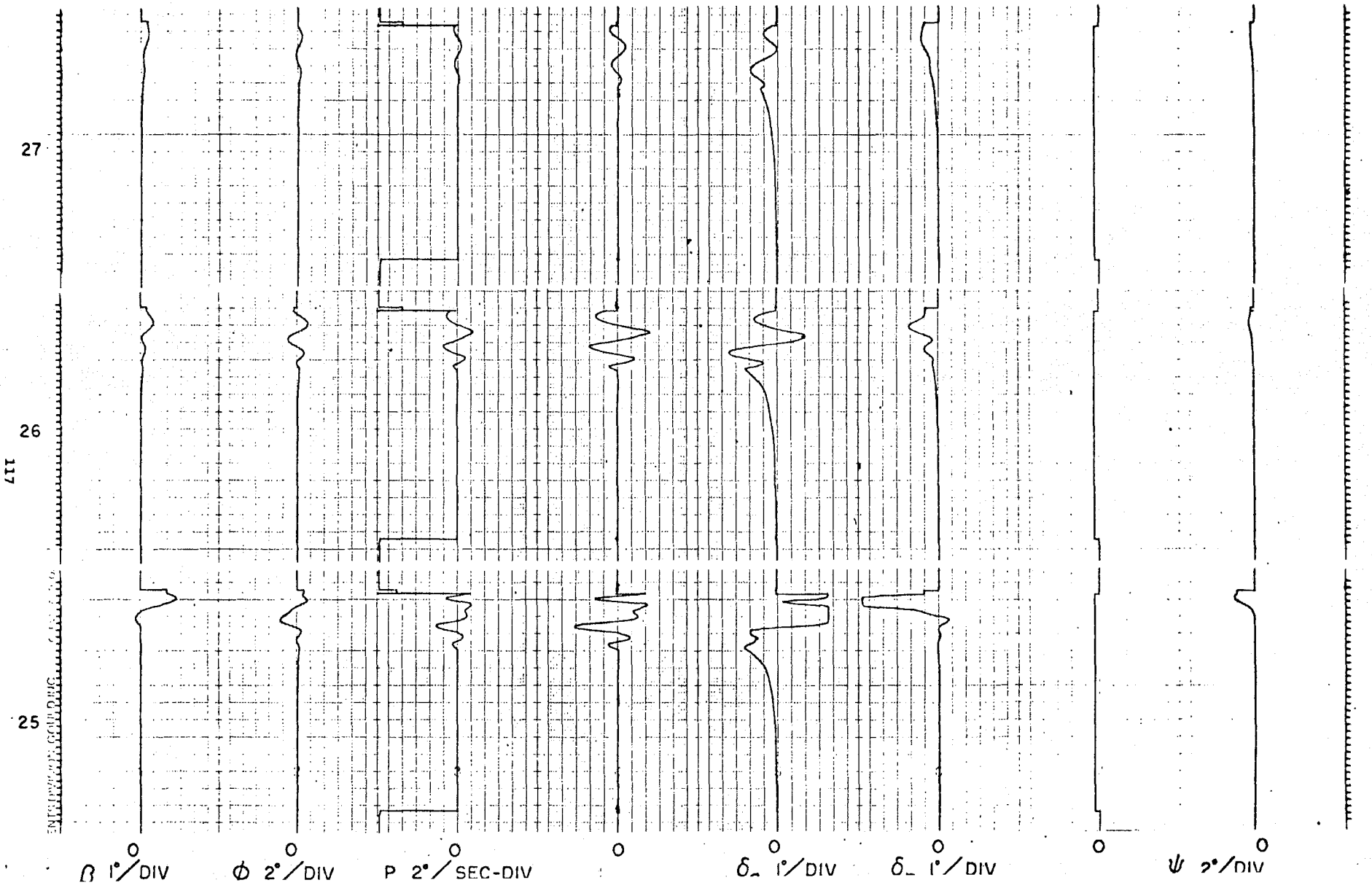
27
26
25
0
β 1°/DIV
0
Φ 2°/DIV
0
P 2°/SEC-DIV
0
0
δ_ 1°/DIV
0
δ_ 1°/DIV
0
0
ψ 2°/DIV

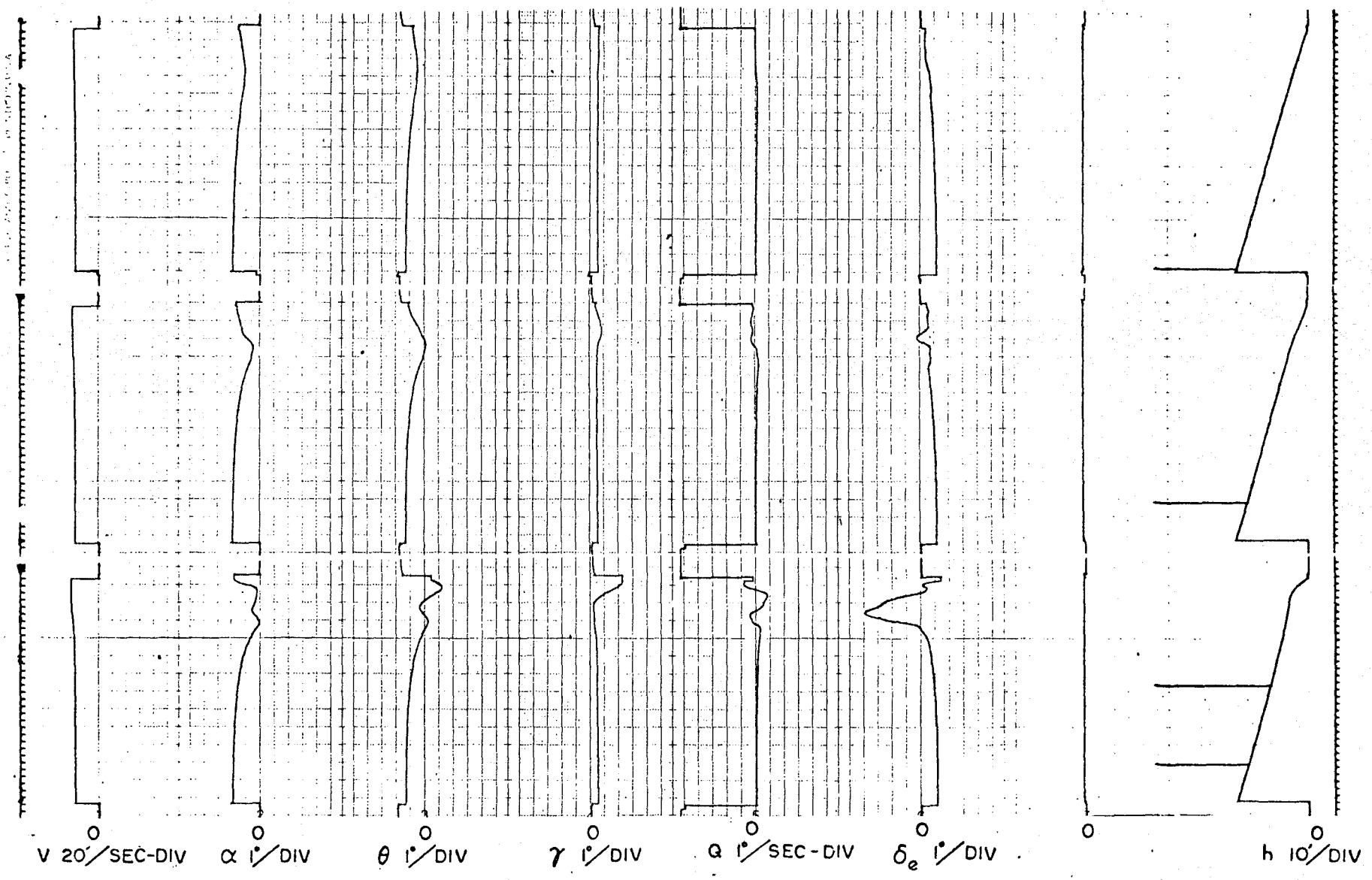
27
26
25
0
V 20'/SEC-DIV
0
α 1°/DIV
0
θ 1°/DIV
0
γ 1°/DIV
0
Q 1°/SEC-DIV
0
δe 1°/DIV
0
0
h 10'/DIV

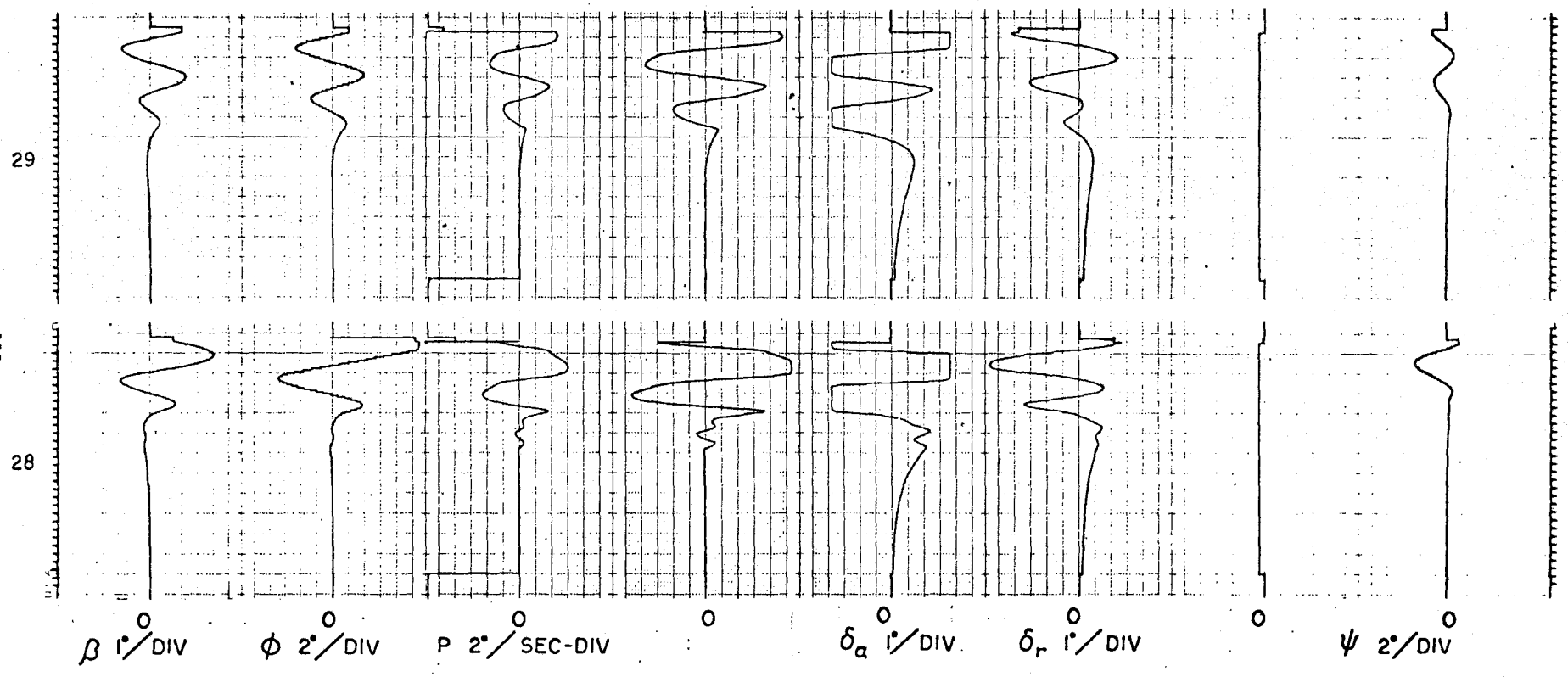
29
28
0
β 1°/DIV
0
φ 2°/DIV
0
P 2°/SEC-DIV
0
0
δa 1°/DIV
0
δr 1°/DIV
0
0
ψ 2°/DIV

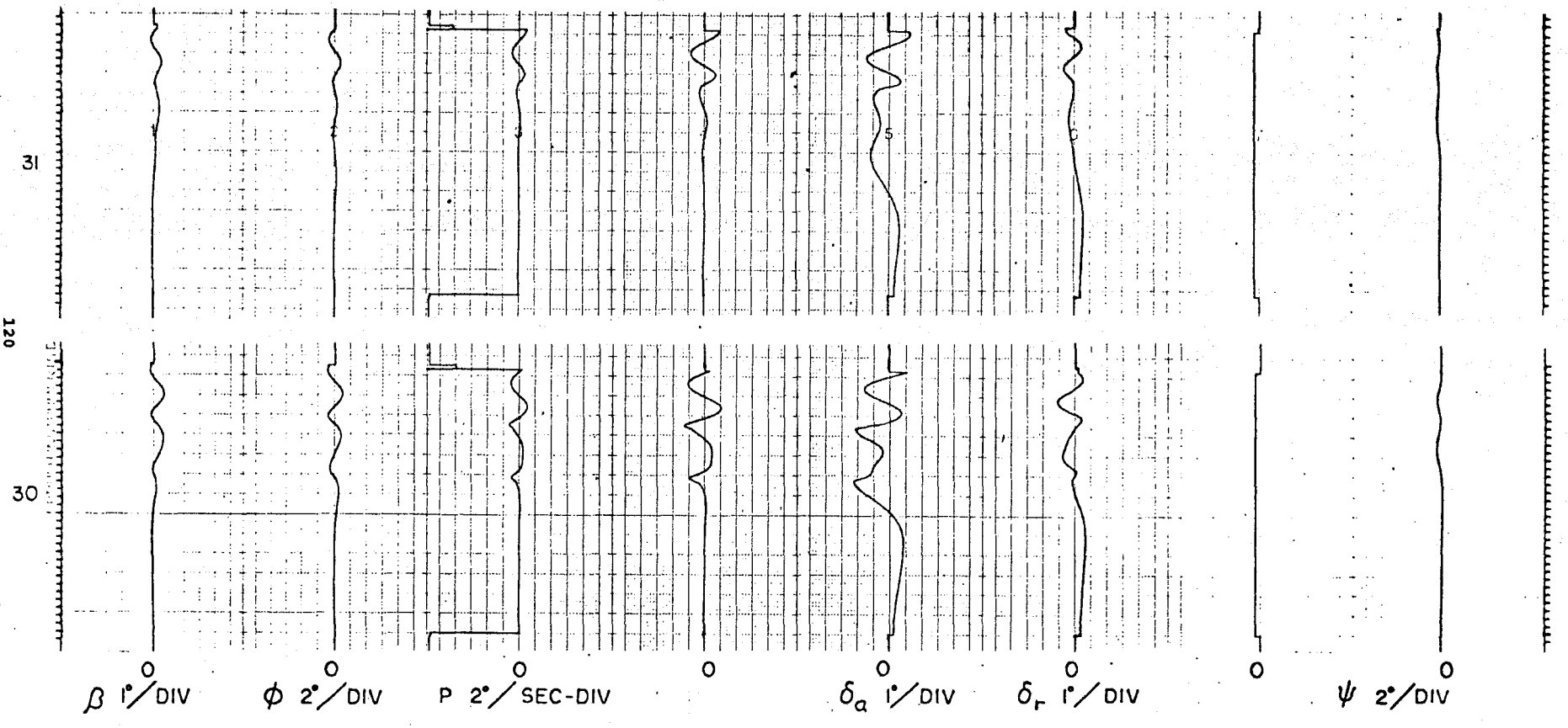
31
30
0
0
0
0
0
0
0
0
β 1°/DIV
φ 2°/DIV
P 2°/SEC-DIV
δa 1°/DIV
δr 1°/DIV
ψ 2°/DIV

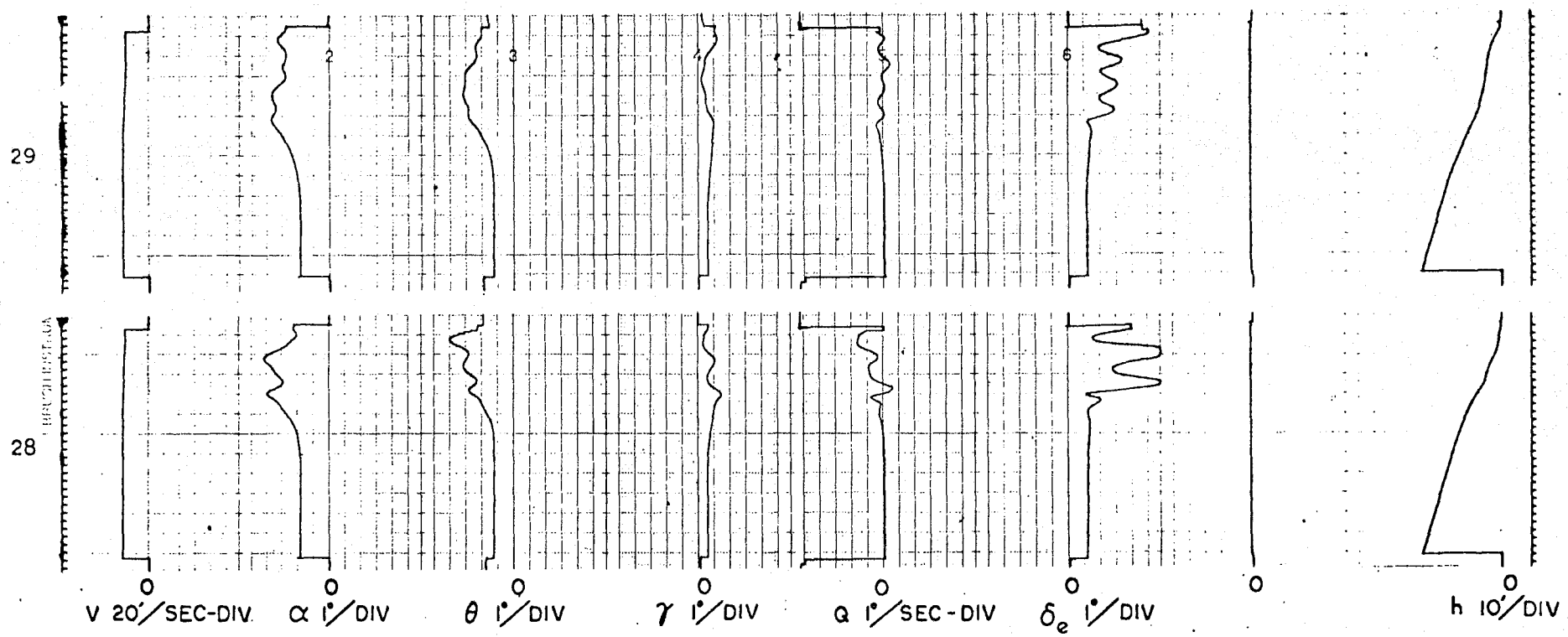
29
28
1
2
3
4
5
6
0
V 20'/SEC-DIV
α 1°/DIV
θ 1°/DIV
γ 1°/DIV
Q 1°/SEC-DIV
δe 1°/DIV
h 10'/DIV

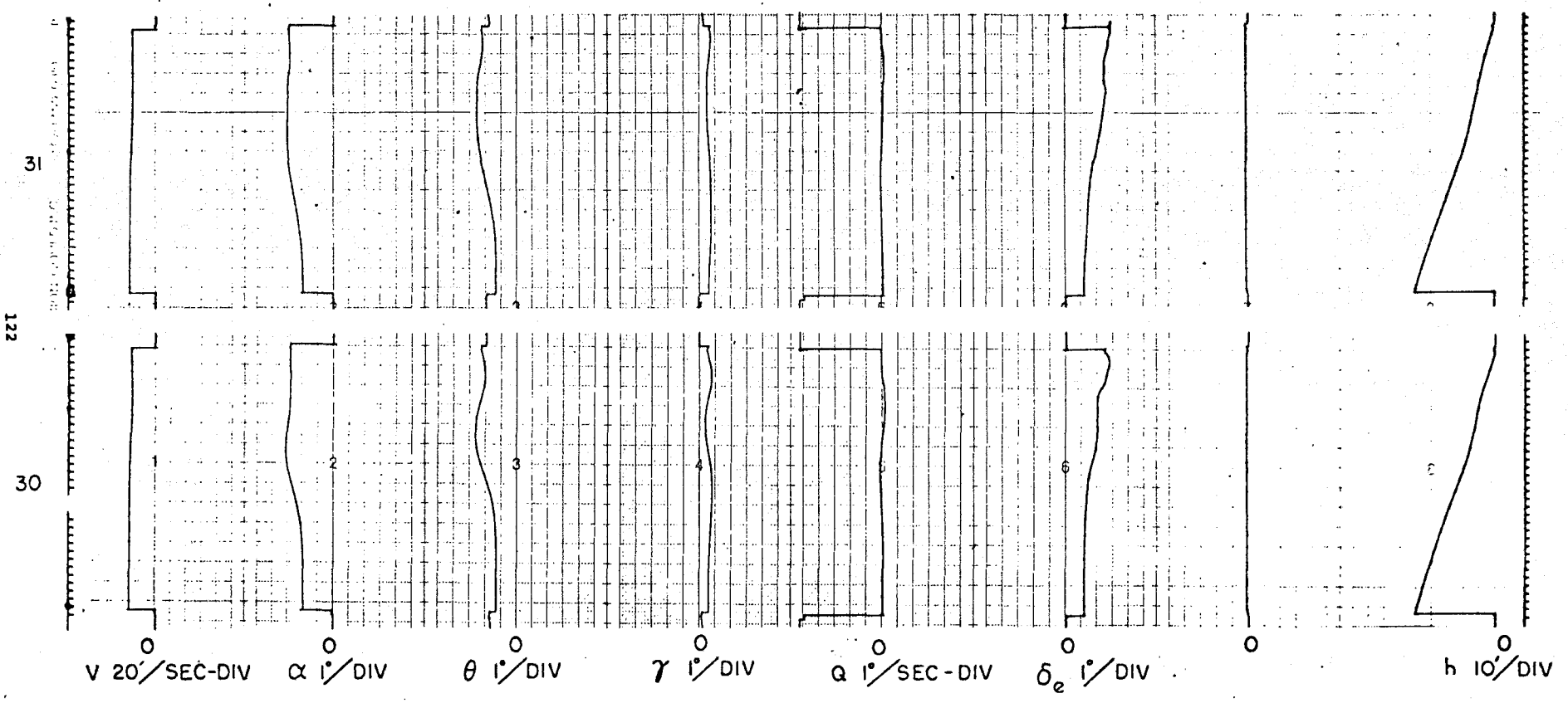
31
30
1
2
3
4
5
6
0
V 20'/SEC-DIV
α 1°/DIV
θ 1°/DIV
γ 1°/DIV
Q 1°/SEC-DIV
δe 1°/DIV
h 10'/DIV

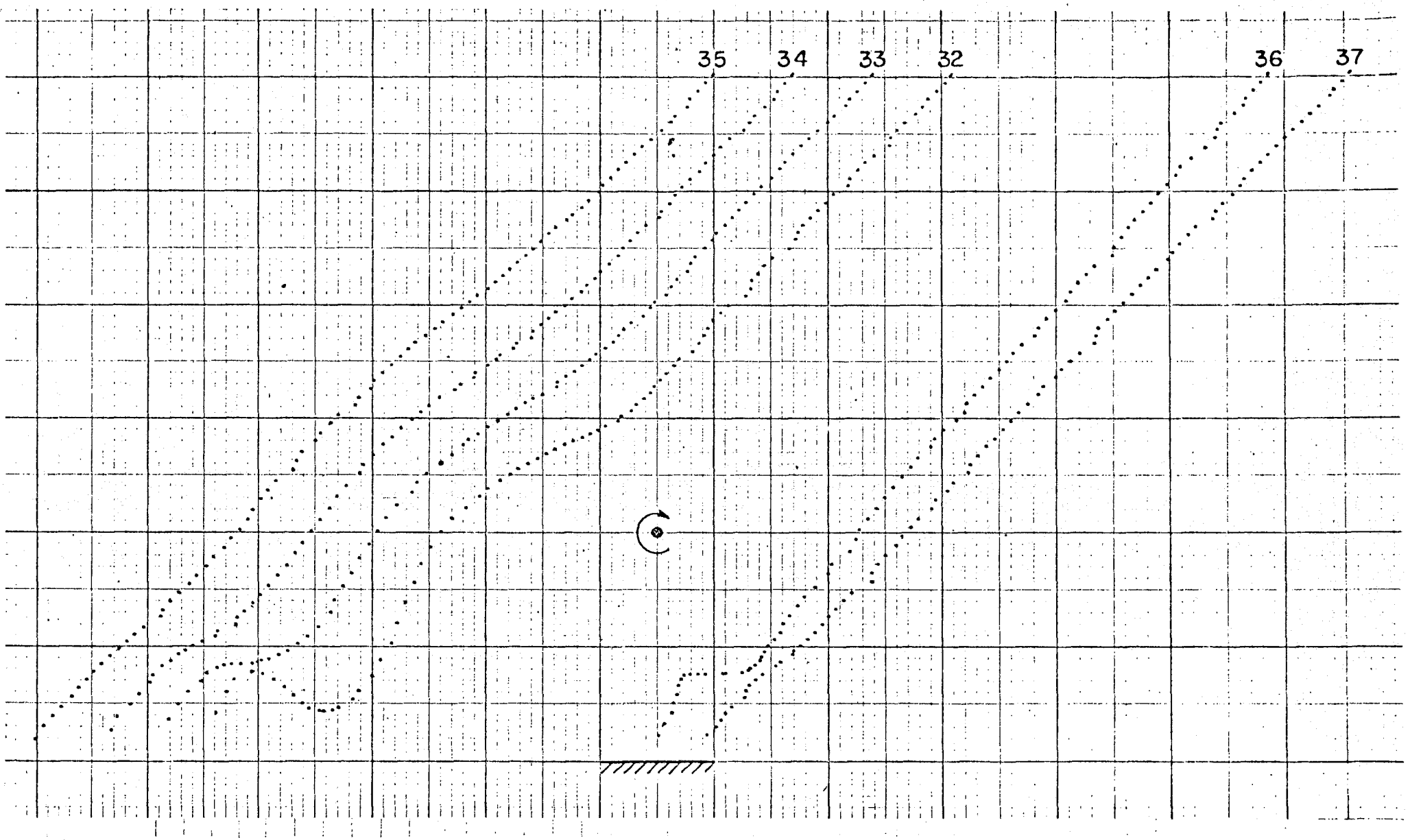
35
34
33
32
36
37

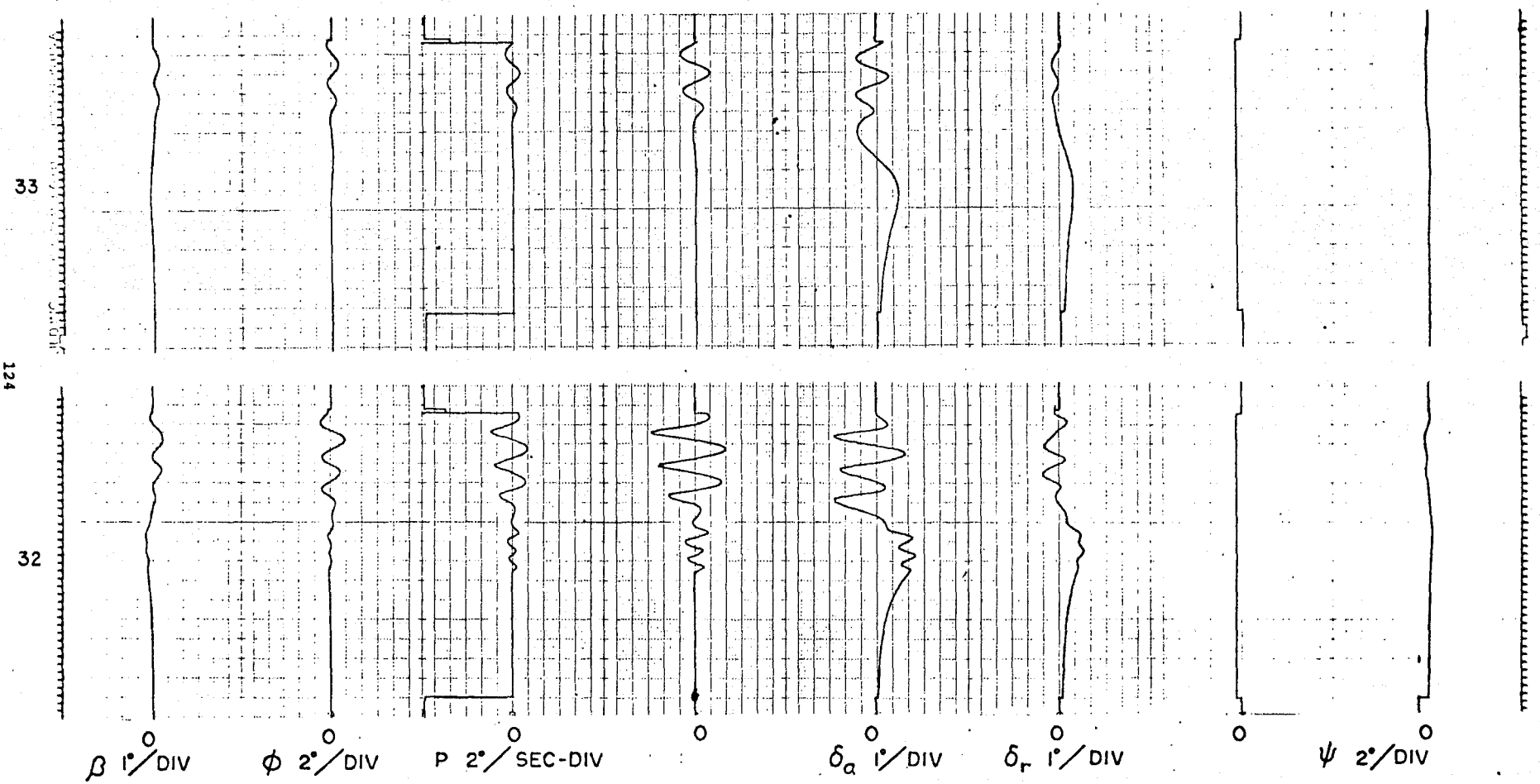
33
32
0
β 1°/DIV
0
φ 2°/DIV
0
P 2°/SEC-DIV
0
0
δa 1°/DIV
0
δr 1°/DIV
0
0
ψ 2°/DIV

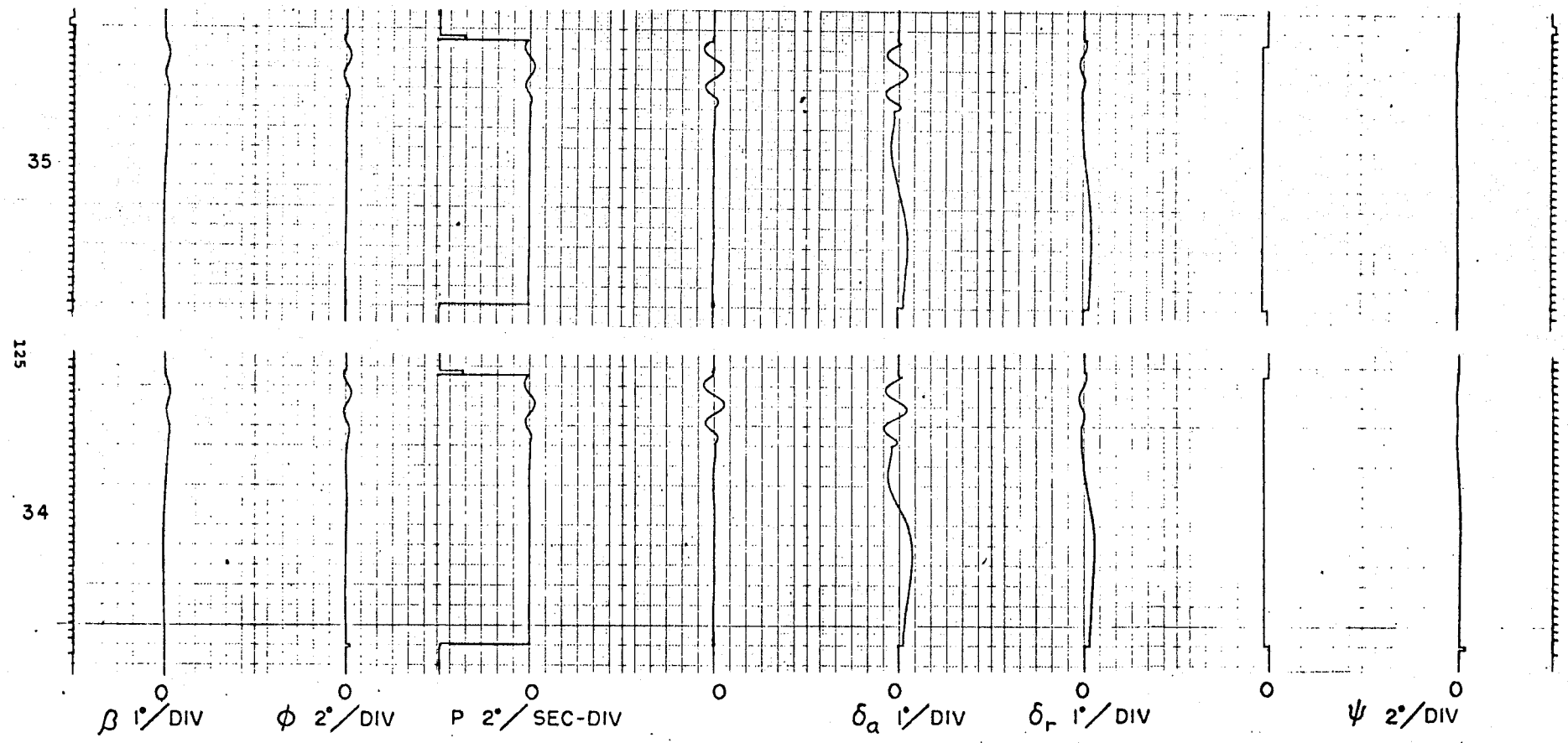
35
34
0
0
0
0
0
0
0
0
β 1°/DIV
φ 2°/DIV
P 2°/SEC-DIV
δa 1°/DIV
δr 1°/DIV
ψ 2°/DIV

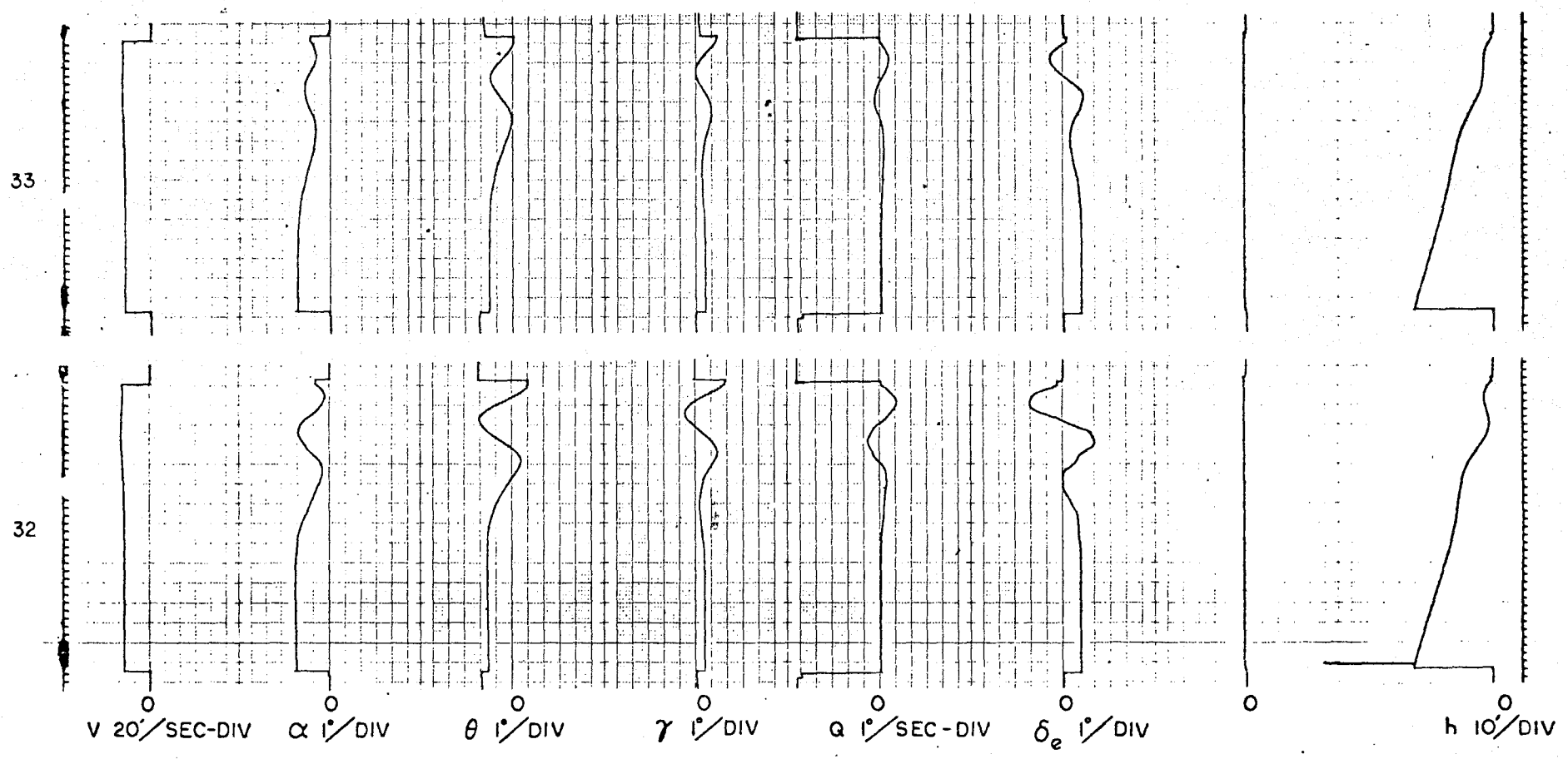
33
32
0
V 20'/SEC-DIV
0
α 1°/DIV
0
θ 1°/DIV
0
γ 1°/DIV
0
Q 1°/SEC-DIV
0
δe 1°/DIV
0
0
h 10'/DIV

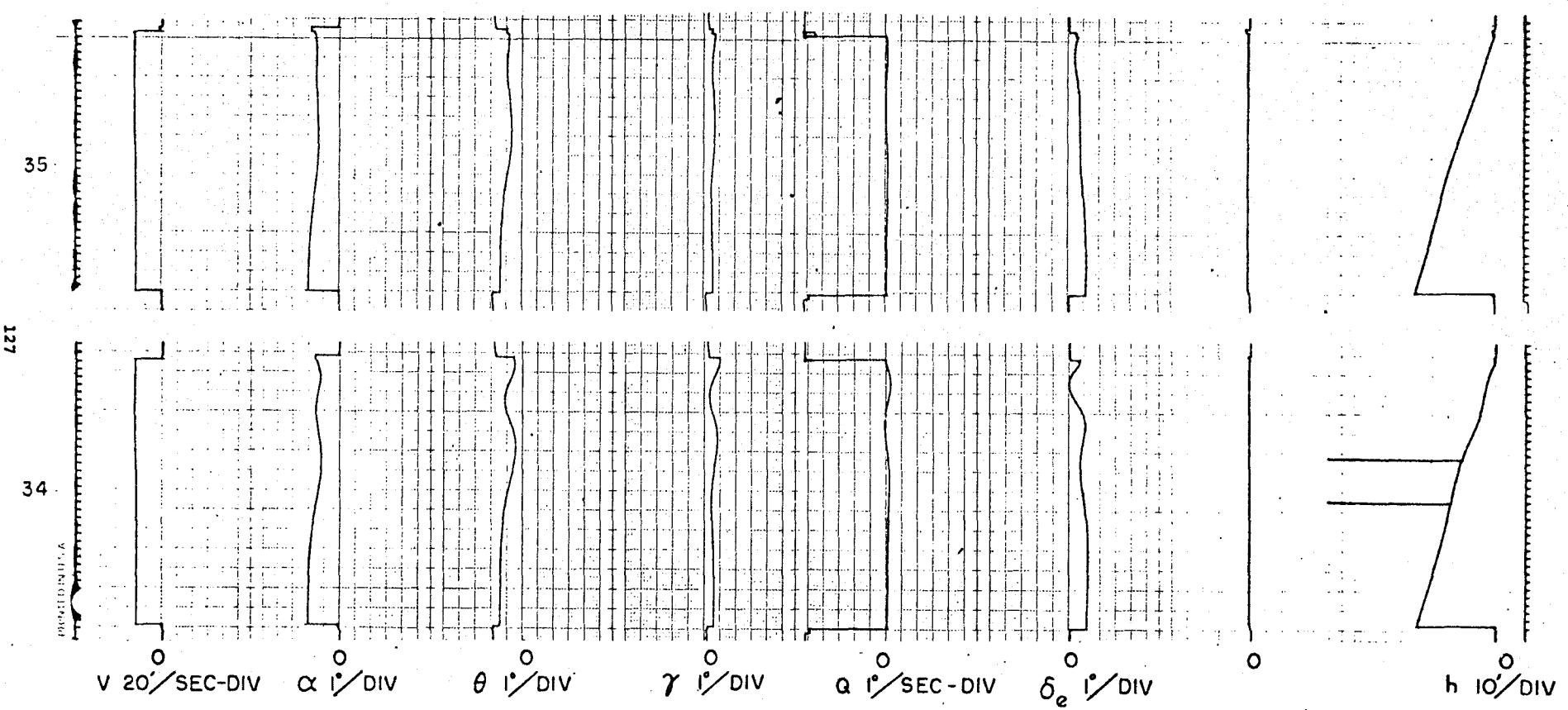
35
34
0
V 20'/SEC-DIV
0
α 1°/DIV
0
θ 1°/DIV
0
γ 1°/DIV
0
Q 1°/SEC-DIV
0
δe 1°/DIV
0
0
h 10'/DIV

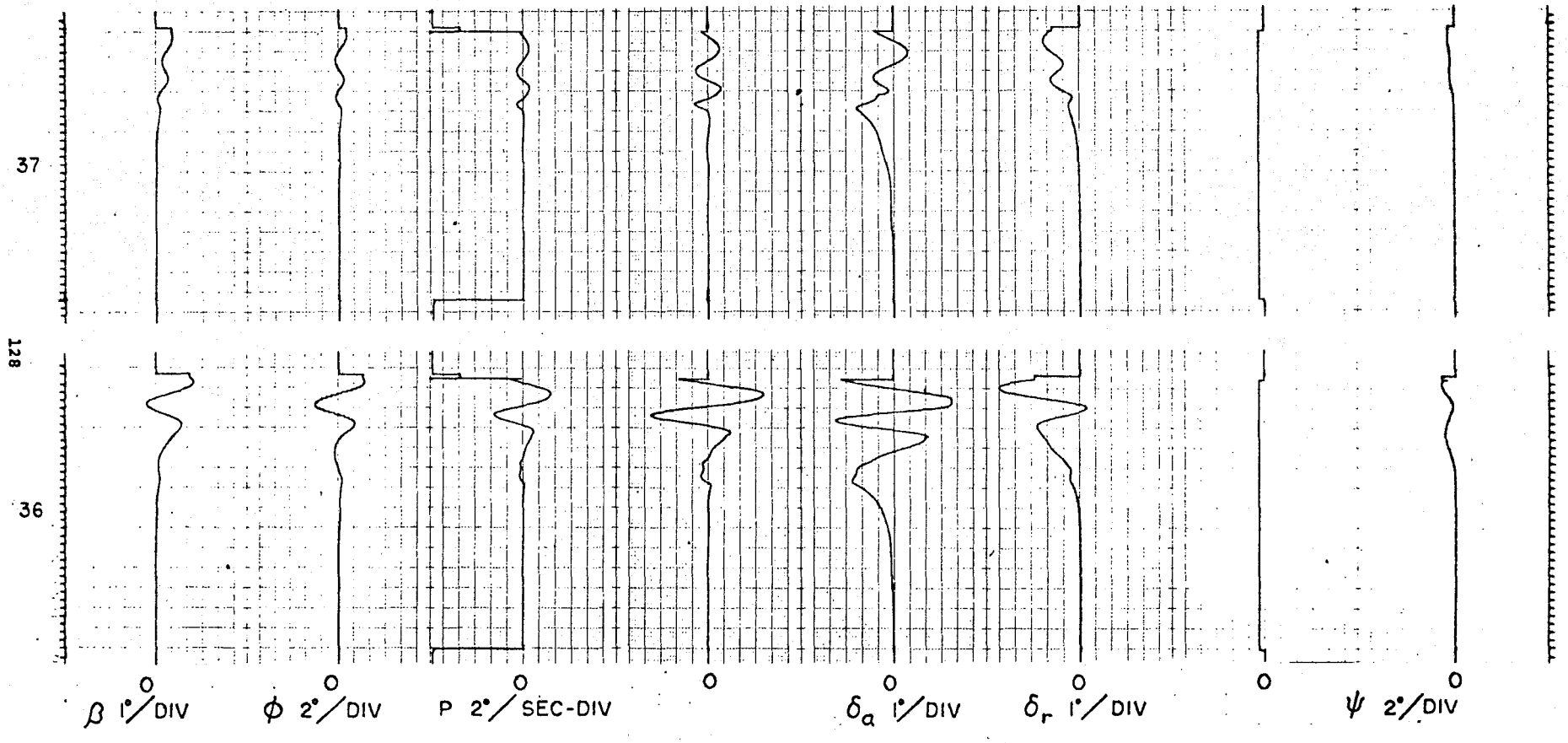
37
36
0
0
0
0
0
0
0
β 1°/DIV
φ 2°/DIV
P 2°/SEC-DIV
δa 1°/DIV
δr 1°/DIV
ψ 2°/DIV

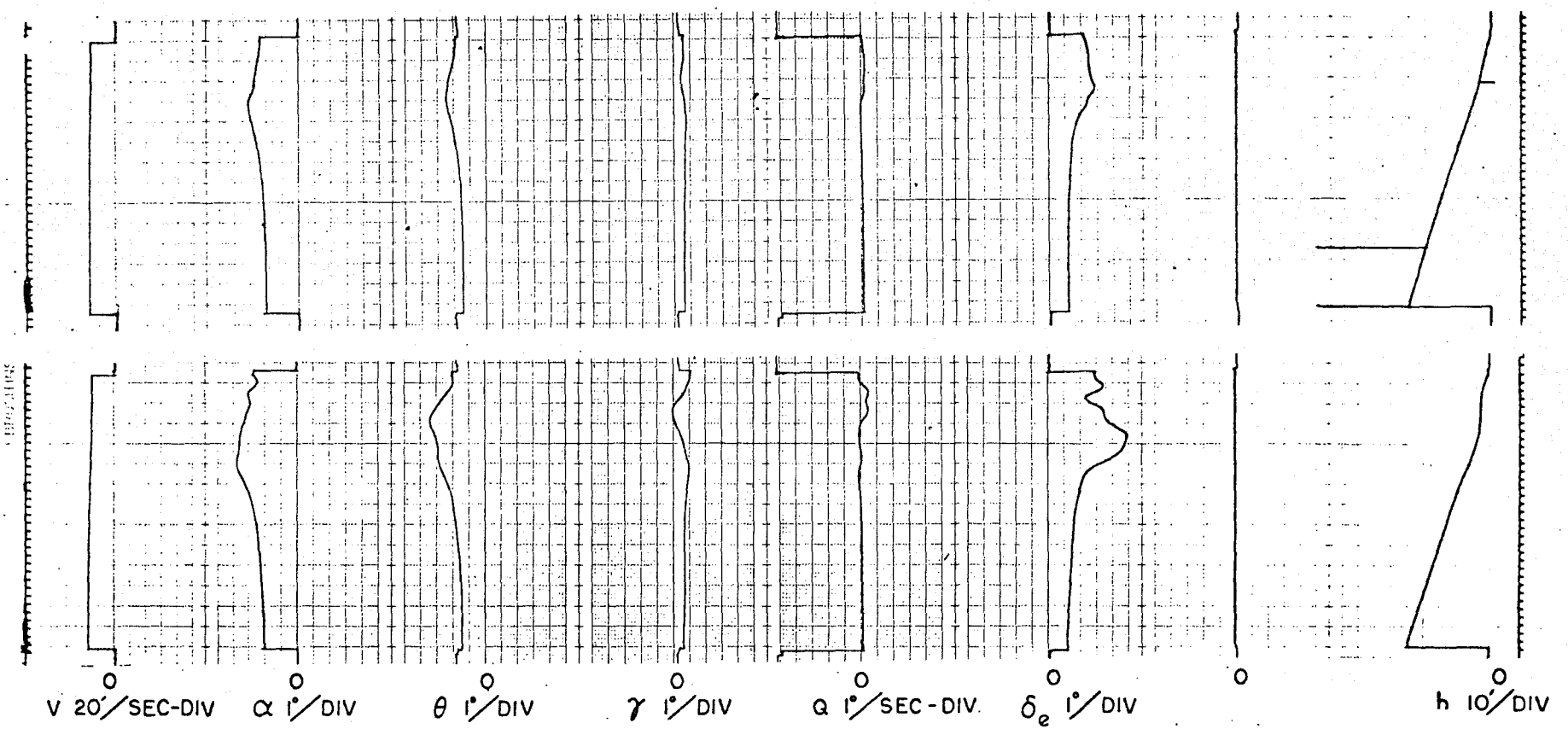
37
36
0
V 20'/SEC-DIV
α 1°/DIV
θ 1°/DIV
γ 1°/DIV
Q 1°/SEC-DIV
δe 1°/DIV
h 10'/DIV

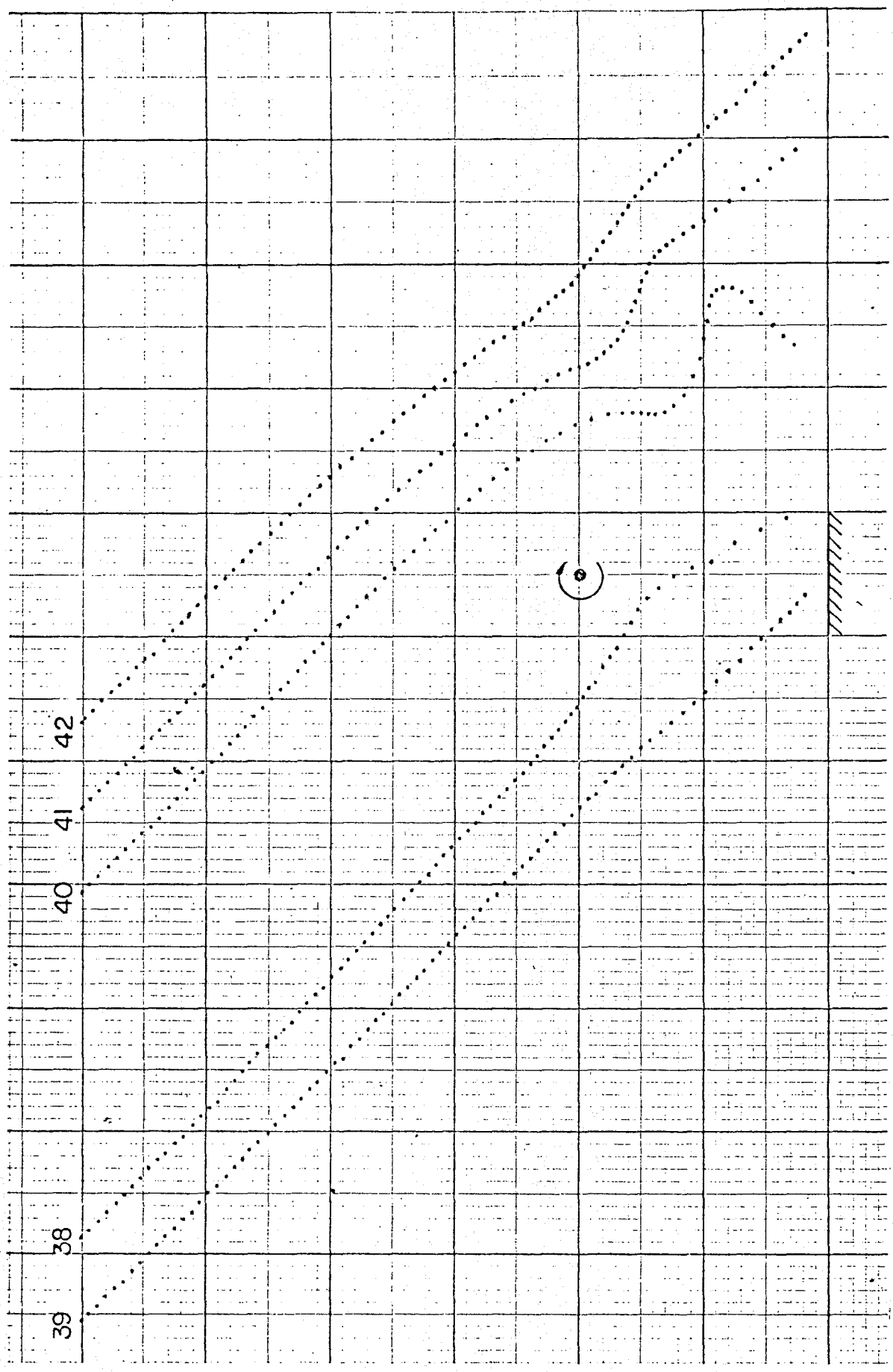
39
38
40
41
42

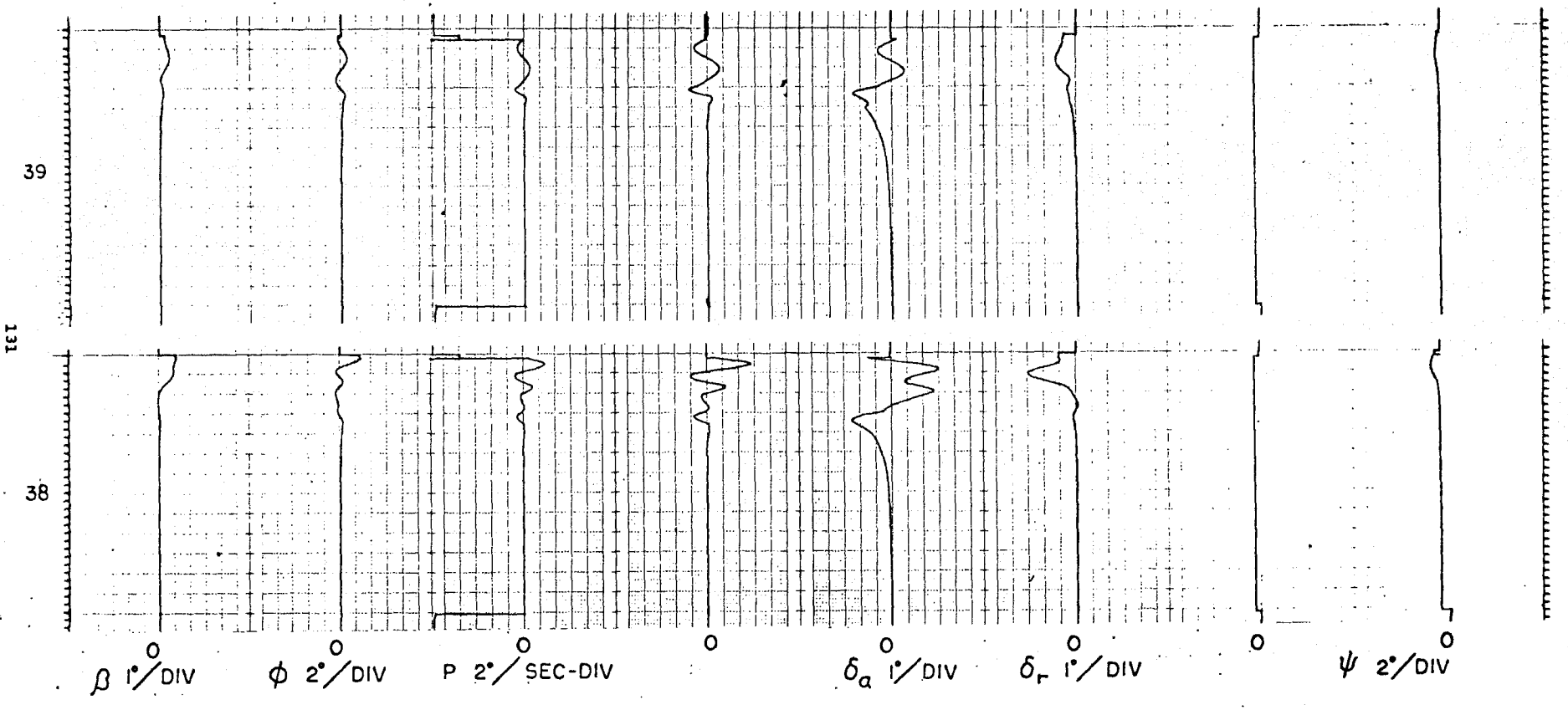
39
38
0
0
0
0
0
0
0
0
β 1°/DIV
φ 2°/DIV
P 2°/SEC-DIV
δa 1°/DIV
δr 1°/DIV
ψ 2°/DIV

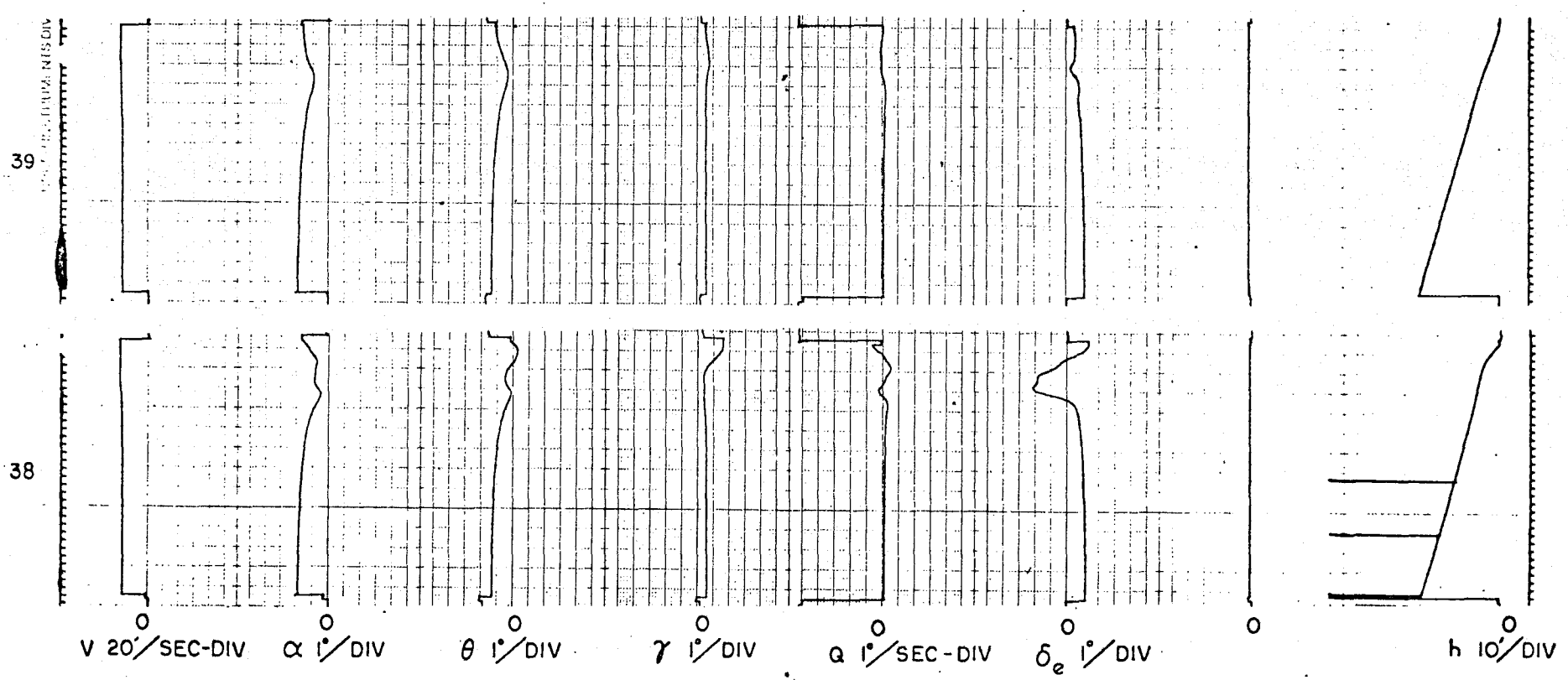
39
38
0
V 20'/SEC-DIV
0
α 1°/DIV
0
θ 1°/DIV
0
γ 1°/DIV
0
Q 1°/SEC-DIV
0
δe 1°/DIV
0
0
h 10'/DIV

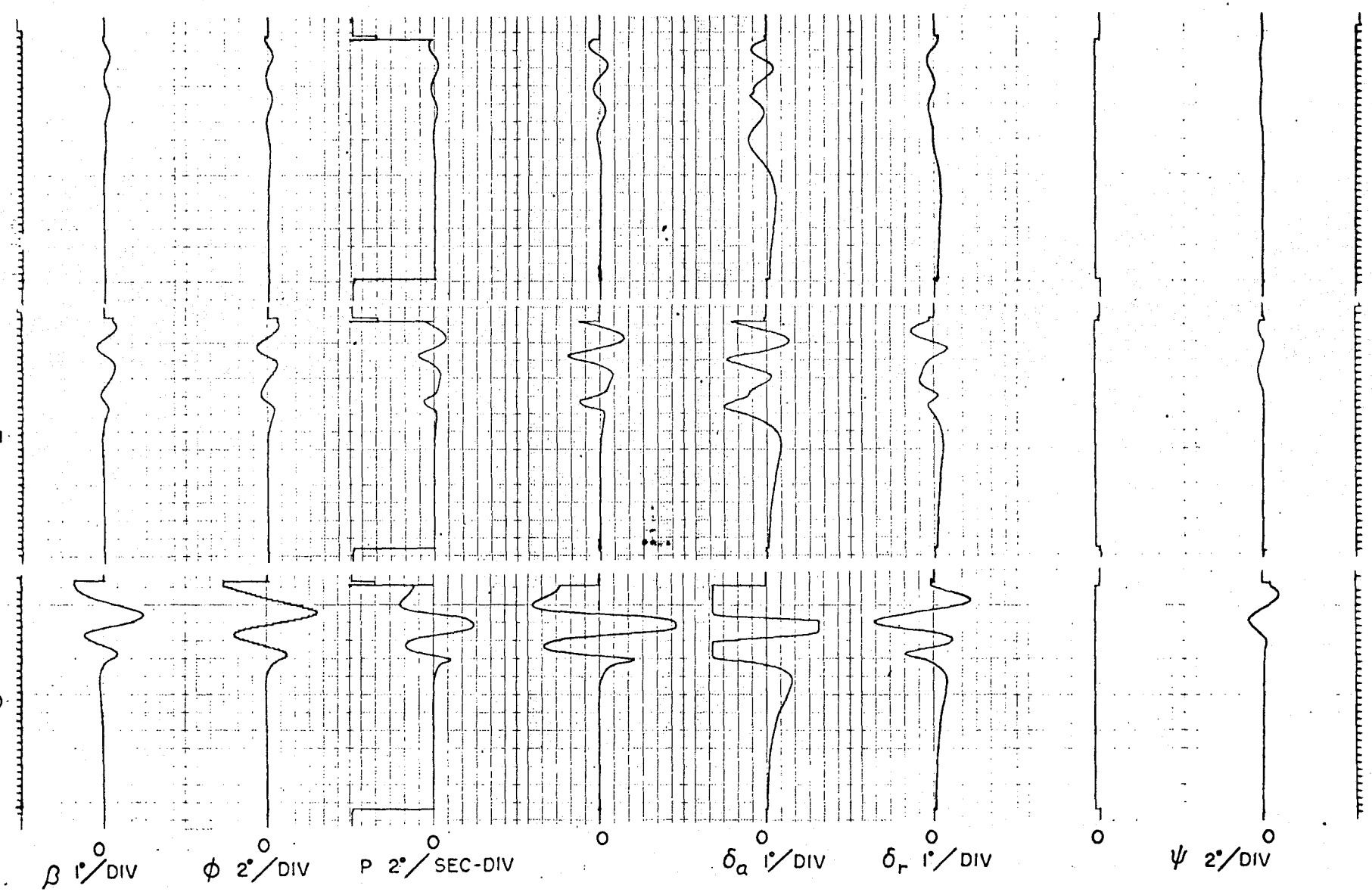
42
41
40
0
β 1°/DIV
0
φ 2°/DIV
0
P 2°/SEC-DIV
0
0
δa 1°/DIV
0
δr 1°/DIV
0
0
ψ 2°/DIV

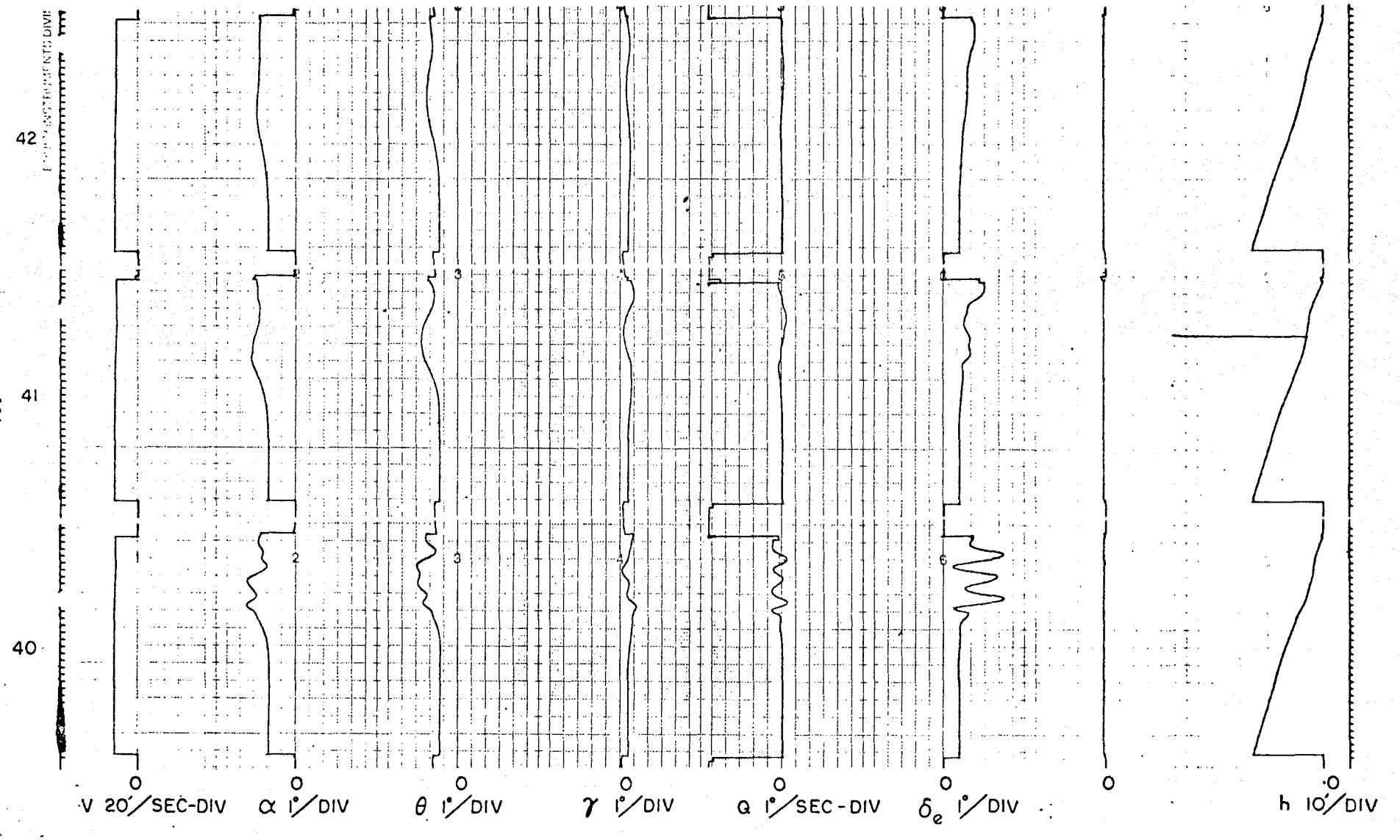
42
41
40
V 20'/SEC-DIV
α 1°/DIV
θ 1°/DIV
γ 1°/DIV
Q 1°/SEC-DIV
δe 1°/DIV
h 10'/DIV
0
2
3
4
5
6

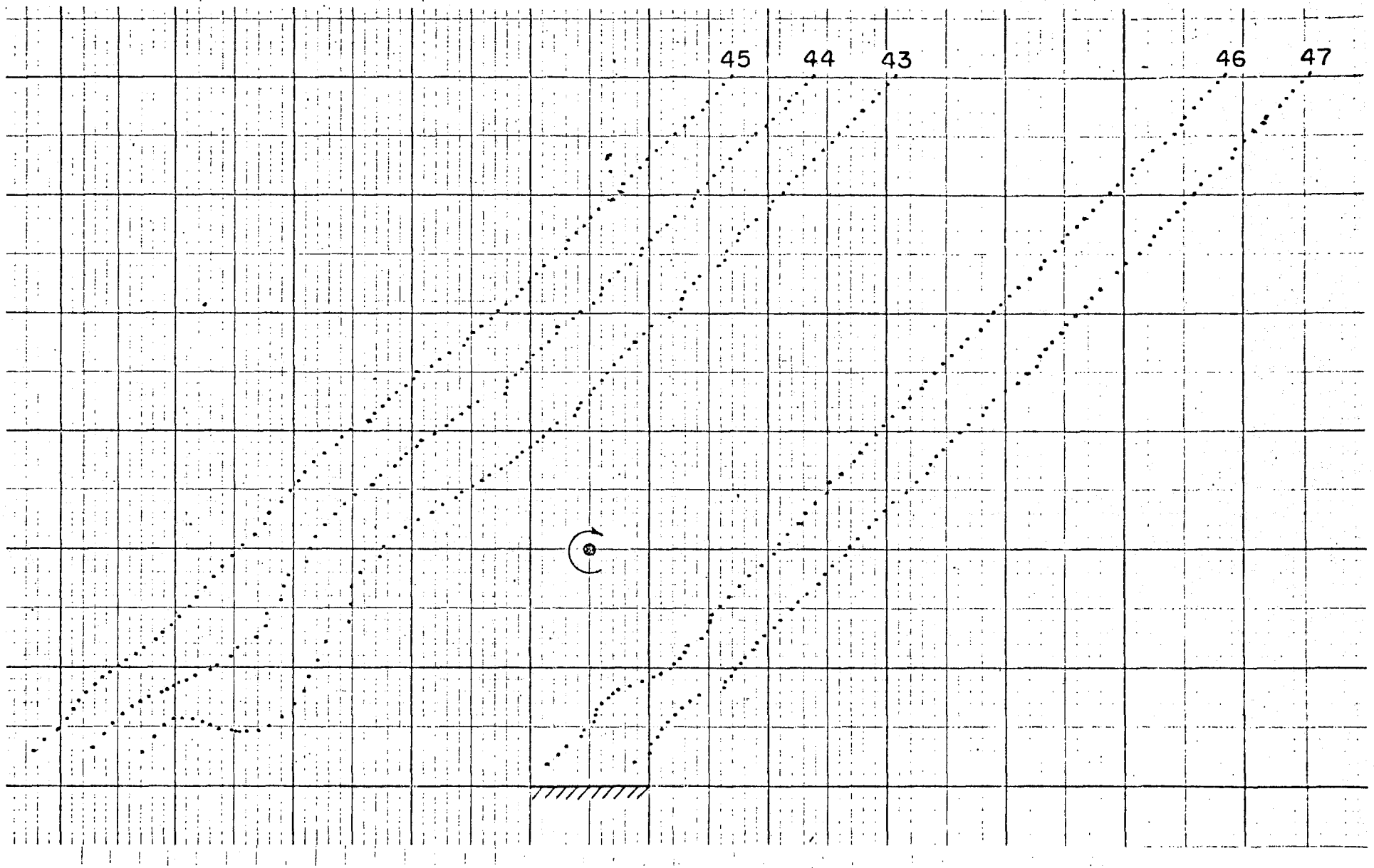
45
44
43
46
47

0
0
0
0
0
0
0
0
0
0
0
0
45
44
43

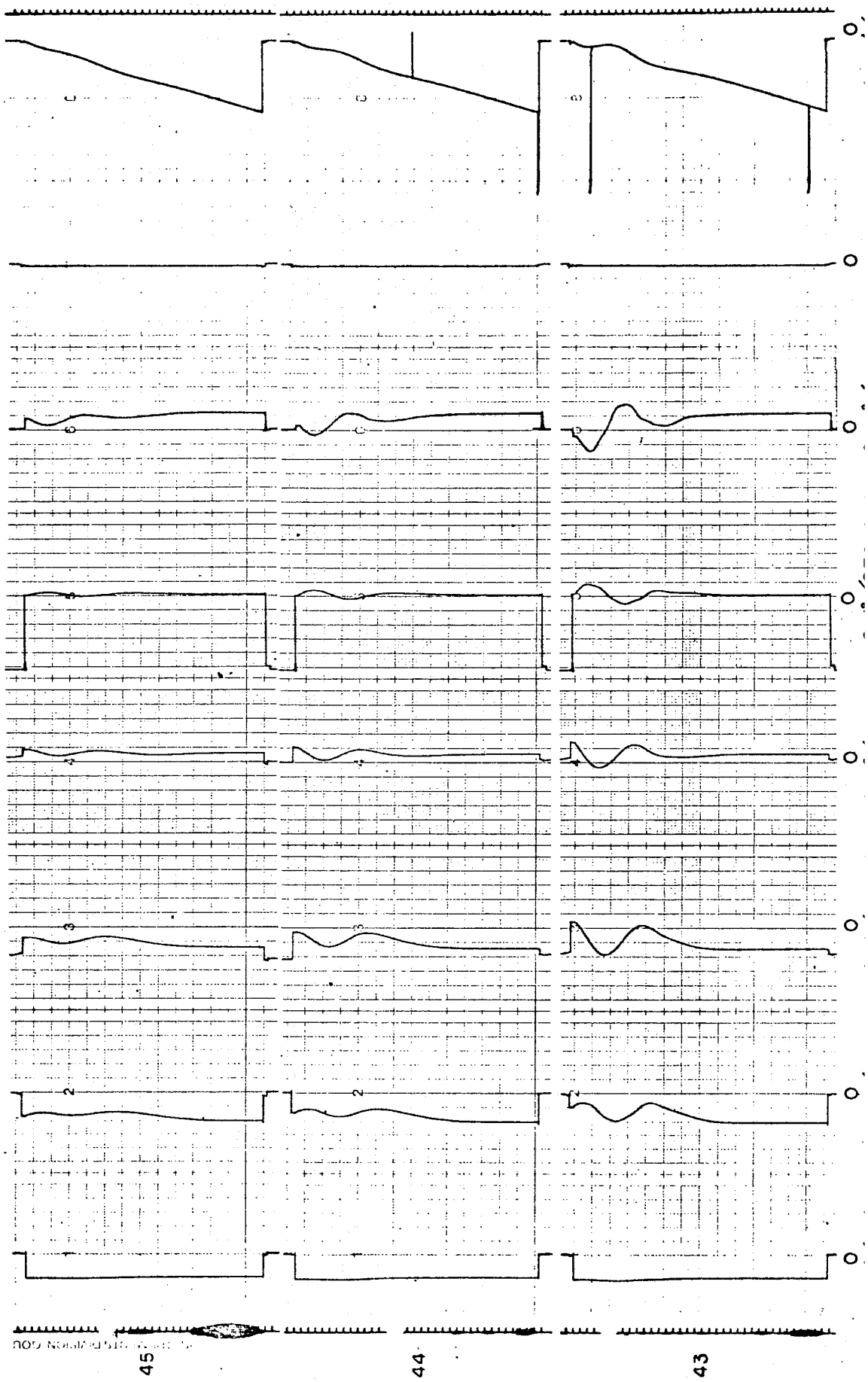
45
44
43

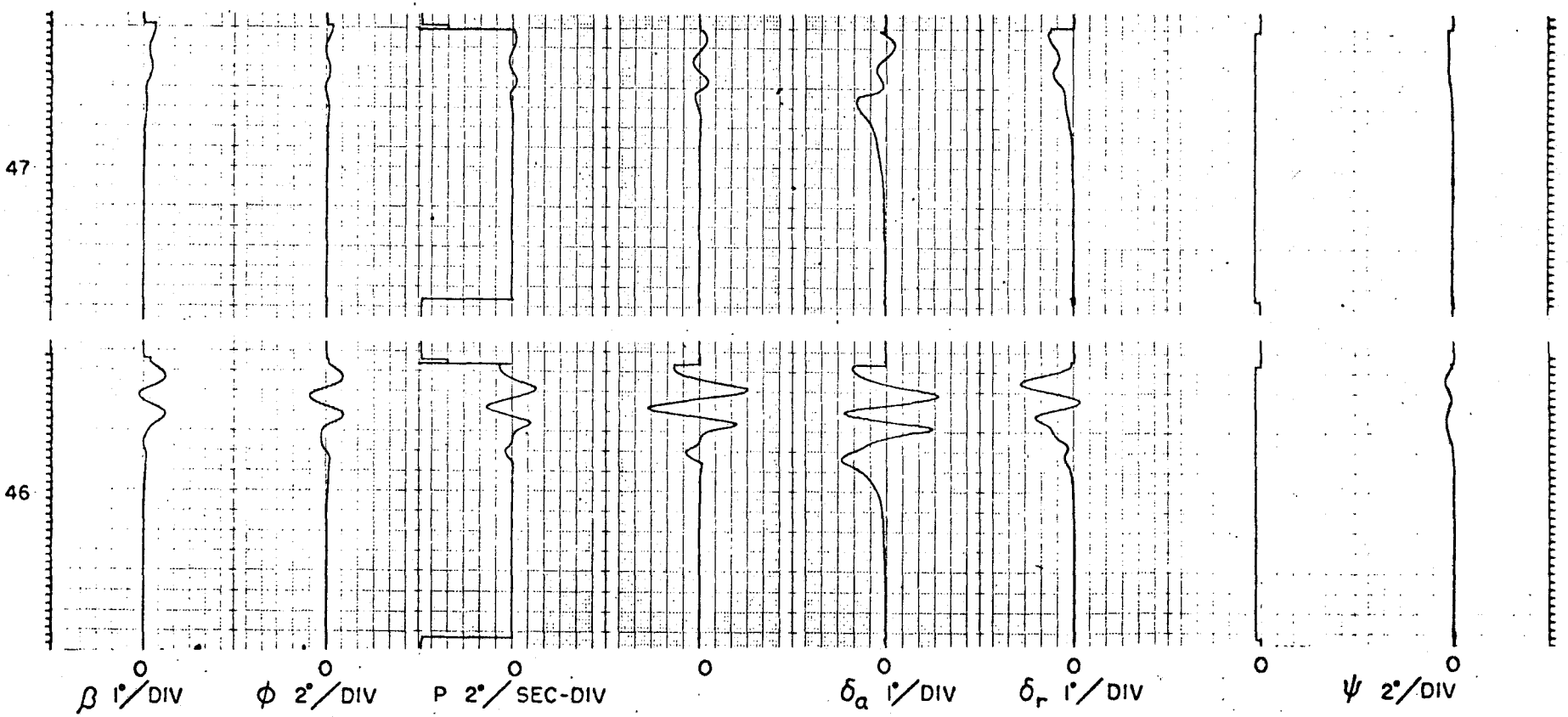
47
46
0
β 1°/DIV
0
φ 2°/DIV
0
P 2°/SEC-DIV
0
0
δa 1°/DIV
0
δr 1°/DIV
0
0
ψ 2°/DIV

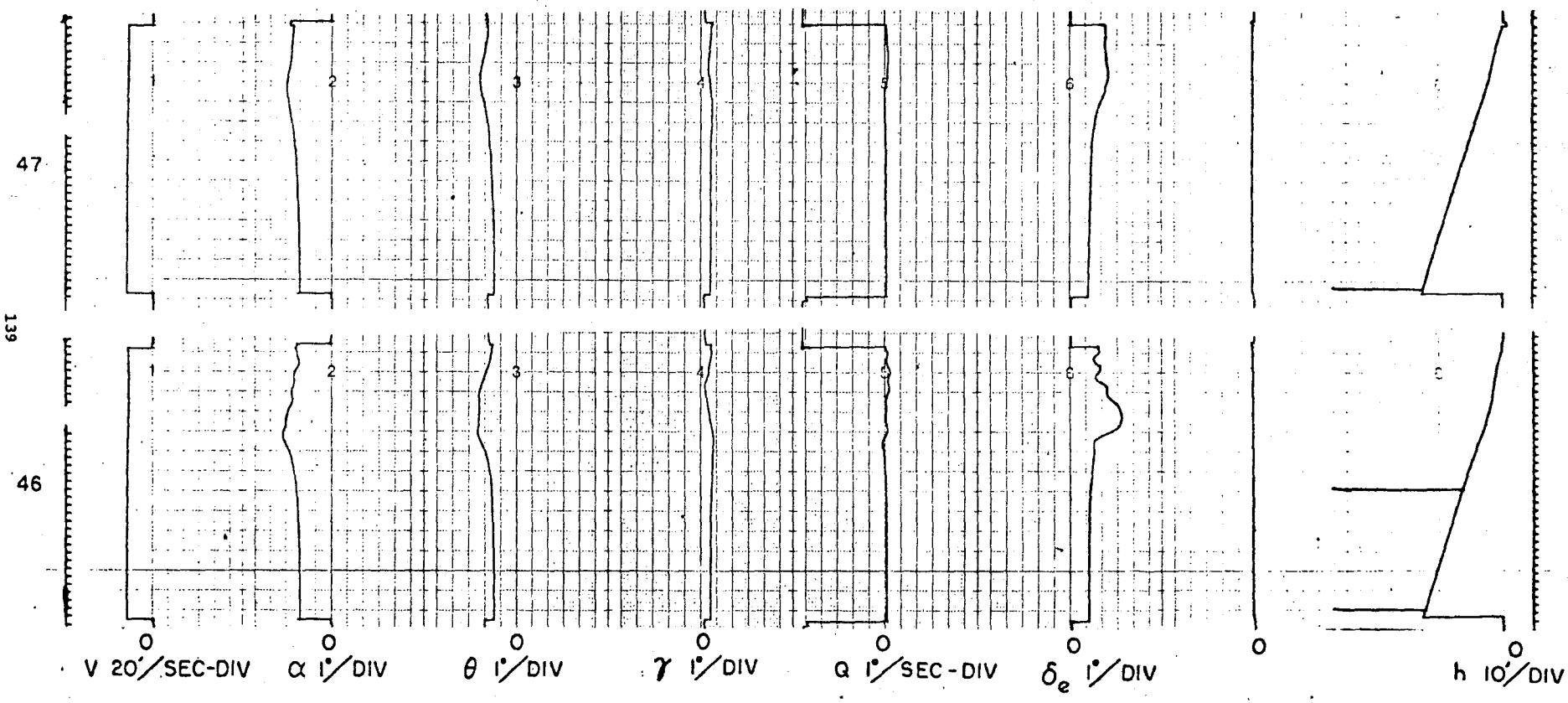
47
46
1
2
3
4
5
6
0
V 20'/SEC-DIV
α 1°/DIV
θ 1°/DIV
γ 1°/DIV
Q 1°/SEC-DIV
δ_e 1°/DIV
h 10'/DIV

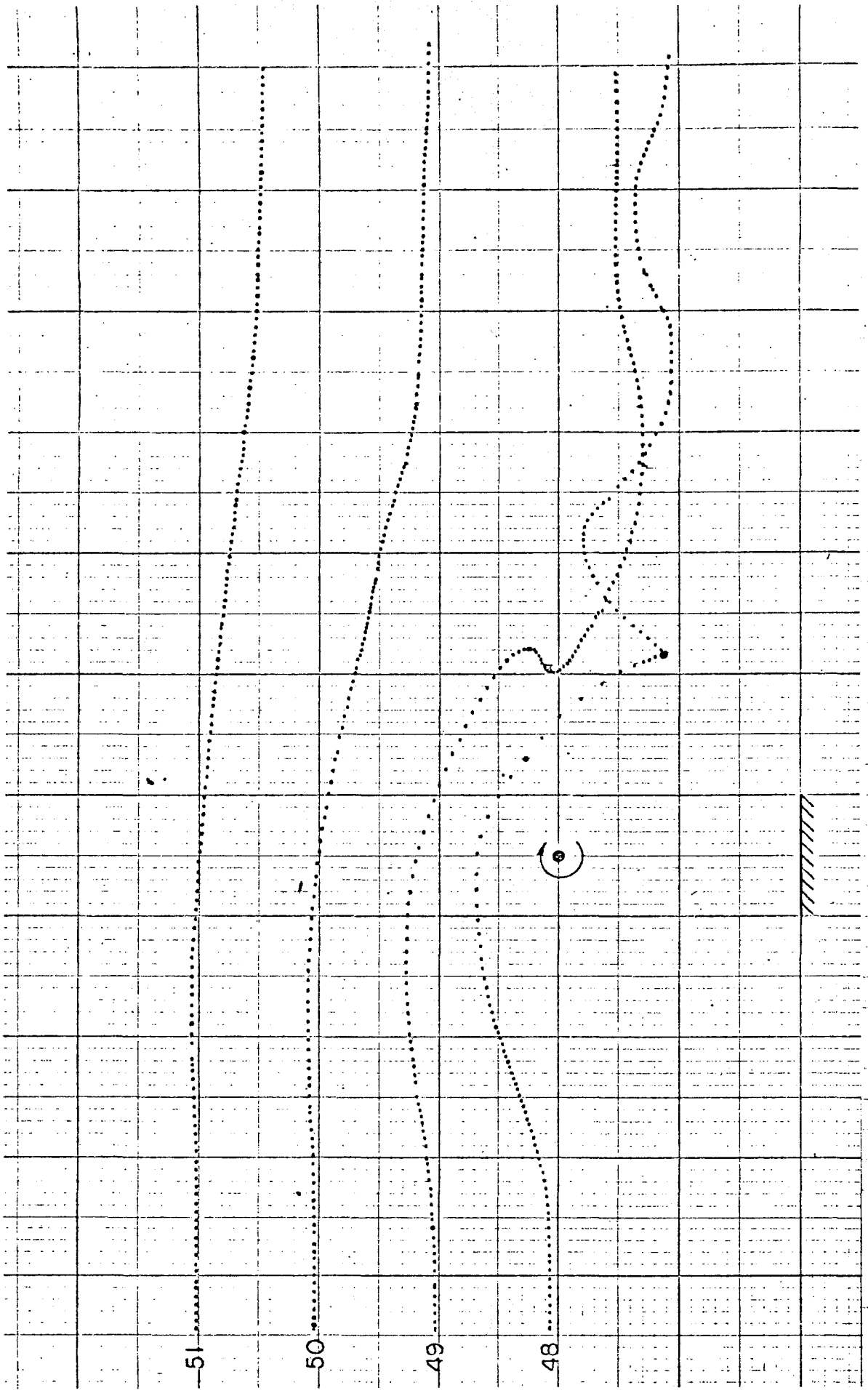
51
50
49
48

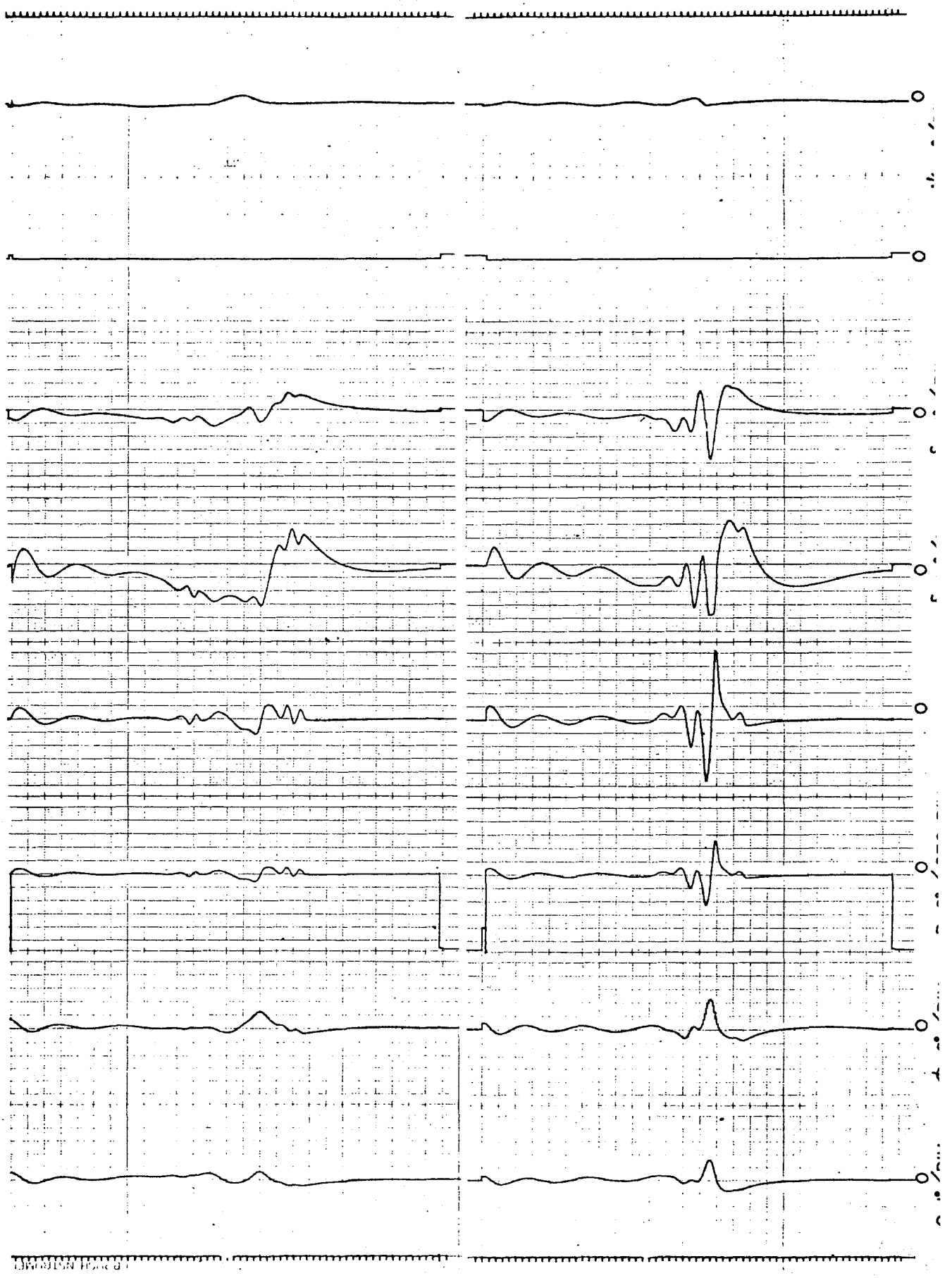

49 48

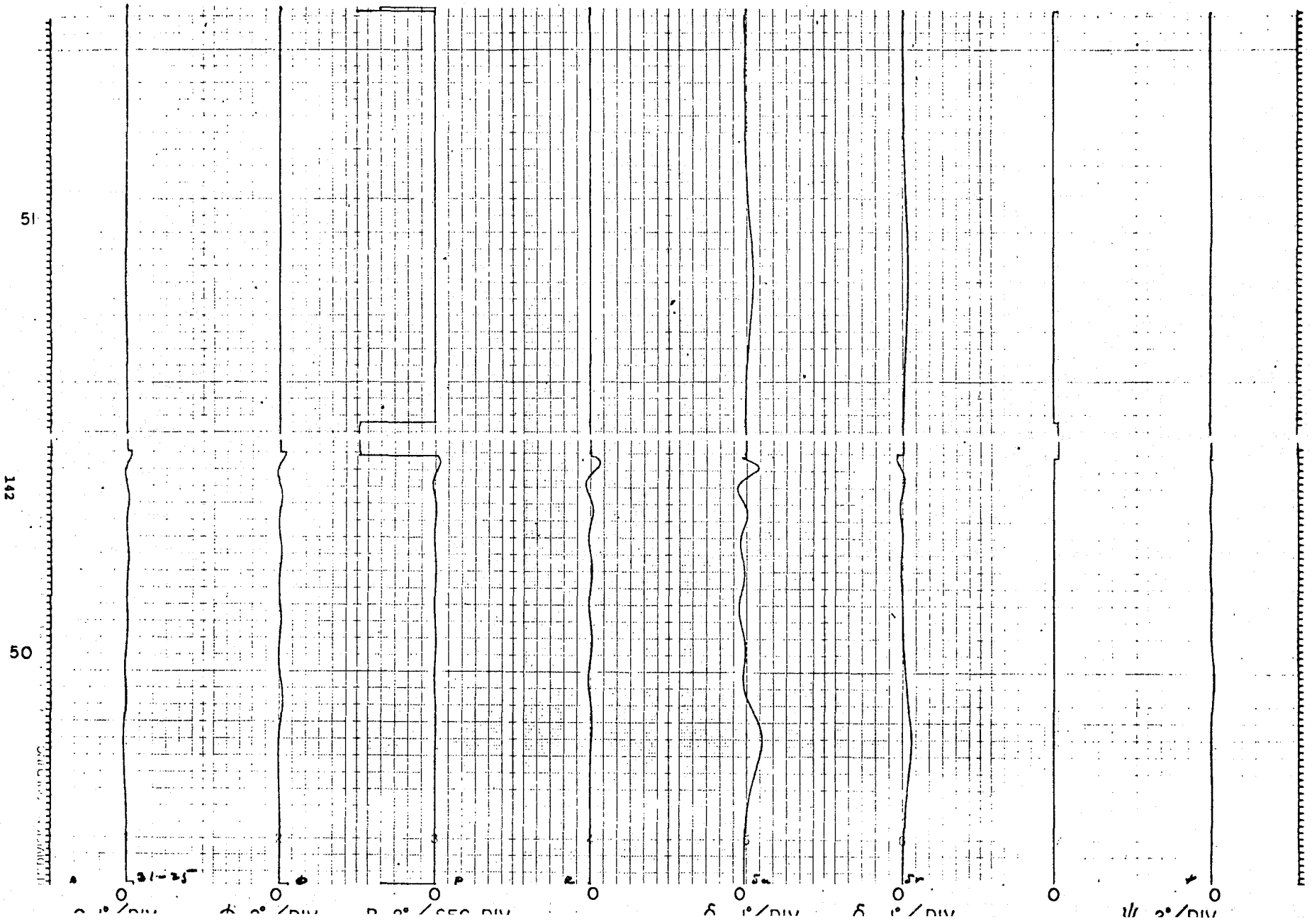
51
50
0
0
0
0
0
0
0

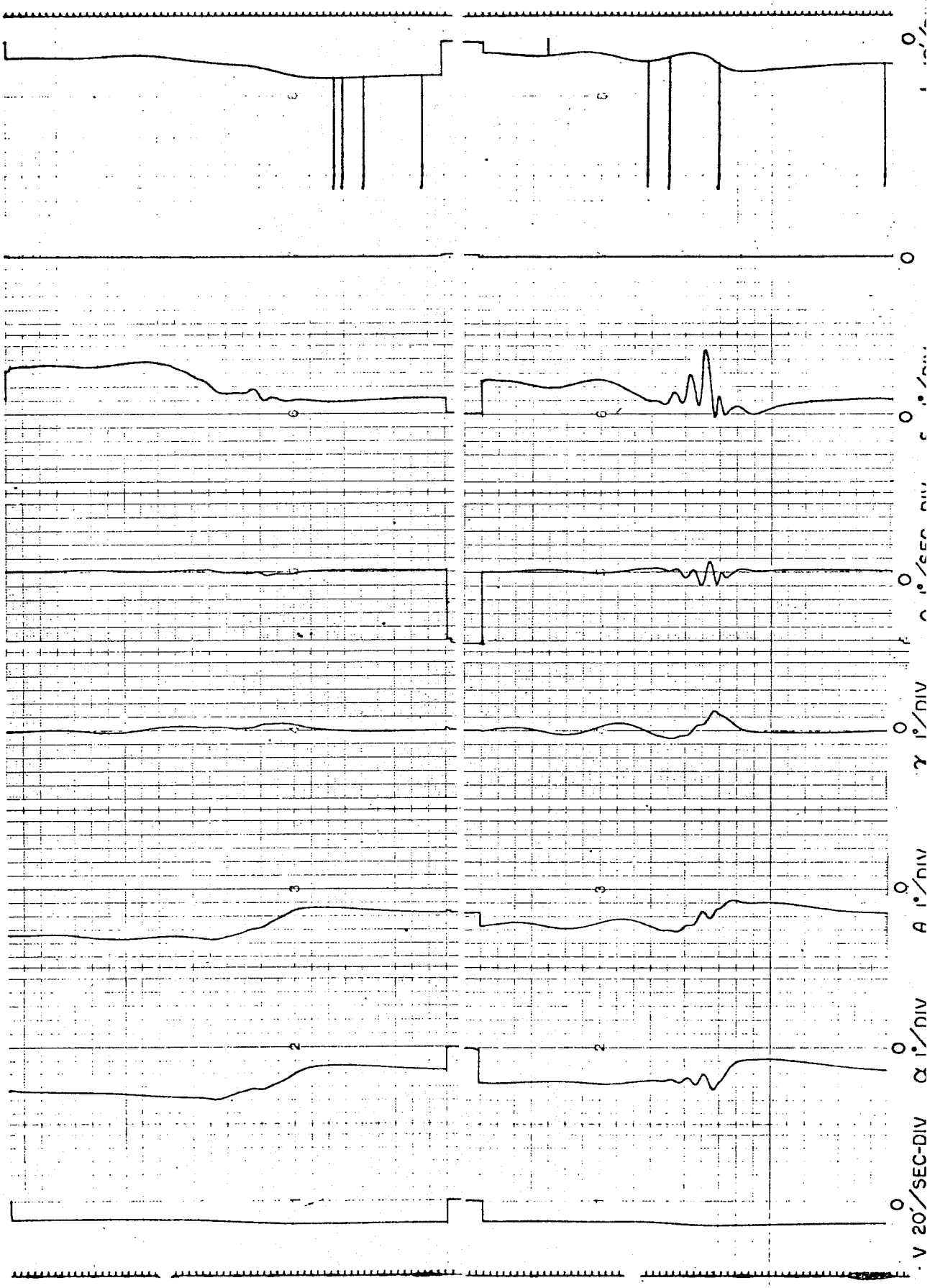
V 20°/SEC-DIV
α 1°/DIV
A 1°/DIV
γ 1°/DIV
0
49
48

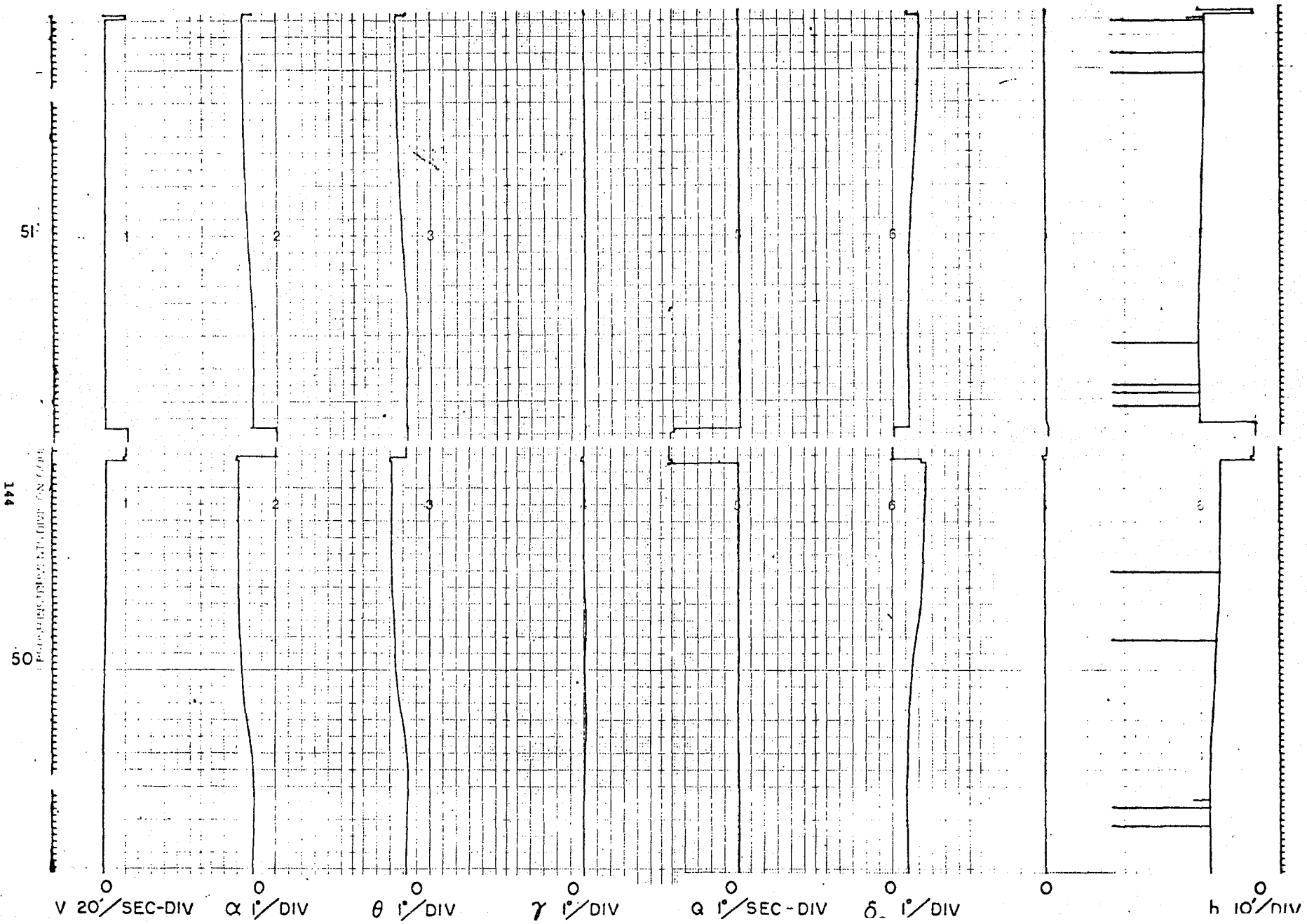
51
50
1
2
3
4
5
6
0
V 20'/SEC-DIV
α 1°/DIV
θ 1°/DIV
γ 1°/DIV
Q 1°/SEC-DIV
δ 1°/DIV
h 10'/DIV

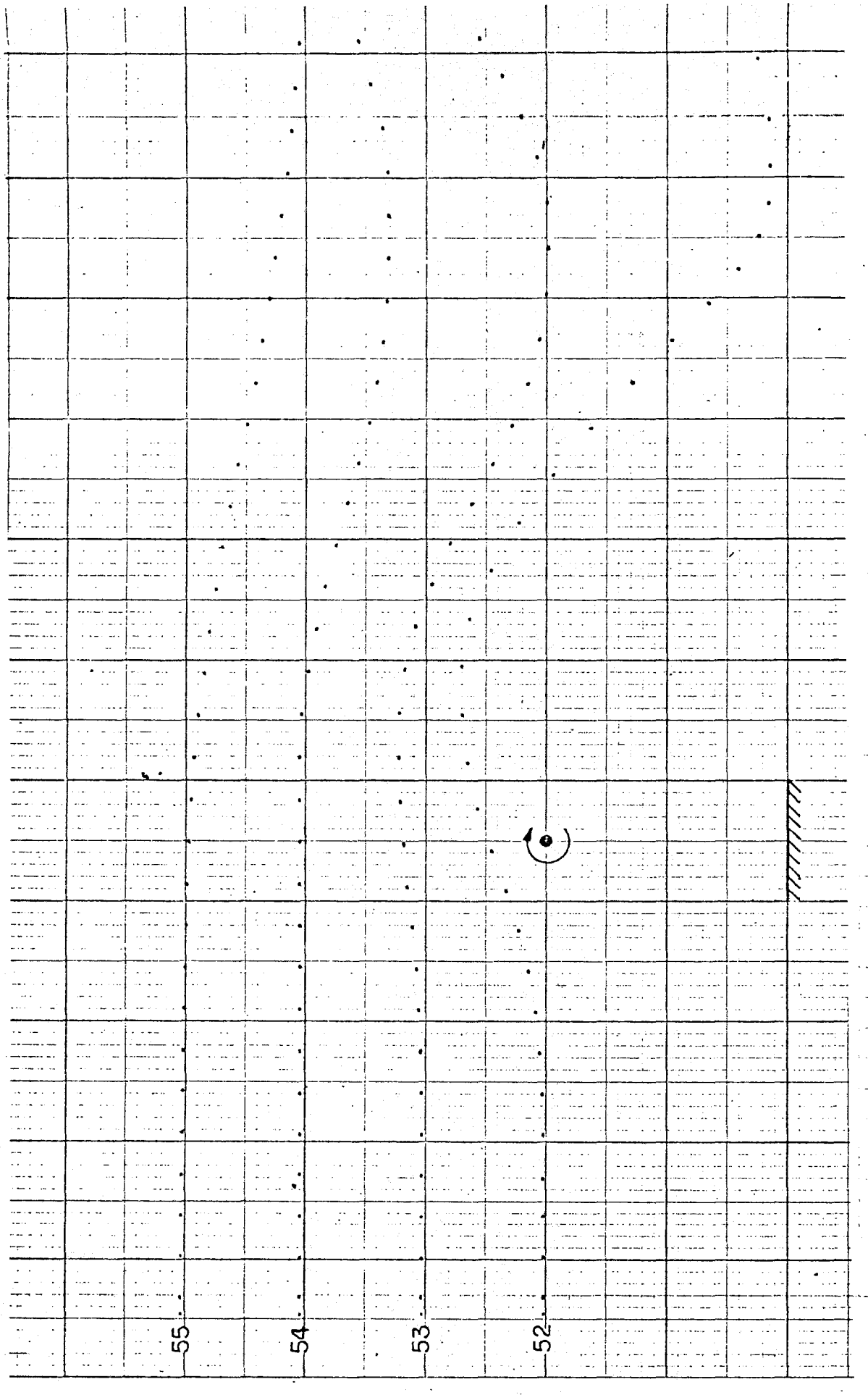
55
54
53
52

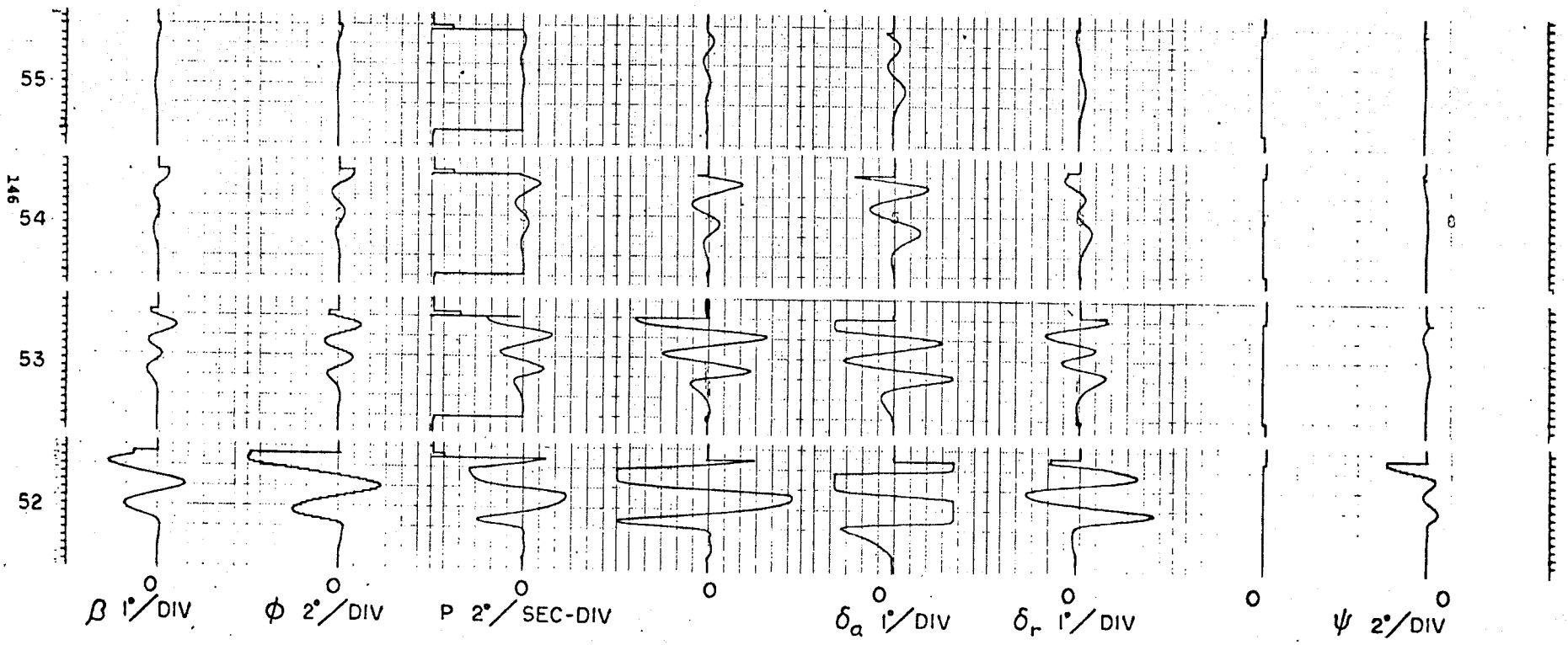
55
54
53
52
β 1°/DIV
φ 2°/DIV
P 2°/SEC-DIV
δa 1°/DIV
δr 1°/DIV
ψ 2°/DIV
0

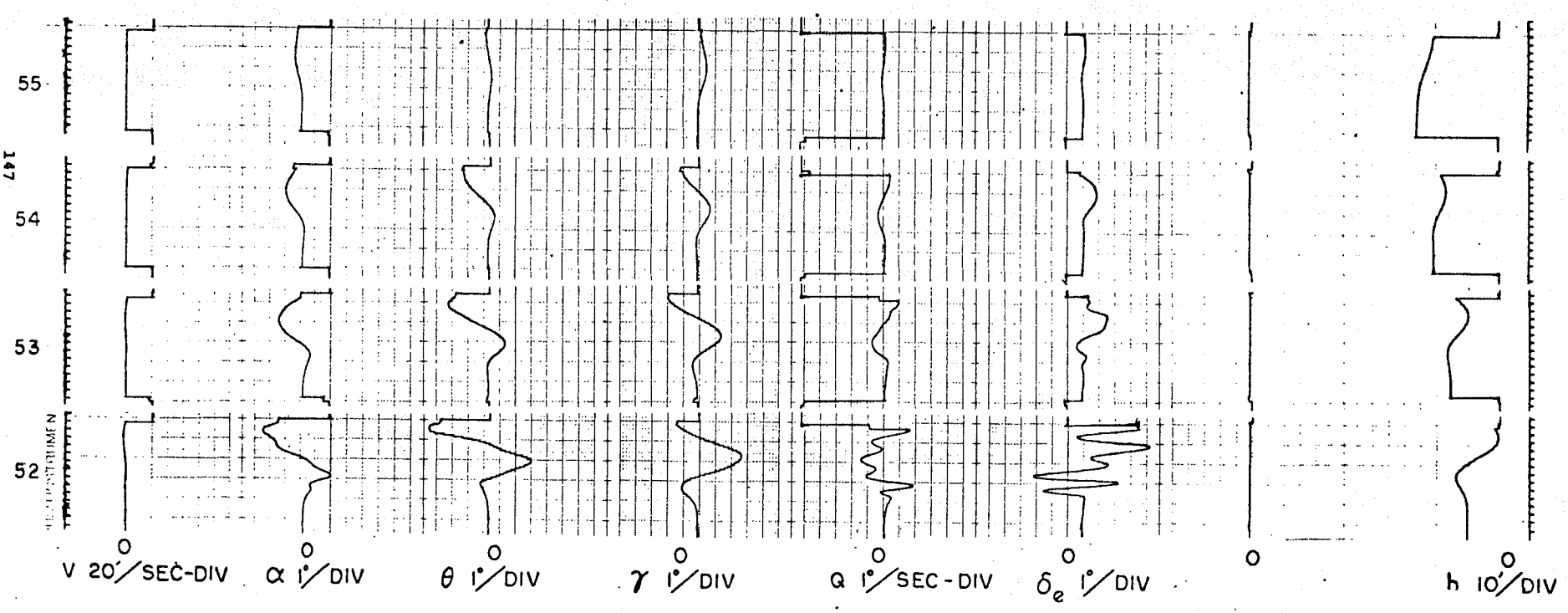
55
54
53
52
V 20'/SEC-DIV
α 1°/DIV
θ 1°/DIV
γ 1°/DIV
Q 1°/SEC-DIV
δe 1°/DIV
h 10'/DIV
0

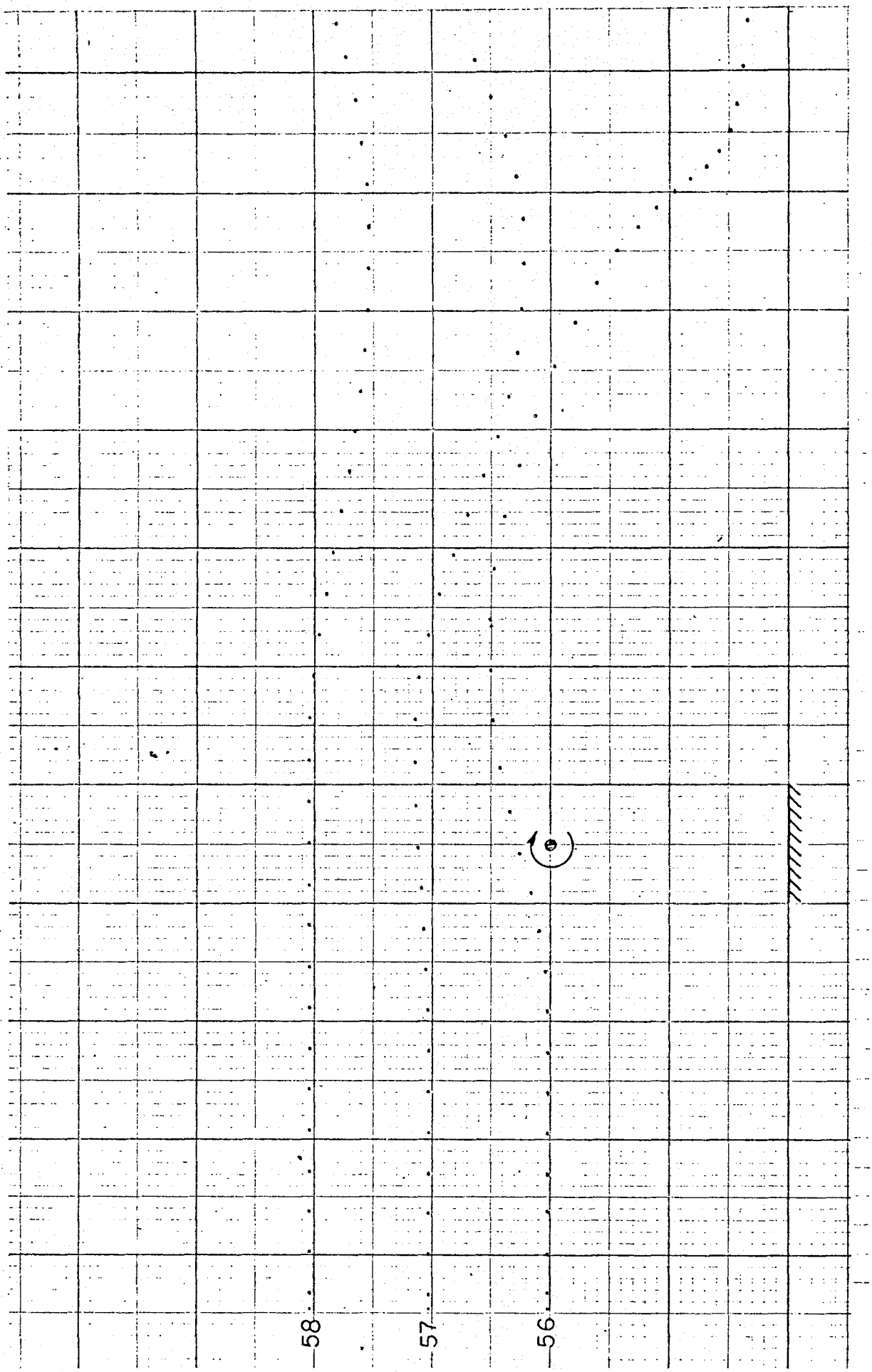
58
57
56

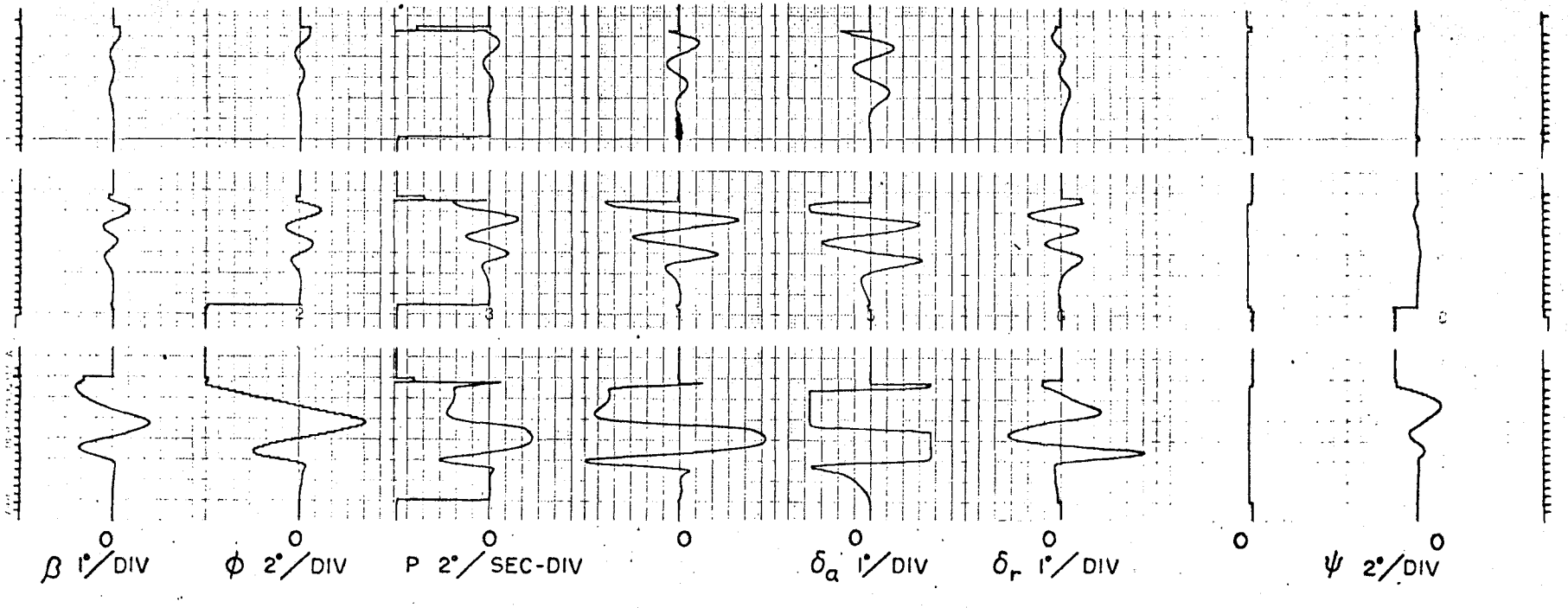
58
57
56
β 1°/DIV
φ 2°/DIV
P 2°/SEC-DIV
δa 1°/DIV
δr 1°/DIV
ψ 2°/DIV
0

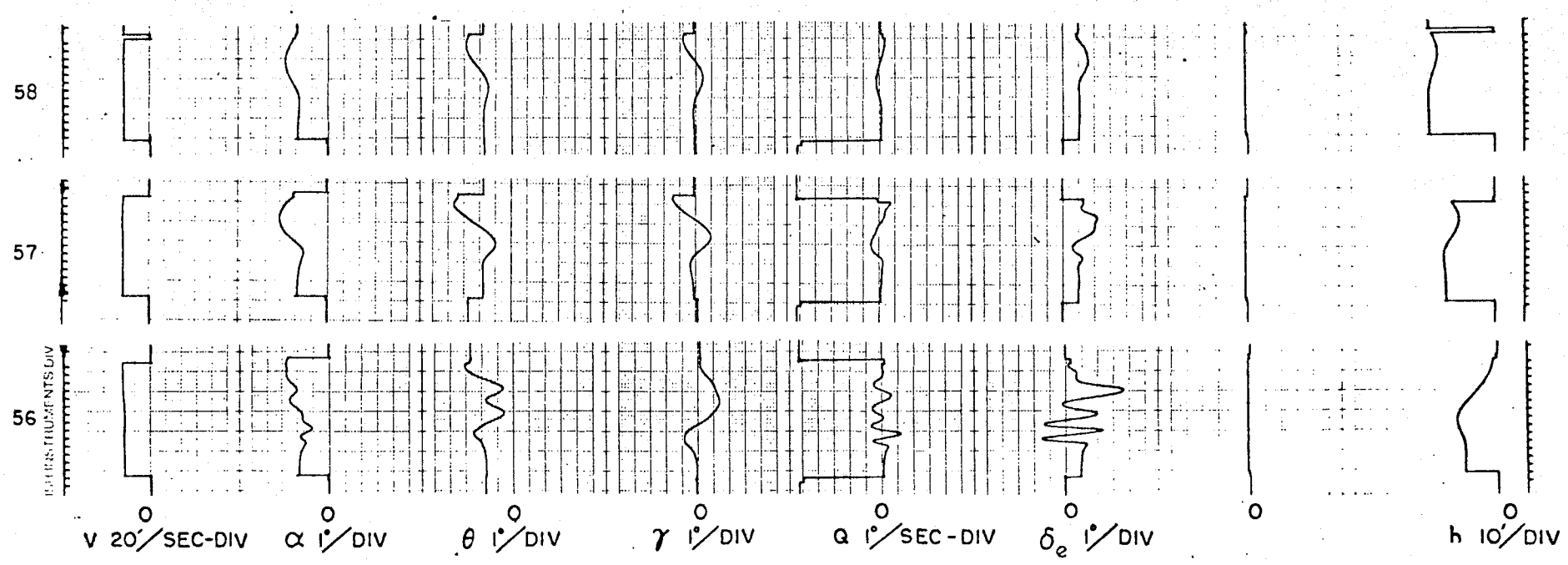
58
57
56
INSTRUMENTS DIV
0
V 20'/SEC-DIV
0
α 1°/DIV
0
θ 1°/DIV
0
γ 1°/DIV
0
Q 1°/SEC-DIV
0
δe 1°/DIV
0
0
h 10'/DIV

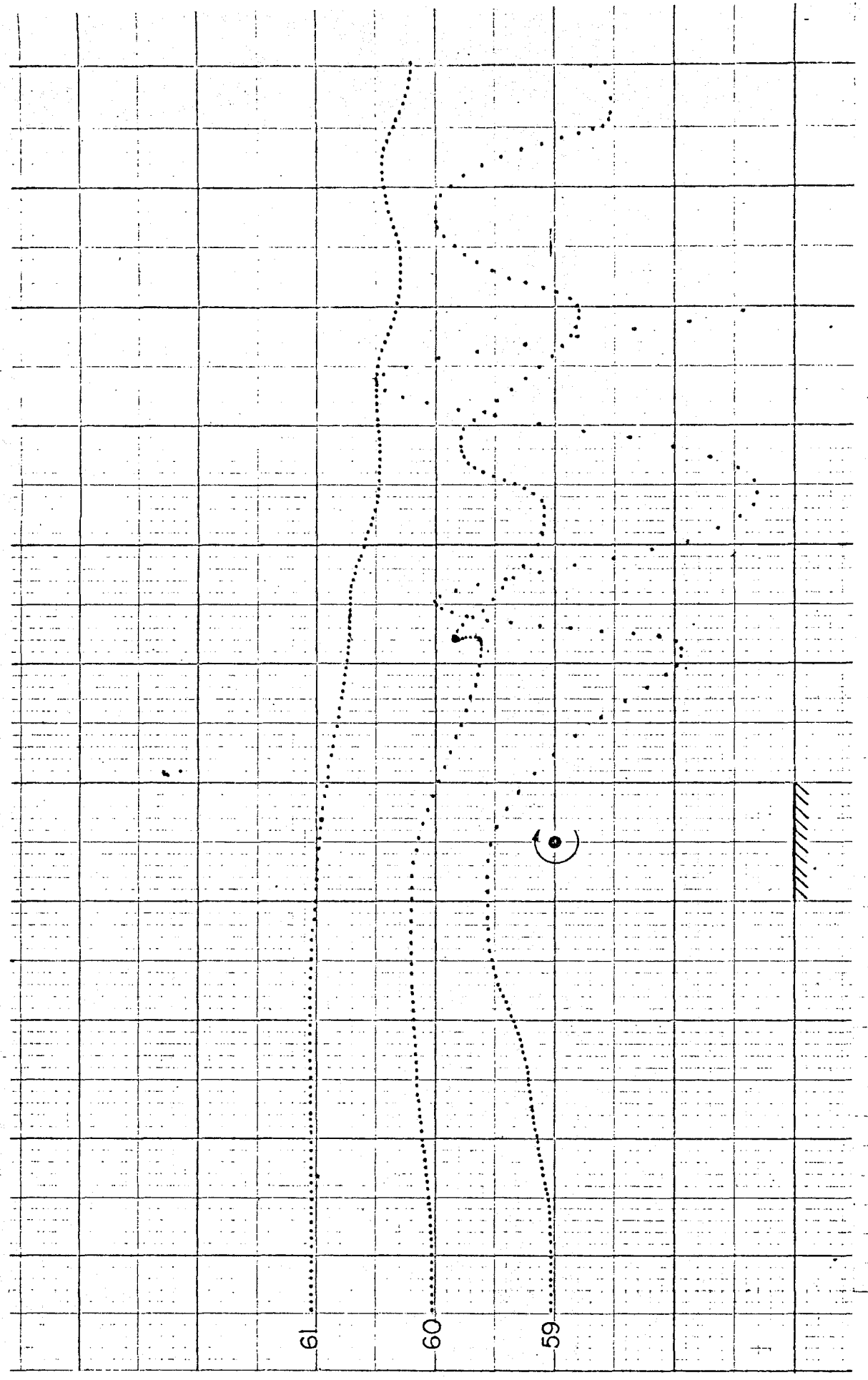
61
60
59

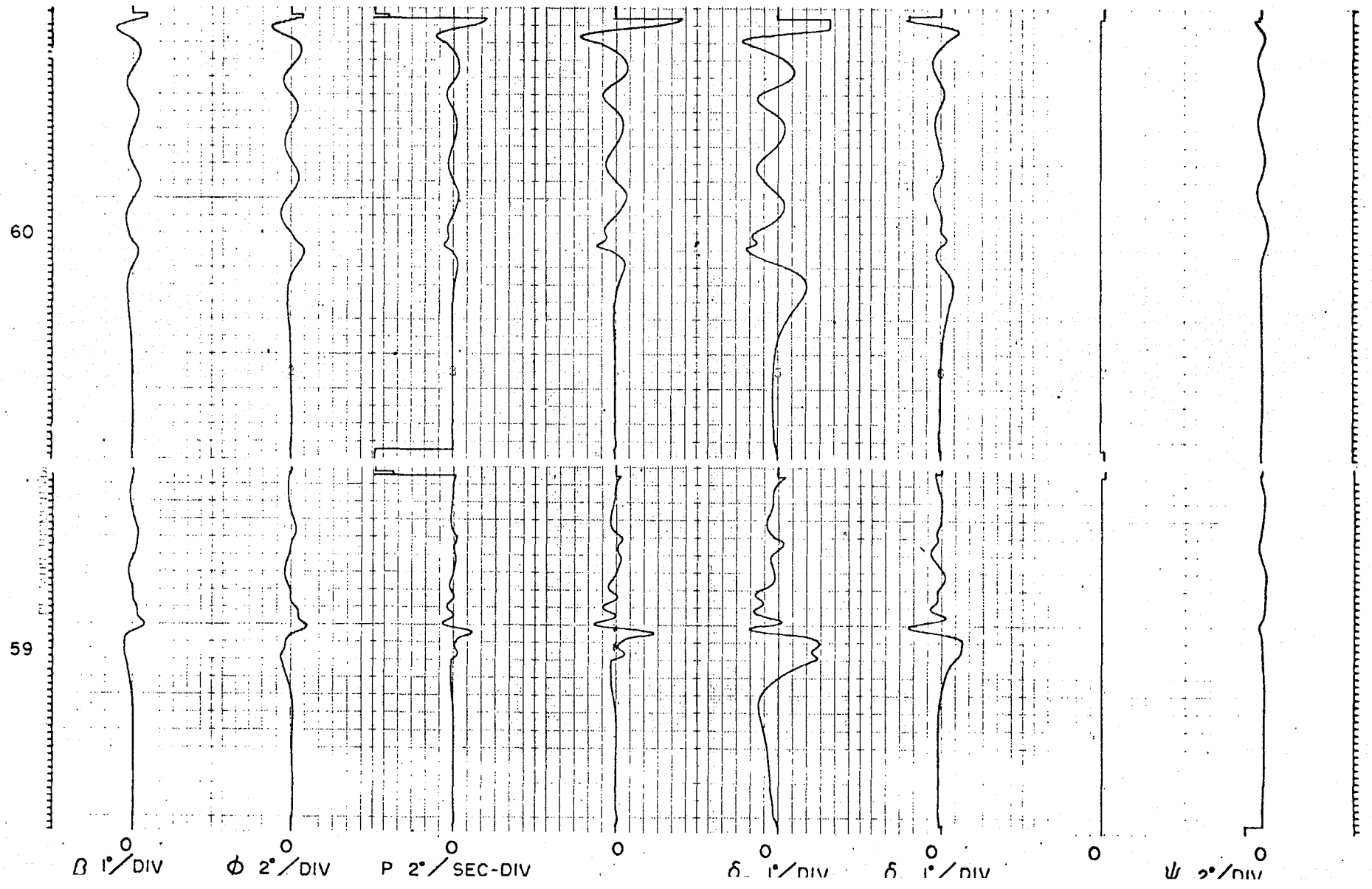
60
59
0
β 1°/DIV
0
Φ 2°/DIV
0
P 2°/SEC-DIV
0
0
δ 1°/DIV
0
δ 1°/DIV
0
0
ψ 2°/DIV

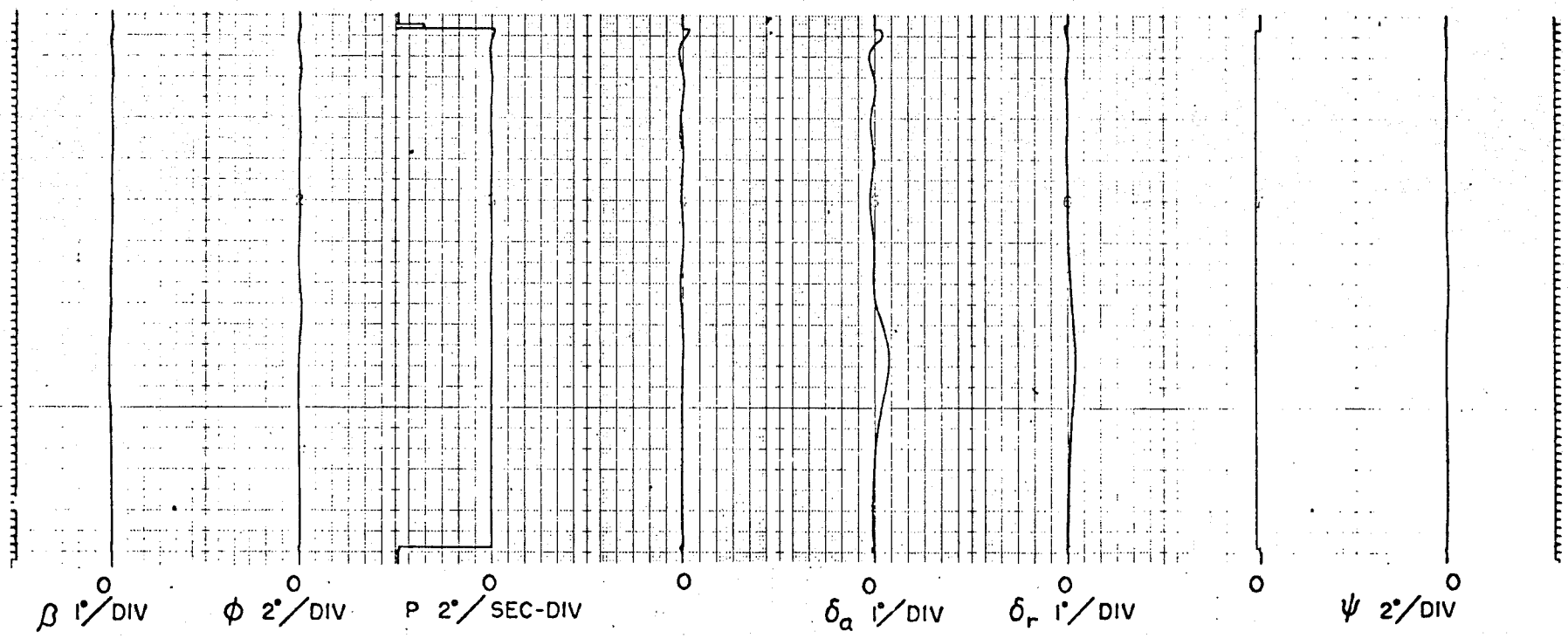
0
β 1°/DIV
0
φ 2°/DIV
0
P 2°/SEC-DIV
0
0
δa 1°/DIV
0
δr 1°/DIV
0
0
ψ 2°/DIV

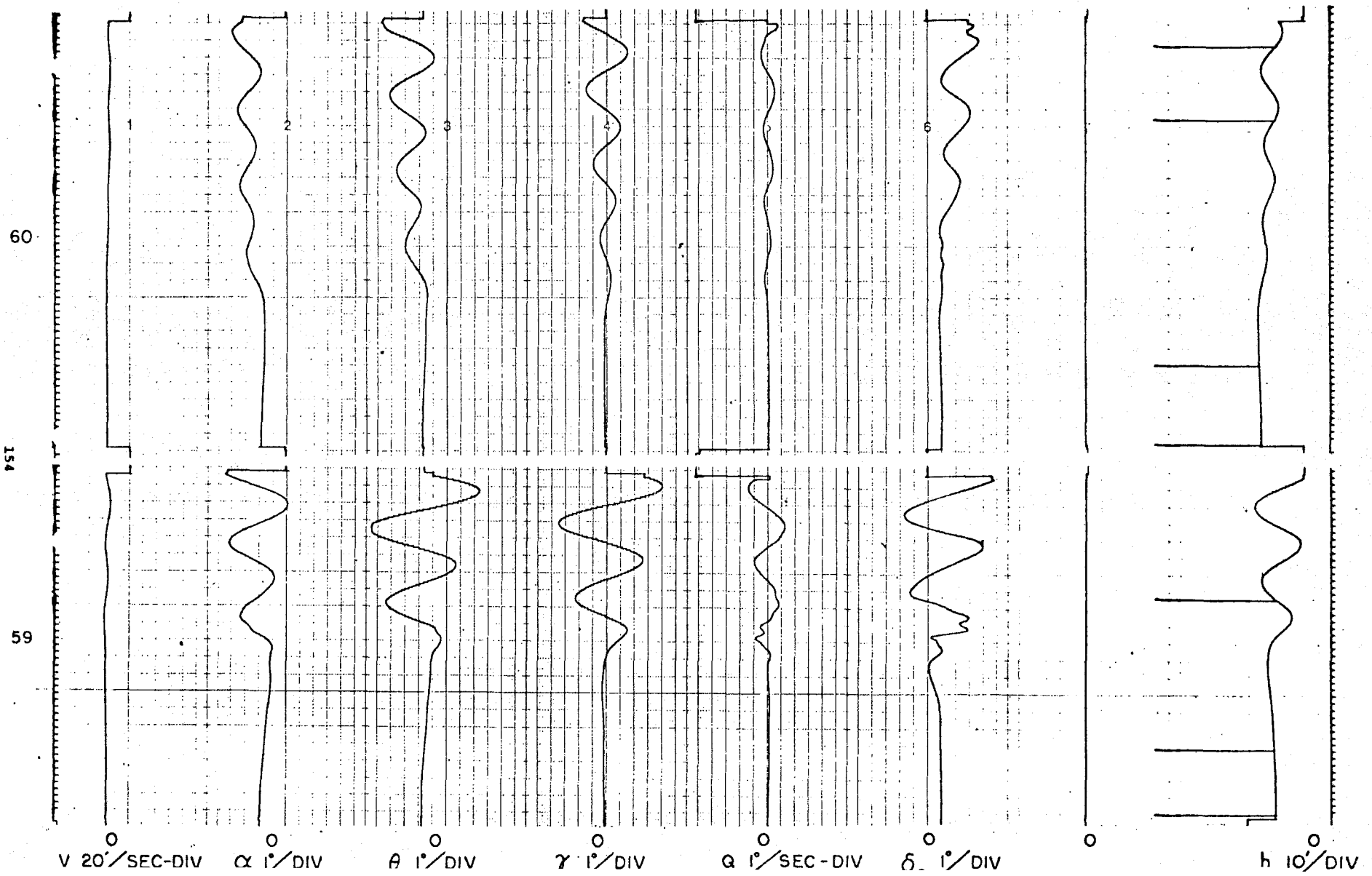
60
59
1
2
3
4
5
6
0
V 20'/SEC-DIV
α 1°/DIV
θ 1°/DIV
γ 1°/DIV
Q 1°/SEC-DIV
δ 1°/DIV
h 10'/DIV

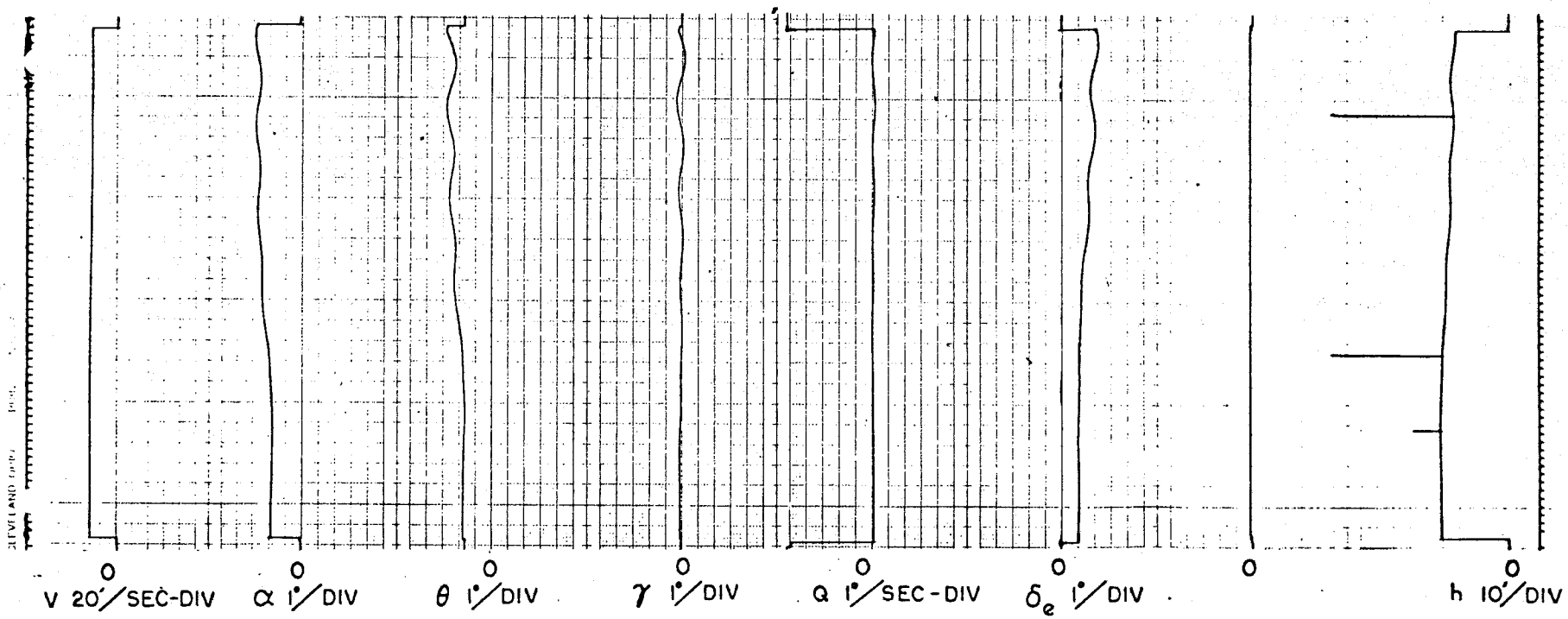
0
V 20'/SEC-DIV
0
α 1°/DIV
0
θ 1°/DIV
0
γ 1°/DIV
0
Q 1°/SEC-DIV
0
δe 1°/DIV
0
0
h 10'/DIV

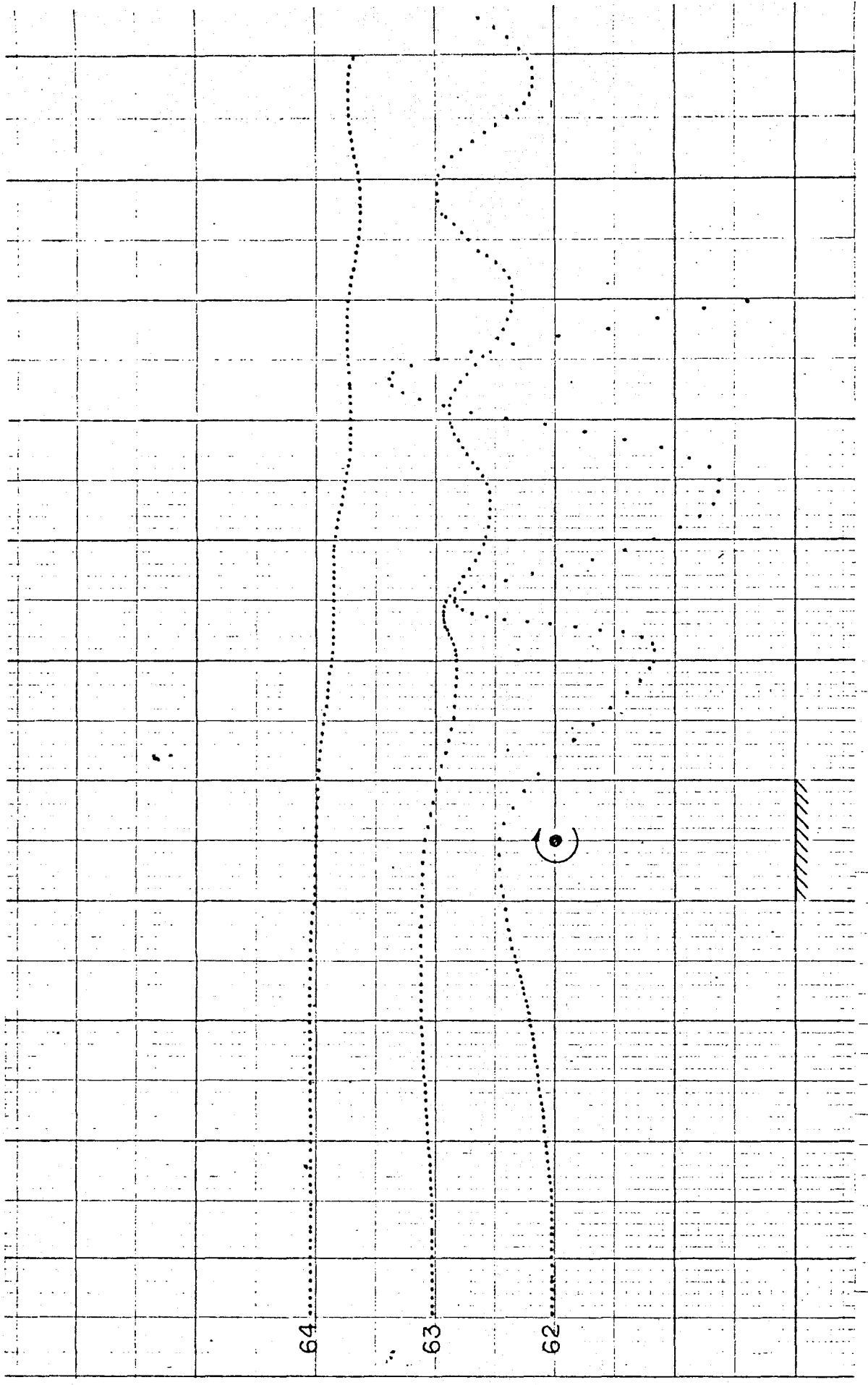
64
63
62

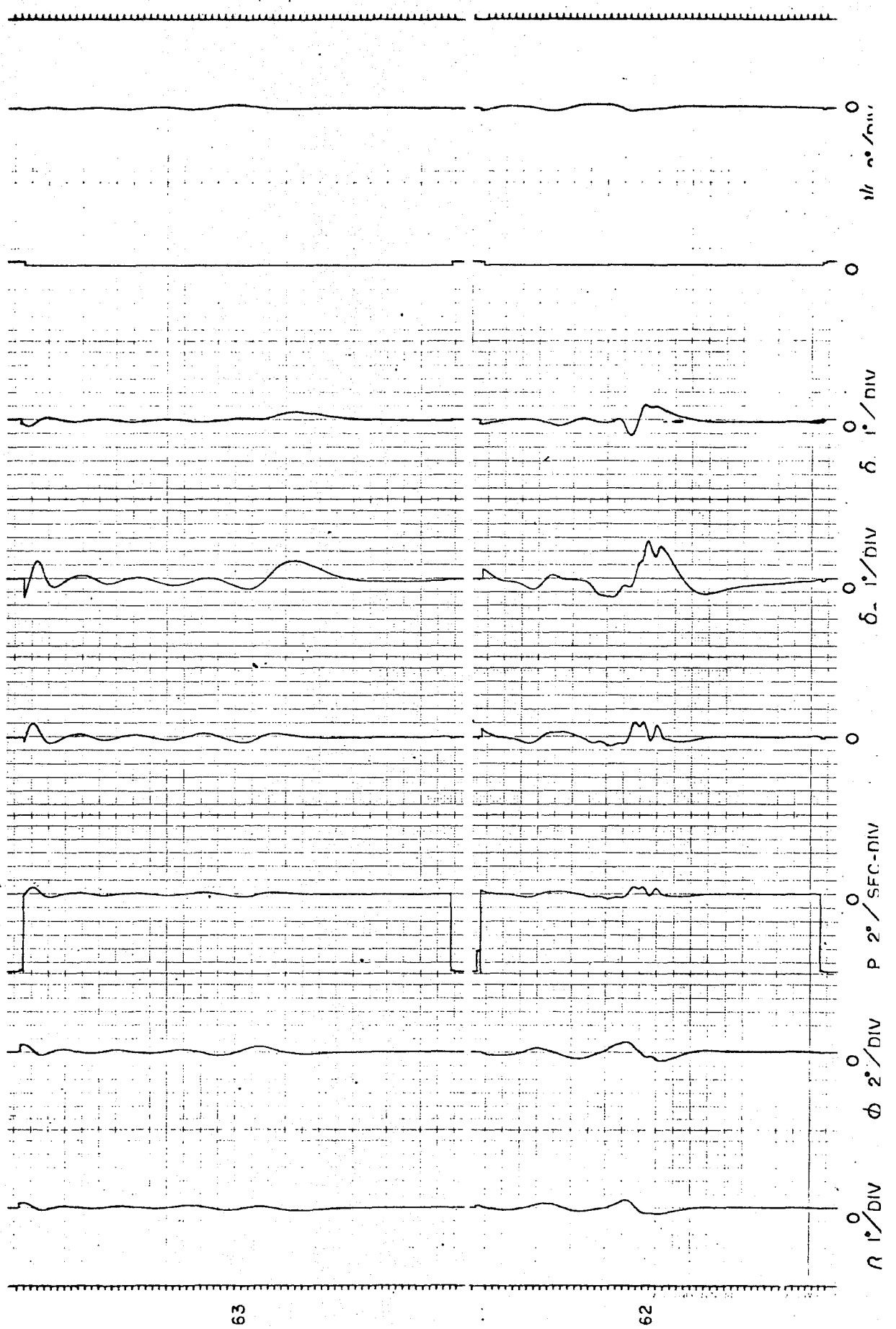
0
0
0
0
0
0
0
0
1°/DIV
1°/DIV
2°/SEC-DIV
2°/DIV
1°/DIV
63
62

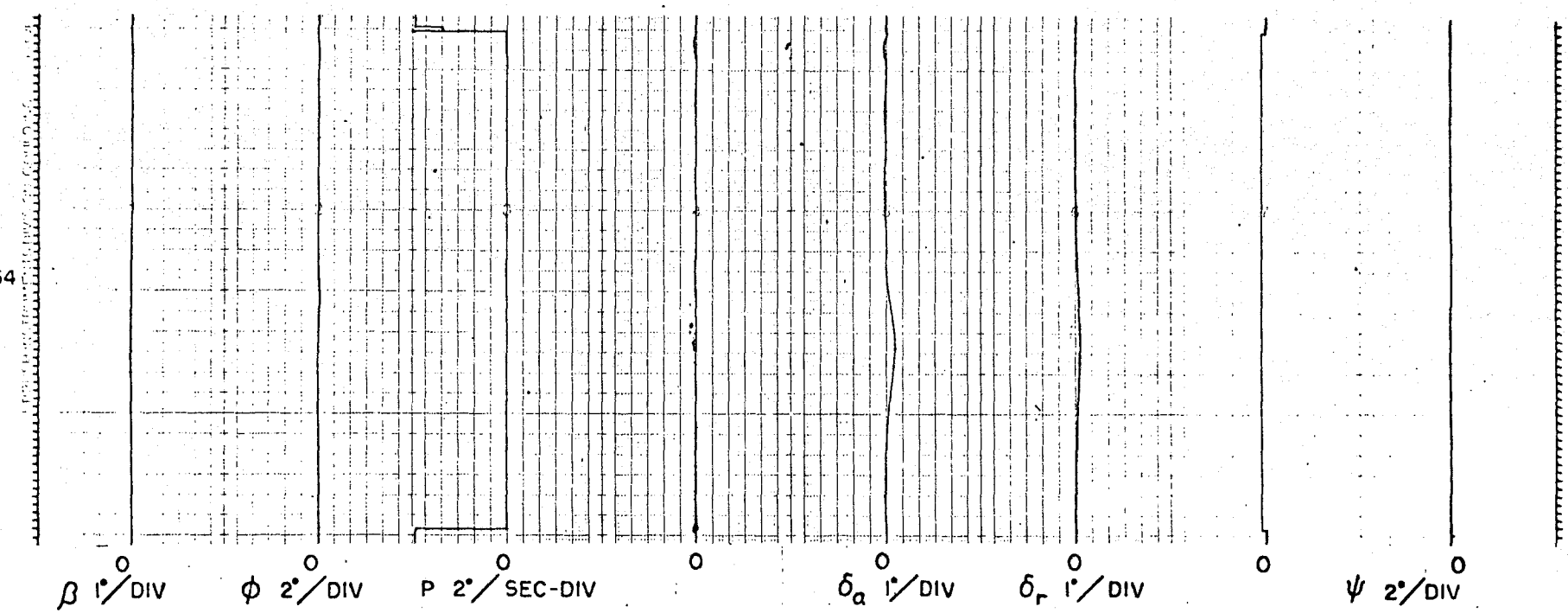
0
β 1°/DIV
0
φ 2°/DIV
0
P 2°/SEC-DIV
0
0
δa 1°/DIV
0
δr 1°/DIV
0
0
ψ 2°/DIV

V 20'/SEC-DIV
63
62

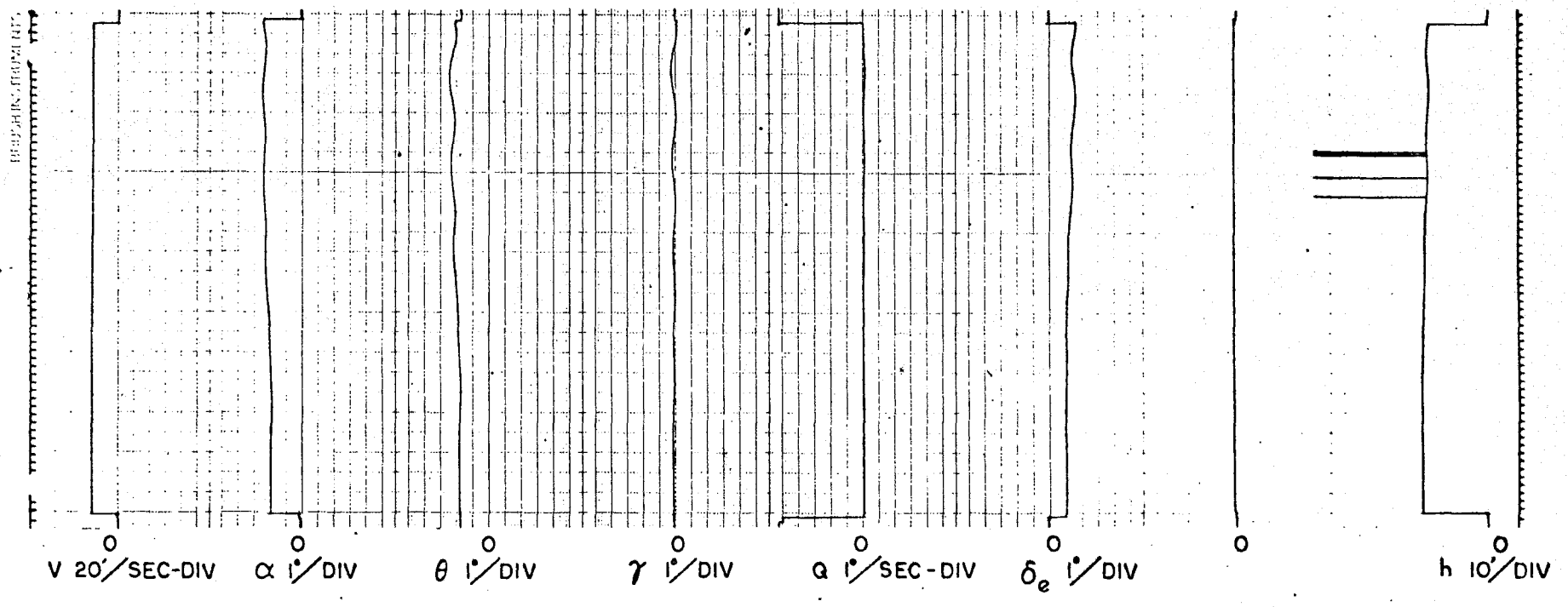
V 20'/SEC-DIV
α 1°/DIV
θ 1°/DIV
γ 1°/DIV
Q 1°/SEC-DIV
δe 1°/DIV
h 10'/DIV
0

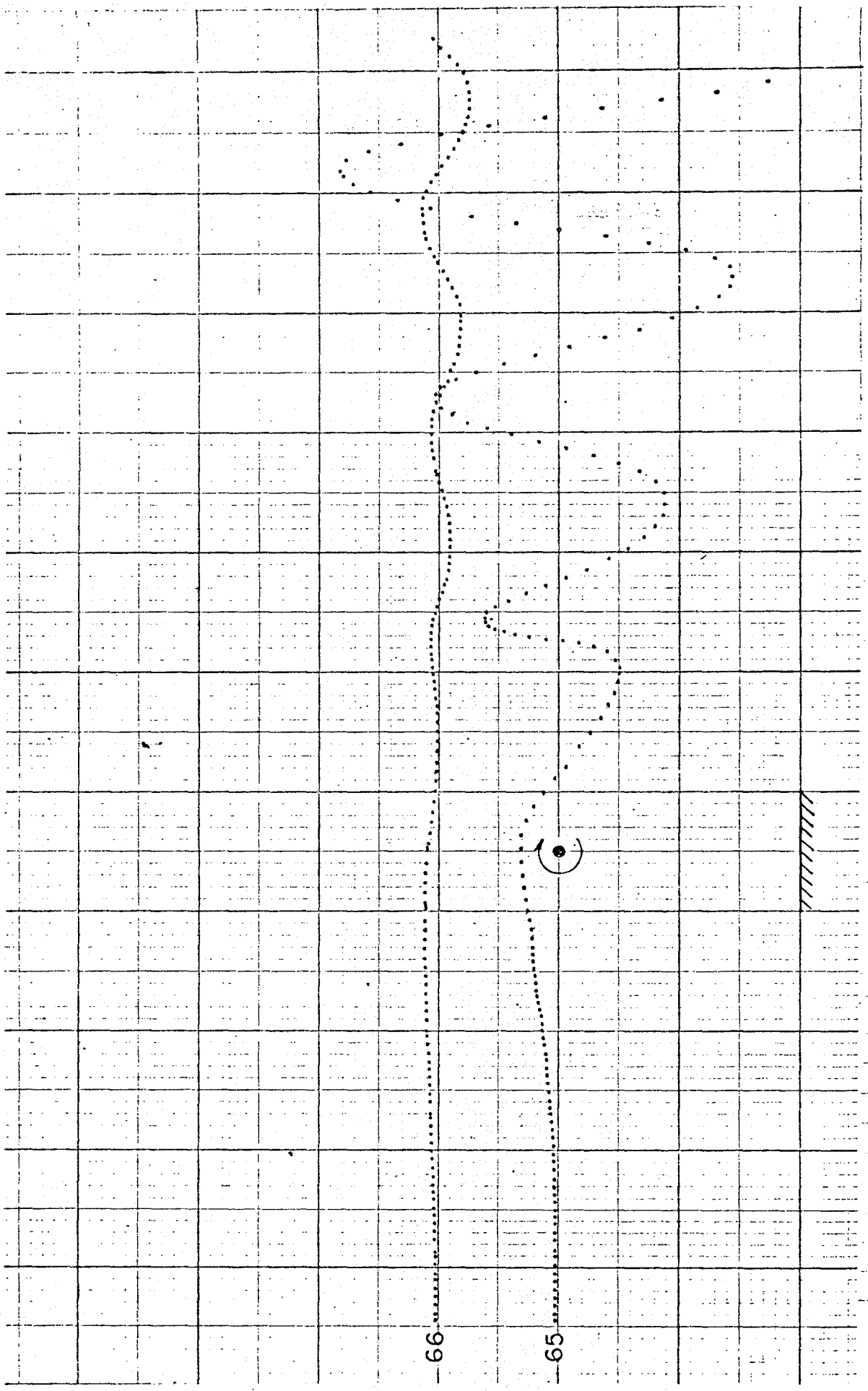
66
65

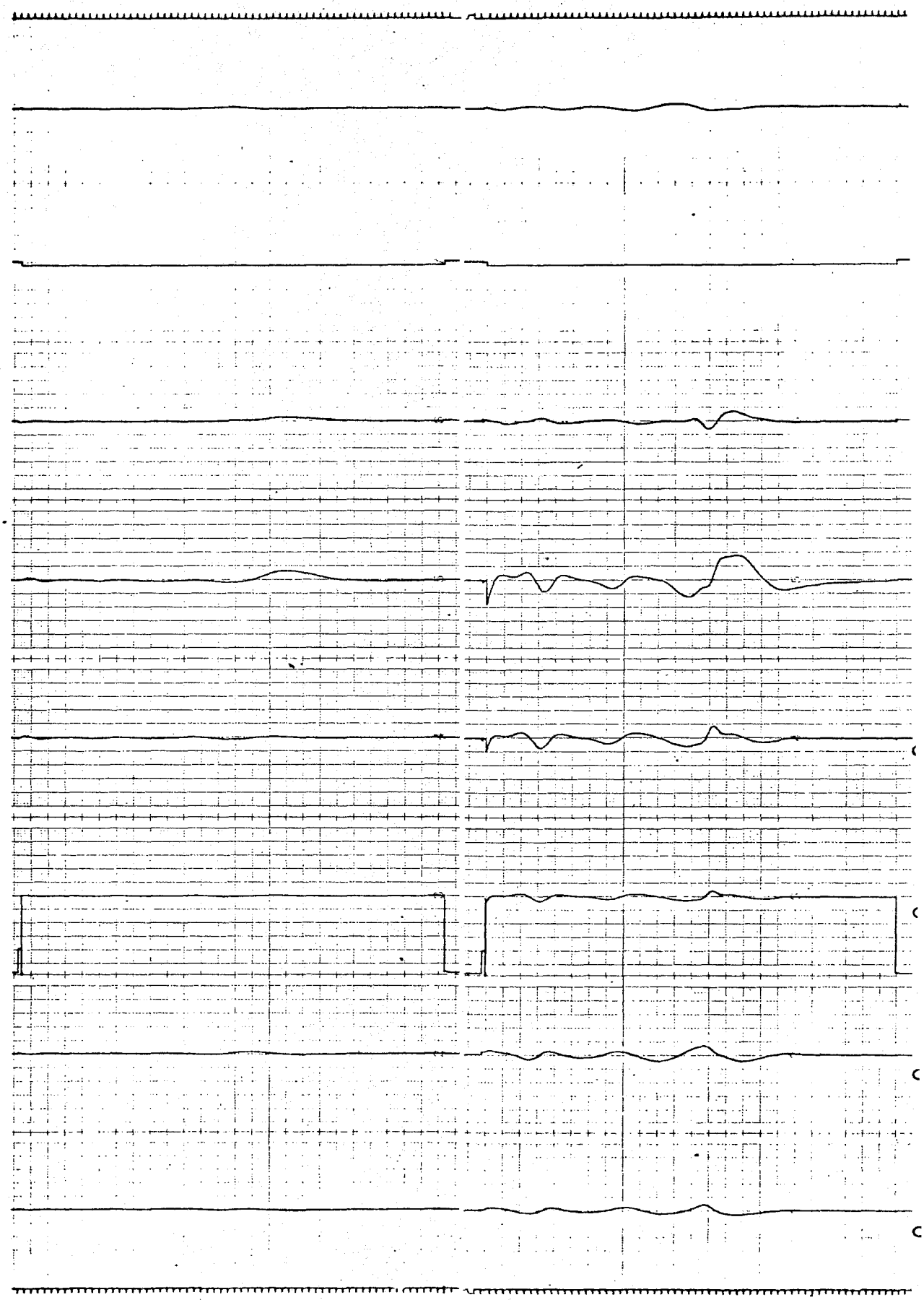
66
65

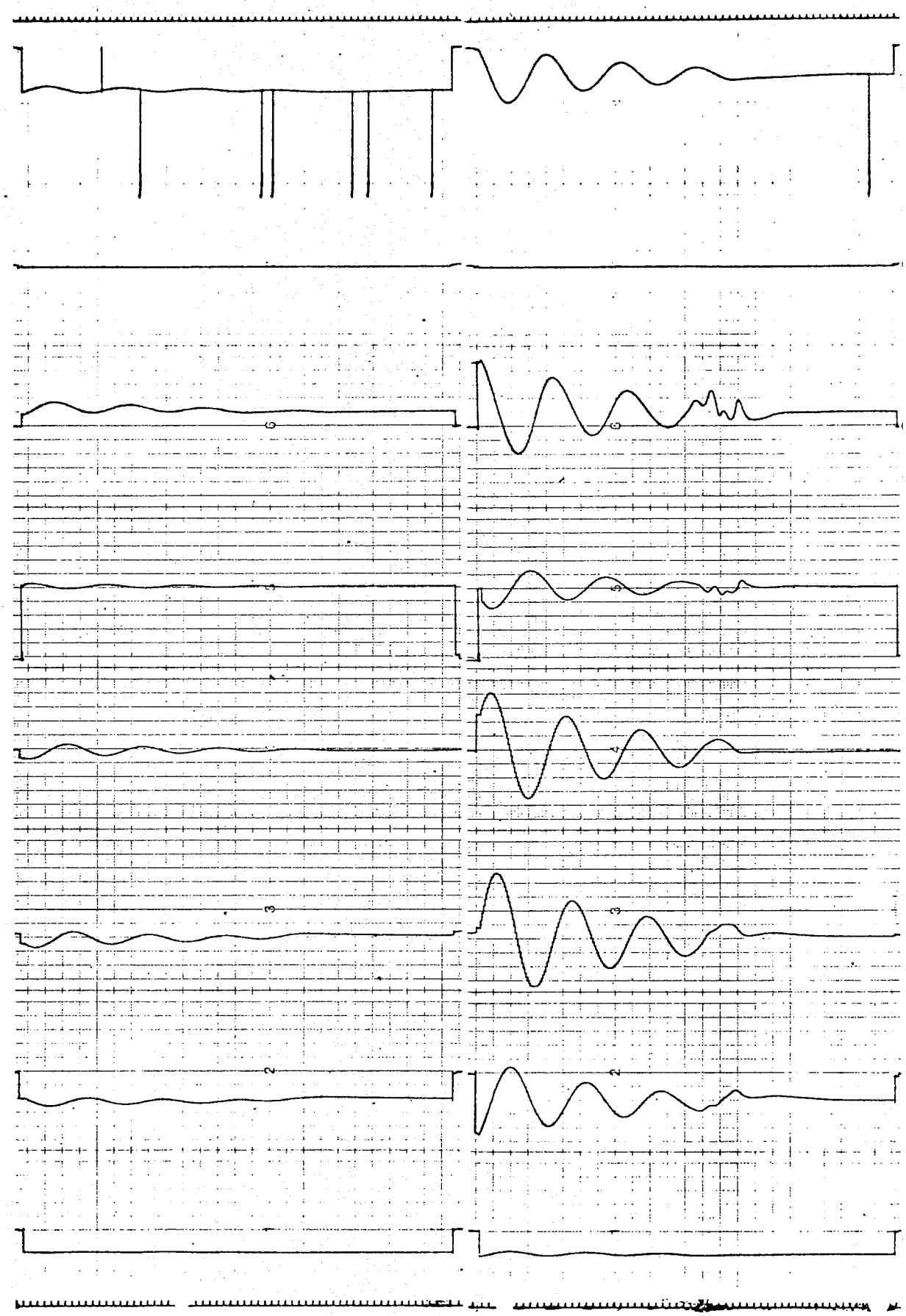
66
65

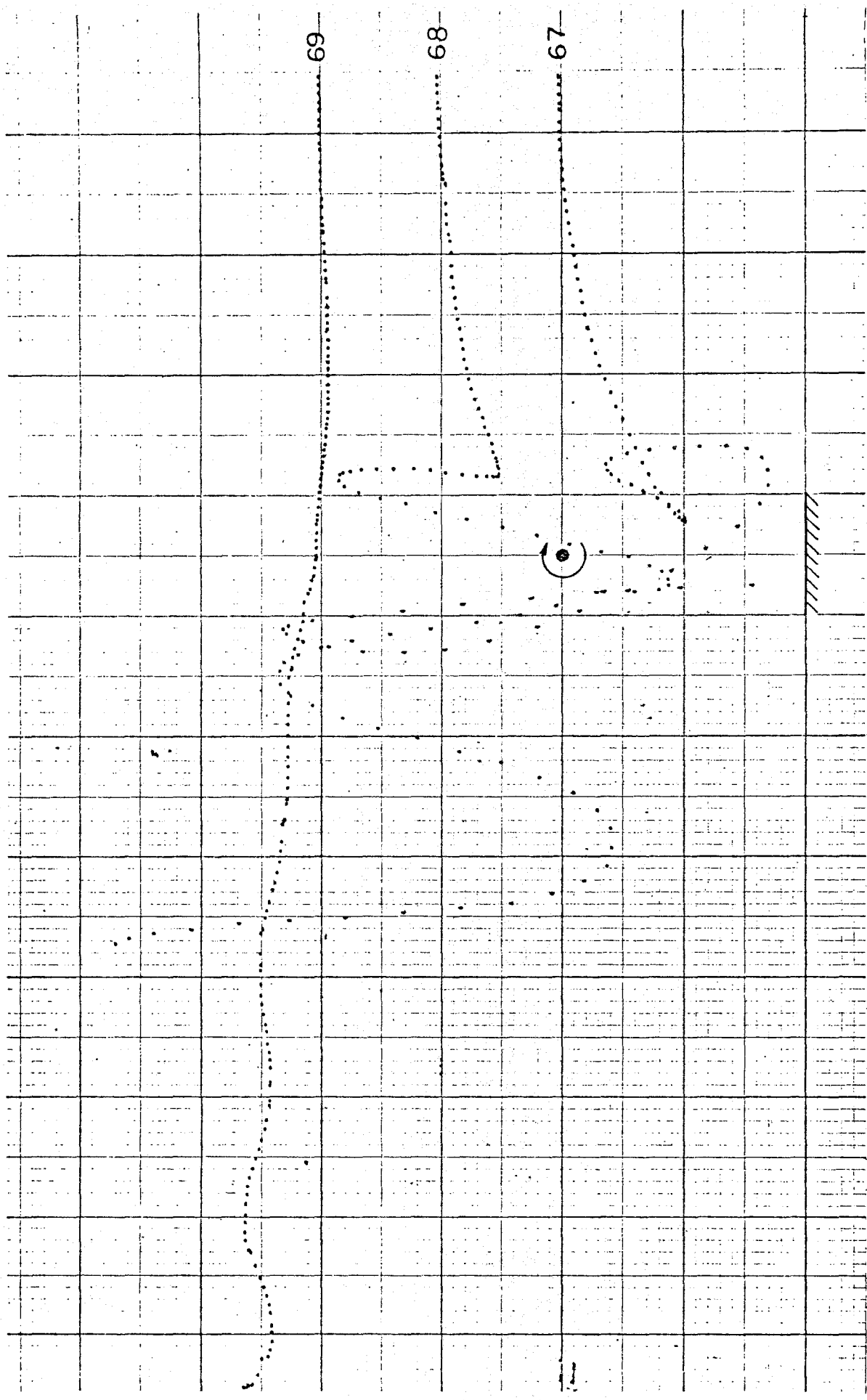
69
68
67

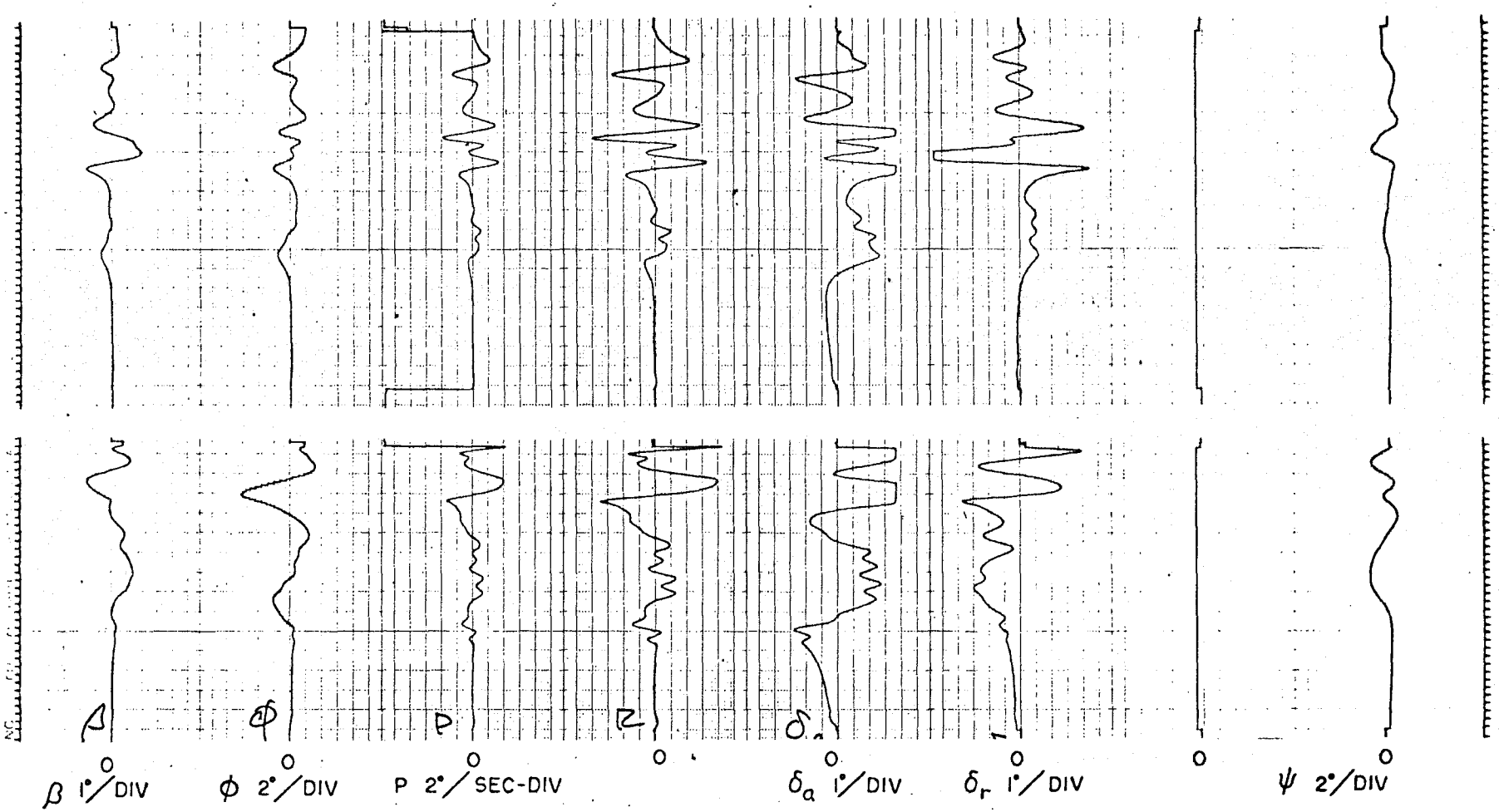
68
67
β
φ
P
R
δa
0
0
0
0
0
0
0
0
β 1°/DIV
φ 2°/DIV
P 2°/SEC-DIV
δa 1°/DIV
δr 1°/DIV
ψ 2°/DIV

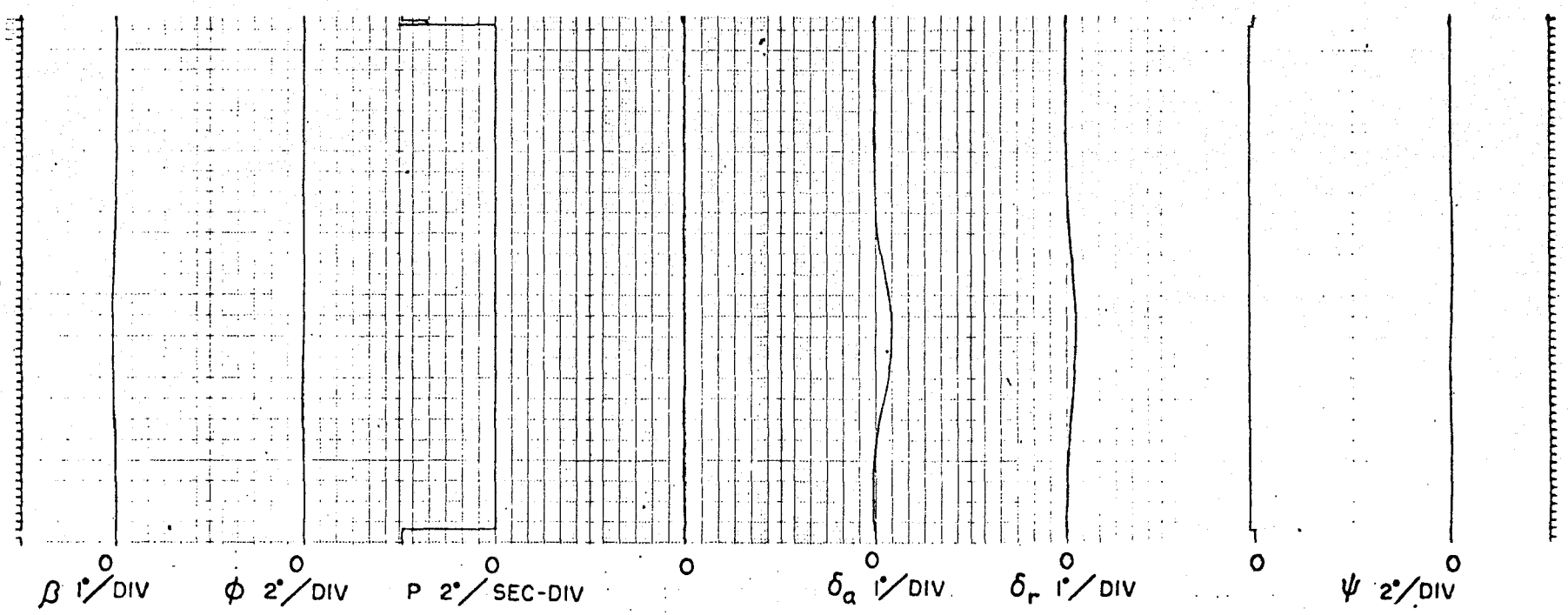
0
β 1°/DIV
0
φ 2°/DIV
0
P 2°/SEC-DIV
0
0
δa 1°/DIV
0
δr 1°/DIV
0
0
ψ 2°/DIV

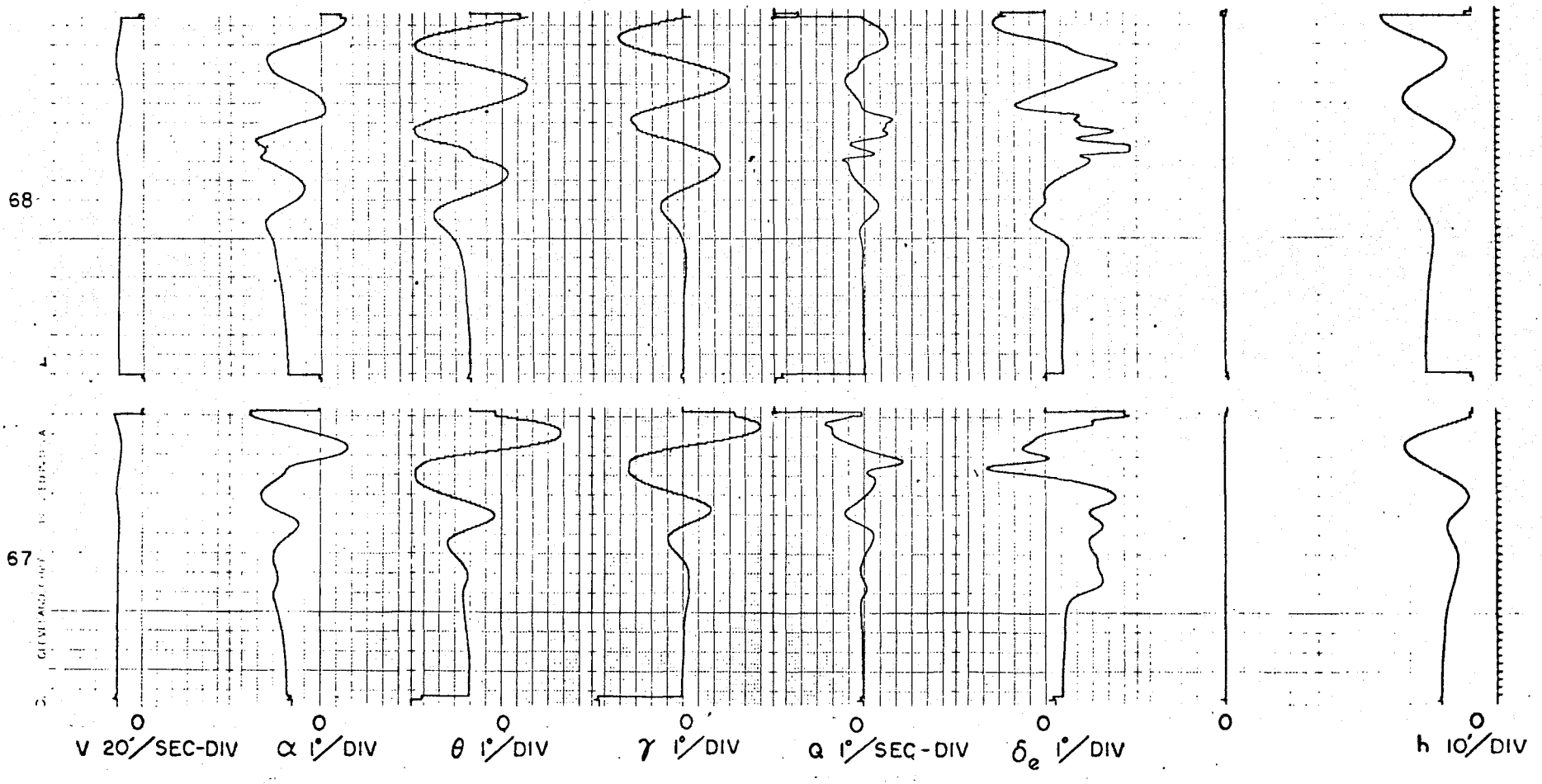
68
67
0
V 20'/SEC-DIV
0
α 1°/DIV
0
θ 1°/DIV
0
γ 1°/DIV
0
Q 1°/SEC-DIV
0
δe 1°/DIV
0
0
h 10'/DIV

h 10'/DIV
0
0
δ_e 1°/DIV
0
Q 1°/SEC-DIV
0
γ 1°/DIV
0
θ 1°/DIV
0
α 1°/DIV
0
V 20'/SEC-DIV
0

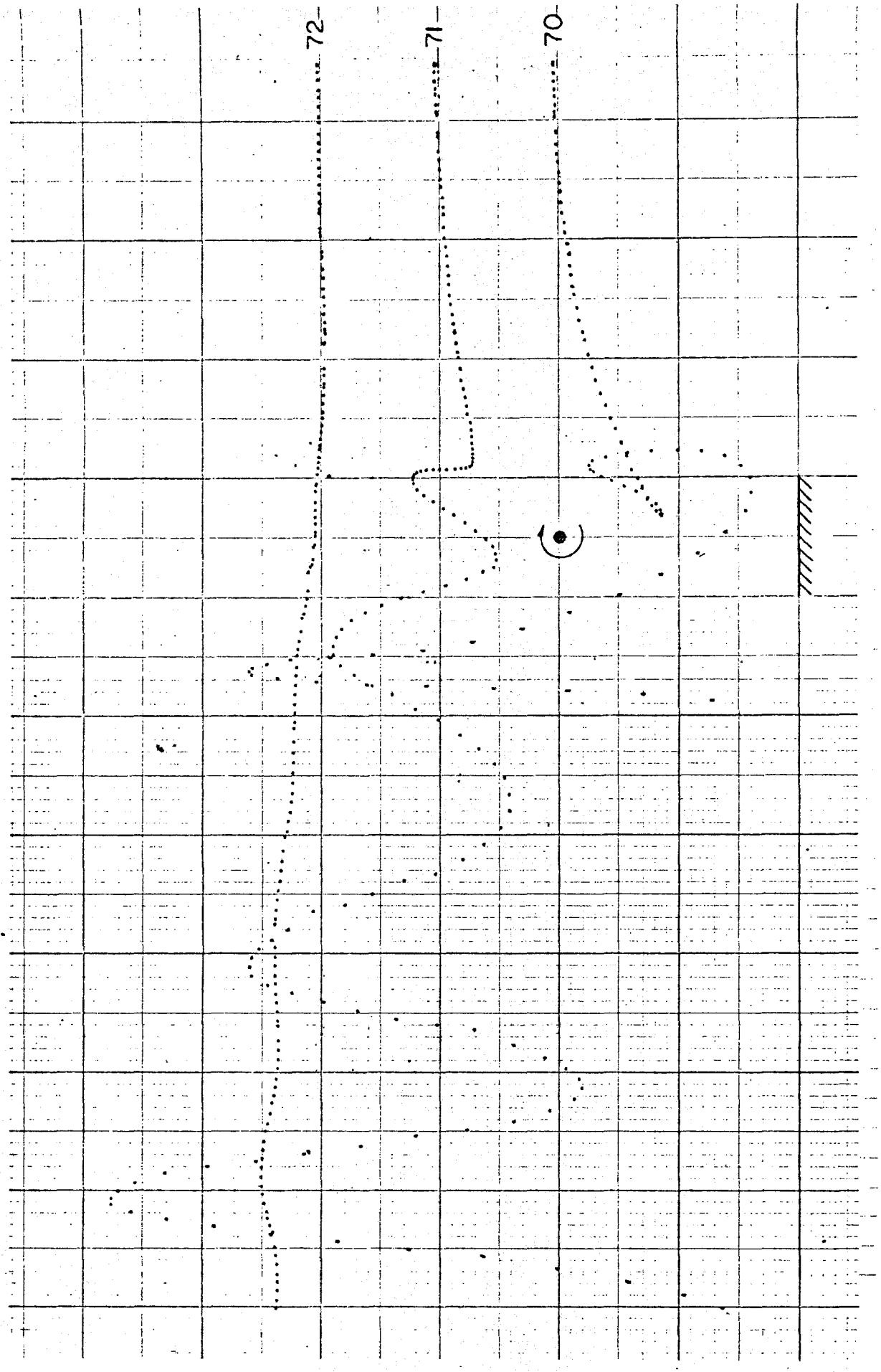
72
71
70

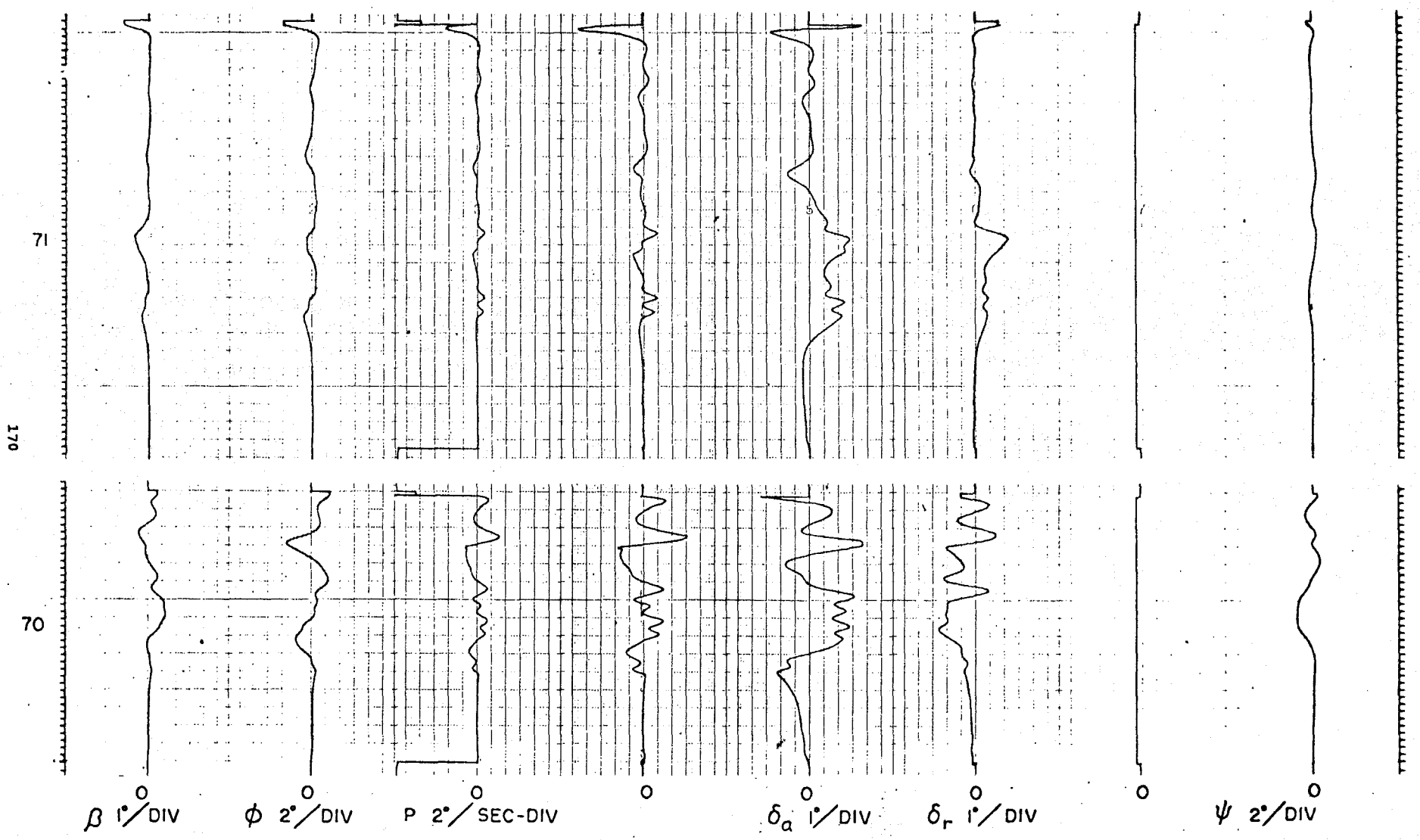
71
70
0
0
0
0
0
0
0
β 1°/DIV
φ 2°/DIV
P 2°/SEC-DIV
δa 1°/DIV
δr 1°/DIV
ψ 2°/DIV

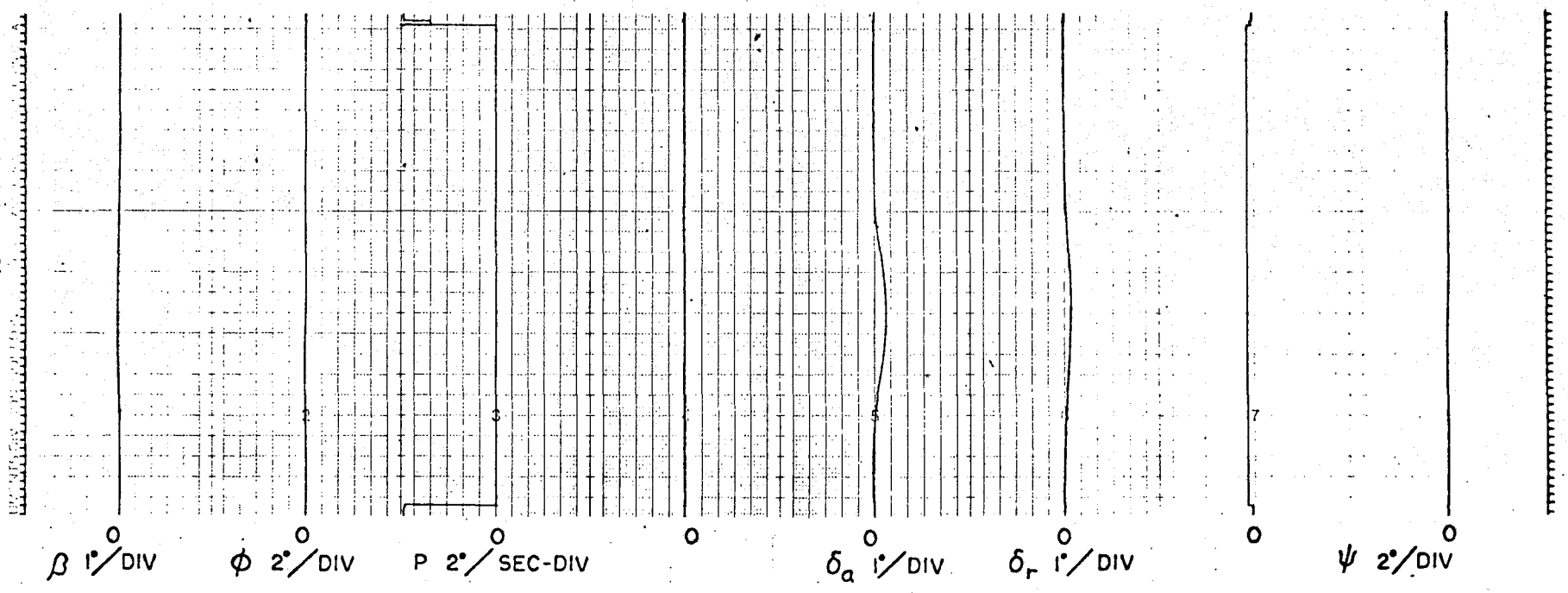
72
0
β 1°/DIV
0
φ 2°/DIV
0
P 2°/SEC-DIV
0
0
δa 1°/DIV
0
δr 1°/DIV
0
0
ψ 2°/DIV

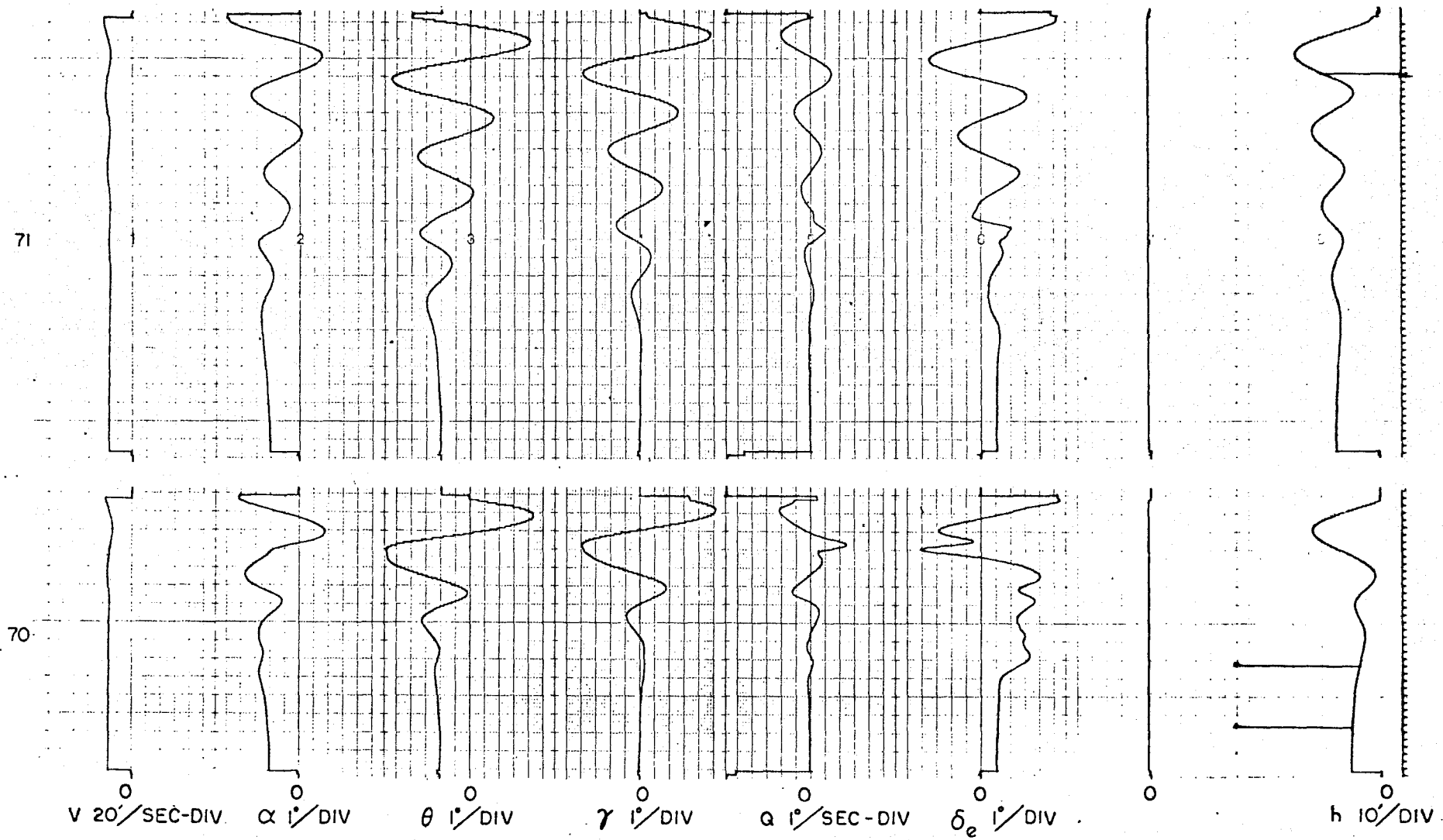
71
70
1
2
3
4
5
6
0
V 20'/SEC-DIV
0
α 1°/DIV
0
θ 1°/DIV
0
γ 1°/DIV
0
Q 1°/SEC-DIV
0
δe 1°/DIV
0
0
h 10'/DIV

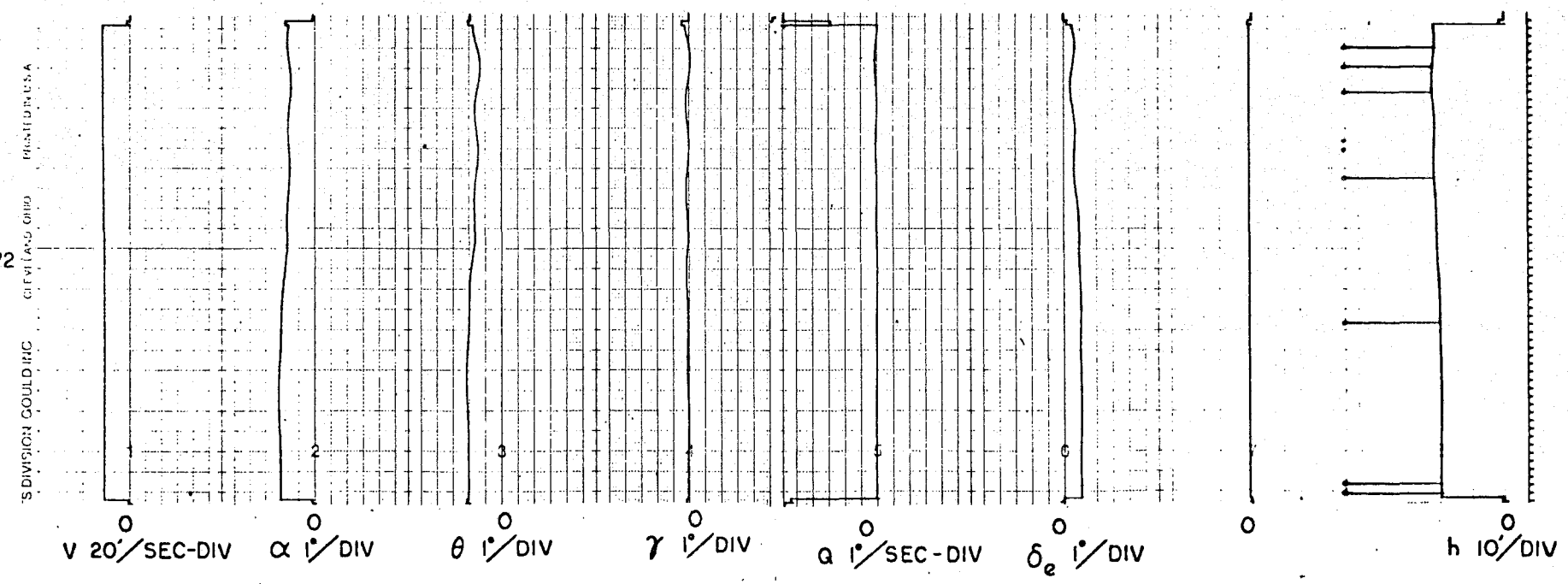
72
0
V 20'/SEC-DIV
0
α 1°/DIV
0
θ 1°/DIV
0
γ 1°/DIV
0
Q 1°/SEC-DIV
0
δe 1°/DIV
0
0
h 10'/DIV

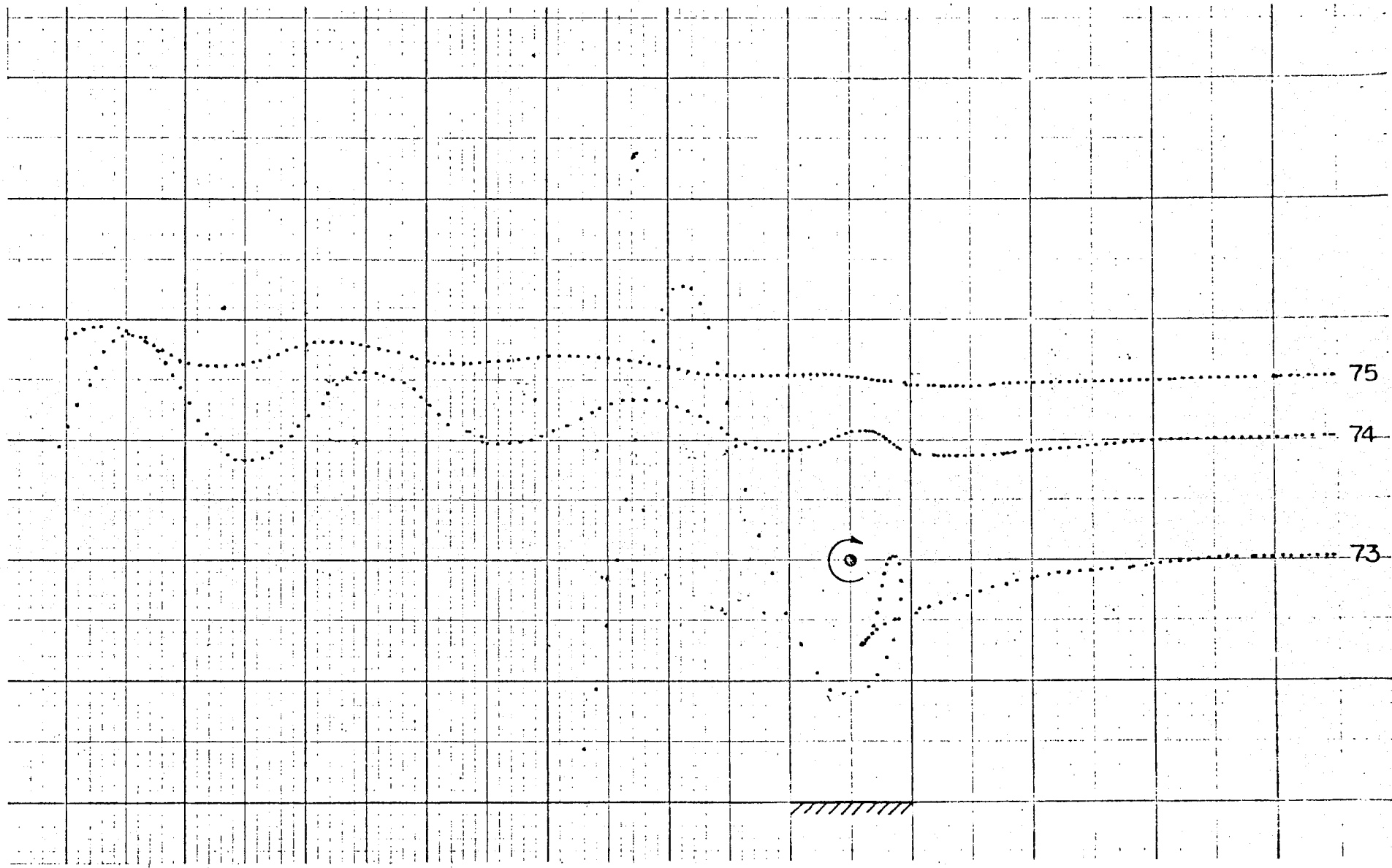
75
74
73

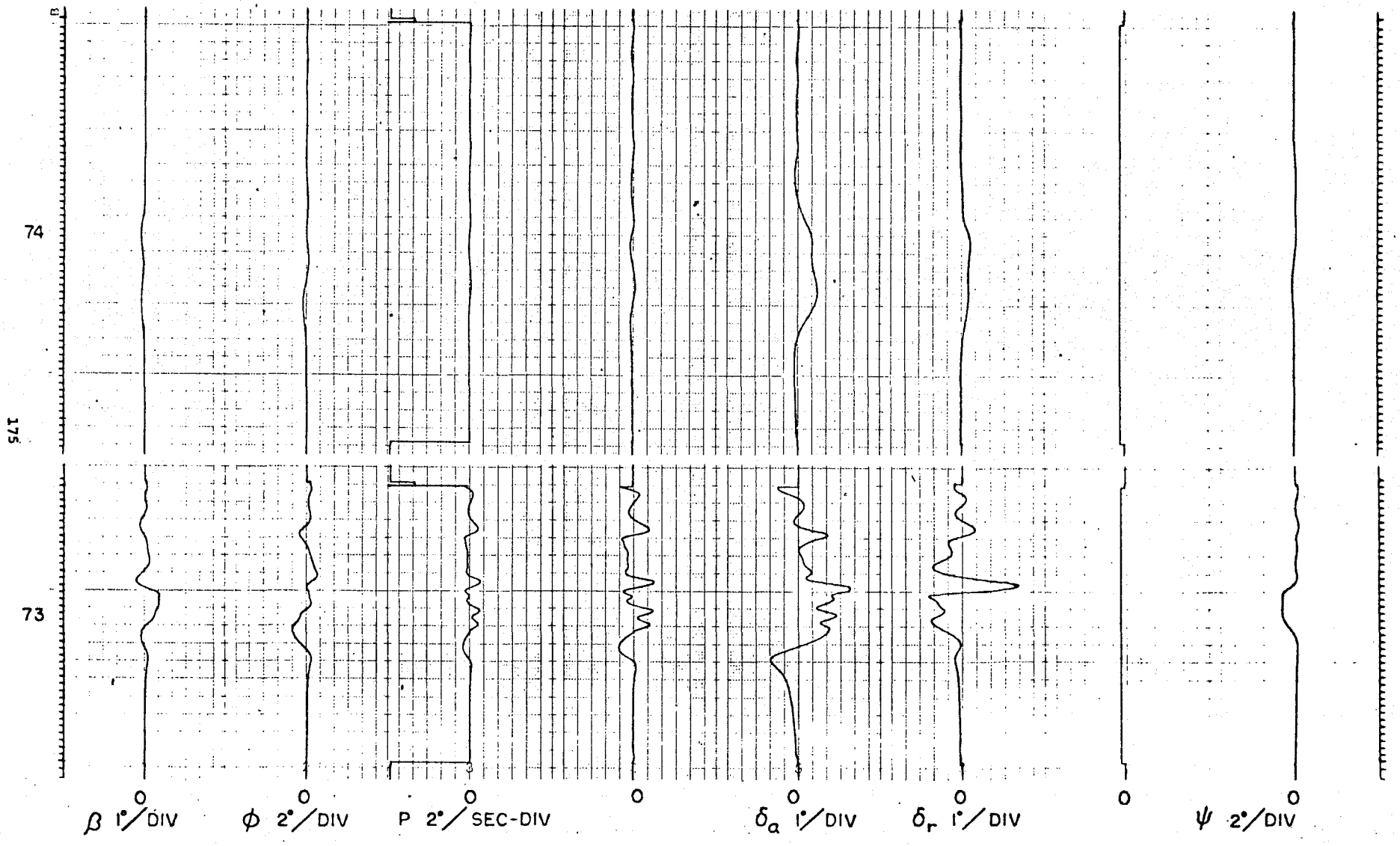
74
73
0
0
0
0
0
0
0
0
β 1°/DIV
φ 2°/DIV
P 2°/SEC-DIV
δa 1°/DIV
δr 1°/DIV
ψ 2°/DIV

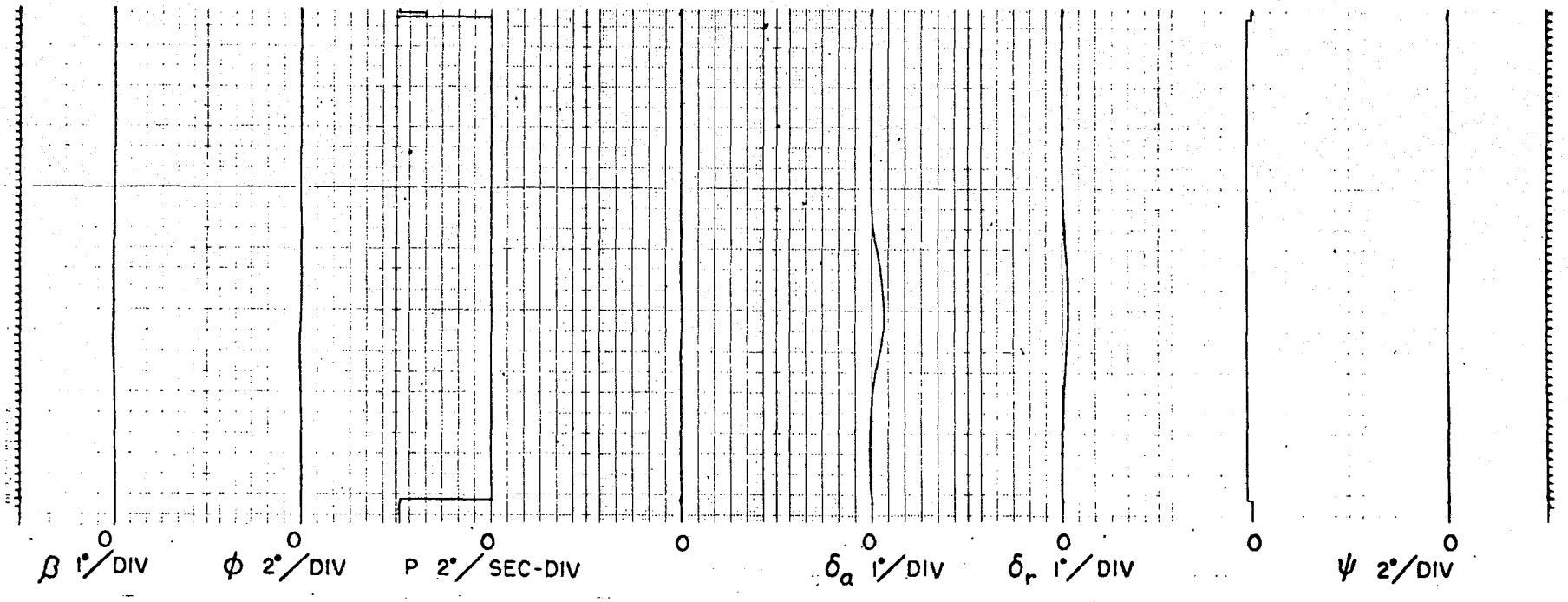
75
0
β 1°/DIV
0
φ 2°/DIV
0
P 2°/SEC-DIV
0
0
δa 1°/DIV
0
δr 1°/DIV
0
0
ψ 2°/DIV

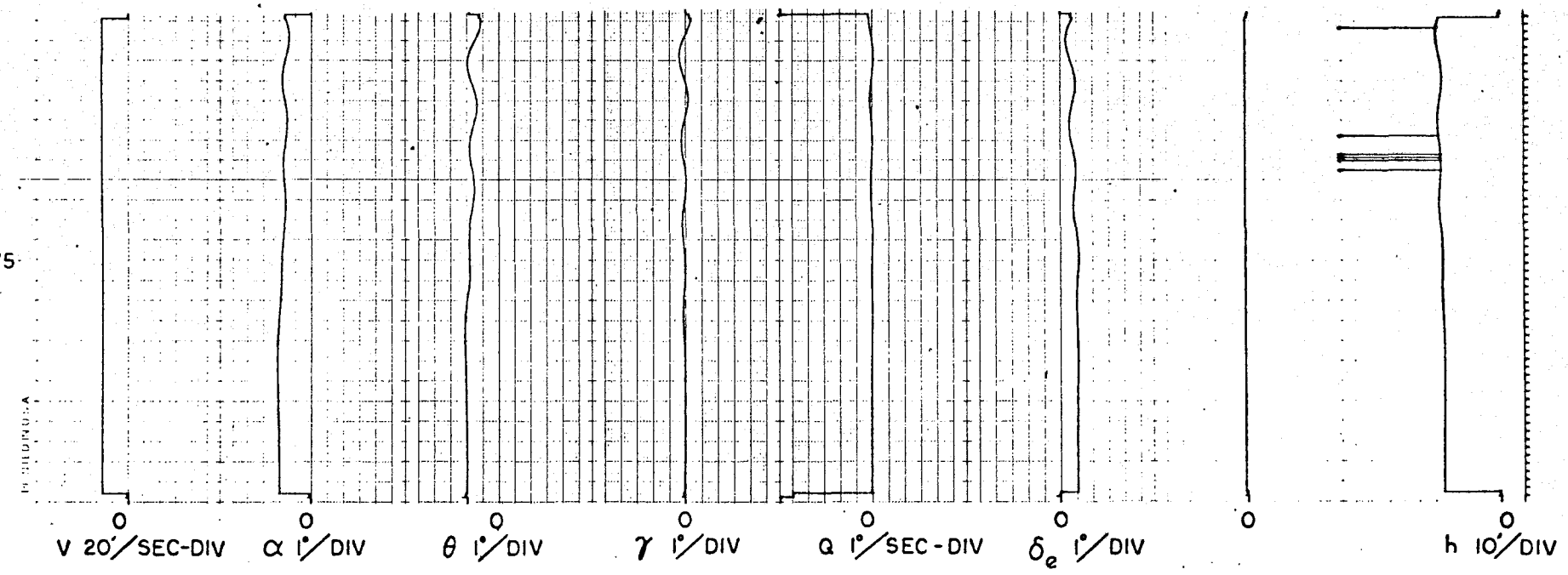
0
V 20'/SEC-DIV
0
α 1°/DIV
0
θ 1°/DIV
0
γ 1°/DIV
0
Q 1°/SEC-DIV
0
δe 1°/DIV
0
0
h 10'/DIV

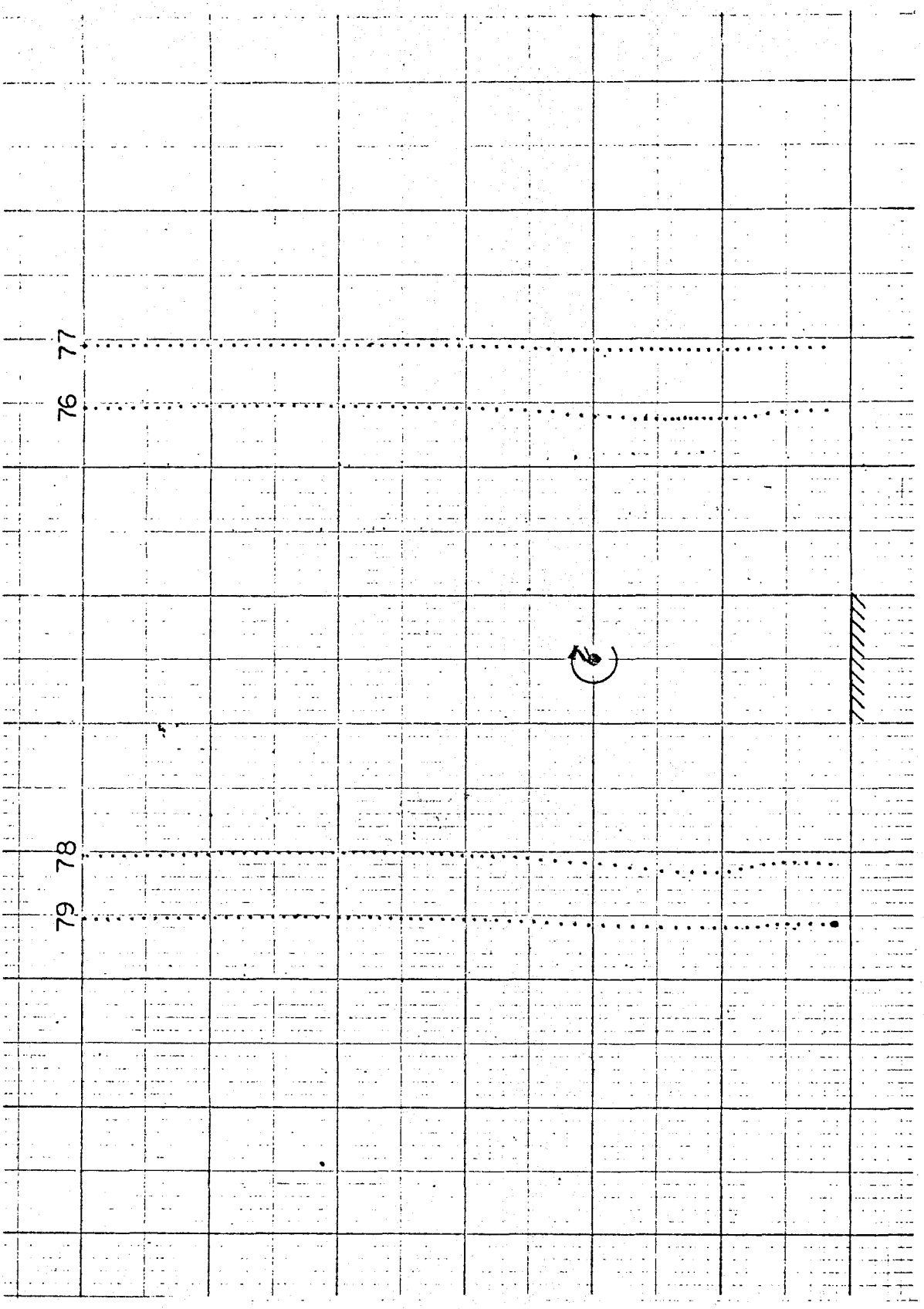
77
76
78
79

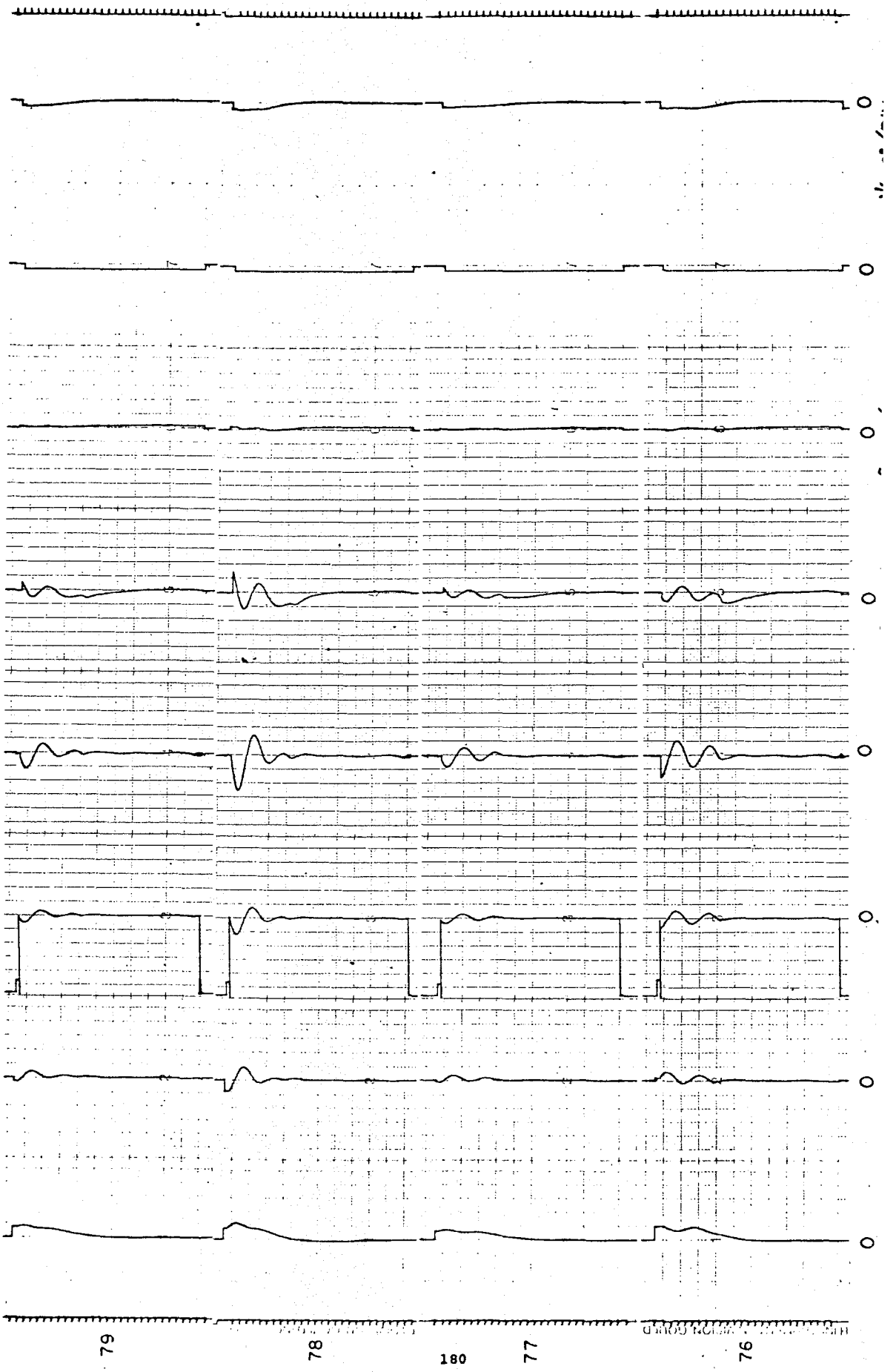
0
0
0
0
0
0
0
0
79
78
180
77
76

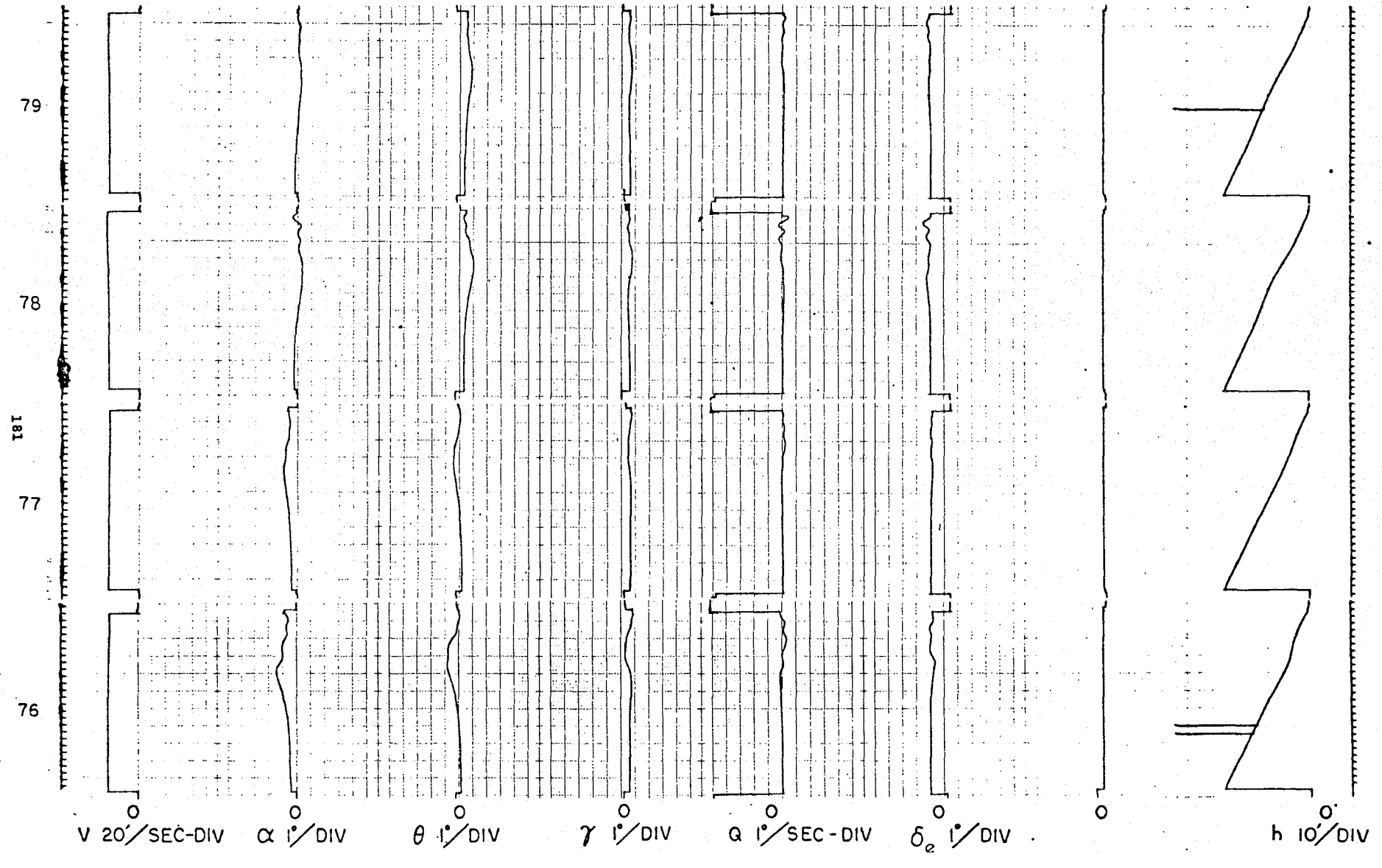
79
78
77
76
0
V 20′/SEC-DIV
0
α 1°/DIV
0
θ 1°/DIV
0
γ 1°/DIV
0
Q 1°/SEC-DIV
0
δe 1°/DIV
0
0°
h 10′/DIV

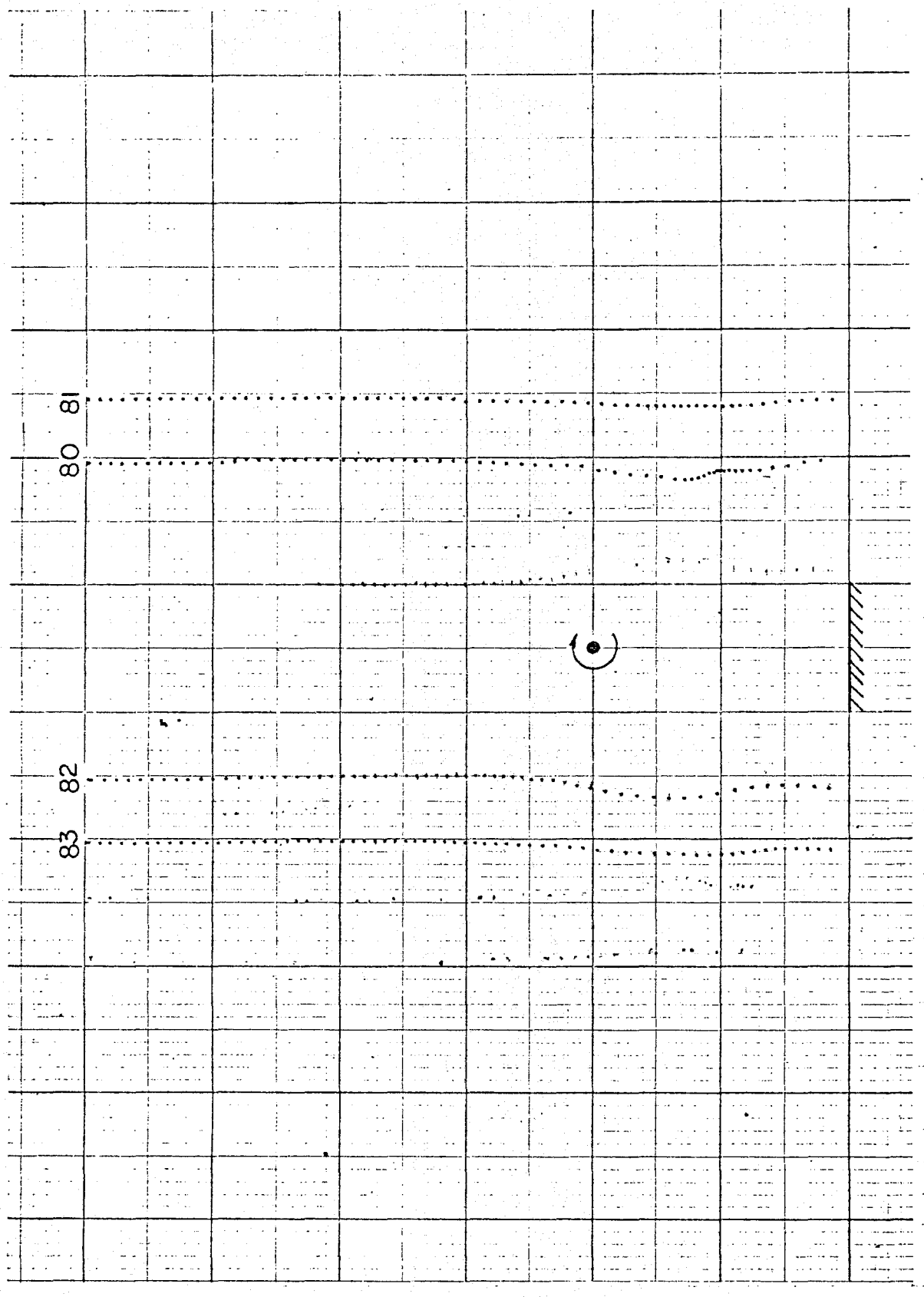
81
80
82
83

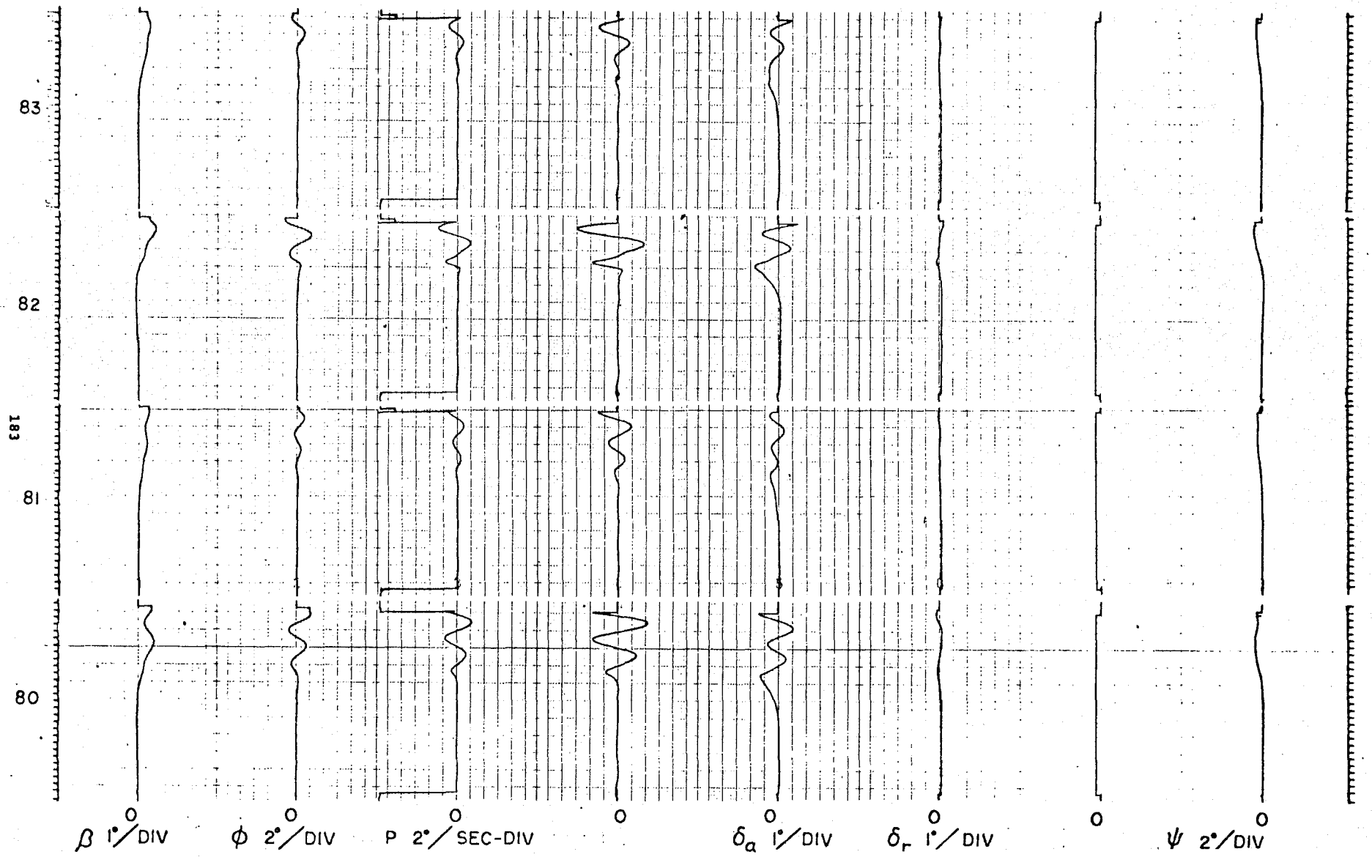
83
82
81
80
0
β 1°/DIV
0
φ 2°/DIV
0
P 2°/SEC-DIV
0
0
δa 1°/DIV
0
δr 1°/DIV
0
0
ψ 2°/DIV

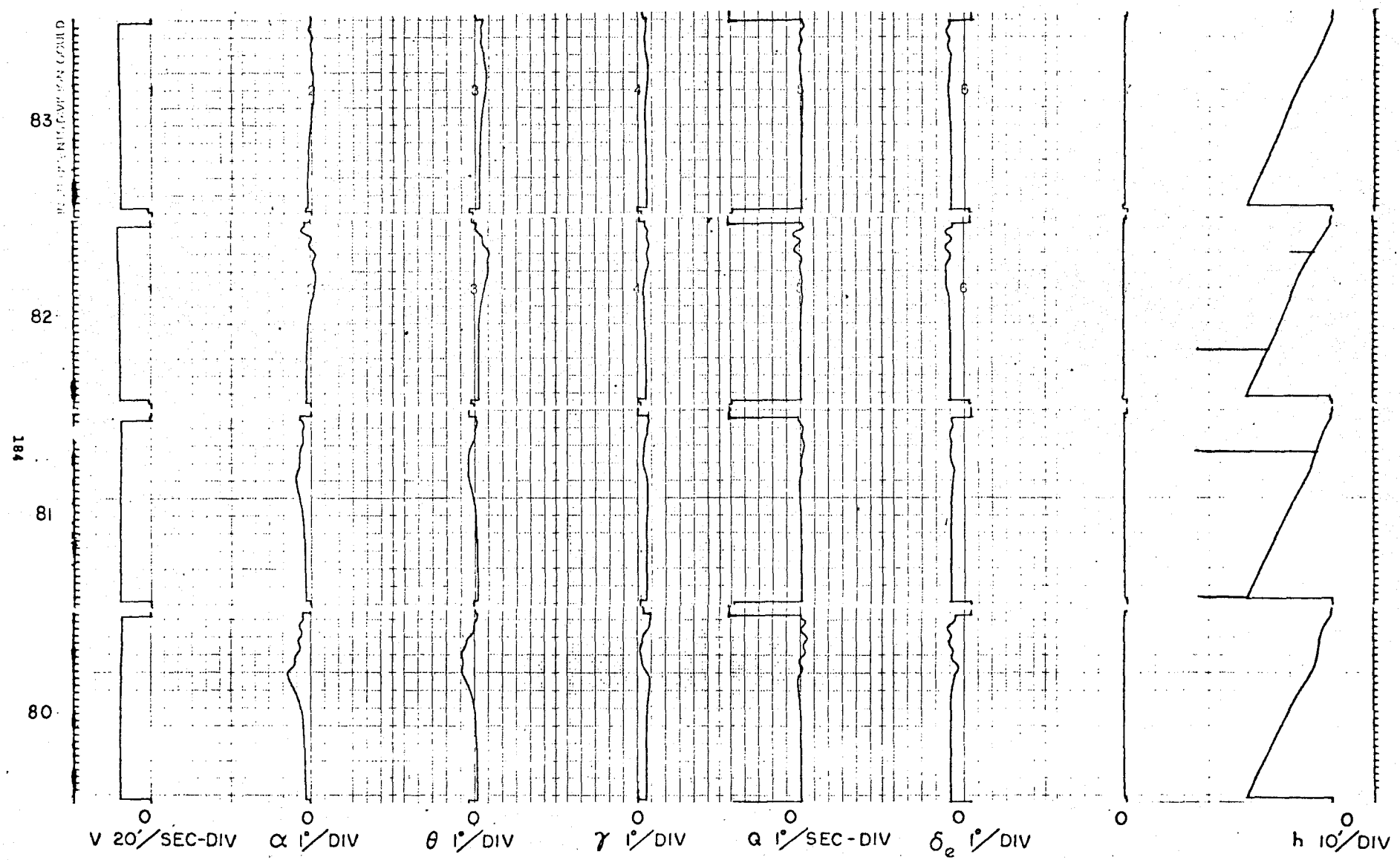
83
82
81
80
V 20'/SEC-DIV
α 1°/DIV
θ 1°/DIV
γ 1°/DIV
Q 1°/SEC-DIV
δe 1°/DIV
h 10'/DIV

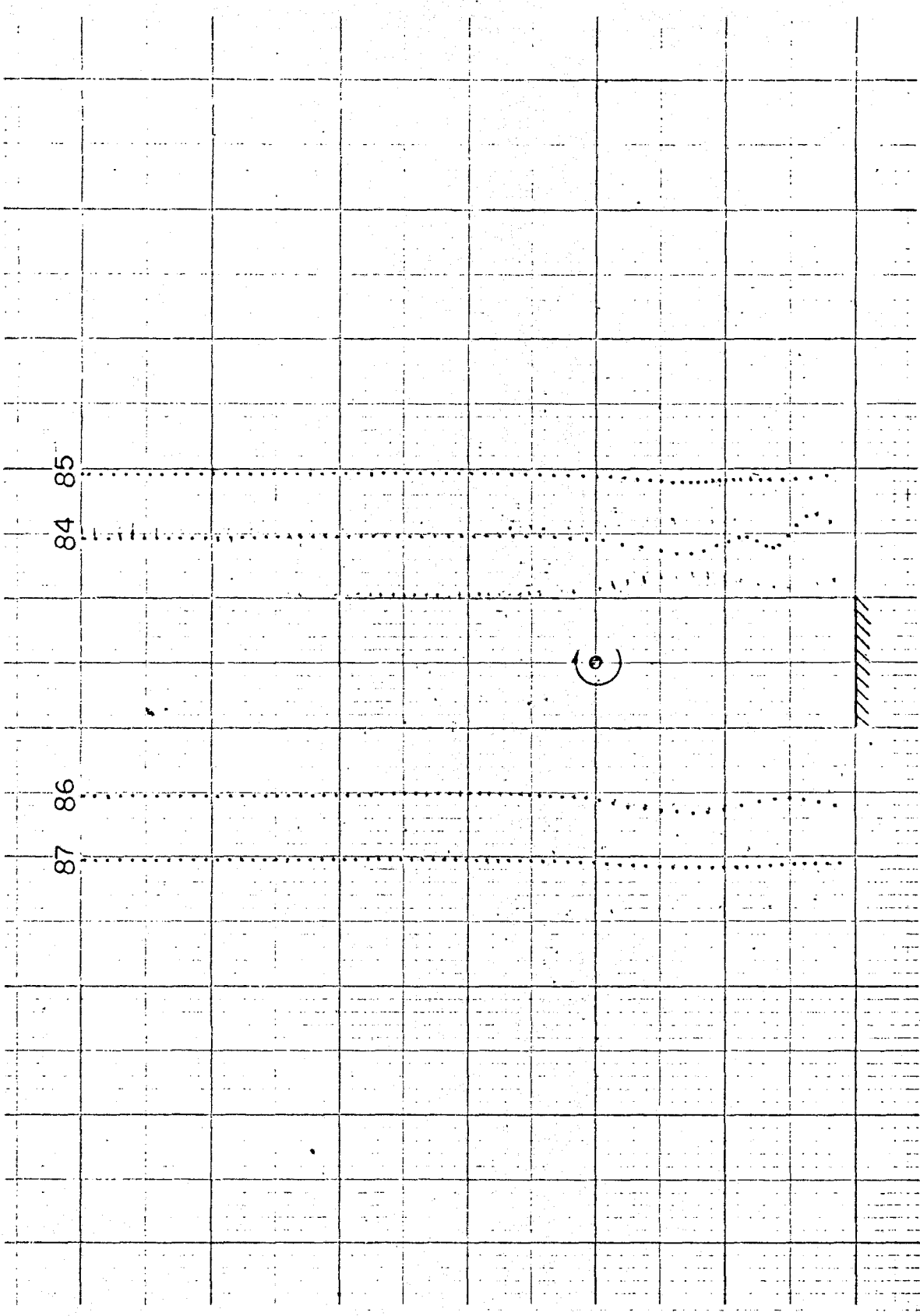
85
84
86
87

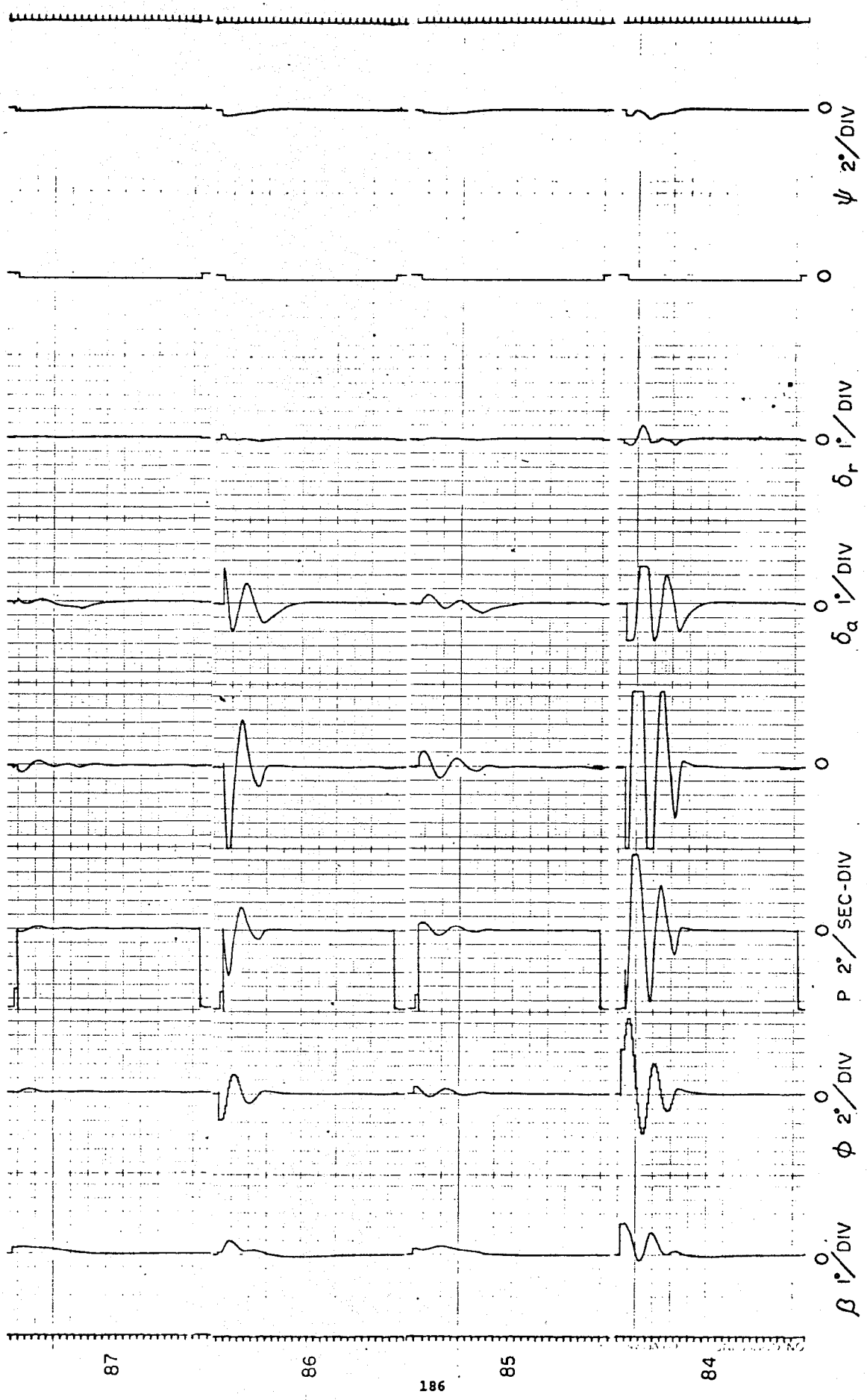
ψ 2°/DIV
0
0
δr 1°/DIV
0
δa 1°/DIV
0
0
P 2°/SEC-DIV
0
φ 2°/DIV
0
β 1°/DIV
0
87
86
85
84

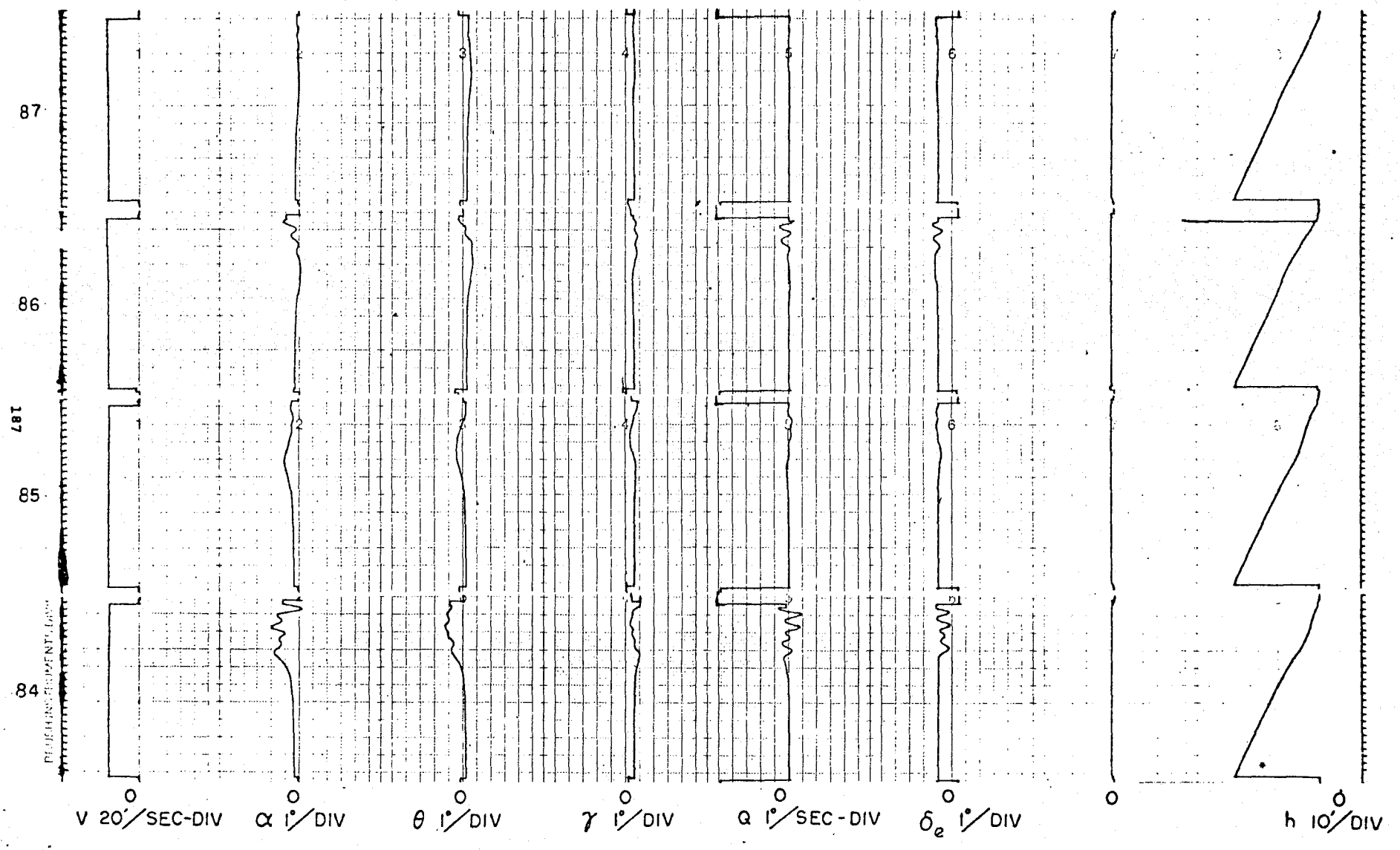
87
86
85
84
1
2
3
4
5
6
0
V 20'/SEC-DIV
α 1°/DIV
θ 1°/DIV
γ 1°/DIV
Q 1°/SEC-DIV
δe 1°/DIV
h 10'/DIV

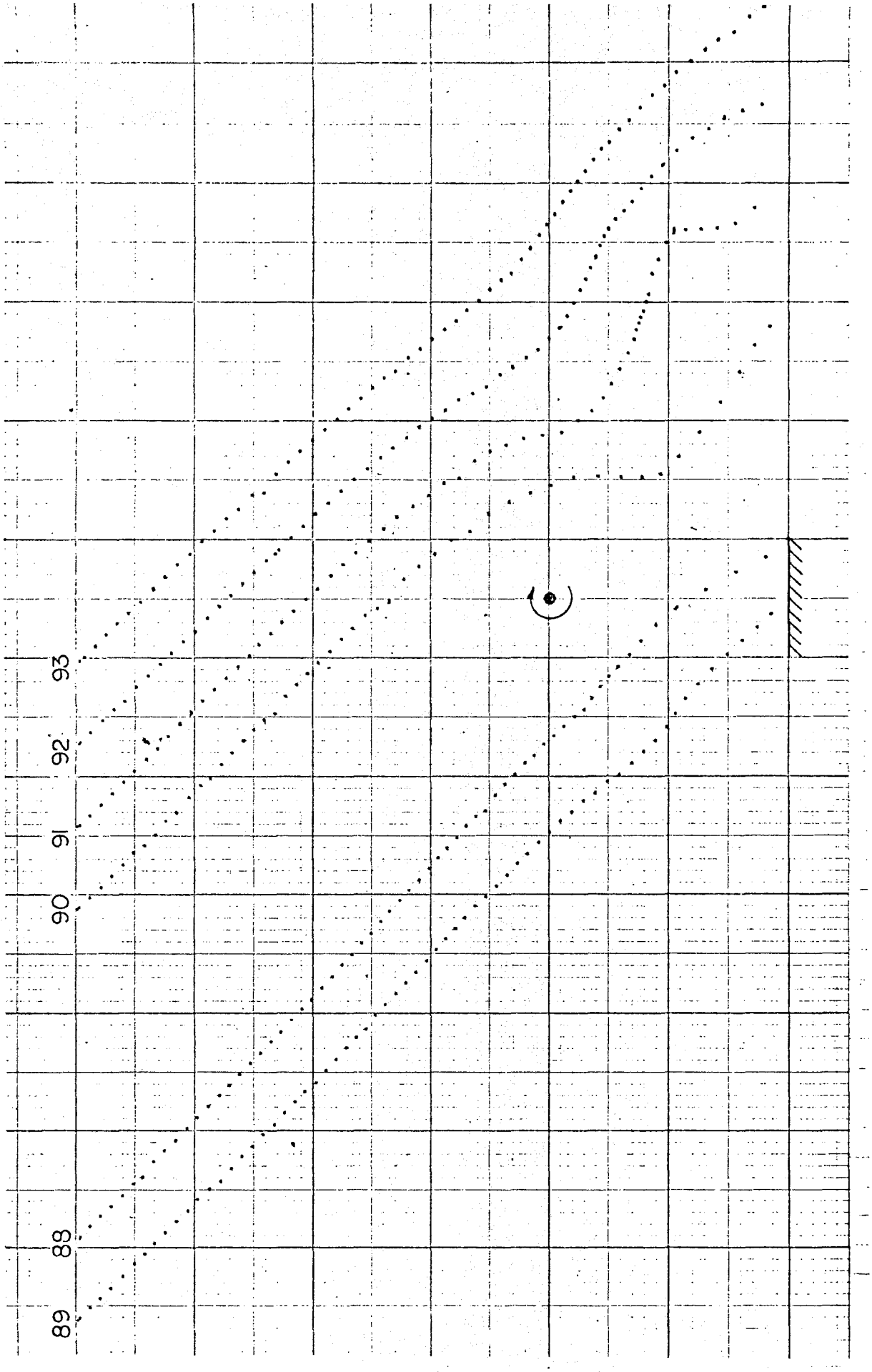
89
88
90
91
92
93

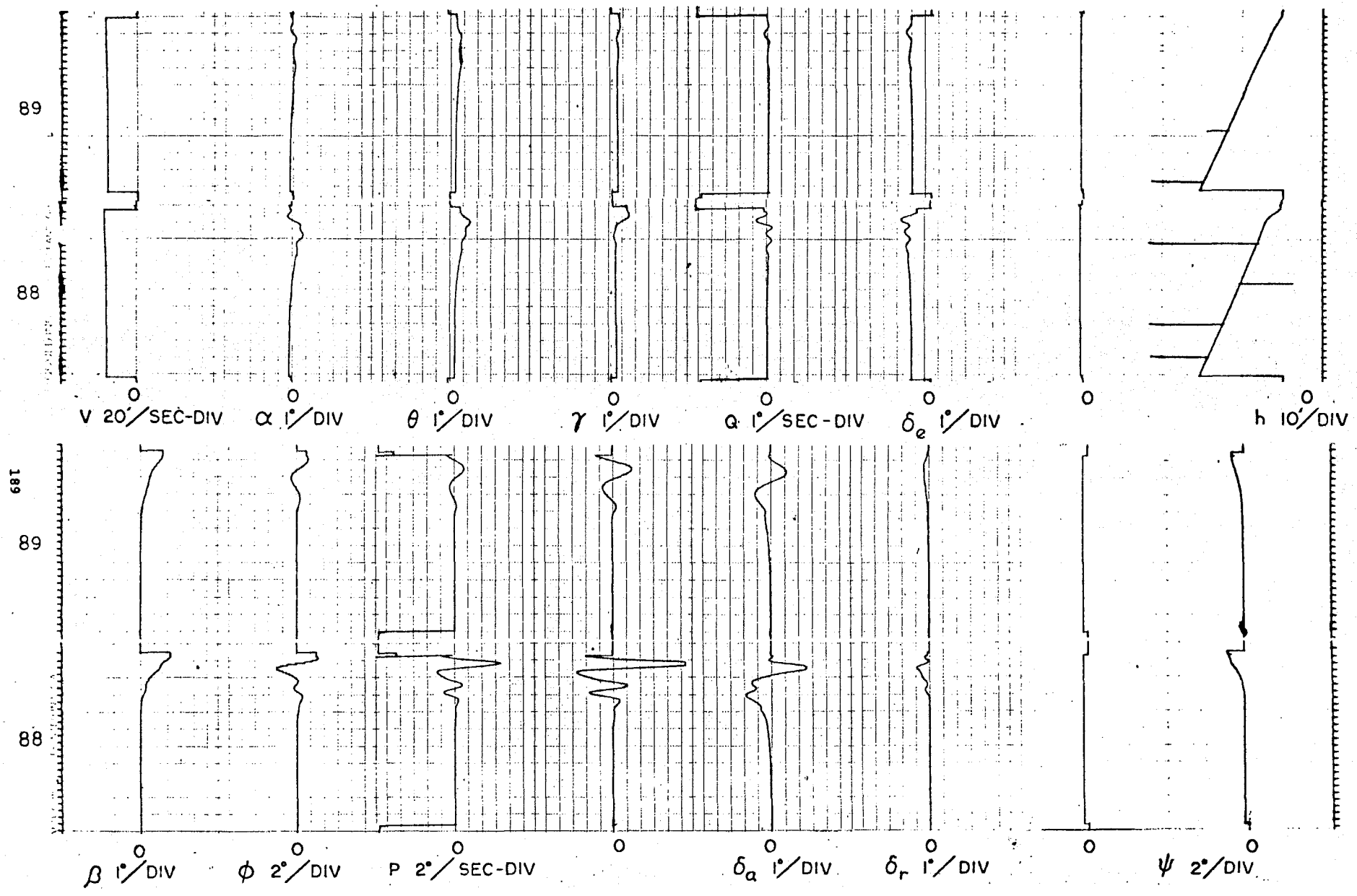
89
88
0
V 20'/SEC-DIV
α 1°/DIV
θ 1°/DIV
γ 1°/DIV
Q 1°/SEC-DIV
δe 1°/DIV
h 10'/DIV
β 1°/DIV
φ 2°/DIV
P 2°/SEC-DIV
δa 1°/DIV
δr 1°/DIV
ψ 2°/DIV

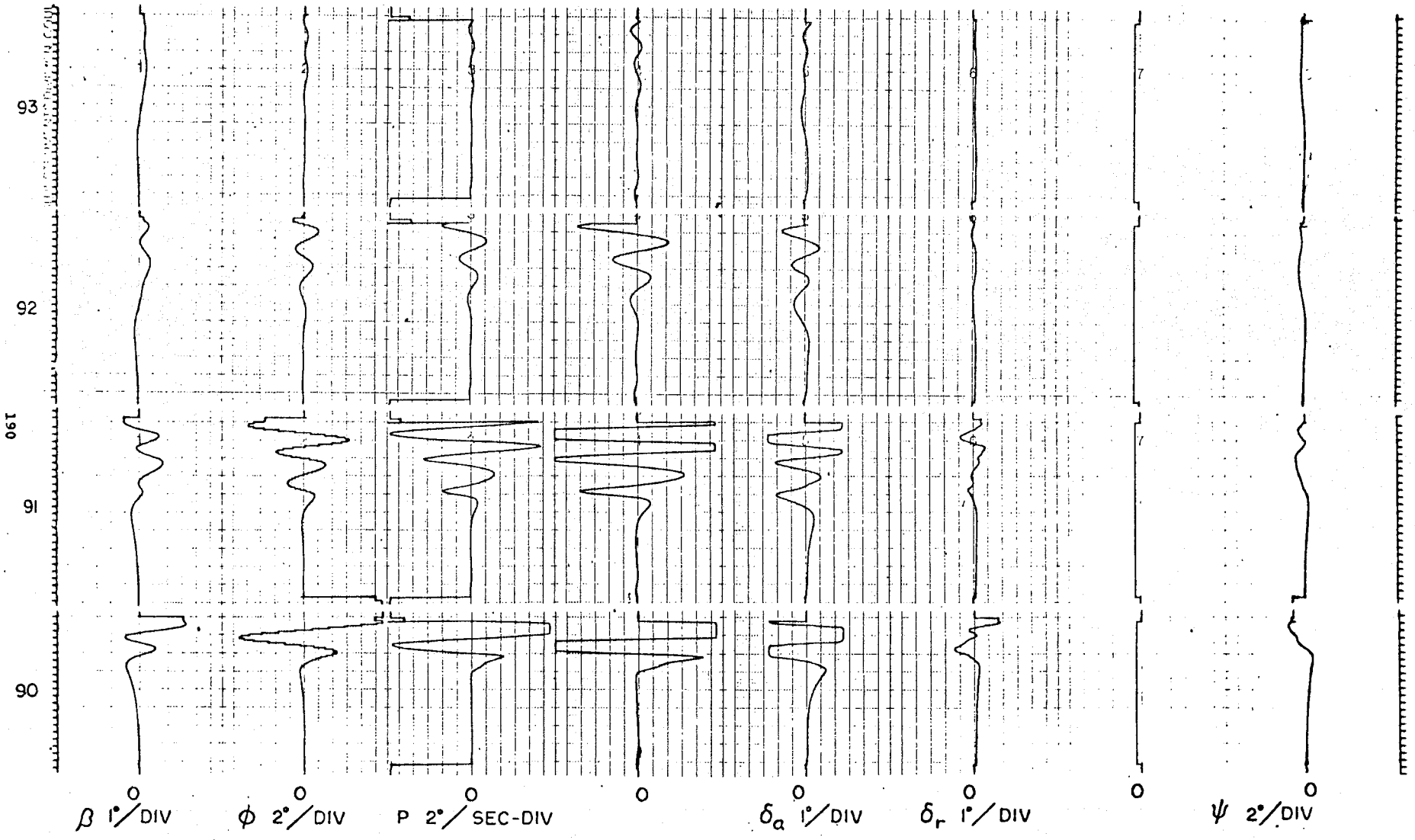
90
91
92
93
0
β 1°/DIV
0
φ 2°/DIV
0
P 2°/SEC-DIV
0
0
δa 1°/DIV
0
δr 1°/DIV
0
0
ψ 2°/DIV

h 10'/DIV
0
0
δ_e 1°/DIV
0
Q 1°/SEC-DIV
0
γ 1°/DIV
0
θ 1°/DIV
0
α 1°/DIV
0
V 20'/SEC-DIV
0
93
92
91
90

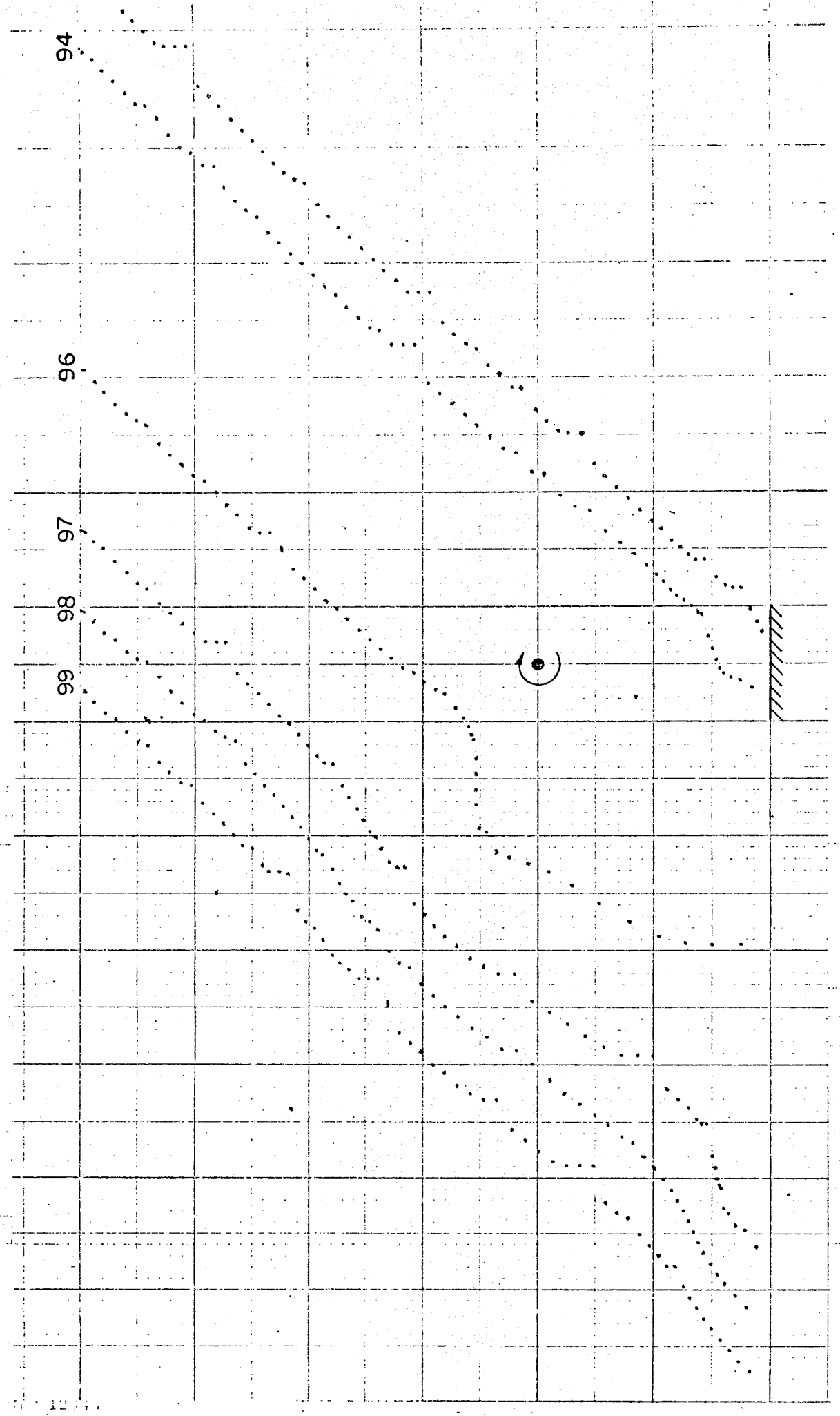
94
96
97
98
99

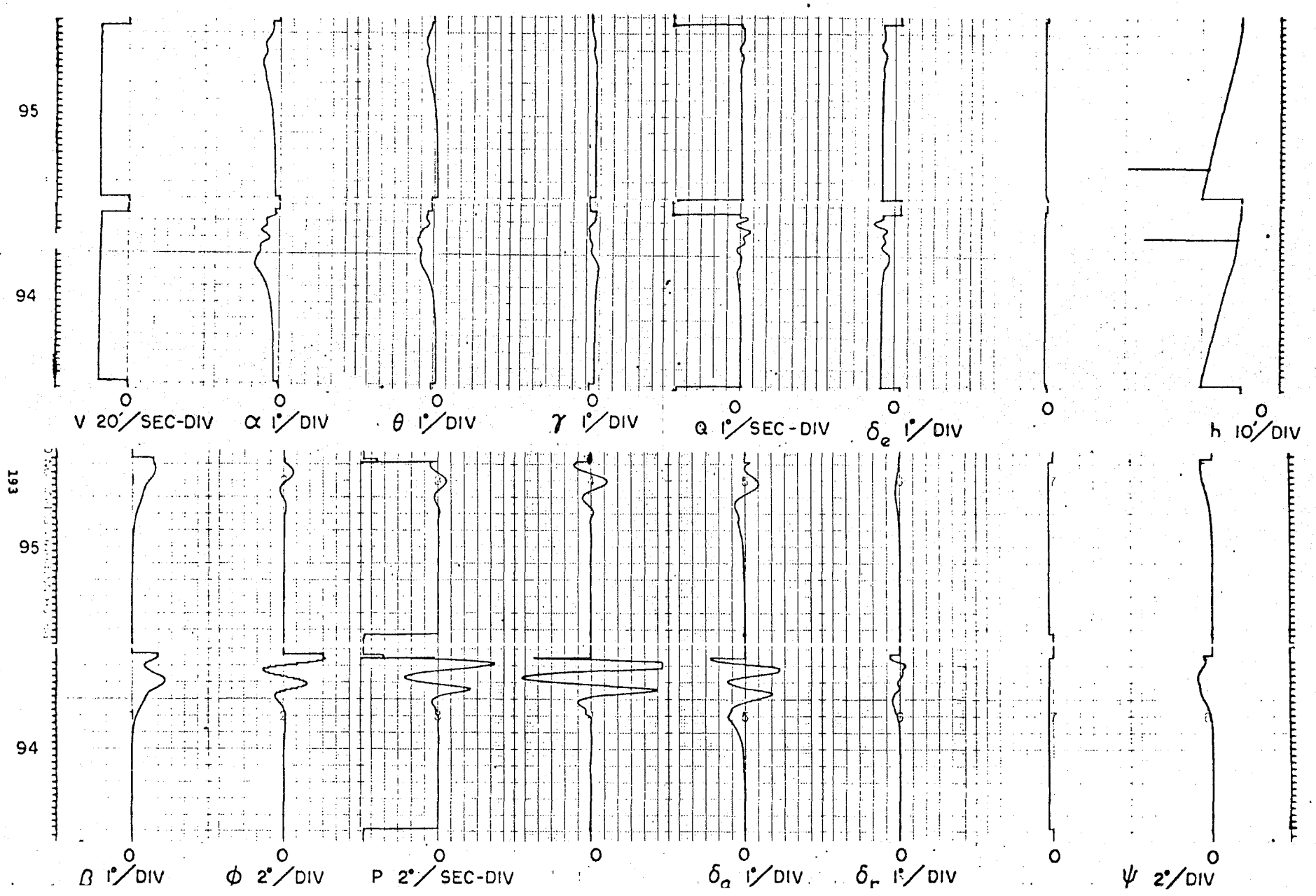
95
94
0
V 20'/SEC-DIV
0
α 1°/DIV
0
θ 1°/DIV
0
γ 1°/DIV
0
Q 1°/SEC-DIV
0
δe 1°/DIV
0
0
h 10'/DIV
95
94
0
β 1°/DIV
0
φ 2°/DIV
0
P 2°/SEC-DIV
0
0
δa 1°/DIV
0
δr 1°/DIV
0
0
ψ 2°/DIV

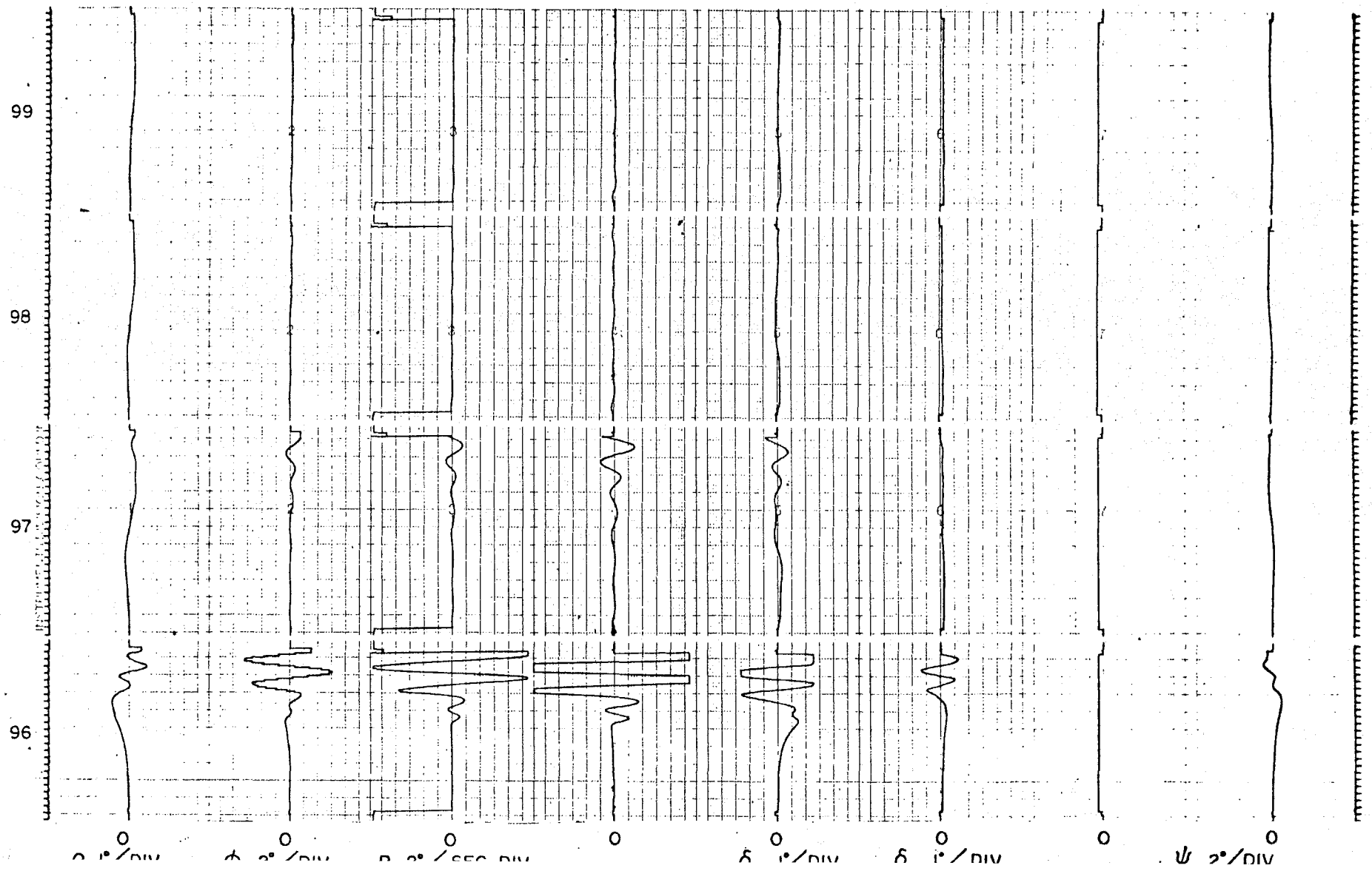
96
97
98
99
0
0
0
0
0
0
0
0

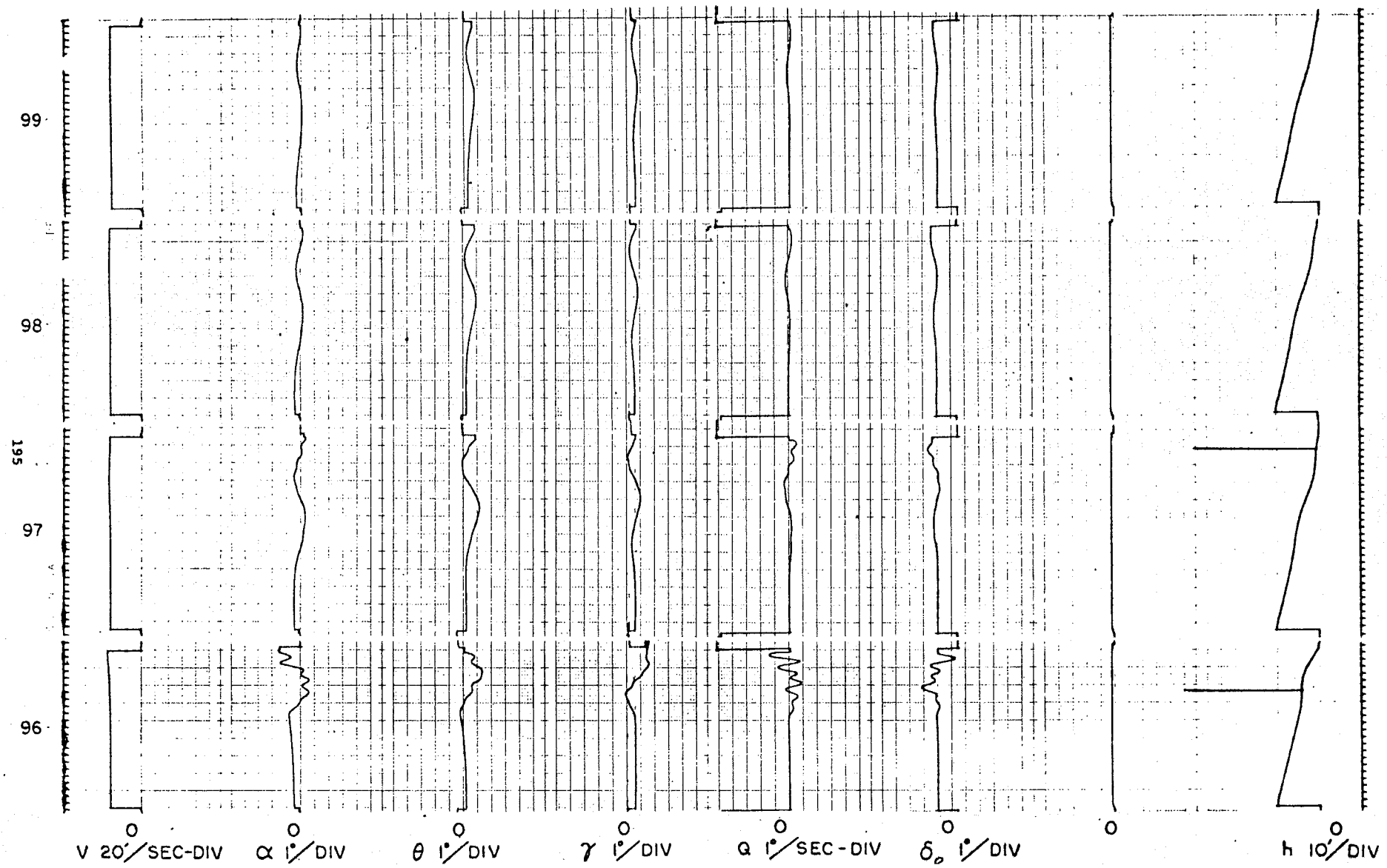
99
98
195
97
96
0
V 20'/SEC-DIV
0
α 1°/DIV
0
θ 1°/DIV
0
γ 1°/DIV
0
Q 1°/SEC-DIV
0
δ₀ 1°/DIV
0
0
h 10'/DIV

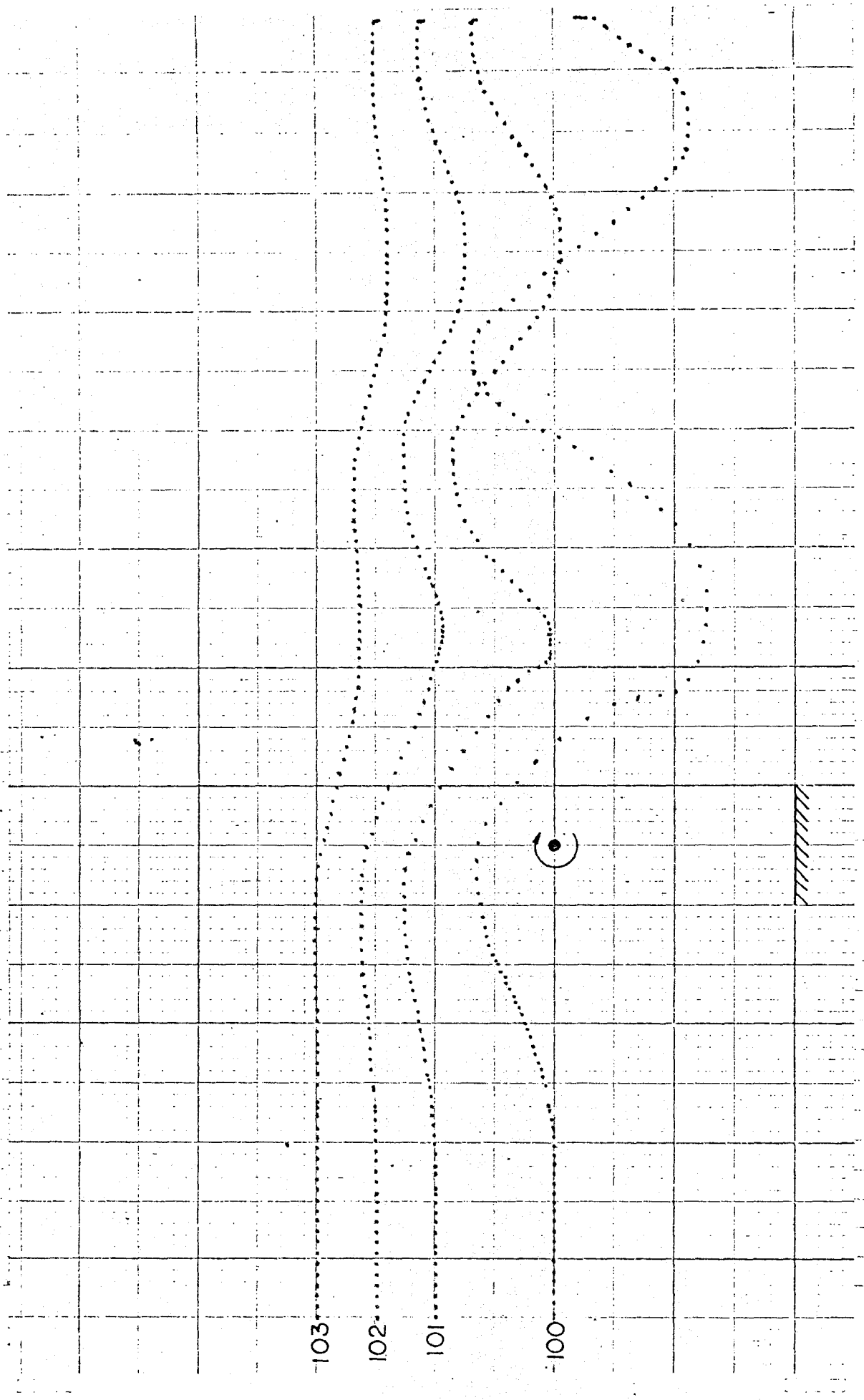
103
102
101
100

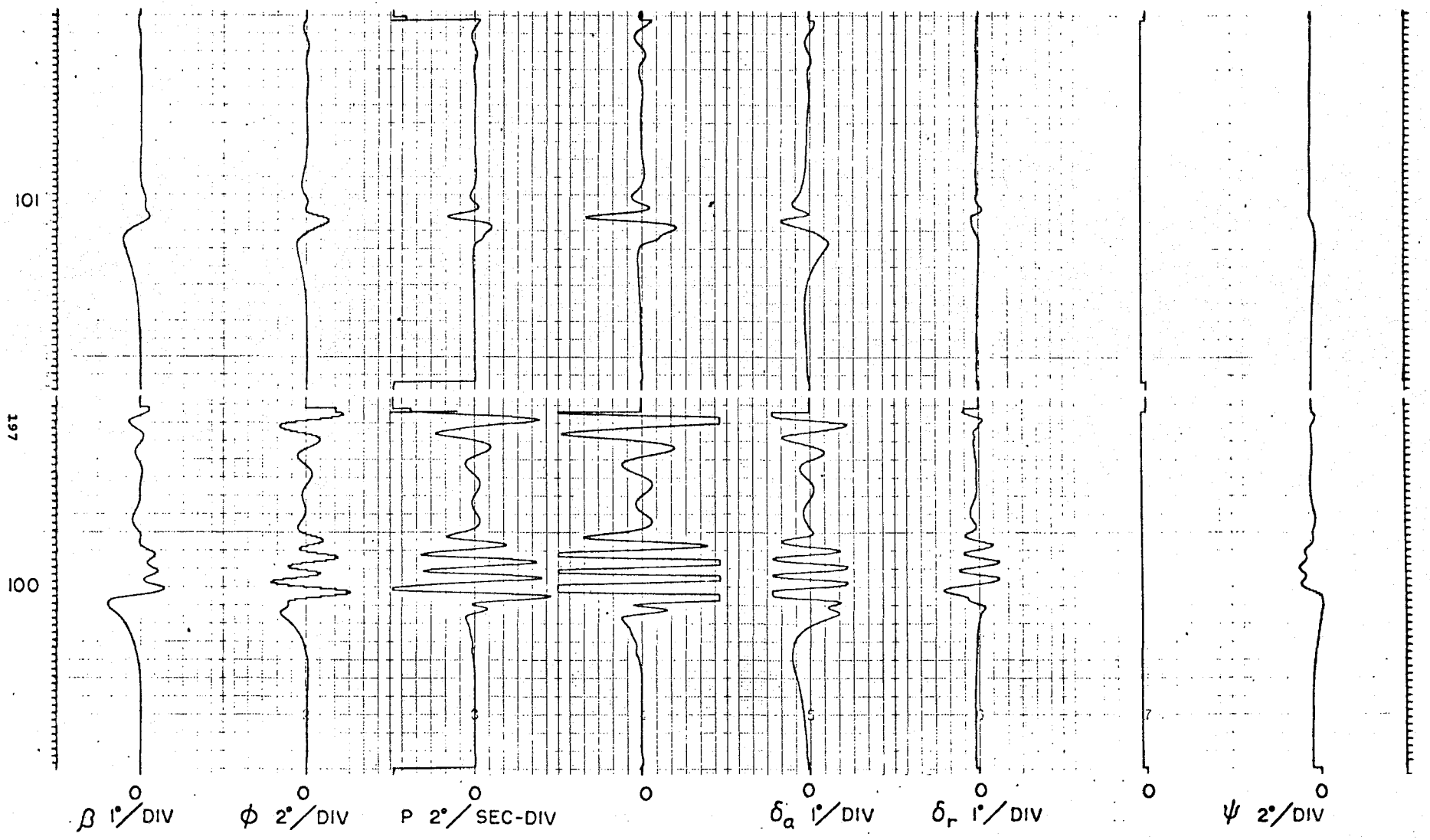
101
100
0
β 1°/DIV
0
φ 2°/DIV
0
P 2°/SEC-DIV
0
0
δa 1°/DIV
0
δr 1°/DIV
0
0
ψ 2°/DIV

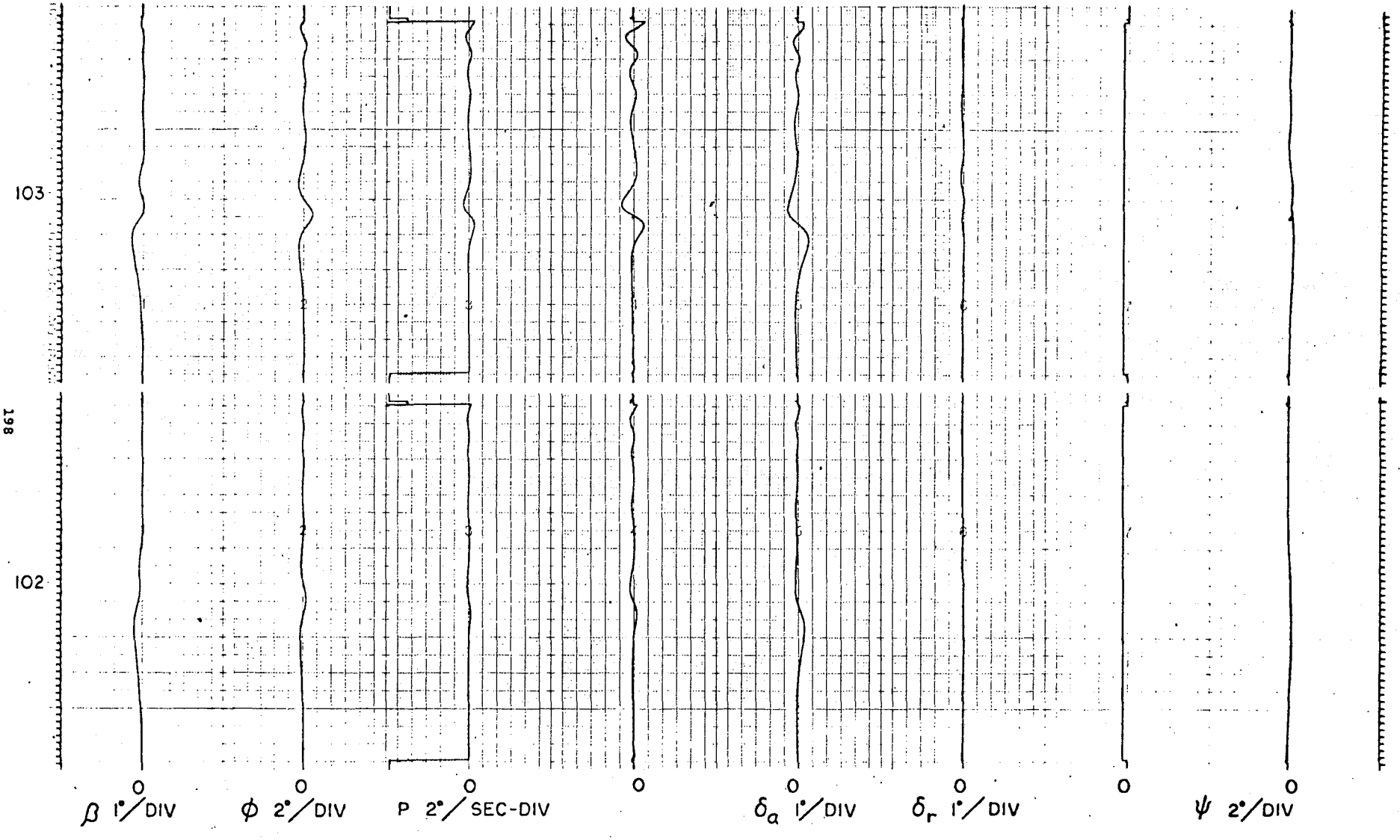
103
102
0
0
0
0
0
0
0
0
β 1°/DIV
φ 2°/DIV
P 2°/SEC-DIV
δa 1°/DIV
δr 1°/DIV
ψ 2°/DIV

h 10'/DIV
0
0
δ_e 1°/DIV
0
Q 1°/SEC-DIV
0
γ 1°/DIV
0
θ 1°/DIV
0
α 1°/DIV
0
V 20'/SEC-DIV
0
101
100

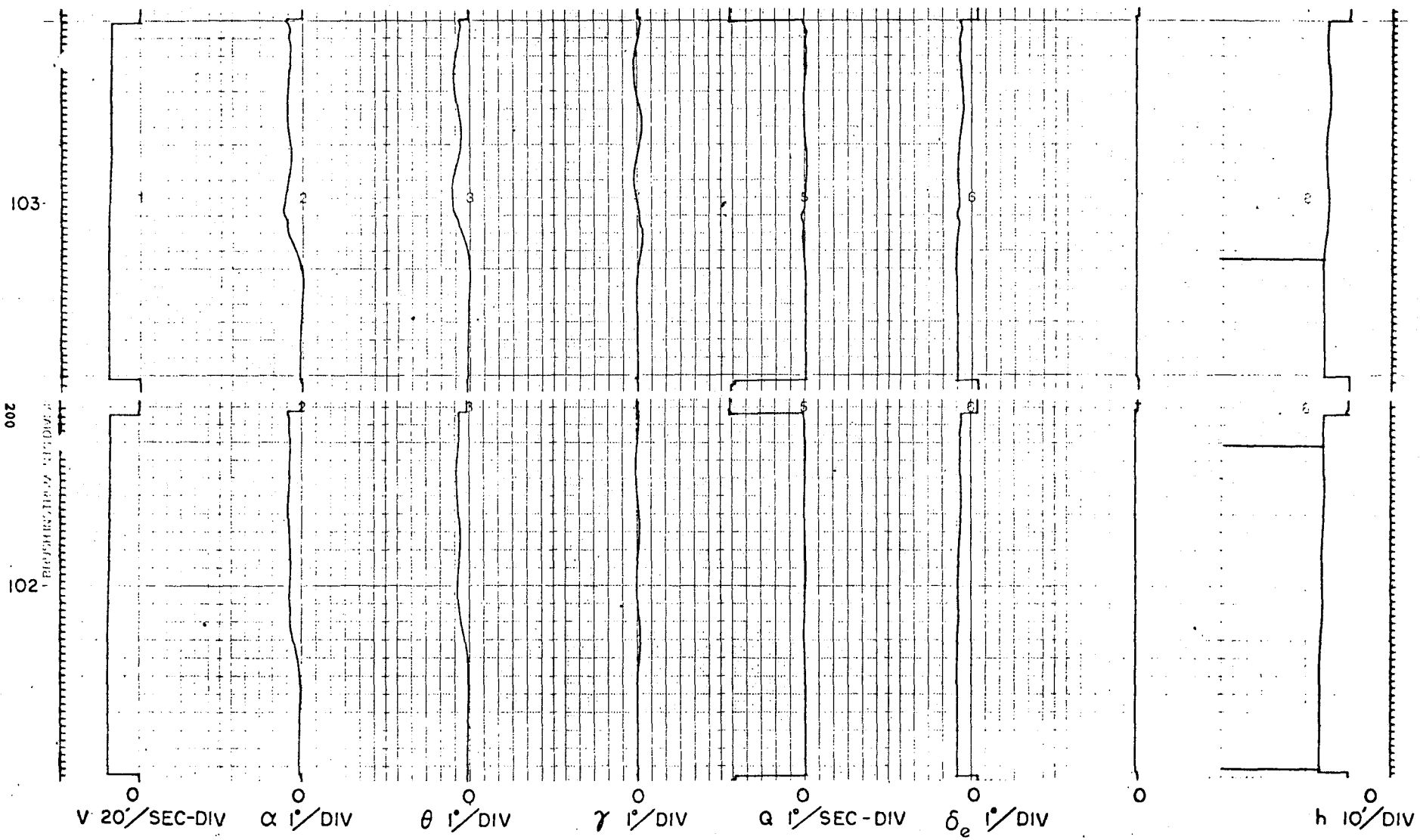
103
102
200
V 20'/SEC-DIV
α 1°/DIV
θ 1°/DIV
γ 1°/DIV
Q 1°/SEC-DIV
δe 1°/DIV
h 10'/DIV

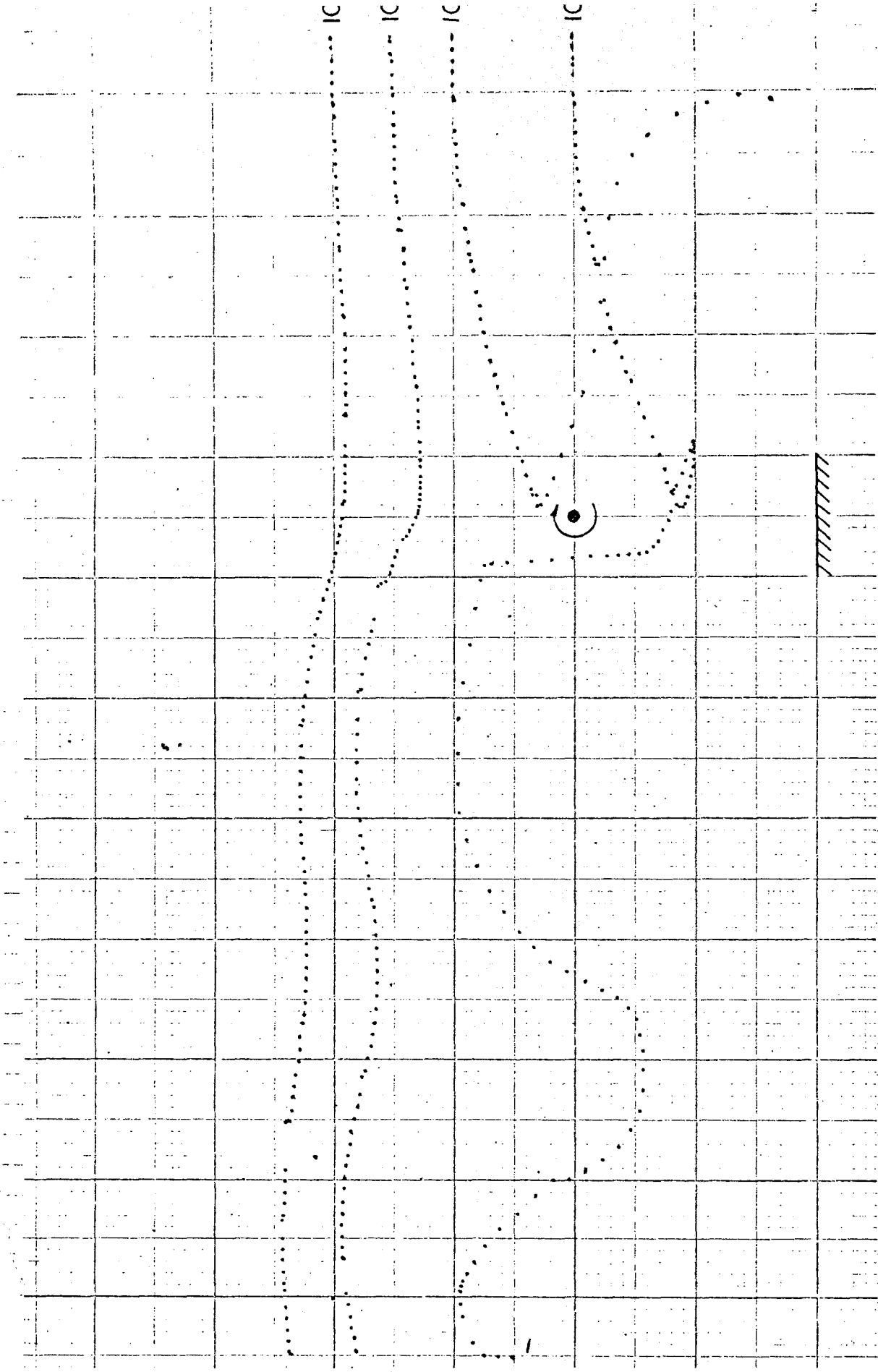

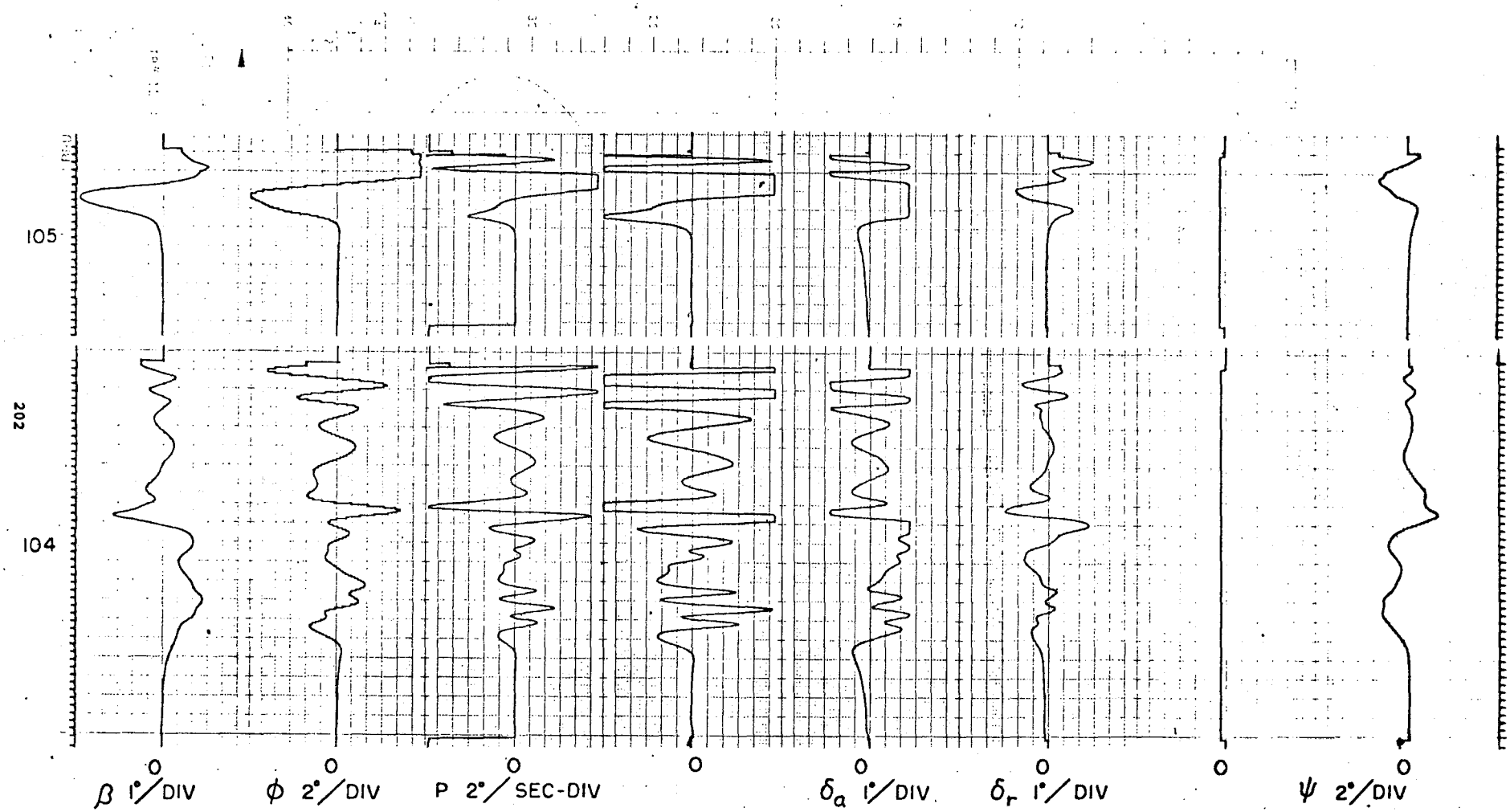
105
104
0
0
0
0
0
0
0
0
β 1°/DIV
φ 2°/DIV
P 2°/SEC-DIV
δa 1°/DIV
δr 1°/DIV
ψ 2°/DIV

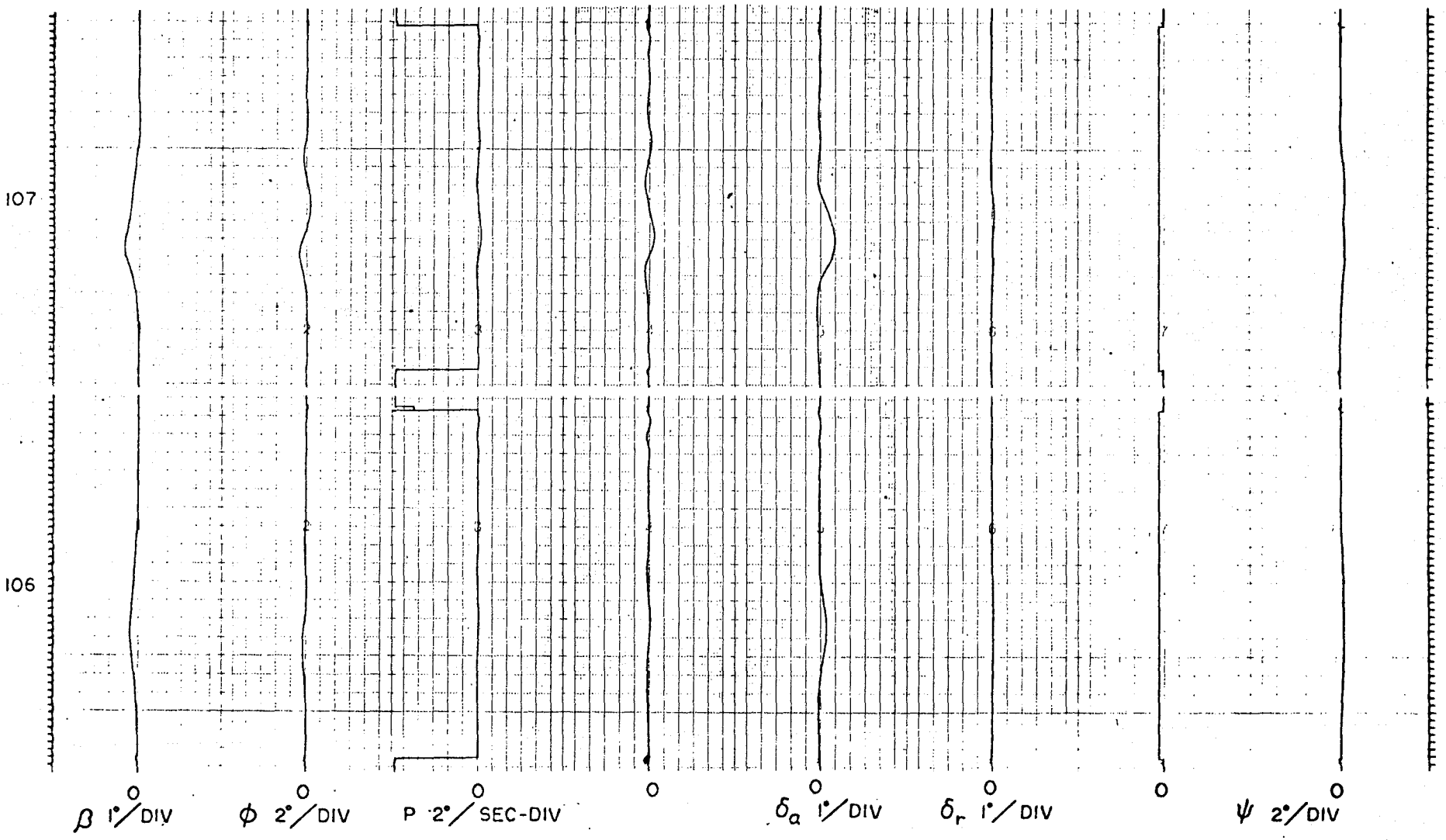
107
106
0
β 1°/DIV
0
φ 2°/DIV
0
P 2°/SEC-DIV
0
0
δa 1°/DIV
0
δr 1°/DIV
0
ψ 2°/DIV
0

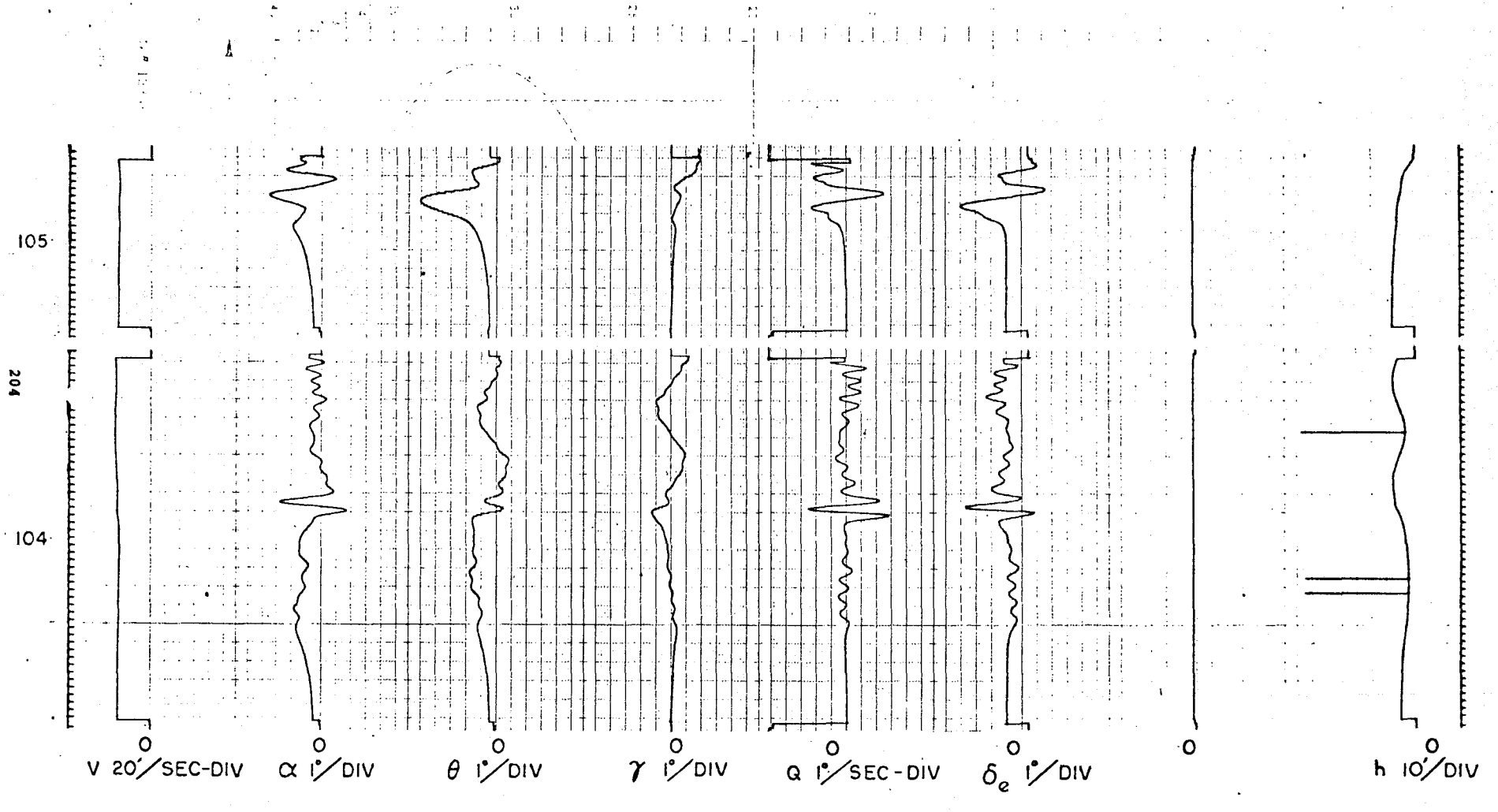
105
104
V 20'/SEC-DIV
α 1°/DIV
θ 1°/DIV
γ 1°/DIV
Q 1°/SEC-DIV
δ_e 1°/DIV
h 10'/DIV
0

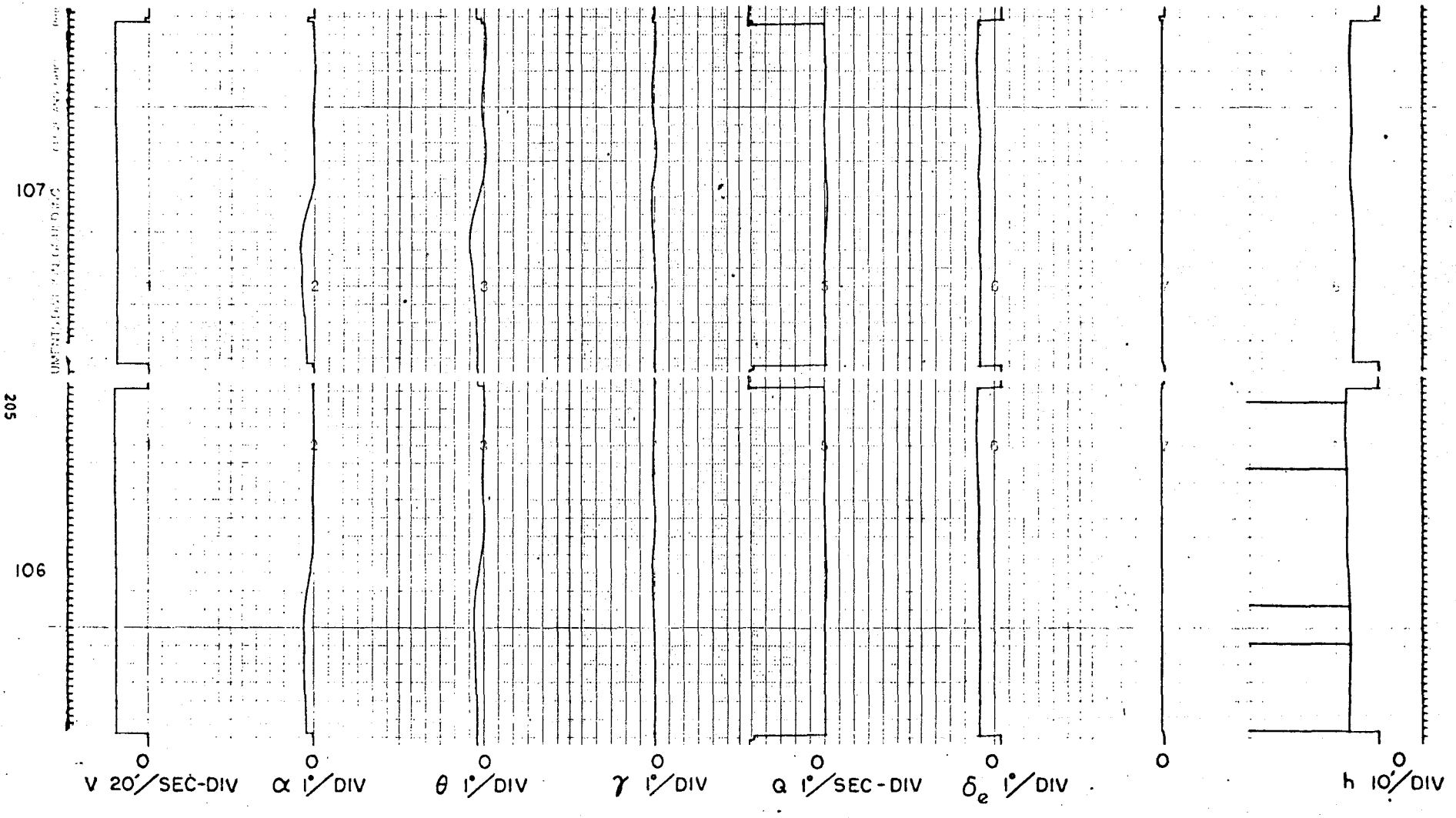
107
106
V 20′/SEC-DIV
α 1°/DIV
θ 1°/DIV
γ 1°/DIV
Q 1°/SEC-DIV
δe 1°/DIV
h 10′/DIV

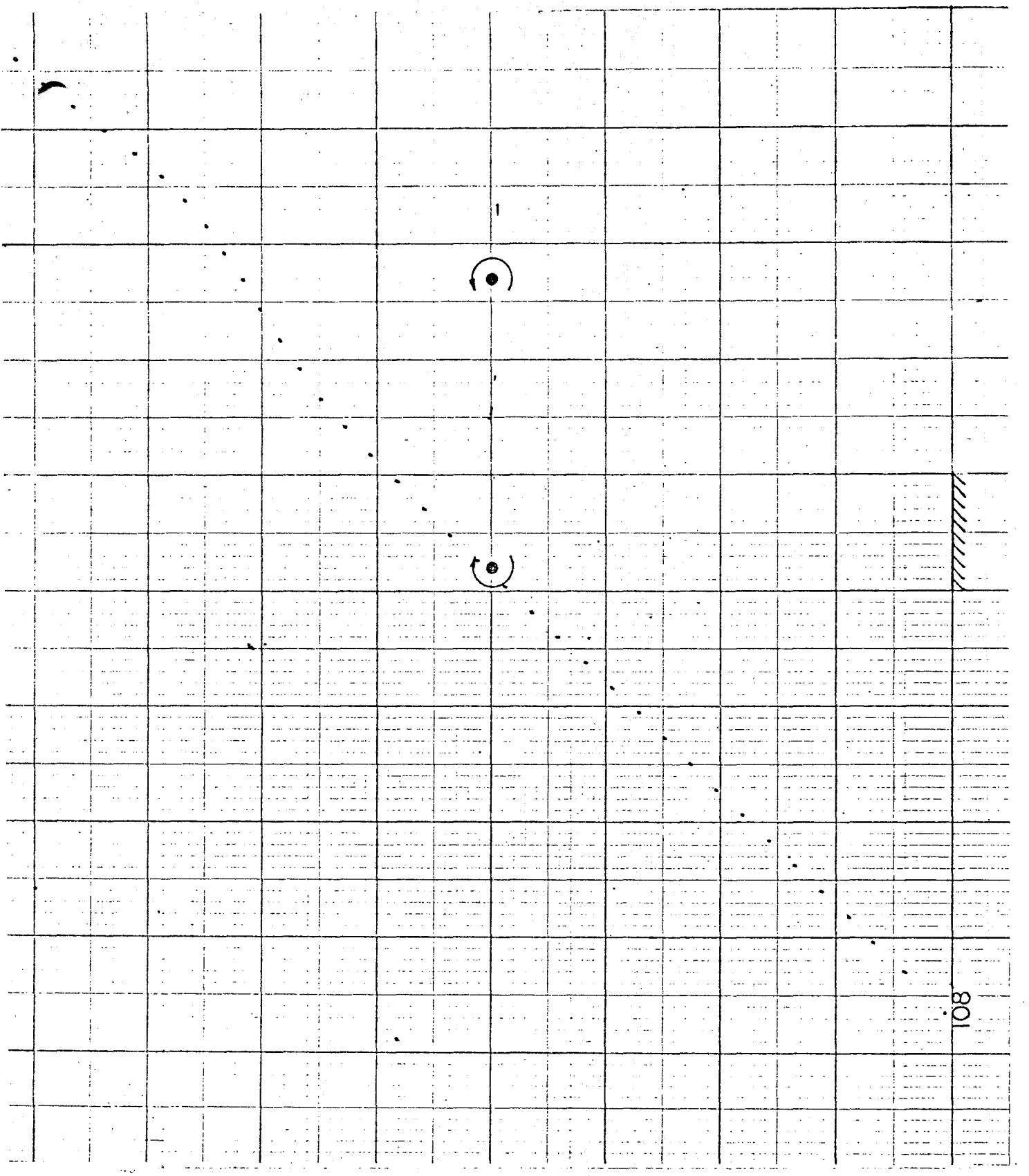
801

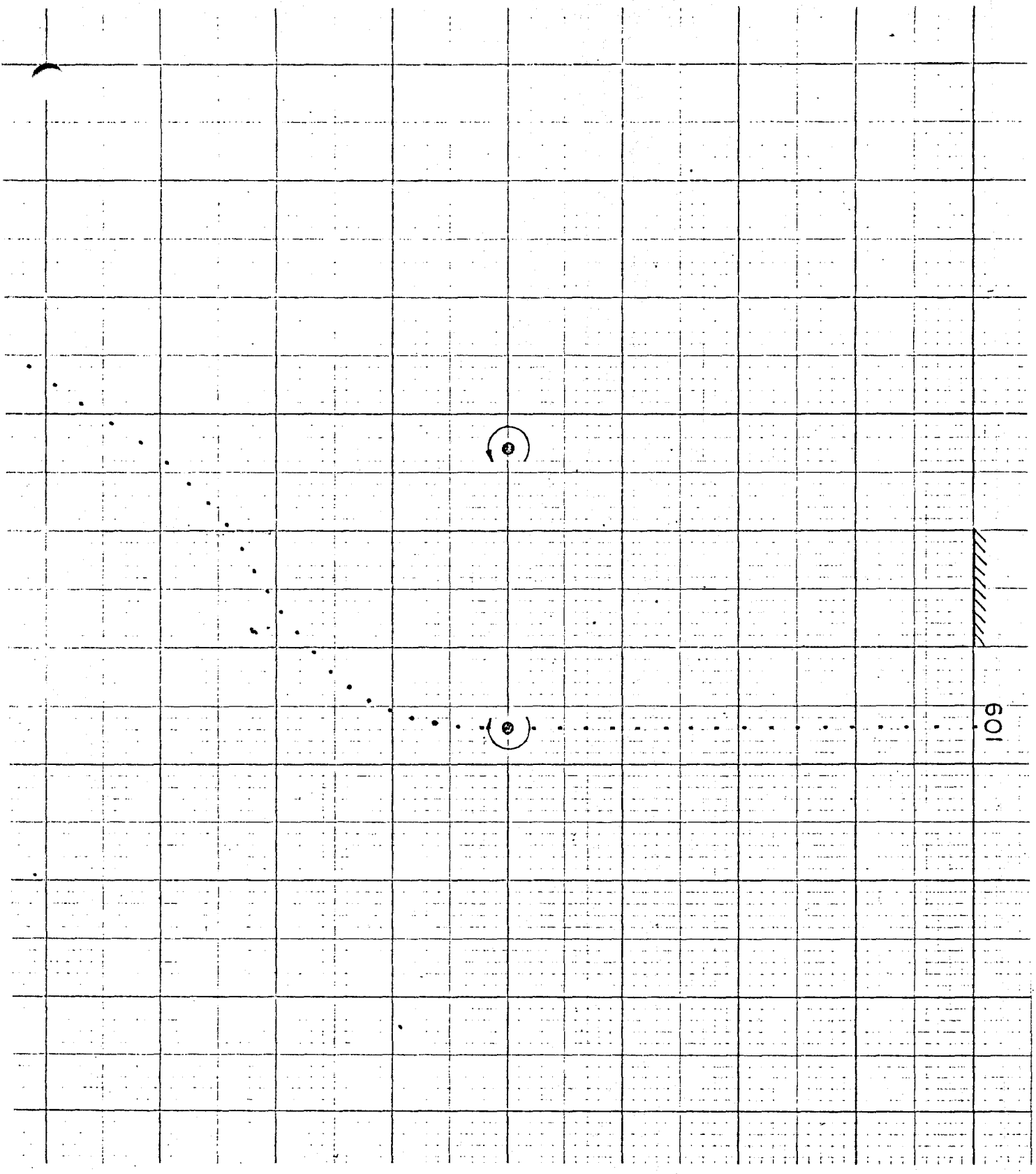
109

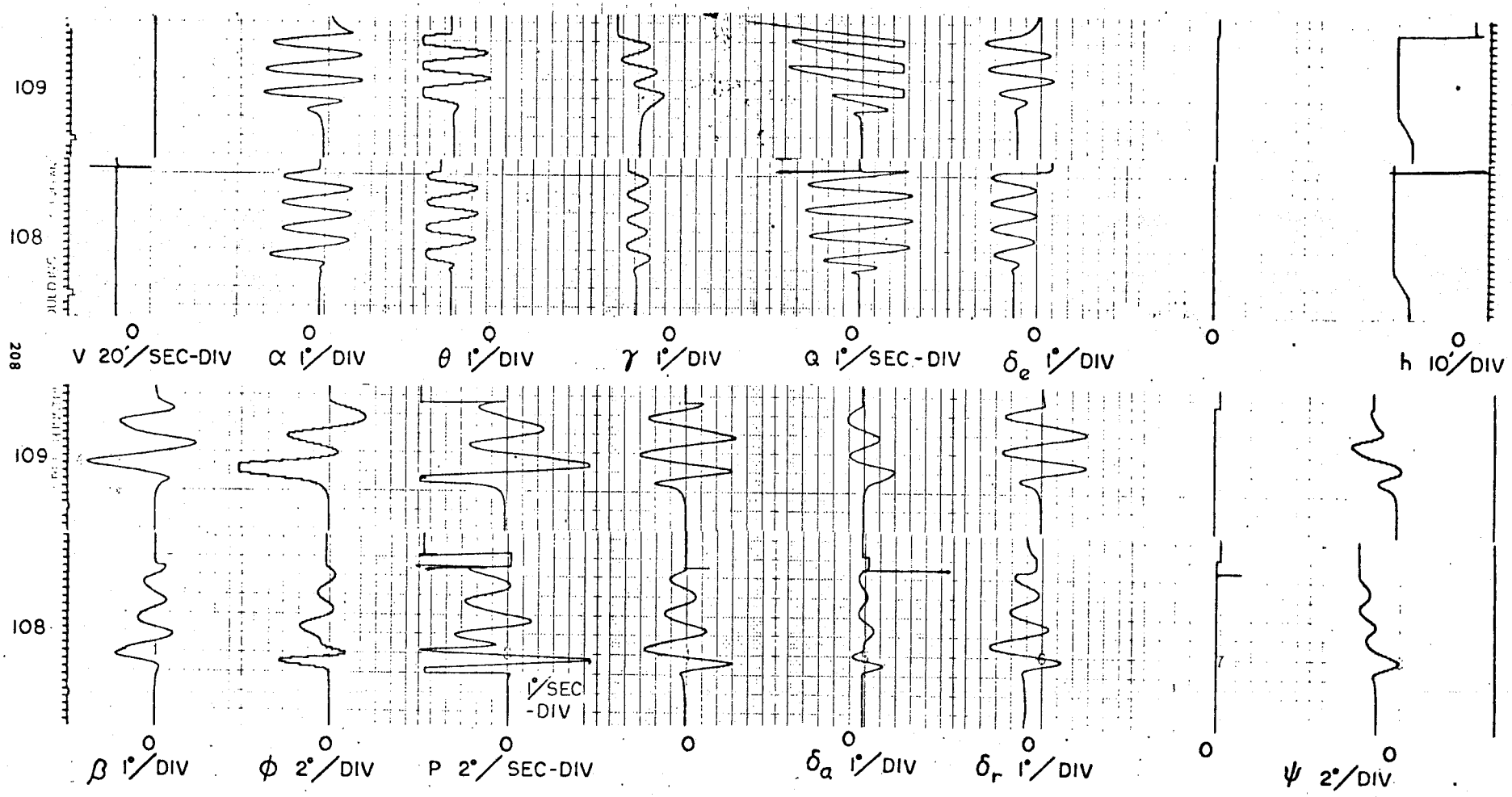
109
108
V 20'/SEC-DIV
α 1°/DIV
θ 1°/DIV
γ 1°/DIV
Q 1°/SEC-DIV
δe 1°/DIV
h 10'/DIV
β 1°/DIV
φ 2°/DIV
P 2°/SEC-DIV
1°/SEC -DIV
δa 1°/DIV
δr 1°/DIV
ψ 2°/DIV

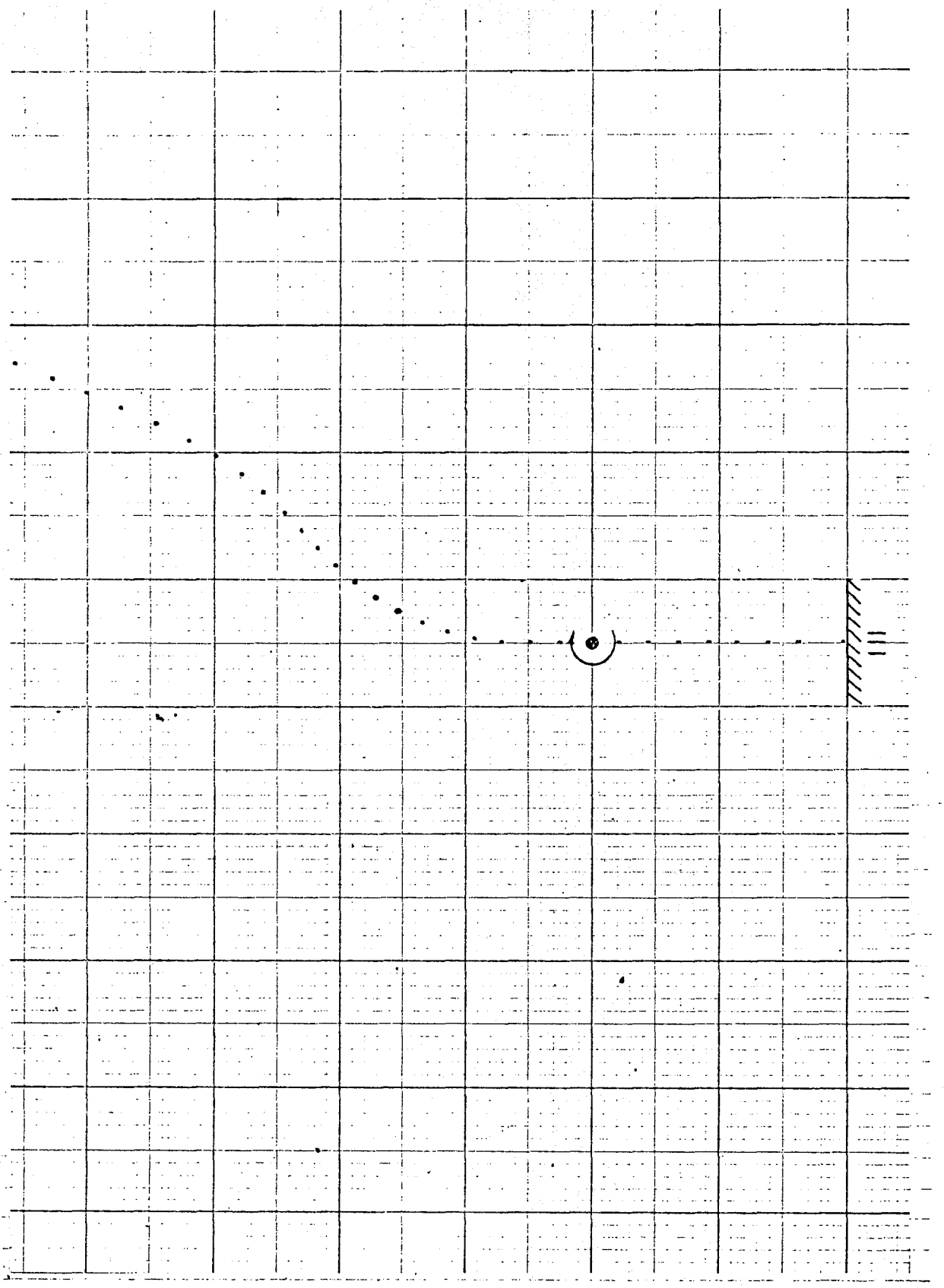

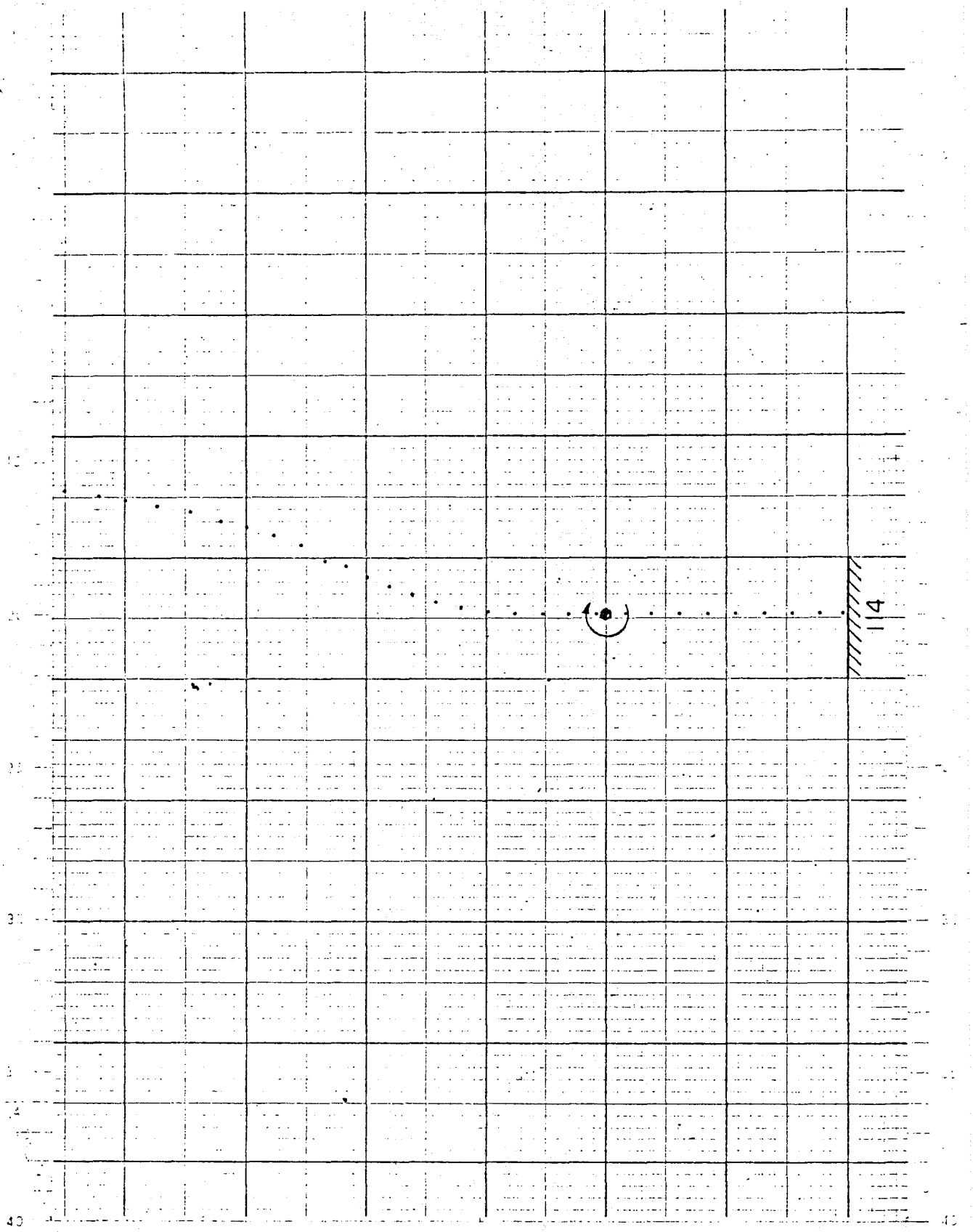
14

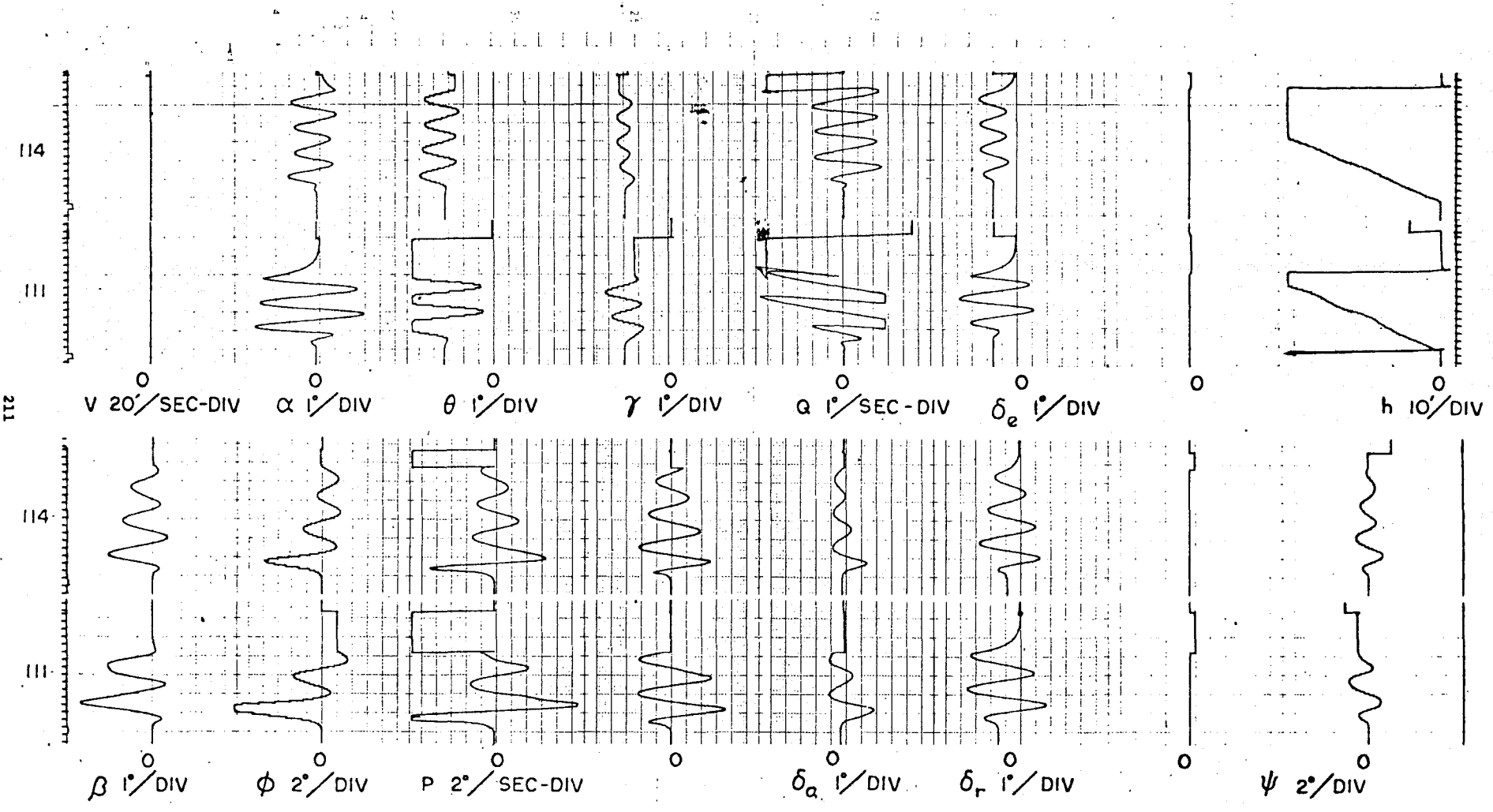
114
111
0
V 20'/SEC-DIV
α 1°/DIV
θ 1°/DIV
γ 1°/DIV
Q 1°/SEC-DIV
δe 1°/DIV
h 10'/DIV
β 1°/DIV
φ 2°/DIV
P 2°/SEC-DIV
δa 1°/DIV
δr 1°/DIV
ψ 2°/DIV

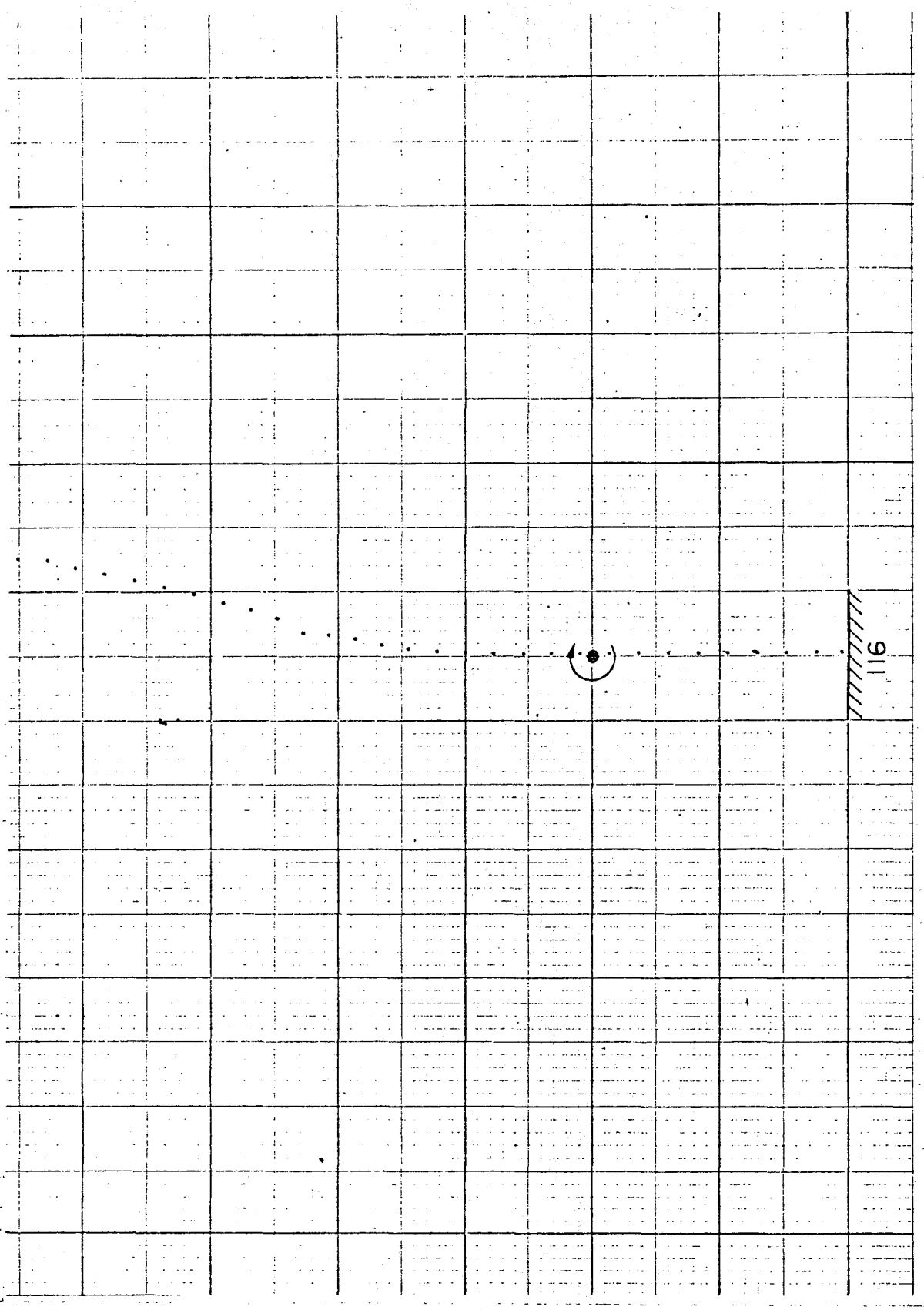
116

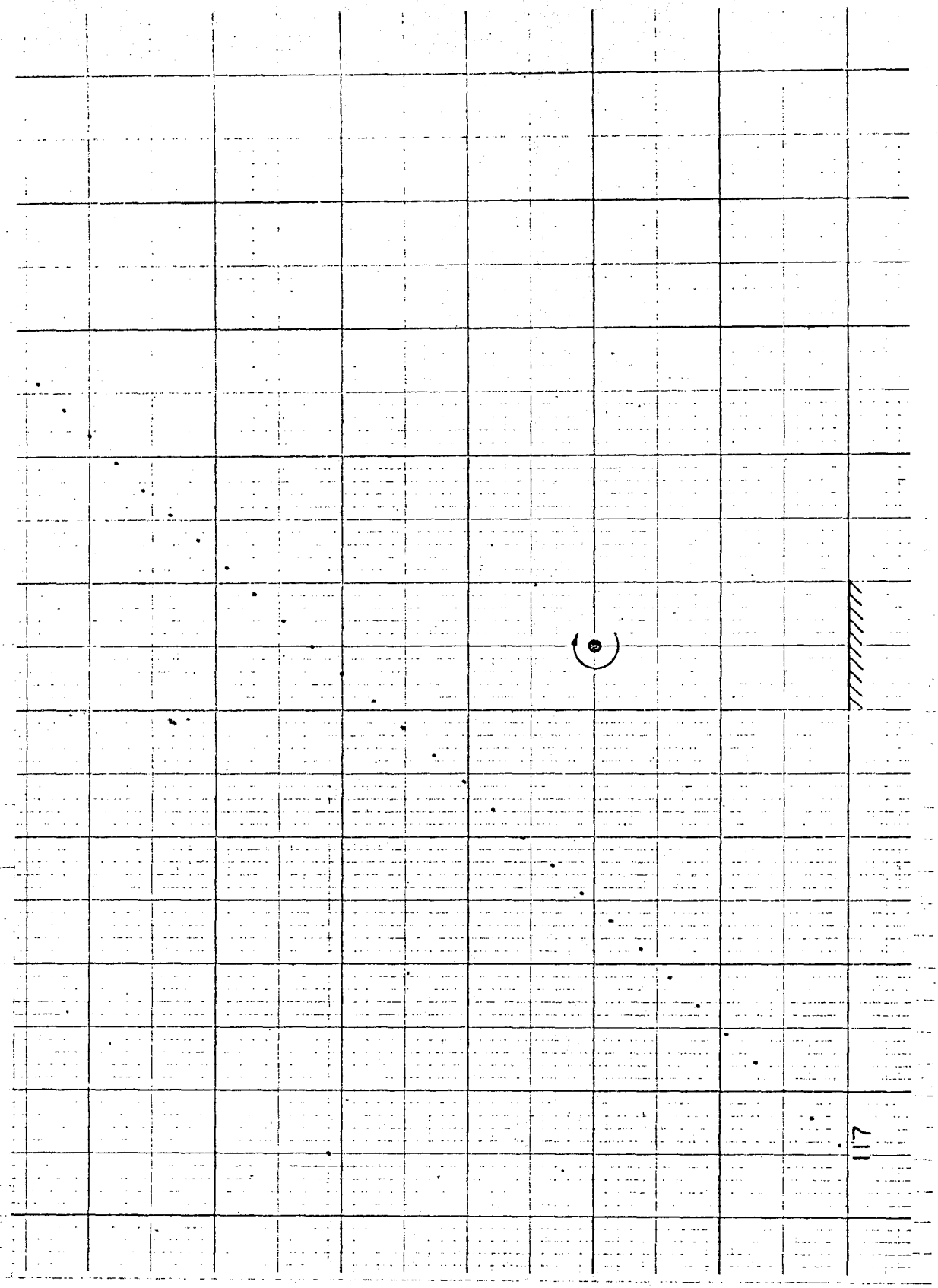
117

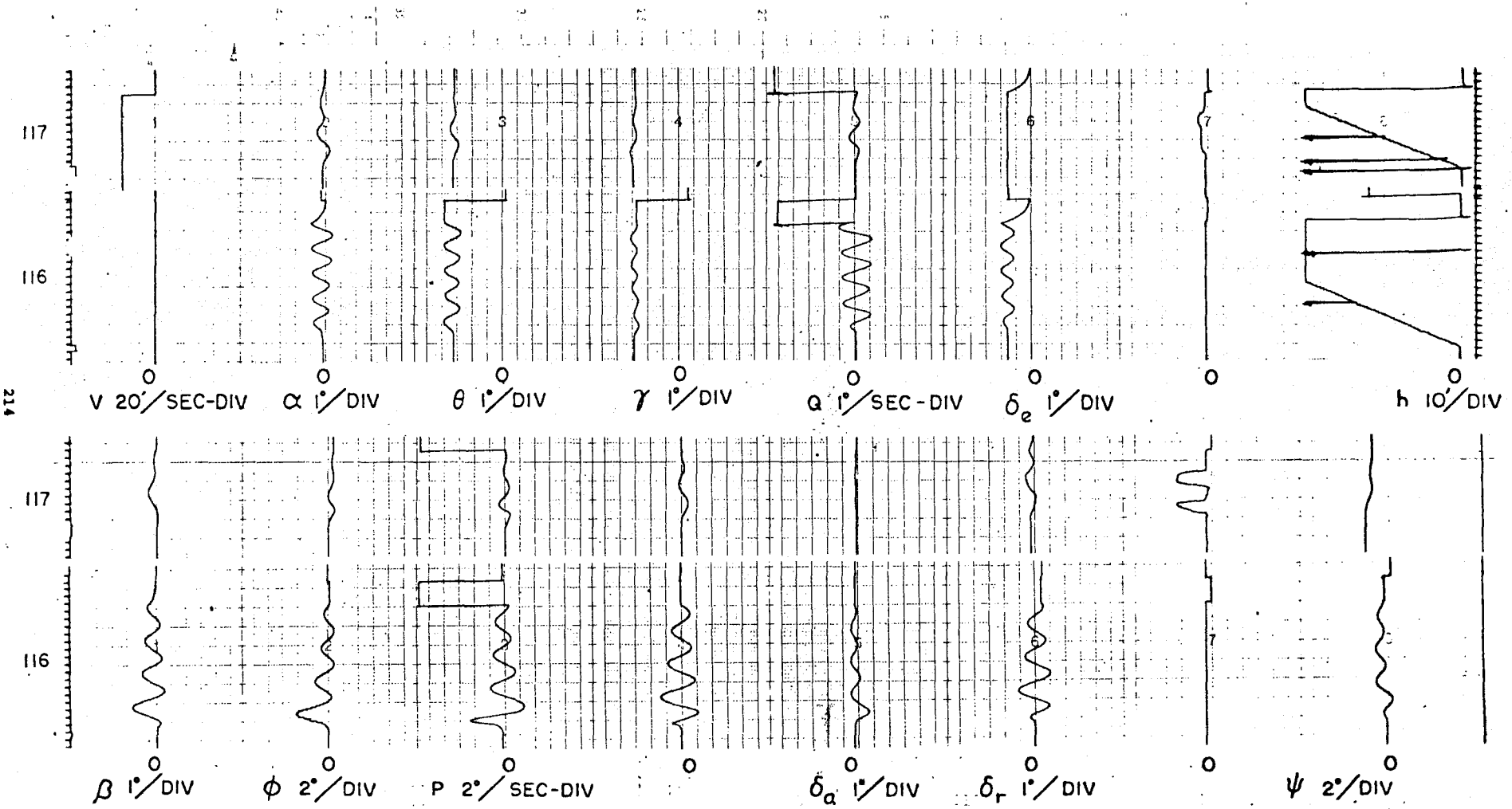
117
116
V 20'/SEC-DIV
α 1°/DIV
θ 1°/DIV
γ 1°/DIV
Q 1°/SEC-DIV
δe 1°/DIV
h 10'/DIV
β 1°/DIV
φ 2°/DIV
P 2°/SEC-DIV
δa 1°/DIV
δr 1°/DIV
ψ 2°/DIV

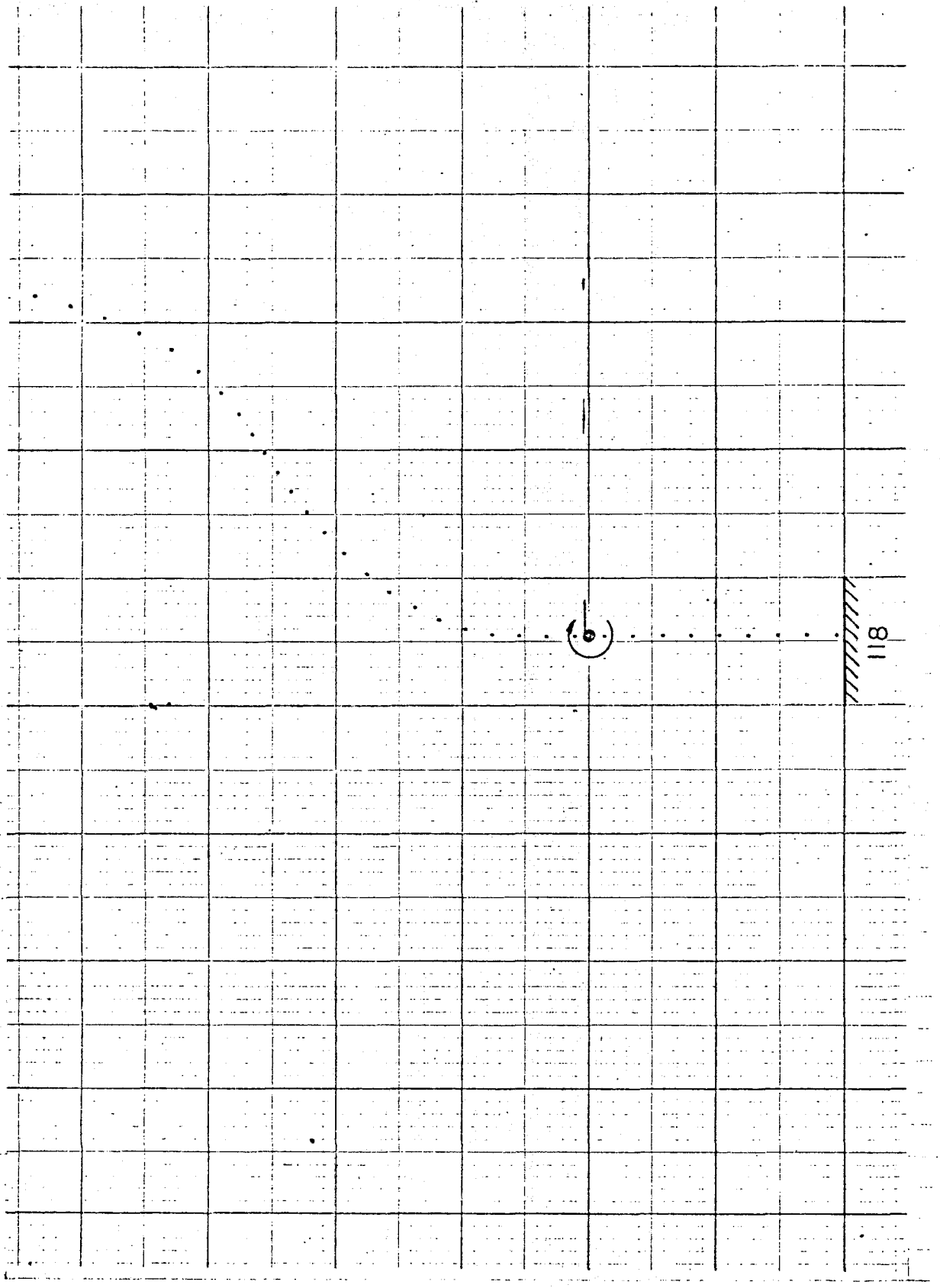
118

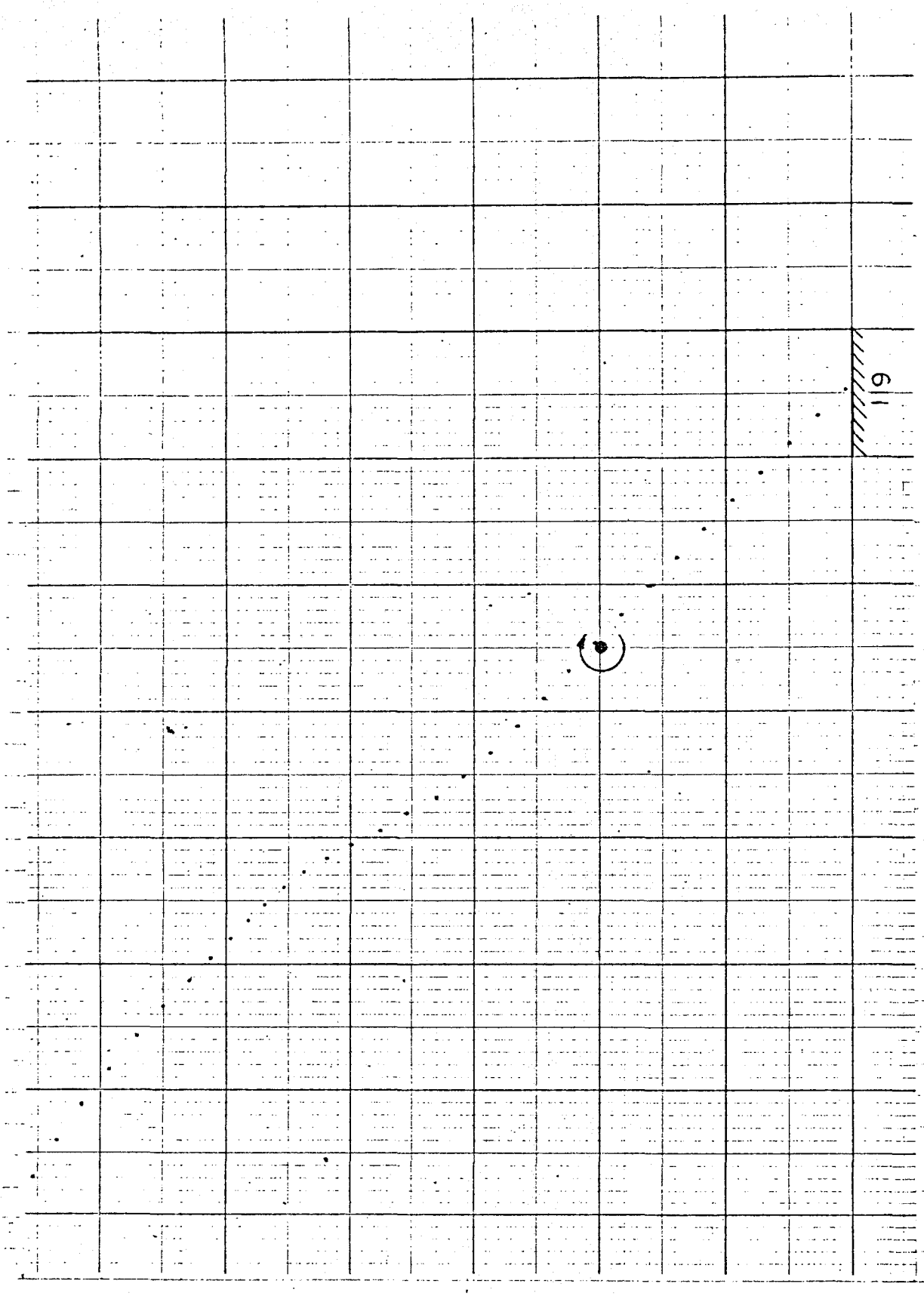
6|1

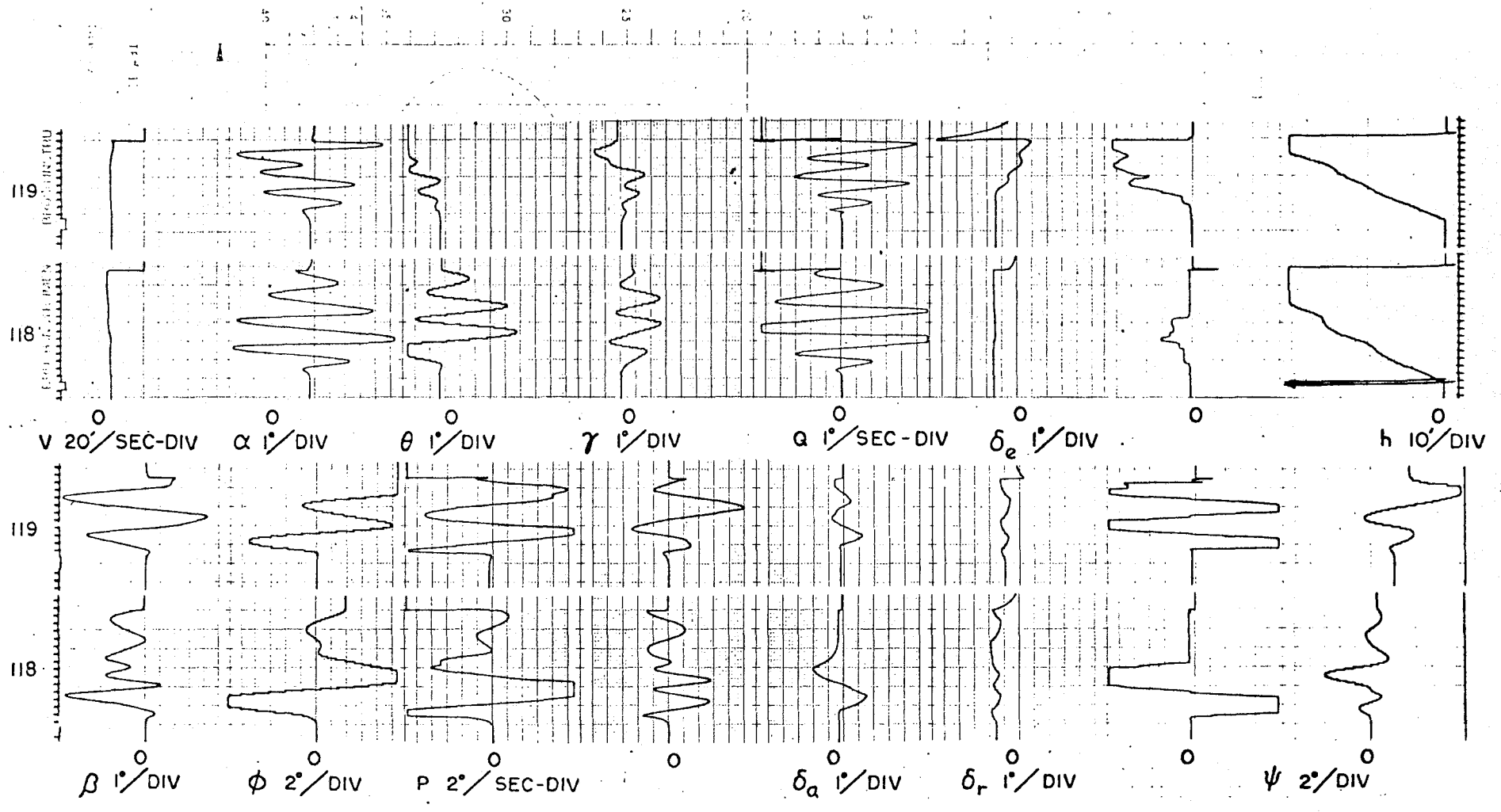
119
118
V 20'/SEC-DIV
α 1°/DIV
θ 1°/DIV
γ 1°/DIV
Q 1°/SEC-DIV
δe 1°/DIV
h 10'/DIV
β 1°/DIV
φ 2°/DIV
P 2°/SEC-DIV
δa 1°/DIV
δr 1°/DIV
ψ 2°/DIV

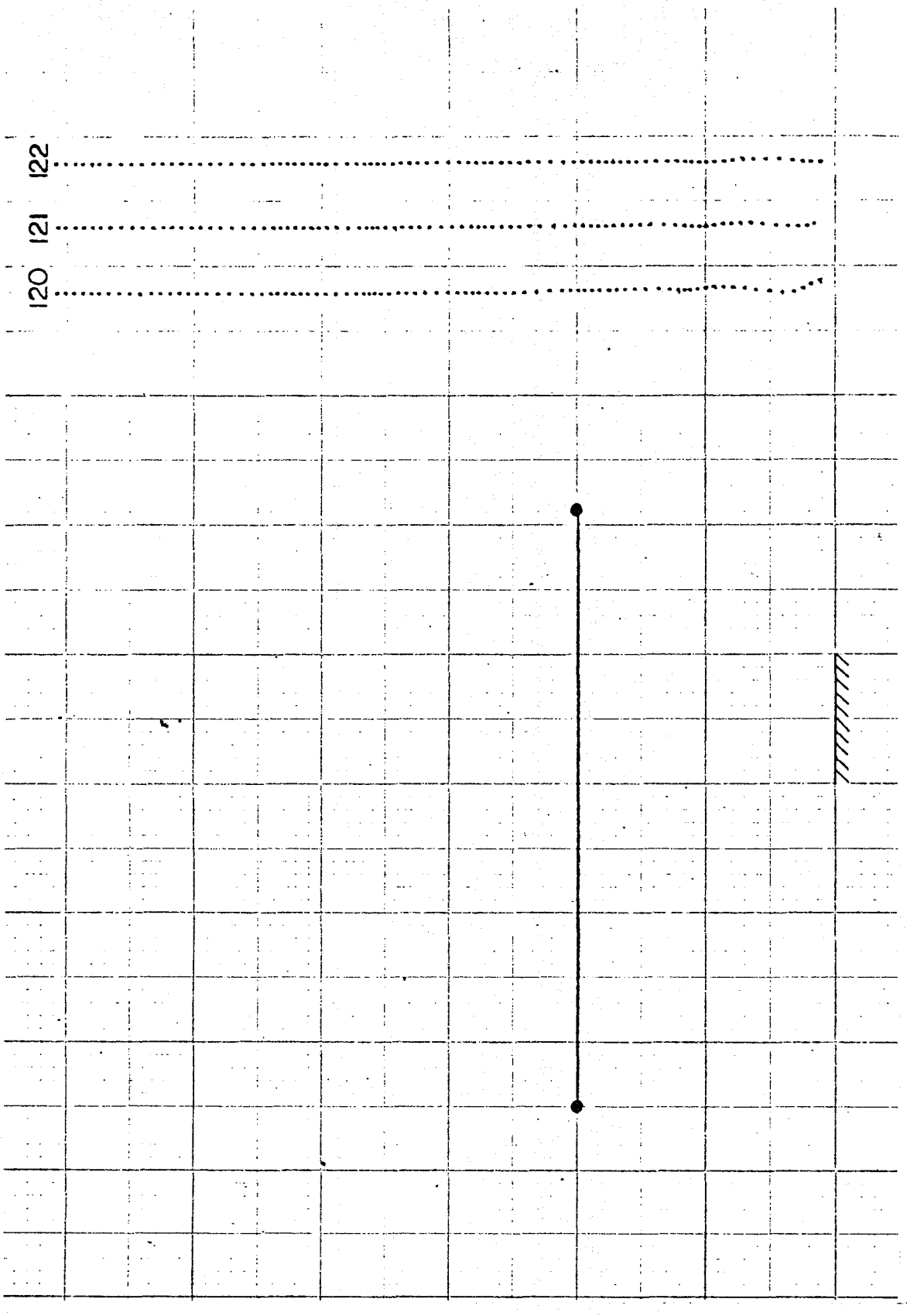
122
121
120

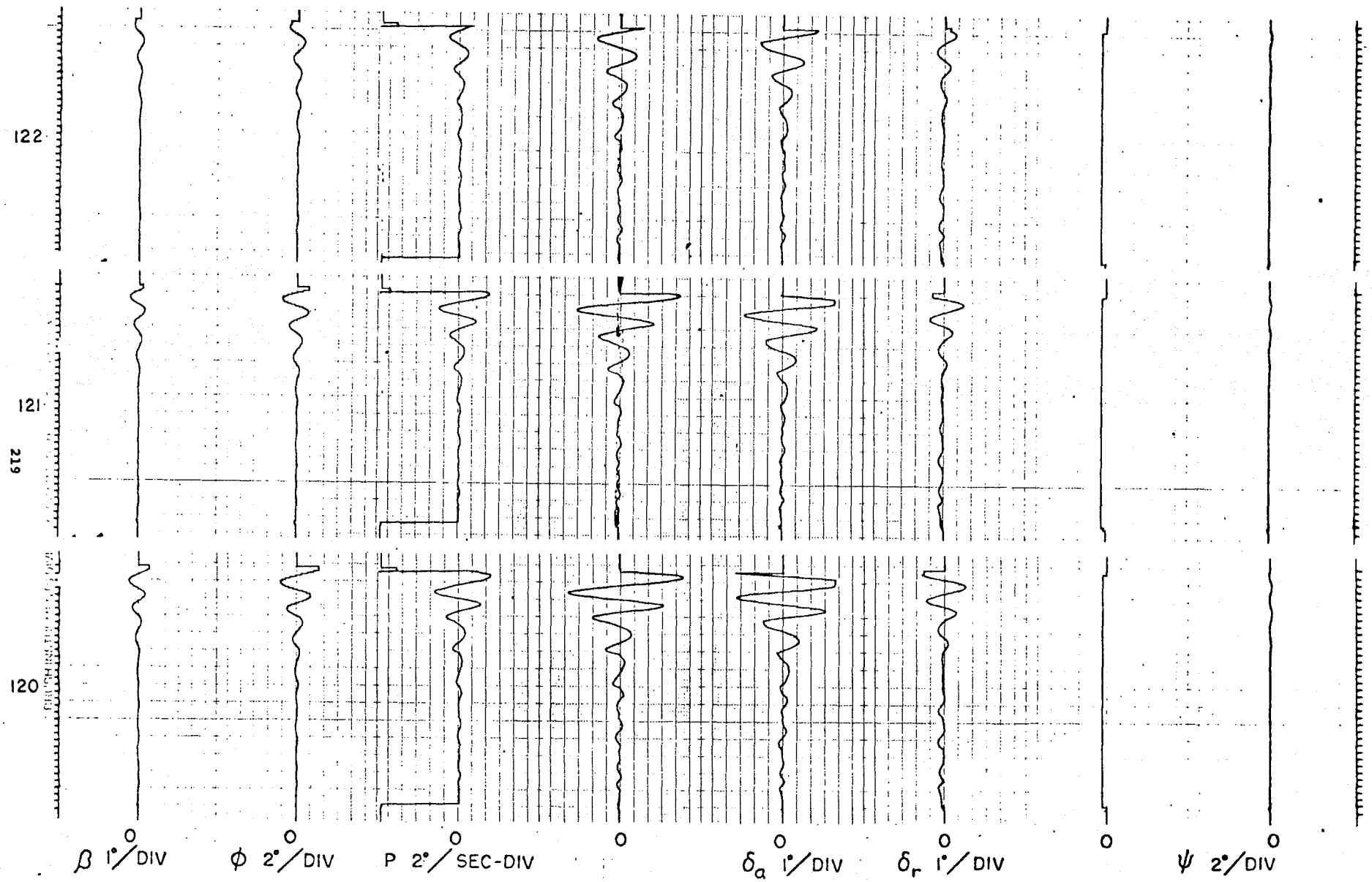
122
121
120
0
β 1°/DIV
0
φ 2°/DIV
0
P 2°/SEC-DIV
0
0
δa 1°/DIV
0
δr 1°/DIV
0
0
ψ 2°/DIV

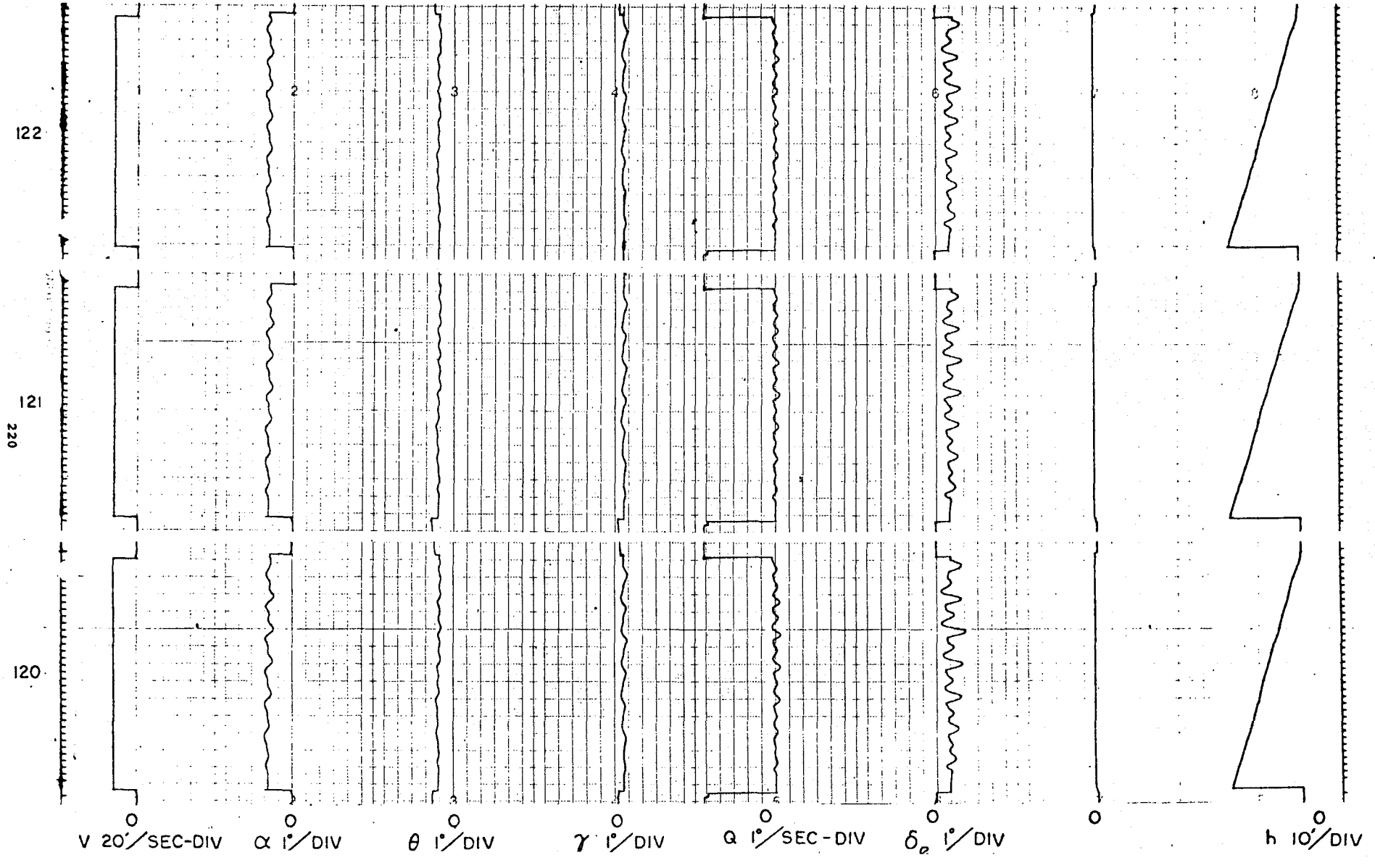
122
121
120
V 20'/SEC-DIV
α 1°/DIV
θ 1°/DIV
γ 1°/DIV
Q 1°/SEC-DIV
δe 1°/DIV
h 10'/DIV

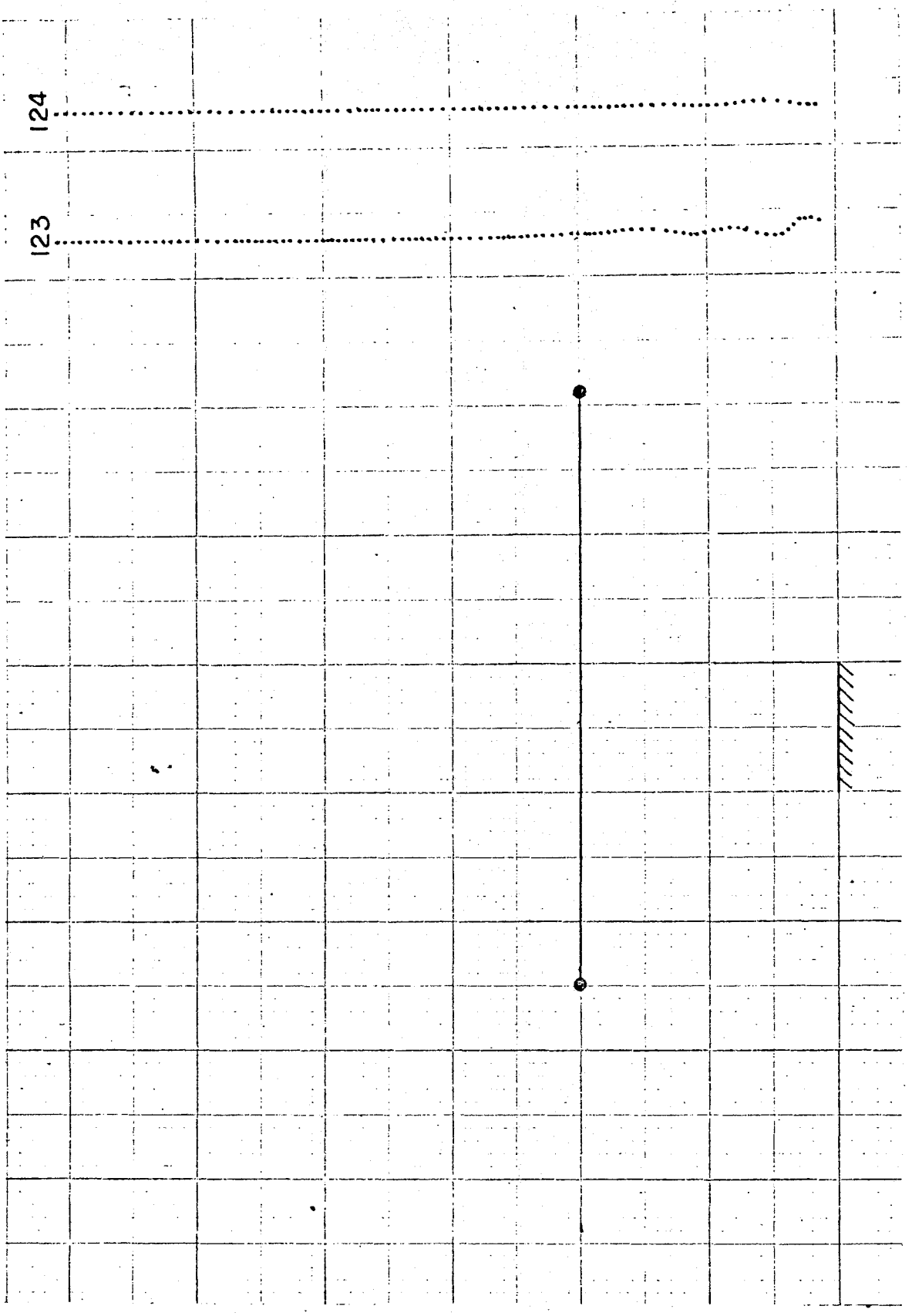
124
123

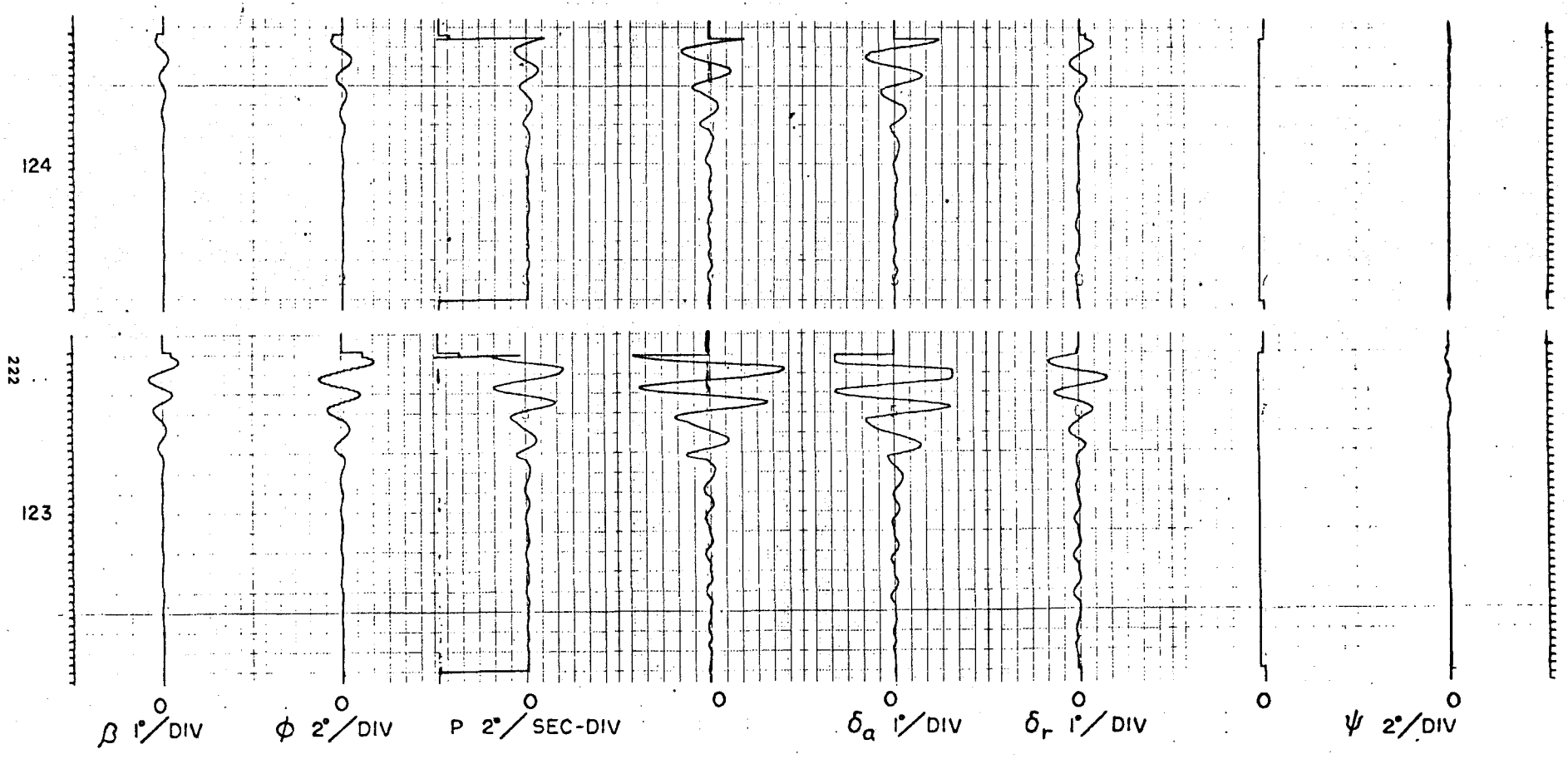
124
222
123
0
β 1°/DIV
0
φ 2°/DIV
0
P 2°/SEC-DIV
0
0
δa 1°/DIV
0
δr 1°/DIV
0
0
ψ 2°/DIV

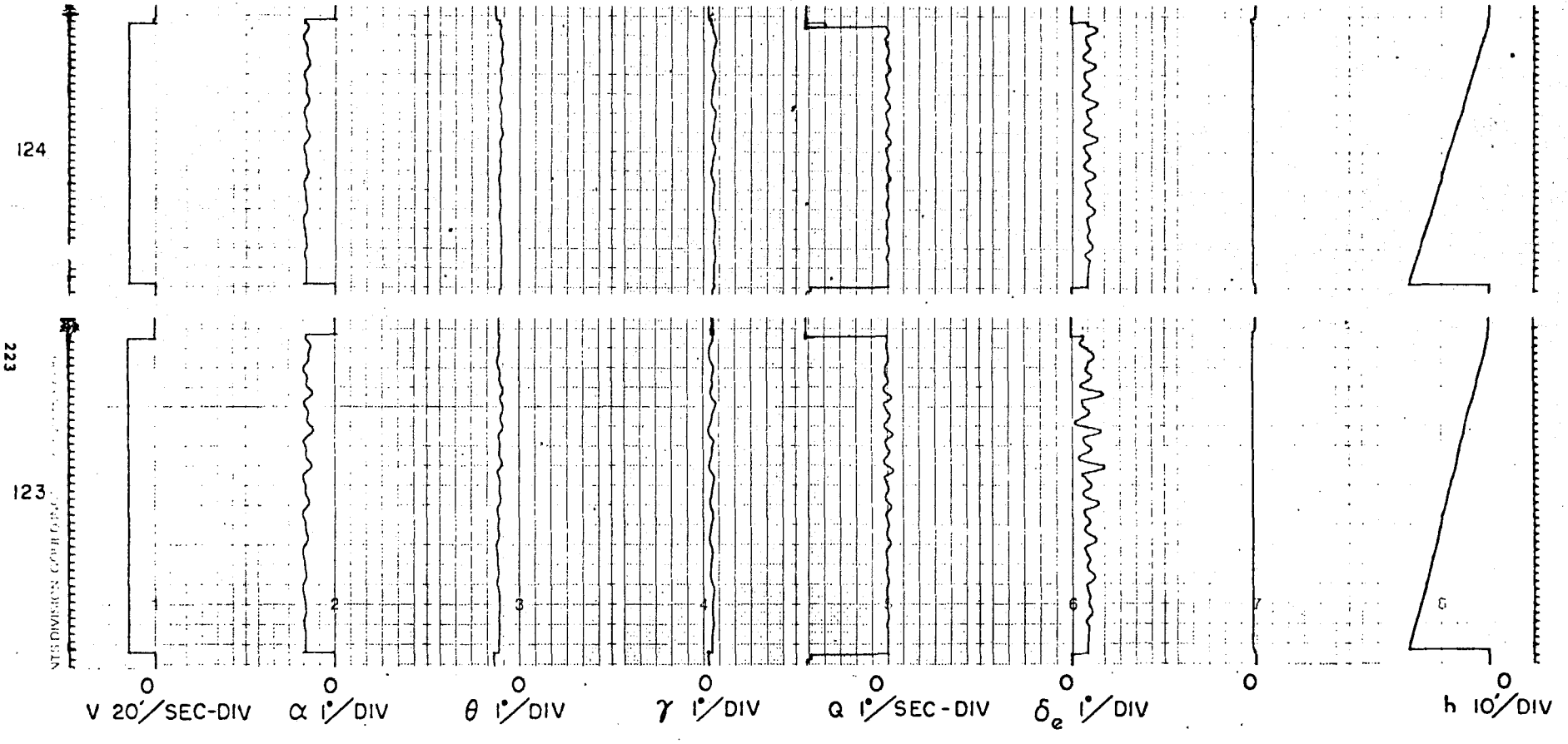
124
223
123
0
V 20'/SEC-DIV
0
α 1°/DIV
0
θ 1°/DIV
0
γ 1°/DIV
0
Q 1°/SEC-DIV
0
δe 1°/DIV
0
0
h 10'/DIV

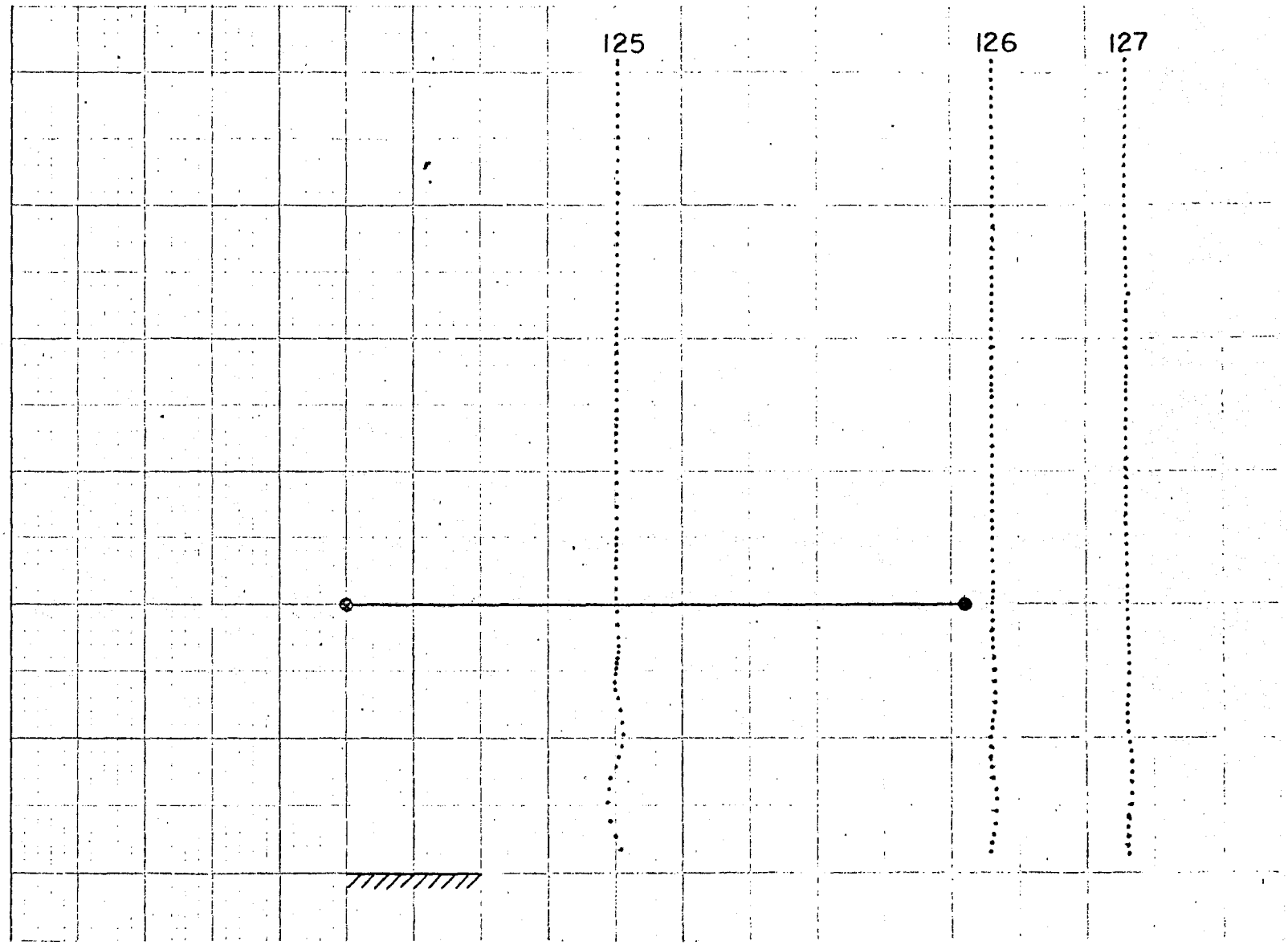
125
126
127

ψ 2°/DIV
0
0
δr 1°/DIV
0
δa 1°/DIV
0
0
P 2°/SEC-DIV
0
φ 2°/DIV
0
β 1°/DIV
0
127
126
125

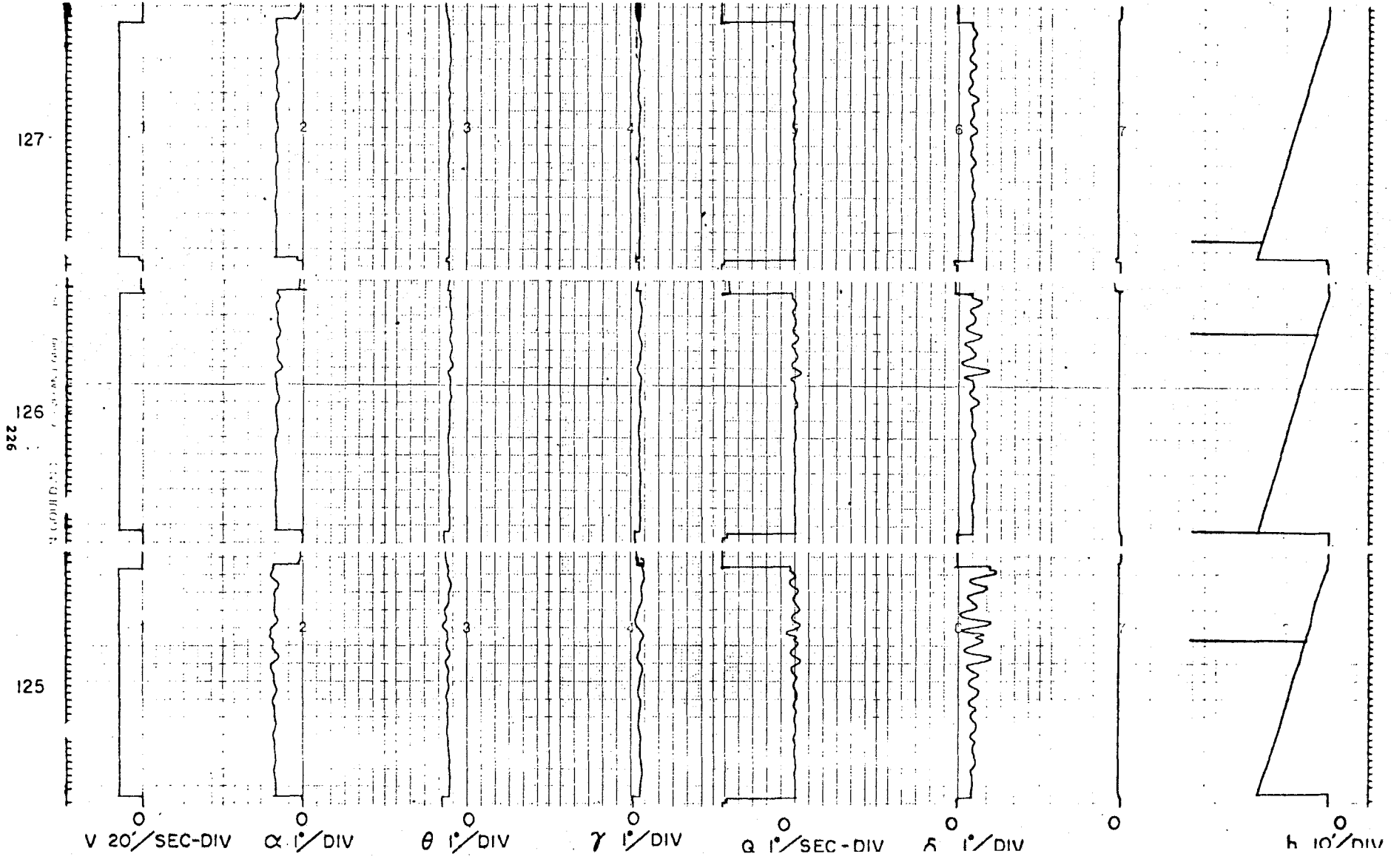
127
126
125
1
2
3
4
5
6
7
0
V 20'/SEC-DIV
α 1°/DIV
θ 1°/DIV
γ 1°/DIV
Q 1°/SEC-DIV
δ 1°/DIV
h 10'/DIV

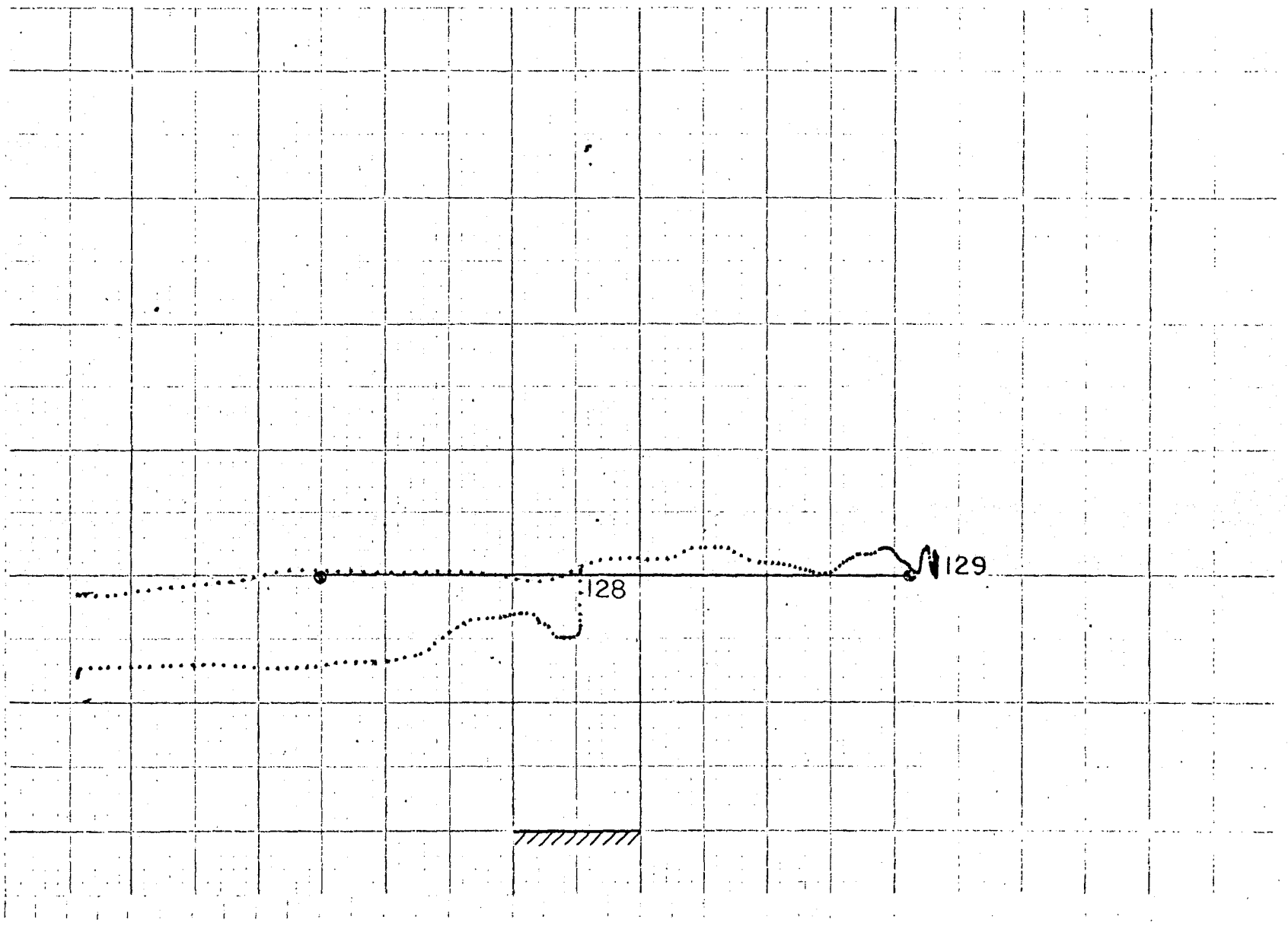
128
129

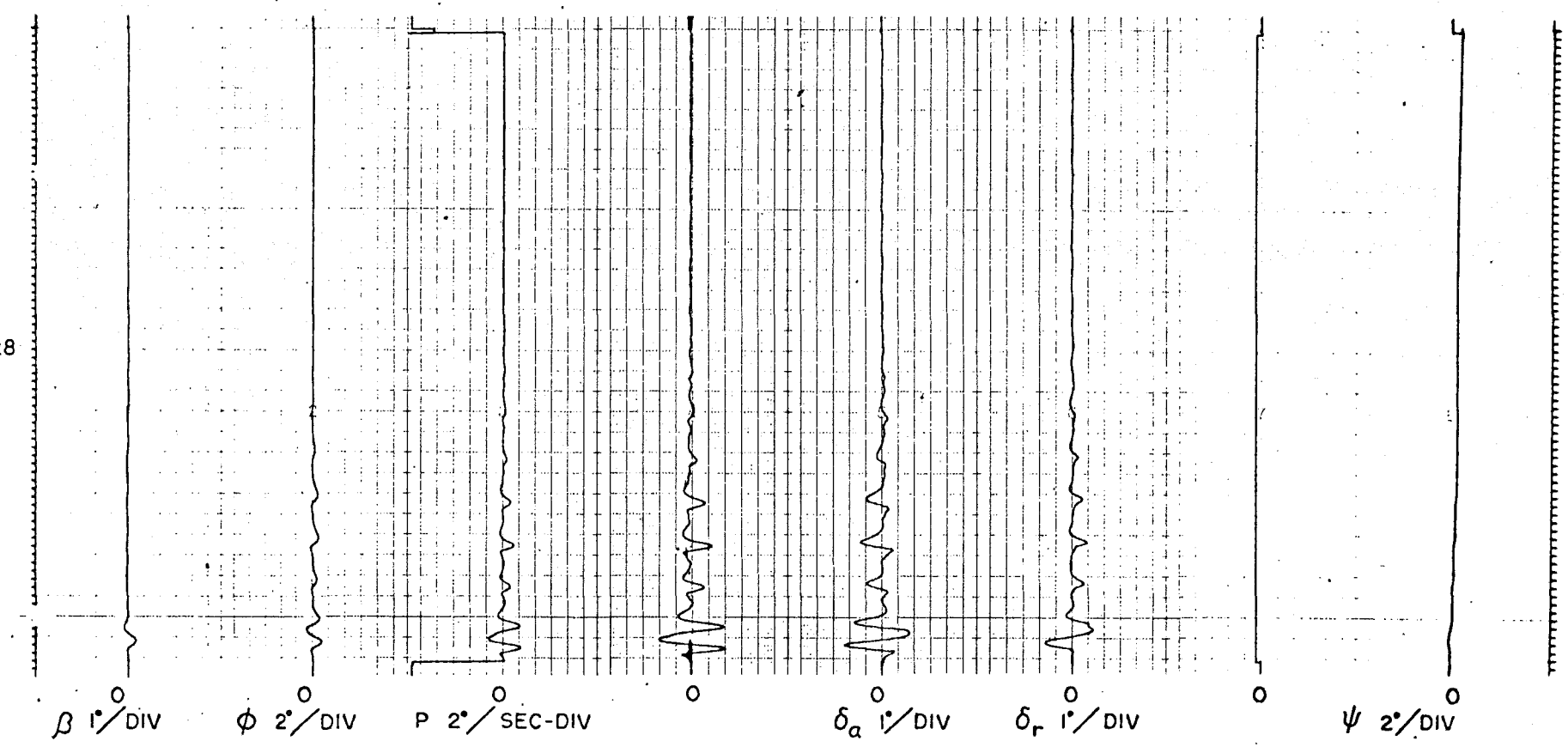
0
β 1°/DIV
0
φ 2°/DIV
0
P 2°/SEC-DIV
0
0
δa 1°/DIV
0
δr 1°/DIV
0
0
ψ 2°/DIV

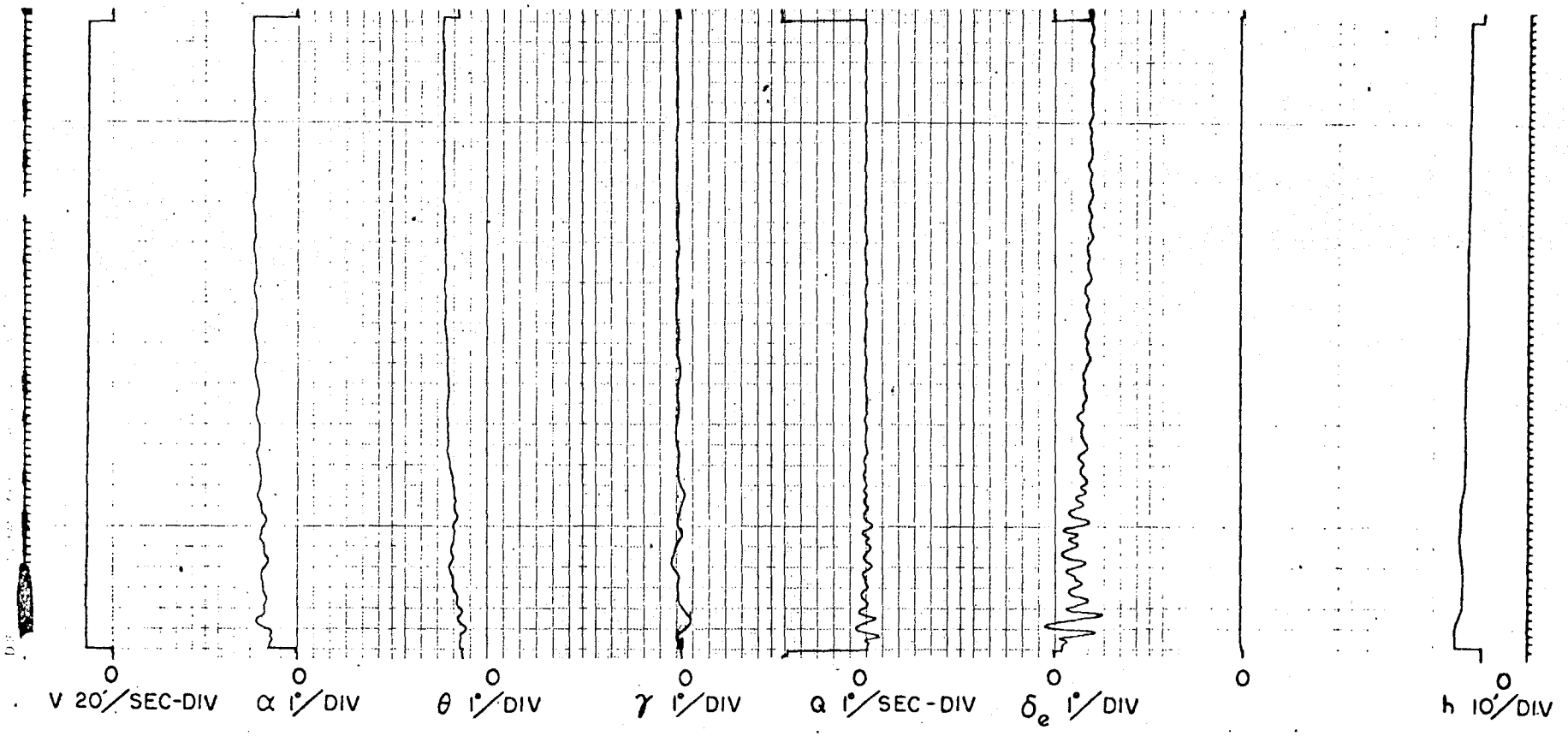
0
V 20'/SEC-DIV
0
α 1°/DIV
0
θ 1°/DIV
0
γ 1°/DIV
0
Q 1°/SEC-DIV
0
δe 1°/DIV
0
0
h 10'/DIV

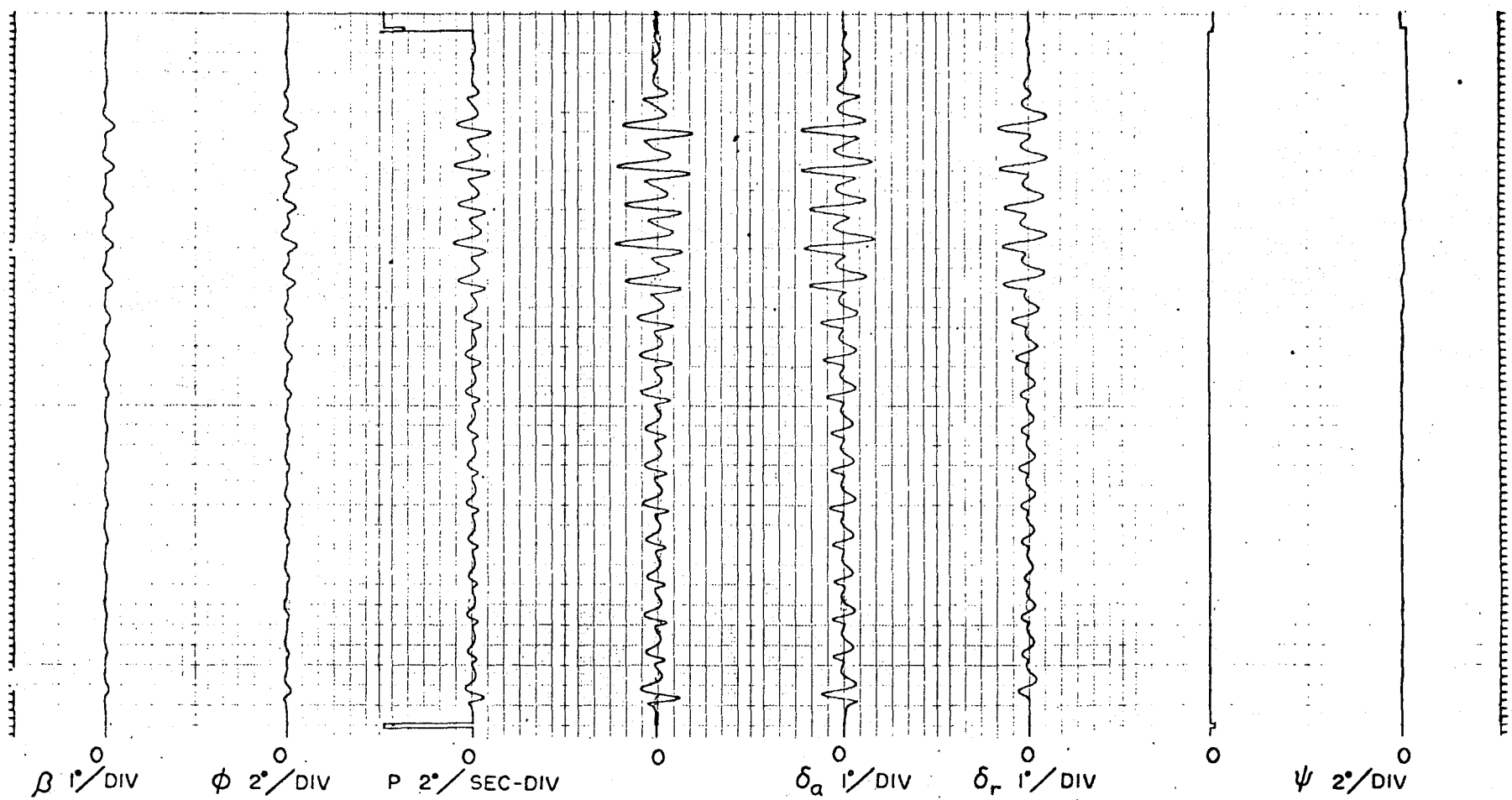
0
β 1°/DIV
0
φ 2°/DIV
0
P 2°/SEC-DIV
0
0
δa 1°/DIV
0
δr 1°/DIV
0
0
ψ 2°/DIV

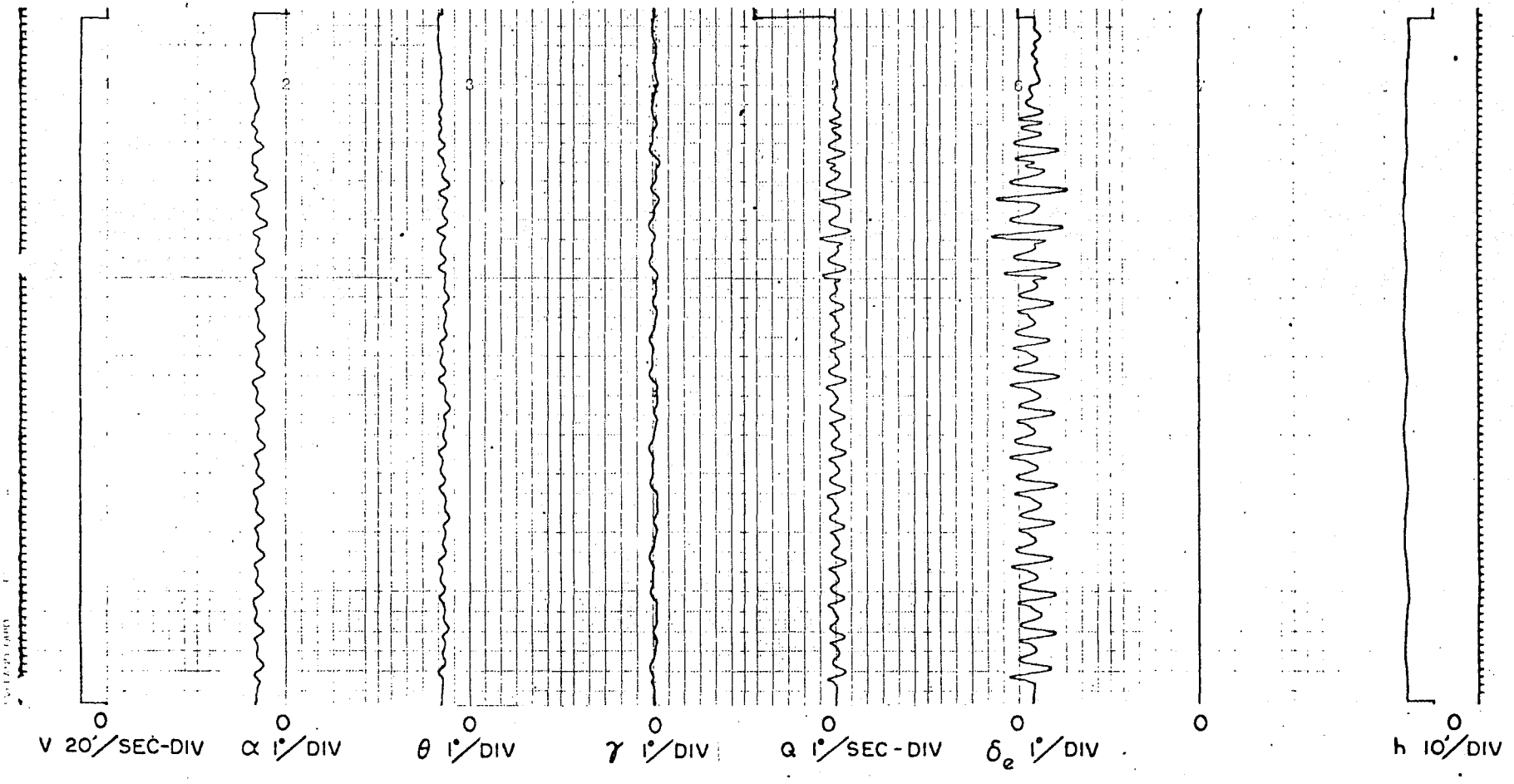
0
V 20'/SEC-DIV
0
α 1°/DIV
0
θ 1°/DIV
0
γ 1°/DIV
0
Q 1°/SEC-DIV
0
δe 1°/DIV
0
0
h 10'/DIV